

OPTICAL PHYSICS FOR OPTIMAL VOLUMETRIC BIOLOGICAL IMAGING

by

Kevin Keomanee-Dizon

A Dissertation Presented to the
FACULTY OF THE GRADUATE SCHOOL
UNIVERSITY OF SOUTHERN CALIFORNIA
In Partial Fulfillment of the
Requirements for the Degree
DOCTOR OF PHILOSOPHY

August 2021

Acknowledgements

After high school, I played Junior ice hockey for two years before college—I really had no idea what it meant to be a scientist or engineer—so it should be abundantly clear that there are many people to thank for their strong influences on me since then. Gratitude is especially directed at the following people.

To my advisor, Scott Fraser, for taking a chance on me. Instrumentation is a relatively expensive activity, and I’m indebted to Scott for giving me the full freedom to explore my interests, to tinker, and to let me fail, all of which were integral to my scientific development. Scott magically knew when to leave me alone and when to step-in and advise when I needed it most. He consistently provided the right combination of encouragement and criticism throughout my PhD, gently insisting that we strive for ambitious but crisp projects. Most important, he has taught me the joys and fun of the scientific pursuit, a spirit that I will always carry with me, in science and in life. I am hugely grateful, and it is a pleasure to thank him.

To my closest collaborator, Thai Truong, for being a co-conspirator in all my endeavors presented here. Thai picked me up when I was struggling at the end of my first year, and with Scott, created an ideal work environment that gave me mastery, purpose, and autonomy. The energy, feedback, and rigor Thai provided at every stage of my PhD cannot be overestimated. He set an example of an experimental physicist and taught me the rudiments of building optical microscopes. Working with both Scott and Thai has certainly shaped my thinking and left a mark on my view of optical imaging technologies; I hope some of that is recorded faithfully in this thesis.

The Translational Imaging Center (TIC) has been a nurturing environment for interdisciplinary exploration, in part because of the incredibly diverse group of researchers and the perspectives they bring to science and discussions. It has been great fun interacting and learning from all of these people, even when we disagree—perhaps especially then. Many thanks to Le Trinh, Francesco Cutrale, Mimo Arnesano, Dan Holland, Jason Junge, Simon Restrepo, Masahiro Kitano, Ryan Chen, Liana Engie, Daniel Koo, Wen Shi, Pu Wang, and our world-class espresso machine—we all would not have accomplished as much without it. Special thanks also to the neuro-optics group, particularly Sara Madaan, Matt Jones, Peter Luu, and Anna Nadtochiy. Beyond the TIC researchers, I’ve had the good fortune to collaborate with many individuals from different groups, departments, and institutions. Specific contributions to each chapter are listed in the sections marked “Manuscript Information”.

To Andrea Armani and Stephen Bradforth, for serving on my committee and filling gaps in my knowledge. I am also grateful to James Boedicker, who has provided mentorship and feedback ever since I started my graduate school adventure, and has made me feel welcome in the physics department and biophysics community. Peter Kuhn and Fabien Pinaud gave me my first foray into biophysics research and opened many doors for me. Stacey Finley and Jeff Phillips (Loyola Marymount) provided me with honest and crucial encouragement to go for the PhD. Gabe Foong (Unbound Consulting) introduced me to instrumentation in industry, planting the seeds of everything I’ve worked on since.

Over the last couple years of this journey, many remarkable people outside of southern California have shared their time, ideas, resources, and/or advice with me: Eric Betzig, Gokul Upadhyayula, and Hernan Garcia at UC Berkeley, Andrew York at Calico, and Thomas Gregor and Josh Shaevitz at Princeton. I have learned and benefited enormously from my interactions with each of them.

I received financial support through an Alfred E. Mann Doctoral Fellowship. The work reported in this thesis was additionally funded by the National Institutes of Health (1R01MH10-7238-01); the National Science Foundation (1608744, 1650406, 1828793); the Human Frontier

Science Program (RGP0008/2017); the Gordon and Betty Moore Foundation (3396); a Jet Propulsion Laboratory Research Subcontract(1632330); and the USC-Olympus Innovation Partnership in Multiscale Bioimaging. I also need to thank the following administrative staff across campus for making my life as a graduate fellow/student easier: Jona Cura, Georgiann Keller, Socorro Aguirre, Claire Cato, William Yang, Mischal Diasanta, and Susan Cooper.

The completion of a thesis involves much more than the scientific enterprise. Outside of lab, my life in the City of Angels has been nothing short of wonderful because of my friends: Nick, Dan, Jhoel, Steve, Eric, Brian, Moe, Charles, Ryan, and Lauren. Thanks for reminding me that there is much more to life. Quinn, thanks for weathering the highs and lows of this PhD; this entire process has been much better with you by my side.

Finally, I would like to thank my family, especially my mother. Life is full of surprises, isn't it? Thanks mom for your unconditional love, support, and patience in my very nonlinear path.

Table of Contents

Acknowledgements	ii
List of Tables	viii
List of Figures	ix
Abstract	xiii
Chapter 1: Introduction	1
1.1 Fluorescence microscopy	2
1.1.1 Fluorescence	3
1.1.2 Ultrashort laser pulses	6
1.1.3 Gaussian beam optics	7
1.1.4 Image formation: theory and basic principles	10
1.1.5 Point-spread function engineering	15
1.2 Volumetric imaging	17
1.2.1 Light fields	20
1.3 The photon budget	24
1.4 Overview	26
Chapter 2: A versatile, multi-laser twin-microscope system for light-sheet imaging	28
2.1 Introduction	28
2.2 Instrument design, integration, and configuration	31
2.2.1 Multi-laser subsystem	34
2.2.2 Illumination-scanning optics subsystem	37
2.2.3 Detection subsystem	39
2.2.4 Sample mounting and motion control subsystem	41
2.2.5 Instrument control module	44
2.2.6 Auxiliary module	44
2.3 Instrument performance	45
2.3.1 Resolution characterization	45
2.3.2 Light-sheet imaging of the beating zebrafish heart	48

2.3.3	Imaging of thick, patient-derived tumor organoids	50
2.3.4	Whole-brain functional imaging of behaving zebrafish	54
2.4	Discussion	59
2.5	Ethical approval statement	60
2.6	Supplementary Material	60
2.6.1	Simulations of scan performance using an achromatic doublet	60
2.7	Acknowledgements	62
2.8	Manuscript information	62
2.8.1	Previously published as	62
2.8.2	Author contributions	62
Chapter 3: Extended depth-of-field improves light-sheet microscopy at high numerical aperture		64
3.1	Introduction	64
3.2	Results	70
3.2.1	Simulations of imaging performance	70
3.2.2	Experimental imaging performance	73
3.2.3	ExD-SPIM reduces photobleaching <i>in vivo</i>	73
3.2.4	ExD-SPIM improves brain-wide imaging of neural activity	78
3.3	Discussion	78
3.4	Methods	80
3.4.1	Theory and numerical simulations	80
3.4.2	Microscope optics	82
3.4.3	Sample preparation and imaging conditions	83
3.5	Acknowledgements	84
3.6	Manuscript information	85
3.6.1	Author contributions	85
Chapter 4: High-contrast, synchronous volumetric imaging with selective-volume illumination microscopy		86
4.1	Introduction	86
4.2	Results	87
4.2.1	Overview of SVIM instrument	87
4.2.2	SVIM imaging performance	89
4.2.3	SVIM enhances imaging of biological components moving in 3D	98
4.2.4	SVIM enhances brain-wide functional neuroimaging	108
4.3	Discussion	114
4.4	Methods	115
4.4.1	Microscopy setup and implementation	115
4.4.2	Sample handling and imaging procedure	119
4.4.3	Light-field image processing and 3D reconstruction	120
4.4.4	Image analysis and presentation	121
4.4.5	Image contrast, simulated noise, and effective resolution	123
4.4.6	Data availability	125
4.4.7	Code availability	125

4.5	Supplementary Information	126
4.5.1	Discussion on implementations of selective-volume illumination	126
4.5.2	Volumetric imaging rate normalized by the number of diffraction-limited voxels	128
4.6	Acknowledgements	133
4.7	Manuscript information	133
4.7.1	Previously published as	133
4.7.2	Author contributions	133
Chapter 5:	Single-objective selective-volume illumination microscopy enables high-contrast light-field imaging	135
5.1	Introduction	135
5.2	Axial single-objective selective-volume illumination microscopy	137
5.3	Results	142
5.3.1	ASO-SVIM improves image contrast and effective resolution <i>in vivo</i>	142
5.3.2	ASO-SVIM improves brain-wide activity imaging	147
5.3.3	High-throughput imaging of whole-brain blood flow in zebrafish	149
5.4	Discussion	154
5.5	Microscope optics	155
5.5.1	ASO-SVIM: oblique-angled one-photon excitation and wide-field illumination modes	155
5.5.2	2P-ASO-SVIM: two-photon excitation mode	158
5.5.3	Light-field detection and reconstruction	159
5.5.4	SPIM: one-photon and two-photon light-sheet imaging modes	159
5.5.5	Instrument control	162
5.5.6	Characterizing system resolution	162
5.6	<i>k</i> -space filtering	163
5.7	Supplementary material	168
5.7.1	Improving the signal rate and volumetric imaging speed of 2P-ASO-SVIM	168
5.7.2	Tradeoffs associated with light-field detection in ASO-SVIM	170
5.8	Acknowledgements	171
5.8.1	Funding	171
5.9	Manuscript information	171
5.9.1	Previously published as	171
5.9.2	Author contributions	172
References		173
Appendices		181
A	Detailed list of the main flex-SPIM parts	182
B	List of the key SVIM parts	205
C	SVIM imaging and reconstruction parameters	210

List of Tables

2.1	flex-SPIM functional subsystems and modules	33
4.1	Volumetric imaging rate normalized by the number of diffraction-limited voxels	131
A1	List of main flex-SPIM components	183
A2	Part numbers and descriptions of key components of SVIM setup	206
A3	SVIM imaging and reconstruction parameters for vasculature results	210

List of Figures

1.1	Jablonski diagram of the electronic states of a fluorescent molecule	4
1.2	Selective excitation with multiphoton absorption	5
1.3	Optical pulse train from a mode-locked laser	8
1.4	Propagating Gaussian beam	10
1.5	Bessel beam properties	18
1.6	Overview of light-field microscopy	23
1.7	The limited photon budget	25
2.1	Light-sheet microscopy principle	30
2.2	3D opto-mechanical model of the twin-microscope system	34
2.3	Panoramic photograph of the assembled twin-microscope system	35
2.4	Schematic diagram of multi-laser and illumination-scanning optics subsystems of the instrument	36
2.5	Photograph of an assembled microscope-twin with upright detection	40
2.6	SPIM imaging of intracellular calcium for capturing neuronal activity	43
2.7	Schematic of control signal sequences for objective-scanning mode	45
2.8	System imaging performance and characterization	47
2.9	1P-SPIM imaging of the beating zebrafish heart	48
2.10	Cardiac light-sheet imaging	49

2.11	1P- and 2P-SPIM imaging of thick tumor organoids derived from a patient with colorectal cancer	51
2.12	Volume rendering of patient-derived tumor organoids	53
2.13	Optical transfer function comparisons of patient-derived tumor organoids . .	54
2.14	Whole-brain functional imaging at single-cell resolution in behaving larval zebrafish	56
2.15	2P-SPIM recording of neural activity in a behaving animal	58
2.16	Simulations of scan performance using an achromatic doublet	61
3.1	Simplified schematic of extended depth-of-field light-sheet microscope	66
3.2	Theoretical principle and simulations of extended detection point-spread functions	67
3.3	Extended depth-of-field light-sheet microscopy at high numerical aperture . .	68
3.4	Numerical simulations of ExD-SPIM imaging	71
3.5	Experimental demonstration of improving light-sheet collection with depth-of-field extension	74
3.6	ExD-SPIM offers low photodamage <i>in vivo</i>	76
3.7	ExD-SPIM improves brain-wide imaging of neural activity	79
4.1	Selective-volume illumination microscopy enhances LFM for the synchronous imaging of 3D samples	88
4.2	Imaging of sub-diffractive fluorescent beads to characterize resolution of SVIM	90
4.3	Higher contrast achieved by SVIM	92
4.4	SVIM offers improved contrast over conventional wide-field LFM	93
4.5	Simulation of SVIM contrast degradation with increased background noise .	95
4.6	Enhanced effective resolution enabled by the higher contrast of SVIM	96
4.7	SVIM enables fast, high-contrast, volumetric imaging of live biological systems	99
4.8	Raw light-field-image movie of the bacterial flow around the squid light organ, recorded with SVIM	101
4.9	Comparison of reconstructed movie of the bacterial flow around the squid light organ, recorded with wide-field LFM versus with SVIM	102
4.10	3D flow fields of bacteria around the squid light organ, recorded with SVIM .	103

4.11	3D blood flow and endocardium motion of the entire larval zebrafish beating heart	104
4.12	3D trajectories of individual blood cells flowing through the larval zebrafish beating heart	105
4.13	Contrast enhancement of SVIM in imaging the zebrafish beating heart and blood flow	106
4.14	Functional neuroimaging with SVIM	109
4.15	Zoomed-in, 3D-rendered views of the zebrafish spontaneous brain activity . .	110
4.16	Light-evoked brain response captured by 2P-SVIM	112
4.17	Schematic of the SVIM/SPIM optical setup	116
4.18	SVIM enabled single-bacterium-resolution imaging and quantification of 3D bacterial flow tracks around the squid light organ.	132
5.1	Axial single-objective selective-volume illumination (ASO-SVIM)	139
5.2	System resolution	141
5.3	ASO-SVIM improves contrast and effective resolution in live imaging of zebrafish larvae	143
5.4	ASO-SVIM enhances effective resolution across large tissue volumes	145
5.5	Comparison of line cuts through vessel structures <i>in vivo</i>	146
5.6	ASO-SVIM enhances large-scale <i>in vivo</i> recording of neural activity	148
5.7	2P-ASO-SVIM brain-wide activity imaging	149
5.8	ASO-SVIM enables high-throughput imaging of whole-brain blood flow in zebrafish larvae	150
5.9	Multicolor, high-throughput imaging of nine zebrafish mounted in a standard multi-well plate	151
5.10	1P-ASO-SVIM imaging of blood cells flowing across the entire zebrafish brain	152
5.11	Volumetric view of whole-brain blood flow	153
5.12	Simplified schematic diagram of ASO-SVIM	156
5.13	3D opto-mechanical model of the ASO-SVIM light-field detection path . .	160
5.14	<i>k</i> -space filtering algorithm	164

5.15 <i>k</i> -space filtering reduces artifacts and improves volume reconstruction with uncompromised resolution	166
5.16 <i>k</i> -space filtering improves volume reconstruction quality <i>in vivo</i>	167

Abstract

This thesis describes four applications of optical physics for volumetric imaging, all involving the optimization of photons for deeper, faster, gentler, higher resolution, and more useful biological imaging. In Chapter 2, we present a versatile light-sheet imaging instrument that combines two independently controlled microscope-twins, built so that they can share the same multi-laser source, increasing the throughput and decreasing the cost. We demonstrate the instrument's versatility for biological investigation by imaging a variety of challenging systems, ranging from thick cancer organoids to whole-brain neural activity in a behaving animal. In Chapter 3, we improve light-sheet microscopy by instantaneously extending the depth-of-field, offering up to a threefold enhancement in signal collection and greater sensitivity to transient cellular interactions compared to a conventional high NA system. In Chapter 4, we introduce selective-volume illumination microscopy (SVIM), combining the high contrast associated with light-sheet microscopy and the high synchronous volumetric acquisition rates of light-field microscopy (limited only by the detector and available signal). We use SVIM to perform synchronous, cellular resolution imaging of volumes spanning hundreds of microns, at rates up to two orders of magnitude faster than standard light-sheet approaches. In Chapter 5, we adapt SVIM to a single-objective geometry, making it accessible to almost any fluorescence sample and significantly broadening its utility for biological research.

The Starry Messenger

Revealing great, unusual, and remarkable spectacles, opening these to the consideration of every man, and especially of philosophers and astronomers; as observed by Galileo Galilei, Gentleman of Florence, Professor of Mathematics in the University of Padua, with the aid of a spyglass, lately invented by him, In the surface of the Moon, in innumerable Fixed Stars, in Nebulae, and above all in four planets swiftly revolving about Jupiter at differing distances and periods, and known to no one before the author recently perceived them and decided that they should be named The Medicean Stars.

Galileo Galilei, 1610 [1]

1

Introduction

Most of what we recognize as the phenomena of life are not properties of stationary structures but emerge from dynamic interactions among many elements over time: Many genes and proteins determine the fate of a cell, many cells move and coordinate in the development of an embryo, and many neurons shape our thoughts and memories. Despite the progress in sequencing the genomes of hundreds of animals, from worms all the way to us, we do not understand what the vast majority of genes and their proteins actually do within an organism. Even for those proteins whose function has been identified, the precise nature of how the proteins function within their parent organism is still an abiding mystery, as most functional conclusions coming from biochemistry and molecular biology are indirect. The

major challenge with these techniques is that we cannot see what the proteins do, where they are, how they move, and how they interact as a system.

Optical imaging offers a noninvasive and nondestructive means to *watch* biological events as they unfold in real time, directly in living systems. Although the optical microscope has been around for ~ 400 years [2], we live today in a very special time. In the last few decades, parallel developments in photodetectors, laser physics, computer science, and genetically encoded fluorescent proteins have converged, and the result has been light being harnessed in new ways, fundamentally changing how microscopes are designed and operate. These transformative advances now offer us the ability to observe the organization and dynamics of biological systems at high resolution in space and time (4D: x , y , z , and t).

This thesis is devoted to extending the current capabilities of optical microscopy for volumetric biological imaging. We first provide an introduction to modern optical microscopy, starting with fluorescence, laser beam propagation, and the basic theoretical principles of imaging before progressing to more advanced concepts such as point-spread function engineering, light sheets, and light fields. With this background in mind, we consider the photon budget—the challenges and tradeoffs in biological imaging that underscore our program of research. Then, we outline this dissertation.

1.1 Fluorescence microscopy

This section is intended to give insight into fluorescence microscopy. Fluorescence as an optical signal and mode of contrast are discussed, and Gaussian beam propagation characteristics are introduced. General principles and practical aspects of how images are formed in wide-field microscopy, as well as their connection to Fourier theory are explained. In addition, we describe a class of non-diffracting beam and their unique properties.

1.1.1 Fluorescence

The development of fluorescent probes that bind to specific structures within the cell has made fluorescence microscopy a very powerful technology. Fluorescence is the ability for a molecule to absorb light of a specific wavelength and reemit light with a longer wavelength and lower energy. Some of the energy is lost to the environment through vibrational relaxation (i.e., heat), and the difference between the peak absorption and emission wavelength is known as the Stokes shift. The availability of robust lasers offering high-intensity monochromatic light have made them ideal light sources for efficiently exciting the fluorescent probes [3] (for an excellent historical account of lasers in microscopy, see Chapter 1 of Pawley [4]). Separating the fluorescence from the scattered or reflected excitation light yields target-specific, bright probes that label the structure of interest within the sample.

The electronic states of a fluorescent molecule can be described with the Jablonski diagram shown in Fig. 1.1. A molecule residing in its ground state S_0 is excited by a photon of energy $E = hv$, with Planck's constant h and frequency v , into an excited state S_1 , whose energy gap to the ground state matches the energy of the absorbed photon. From the excited state, it relaxes (within < picosecond) to the lowest S_1 state, and then typically drops back down into the S_0 state by spontaneous decay, emitting a (fluorescent) photon within a characteristic stochastic lifetime τ_f (on the order of nanoseconds). Typically, the fluorescence intensity scales linearly with the excitation intensity.

In addition to more conventional linear fluorescence, Maria Göppert-Mayer worked out the quantum mechanical theory of an atom simultaneously absorbing two photons to produce an atom in an excited electronic state S_1 , whose energy gap to the ground state S_0 matches the addition of the energies of the two photons (Fig. 1.1) [5]. This process depends on the two (or more) photons both interacting with the molecule simultaneously (within a femtosecond), resulting in a quadratic (or supra-quadratic) dependence of the fluorescence on the excitation intensity, and thus is a nonlinear optical effect. The absorption cross section for such an event is ~ 1 GM (10^{-50} cm⁴s; “GM” is the unit for two-photon absorption, in

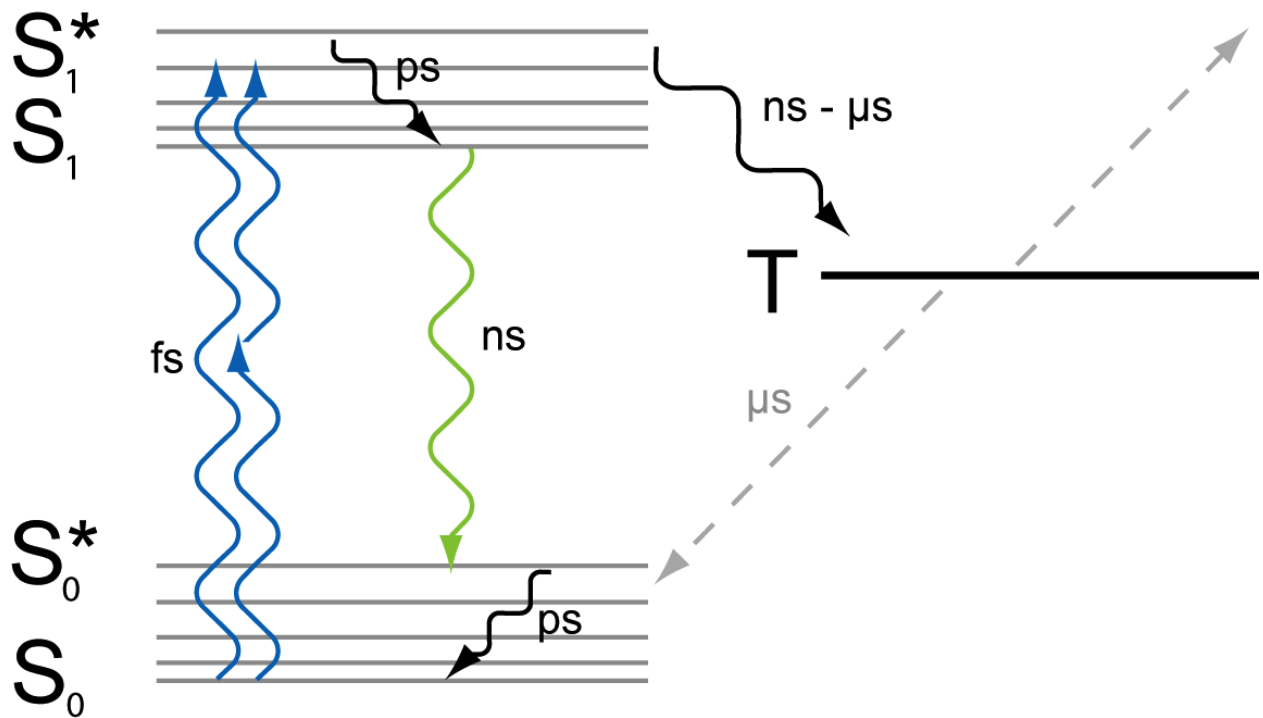


Figure 1.1: Jablonski diagram of the electronic states of a fluorescent molecule and their respective time scales. A fluorescent molecule is excited by one- or multi-photon absorption (blue arrows) to an excited S_1^* state and vibrationally relaxed to S_1 , where all further transitions occur. From here, it can cross non-radiatively to the spin-forbidden triplet state T, or fluoresce by spontaneous emission (green arrow). After fluorescence emission the molecule relaxes back into the lowest S_0 state. T is often involved in photobleaching. fs: femtosecond (10^{-16} s); ps: picosecond (10^{-12} s); ns: nanosecond (10^{-9} s); μ s: microsecond (10^{-6} s).

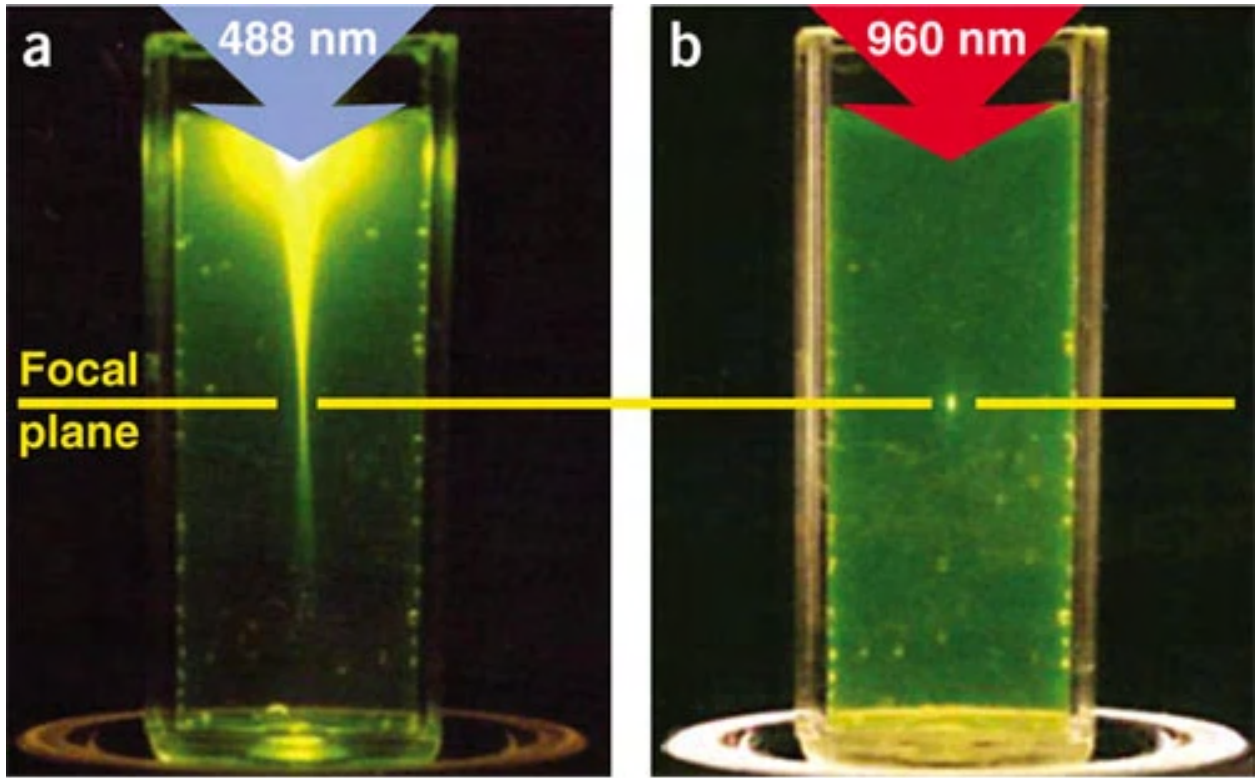


Figure 1.2: Selective excitation with multiphoton absorption. **(a)** Single-photon excitation of fluorescein with focused 488-nm light (0.16 NA). Blue light is absorbed throughout the entire path (above and below the focus) as the laser beam travels through the dye, since the amount of fluorescence is linearly proportional to the intensity of the light. **(b)** Two-photon excitation using focused (0.16 NA) femtosecond pulses of 960-nm light. Red light is absorbed only at the focal volume of the laser beam, since the amount of fluorescence is proportional to the intensity squared. Adapted from [8].

honor of Maria Göppert-Mayer) for most dyes [6]. The nonlinearity of the excitation gives rise to intrinsic localized excitation in three dimensions (3D): fluorescence occurs only at the focal volume, where the intensity of the laser beam is high enough to give rise to the nearly simultaneous absorption of two (or more) photons (Fig. 1.2). Further, the longer, near-infrared excitation wavelength reduces both unwanted scattering and linear absorption compared to the visible. These attributes of multiphoton microscopy have redefined the optical penetration depth of bioimaging [7–11].

Green fluorescent protein

Green fluorescent protein (GFP) and its family of spectral variants are one of the most important innovations in bioimaging [12–14]. A gene encoding for *any* protein of interest in an organism can in principle be fused with a gene encoding for a fluorescent protein (for example GFP). This means that when the protein is expressed, the protein is also fluorescently labeled; the fluorescent gene, cloned from a jellyfish, can even be passed to the next generation of offspring. Genetically encoded fluorescent proteins enable direct visualization of structure and function *in vivo*—within intact living cells or organisms. Osamu Shimomura, Martin Chalfie, and Roger Tsien were awarded the 2008 Nobel Prize in Chemistry for the discovery and development of GFP. Fluorescent proteins are ubiquitous and routinely used today for a myriad of applications, from the dynamics of single molecules [15] to micrometastasis formation in an animal [16].

1.1.2 Ultrashort laser pulses

Although Göppert-Mayer originally predicted multiphoton absorption in her PhD thesis in 1930 and paper in 1931 [5], it wasn't until the invention of the laser by Theodore Maiman 30 years later [17] that the experimental effect was observed [18]. Because of the squared dependence of the signal on the laser intensity, focusing a laser beam alone is not enough to make two-photon microscopy practical. To generate high enough intensity for multiphoton interactions to occur at the focal volume, a pulsed laser is used to increase the probability of two (or more) photons simultaneously interacting with a molecule, increasing the *peak* power while still keeping the average power relatively low (Fig. 1.3). It is natural to wonder: how is the laser excitation intensity I linked to a nonlinear optical process OP of order n ? Given $OP_n \sim I^n$, it is defined as [19]:

$$OP_n \sim \left(\frac{T}{\tau}\right)^{n-1} P_{mean}^n, \quad (1.1)$$

where T is the time between pulses, τ is the pulse width, and P_{mean} is the average power. The laser duty cycle parameters are T and τ , with the pulse repetition rate $f = \frac{1}{T}$. The peak power P_{peak} can be calculated from the energy per pulse E and laser duty cycle:

$$P_{peak} = \frac{E}{\tau} = \frac{P_{mean}}{f \cdot \tau}. \quad (1.2)$$

Common commercial laser systems used to produce ultrashort pulses in microscopy include titanium-sapphire (Ti:Sapphire) and ytterbium, and continue to make multiphoton microscopy accessible to research labs, both on the instrument refinement side and on the biological applications. These ultrafast lasers typically operate at $f = 80$ MHz and $\tau = 140$ fs, with a tunable wavelength range of 900 to 1300 nm and P_{mean} limited to hundreds of mW to minimize photo-induced damage (see Section 1.3). The upper limit of P_{mean} in part motivates the instrument we introduce in Chapter 2. Tailoring the laser duty cycle to the specific multiphoton imaging modality is a new, fruitful avenue of research [19, 20], and we discuss this in our own work in Chapter 5 (Section 5.7.1).

1.1.3 Gaussian beam optics

Light emitted from a laser is well approximated as having a Gaussian profile. The Gaussian beam is a solution of the paraxial wave equation in 2D [21]. In the ray optics approximation of a propagating beam, it is assumed that all rays propagate close to the optical axis and at relatively small angles (i.e. low focusing). The electric field distribution of a Gaussian beam propagating along the x axis is given by [22]:

$$\mathbf{E}(\mathbf{r}, x) = \mathbf{E}_0 \frac{\omega_0}{\omega(x)} \exp\left(\frac{-\mathbf{r}^2}{\omega(x)^2}\right) \exp\left(-i\left(kx + k\frac{\mathbf{r}^2}{2R(x)} - \Phi(x)\right)\right), \quad (1.3)$$

where \mathbf{r} is a position vector transverse to beam propagation (in the y - z plane) with magnitude $|\mathbf{r}| = \sqrt{y^2 + z^2}$, \mathbf{E}_0 is the maximum electric field strength, ω_0 is the beam waist, $\omega(x)$ is the

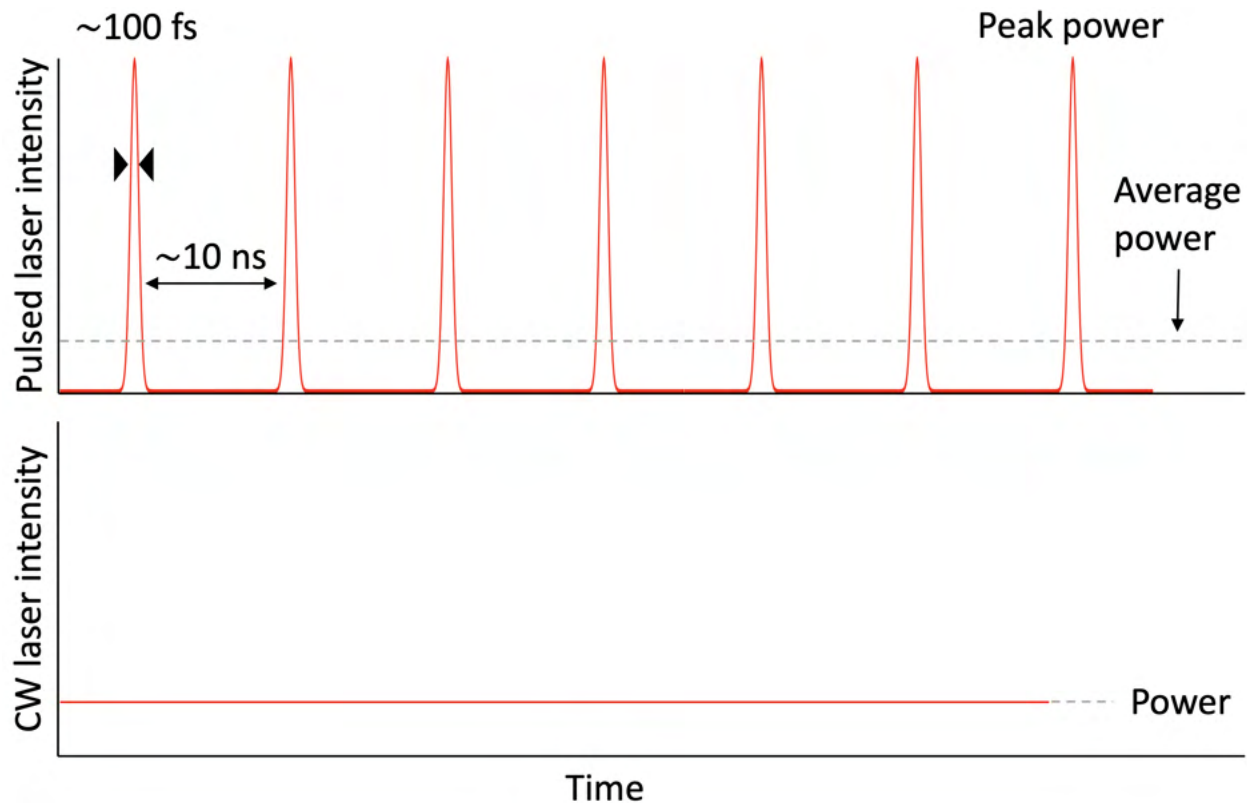


Figure 1.3: (Top) Optical pulse train from a mode-locked laser operating at ~ 100 MHz with a pulse width of ~ 100 fs, generating high peak power at a given average power. (Bottom) A continuous-wave (CW) laser output, in contrast, provides steady emission (i.e., peak, minimum, and average powers are identical). Red lines indicate laser intensity profile.

beam width, $k = 2\pi/\lambda$ is the vacuum wavenumber, $R(x)$ is the wavefront radius of curvature, and $\Phi(x)$ is the Gouy phase [21]. ω_0 , $\omega(x)$, and $R(x)$ are defined as follows.

$$\omega_0 = \frac{\lambda}{\pi\theta}, \quad (1.4)$$

$$\omega(x) = \omega_0 \sqrt{1 + \left(\frac{x}{x_R}\right)^2}, \quad (1.5)$$

$$R(x) = x \left(1 + \left(\frac{x_R}{x}\right)^2\right), \quad (1.6)$$

and

$$x_R = \frac{\pi\omega_0^2}{\lambda}. \quad (1.7)$$

The beam width $\omega(x)$ is defined as the transverse distance over which the electric field strength has dropped to e^{-1} of its on-axis value (Fig. 1.4) [23]. The Rayleigh range x_R is defined as the axial distance from the beam focus ($x = 0$) at which the beam width increases by $\sqrt{2}$; $b = 2x_R$ defines the “useful” fluorescent extent of a beam focus and is known as the confocal parameter. When $|x| \gg x_R$, the beam width increases linearly with increasing $|x|$ and a ray optical treatment of beam propagation is valid over a divergence angle θ . Because of their simplicity and ease of generation, Gaussian beams are used extensively in this thesis.

A Gaussian beam can be crafted with the pupil function (electric field distribution at the back pupil of the lens):

$$P_{\text{Gaussian}}(u, v) = \frac{1}{\sqrt{\pi}} H(1 - \mathbf{u}_r), \quad (1.8)$$

where u and v are the normalized pupil coordinates corresponding to the z - and y - axes, respectively; $\mathbf{u}_r = \sqrt{u^2 + v^2}$, normalized so that $\mathbf{u}_r = 1 \equiv f_r = 2NA/\lambda$; and H is the Heaviside step function.

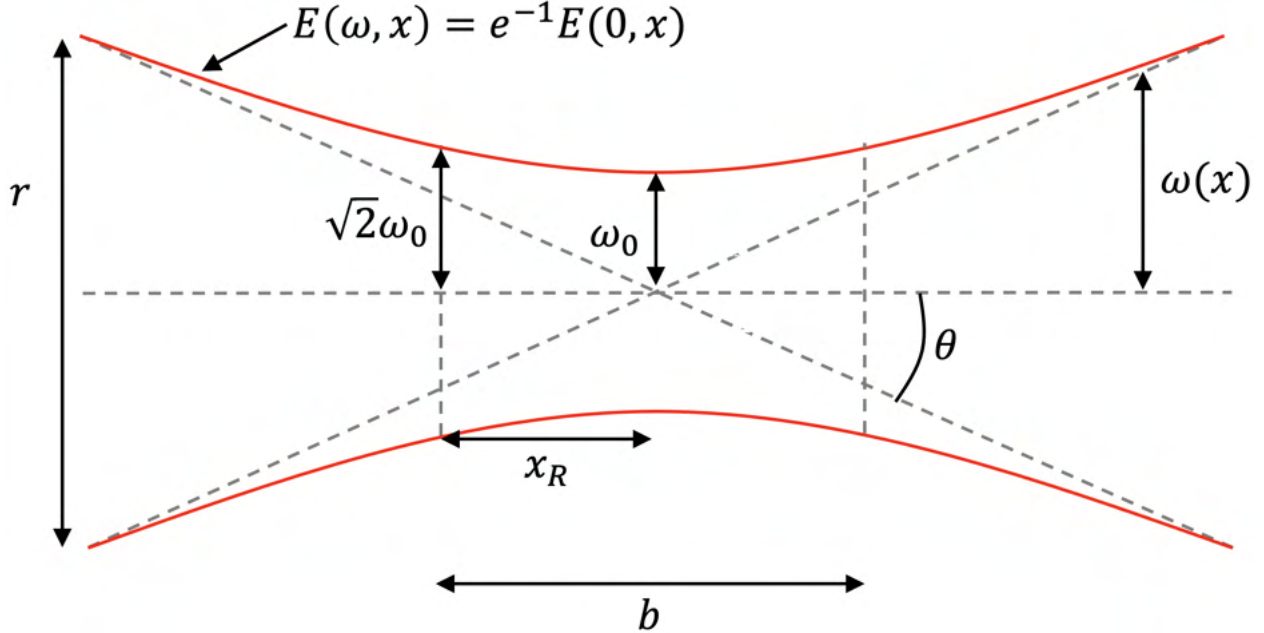


Figure 1.4: Propagating Gaussian beam along x . Beam width of electric field (red lines) around the beam waist ω_0 (focus). $\omega(x)$: beam width; x_R : Rayleigh range; b : confocal parameter; θ : divergence angle of propagating beam.

For a tightly focused beam, Equations 1.4 and 1.7 will deviate significantly, as the paraxial approximation made in Equation 1.3 no longer holds. In a high focusing regime, a treatment of diffraction is more accurate, and will be discussed in the next section (Section 1.1.4).

1.1.4 Image formation: theory and basic principles

In a classical microscope, the sample in the focal plane of the optics is imaged on the image plane. The goal is to produce an image that conveys as much information about the specimen with as much fidelity as possible. This image plane is either observed by eye through an ocular, or a camera is placed in this plane to capture the image (Section 1.1.4); systems can also offer both by splitting the detection path. Microscopes commonly form images using an infinity-corrected system: an objective lens and a tube lens (Fig. 1.6a). The objective lens is often switchable to produce different magnifications of the sample. A key advantage of this system is that the magnification $M = f_{\text{TL}}/f_{\text{OL}}$ depends only on the ratio of the focal lengths of the tube lens and objective lens, not on the length of “infinity space” between them. This

means infinity space can be adjusted without affecting the magnification or image quality, at least until the vignetting occurs as light clips the finite aperture of the lenses. This gives microscopists the freedom to position non-focusing optics (such as filters and dichroics) at any position in infinity space with equal optical performance.

In a conventional wide-field microscope, the sample is flooded uniformly with excitation light throughout the field-of-view that is imaged, and the image is captured by eye, camera, or both. In a wide-field epifluorescence microscope, the same objective lens is used for both excitation and collection, and a set of two filters and a dichroic mirror are typically used to separate the excitation light and fluorescence from the sample [24, 25]. This separation, as mentioned previously, provides highly-specific contrast of the fluorescently labeled structures against the backdrop of the non-labeled, non-fluorescent (dark) surrounding—because of the Stokes shift. In addition to simplicity, the epifluorescence design has the advantage of discarding the majority of the excitation light that has not been absorbed, which would otherwise travel in the direction of observation.

The goal of any fluorescence microscope is to determine the spatial distribution $S(\mathbf{r})$ of the fluorophores within the specimen. Assuming incoherent fluorescence, that is, the image of a sum of fluorophores is the sum of the individual images of each respective fluorophore (and thus linear), the fluorescence emission distribution $F(\mathbf{r})$ is defined as [26, 27]:

$$F(\mathbf{r}) = S(\mathbf{r}) \cdot I_{\text{exc}}(\mathbf{r}), \quad (1.9)$$

where $I_{\text{exc}}(\mathbf{r})$ is the excitation *point-spread function* (PSF), which describes the probability that a fluorophore located at any position \mathbf{r} will emit a photon; and all proportionality constants, such as absorption cross-section and quantum yield, have been suppressed for simplicity. For conventional, uniform, wide-field illumination, $I_{\text{exc}}(\mathbf{r}) \equiv 1$. In much of this thesis, we spatially confine $I_{\text{exc}}(\mathbf{r})$ using a Gaussian beam (Section 1.1.3), generally in the axial dimension (that is, the direction of detection).

As the emitting rays from the point source at the focal plane pass the aperture of the objective lens they are diffracted. For a translation-invariant optical microscope, a ring-like interference structure at the image plane called the *Airy disk* is generated. The resulting intensity 3D distribution is the detection PSF $H_{\text{det}}(\mathbf{r})$, which describes the probability that a photon emitted at \mathbf{r} reaches the detector after having been diffracted by the lens and the rest of the optical system. In other words, the detection PSF $H_{\text{det}}(\mathbf{r})$ is the impulse response of the microscope. The emission distribution $F(\mathbf{r})$ produces an image $D(\mathbf{r})$ given by:

$$D(\mathbf{r}) = F \otimes H_{\text{det}}(\mathbf{r}), \quad (1.10)$$

where \otimes is the convolution operator.

Like all forms of optical imaging, diffraction limits the resolving power. Ernst Abbe described the diffraction limit of optical microscopes over a century ago [28]. In an ideal microscope, the dimensions of a PSF essentially depend on the wavelength of light λ and the numerical aperture $NA = n \cdot \sin(\alpha)$ of the objective lens, where n is the refractive index of the medium, and α is the half opening angle of the cone over which light is collected. The influence of λ is intuitive: shorter wavelengths can produce smaller interference structures. The opening angle also plays a key role, as the greater the opening angle, the more information that can be gathered from the spherical wave emitted by a point source. For Abbe, more information meant more diffraction orders, so that for increasingly larger NA , higher diffraction orders are collected and thus interfere, resulting in a tighter projected spot [4]. With this in mind, he derived that the full-width at half-maximum (FWHM) of the PSF amounts to

$$d_{x,y} = \frac{\lambda}{2NA} \quad (1.11)$$

at the focal plane, and

$$d_z = \frac{2\lambda n}{NA^2} \quad (1.12)$$

for the extent of the PSF along the optical (axial) axis. The FWHM is defined as the width of the PSF when its intensity is half of its maximal intensity. As mentioned previously, diffraction occurs both when imaging *from* object space, and when trying to tightly focus a laser beam *into* object space. So it should come as no surprise that just as a microscope blurs an image of a point source according to the detection PSF H_{det} of the system, focusing a laser yields an imperfect spot according to the excitation PSF I_{exc} . Hence λ corresponds to λ_{exc} or λ_{det} depending on the excitation or detection PSF, respectively. Abbe's diffraction limit describes an isolated point and is an absolute measurement. The PSF can be experimentally characterized by moving a sub-diffractive object (an isolated fluorescent bead, for example) through the focal plane in the axial direction and recording a series of images of the object. The voxel size in all 3D should be slightly smaller than the Nyquist limit (half the theoretical resolution limit).

The light-gathering power of a microscope is proportional to the NA squared [23]. The depth-of-field is approximately equal to axial resolution d_z . Note that d_z is inversely proportional to the square of the NA , in contrast to the lateral resolution $d_{x,y}$, which shrinks to the first power of the NA . In Chapter 3, we explore a method to extend d_z without compromising the light-gathering ability of high NA optics. More precisely, we extend $H_{\text{det}}(\mathbf{r})$ in Equation 1.10 to match $I_{\text{exc}}(\mathbf{r})$ in Equation 1.9, so that all illuminated molecules $F(\mathbf{r})$ are in focus and unwasted, increasing the signal-to-noise ratio (SNR) and photon efficiency of the system. In the Section 1.1.5 we describe a class of non-diffracting beams to give insight into how this is possible.

Another common resolution metric worth mentioning is the Rayleigh criterion, formulated by Lord Rayleigh in 1879 independently of Abbe for spectrometers [29]. Applied to microscopes, Rayleigh's criterion states that two point sources having equal intensity are resolvable when the central maximum of the first PSF (along the direction of interest) coincides with the first minimum of the second PSF. This is slightly more conservative than Abbe's limit.

A lens performs a Fourier transform of the electromagnetic field distribution at its focal plane [30], so it is sometimes more intuitive to think about the performance of a microscope in Fourier space. The finite extent of the NA means the Fourier transform is band-limited and acts as a low-pass spatial filter. Equation 1.10 states the image $D(\mathbf{r})$ is a convolution of a diffraction-limited detection PSF $H(\mathbf{r})$ with the fluorescence emission distribution $F(\mathbf{r})$ in real-space. In Fourier space, the convolution theorem states the convolution is simply the point-wise product:

$$\tilde{D}(\mathbf{k}_x) = \tilde{F}(\mathbf{k}_x) \cdot O_{\text{det}}(\mathbf{k}_x), \quad (1.13)$$

where (\sim) indicates the Fourier transform operator of the corresponding real-space quantities, and $O_{\text{det}}(\mathbf{k}_x) = \tilde{H}_{\text{det}}(\mathbf{k}_x)$ is known as the optical transfer function (OTF, or “detection passband”). The OTF describes the weight in which particular spatial frequencies k_x (or wavenumbers) are transmitted through the microscope. Generally, low spatial frequencies (corresponding to large, coarse features) are passed with less attenuation than high ones (corresponding to small, fine features). The highest non-zero spatial frequency conveyed in the image defines the theoretical resolution limit of the microscope; the cutoff spatial frequency $k_0 = 2NA/\lambda$ elegantly amounts to the Abbe resolution limit.

As the OTF can be complex valued, the absolute magnitude can be taken, sometimes referred to as the modulation transfer function. The advantage of the OTF is that it offers a more complete view of the spatial frequencies passed through the microscope—its angular spectrum, rather than just a single number. Given knowledge of the OTF and sufficient SNR, deconvolution can be used to reduce out-of-focus fluorescence by restoring in-plane high frequency content suggested by the the OTF, while suppressing any spatial frequencies outside the OTF which may have arisen from Poisson noise [31, 32]. The OTF serves as inspiration for the Fourier filter we develop in Chapter 5. And the Fourier transforming property of a lens is central to Chapter 3, where we place a phase mask at the Fourier plane (also called back pupil plane or back aperture plane) of the microscope to manipulate its PSF (Section 1.1.5).

Photodetectors

A curious reader at this point may wonder: how are images recorded? The charge-coupled device (CCD) provided the first light-sensitive silicon chip to store an image and then digitize it [33], eventually leading to the creation of digital imaging and video microscopy [34]. The CCD sensor completely transformed microscopy, as well as astronomy and imaging science in general. The inventors, Willard Boyle and George E. Smith, then members of the research team at Bell Labs, were awarded the 2009 Nobel Prize in Physics for the concept. Today, the scientific complementary metal-oxide-semiconductor (sCMOS) camera has essentially supplanted CCD technology, because it is relatively cheap and very fast, with low readout noise and high photon efficiency over a large field-of-view. sCMOS sensors generally offer two modes of capture: rolling shutter exposes vertical lines at slightly different times as the sensor is read out, and global shutter exposes all pixels simultaneously, which is similar to the exposure mechanism of a CCD. Both modes have their own strengths: rolling shutter achieves the lowest noise and fastest frame rate but compromises true synchronization within a camera exposure, while global shutter is simpler to synchronize with other hardware (such as the light source) but comes at the expense of slightly higher noise; the most optimal mode depends on the specific application. A high-performance sCMOS camera typically has 2048×2048 pixels, $> 80\%$ quantum efficiency, 16-bit digital output, and a frame rate of 100 frames/s (for example, see Table A1 in Appendix A). Left to record on its own, a single camera can collect images at rates up to ~ 0.84 GB/s, or equivalently ~ 3 TB/hr, posing new opportunities and challenges for large-scale quantitative experiments.

1.1.5 Point-spread function engineering

Diffraction-free light beams were first described ~ 30 years ago [35, 36]. A Bessel beam is one class of these so-called non-diffracting beams. They are a solution to the Helmholtz

equation governing diffractive phenomena. The electric field distribution of a Bessel beam of wavelength λ propagating along the z direction is given by:

$$\mathbf{E}(\mathbf{r}, \phi, z) = A_0 \exp(ik_z z) J_n(k_r \mathbf{r}) \exp(\pm i n \phi), \quad (1.14)$$

where r , ϕ , and z are radial, azimuthal, and longitudinal directions in cylindrical coordinates, respectively; $k_r = k \sin \phi$ and $k_z = k \cos \phi$ are the radial and longitudinal wavevectors in which $k = \sqrt{k_r^2 + k_z^2} = 2\pi/\lambda$ is the wavenumber; A_0 is a scalar constant; and J_n is the Bessel function of the first kind of order zero ($n = 0$). The electric field of an ideal Bessel beam propagates without any change in its spatial distribution or amplitude in the x - z plane. Such a beam is *diffraction free*, or *propagation invariant*. The electric field consists of a narrow main peak surrounded by an infinite series of concentric side lobes of opposite phase and decreasing amplitude.

One way to think about a Bessel beam is as a set of plane waves propagating on a cone, which is a ring in Fourier space [37]. In other words, illuminating a uniform, infinitesimally thin ring at the Fourier plane of the focusing lens generates a Bessel beam. However in practice this is not possible, so an approximation of the Bessel beam using an annular aperture at the back pupil of the objective lens can be made (Fig. 1.5). In either case of illumination or detection, the annular pupil mask permits only a ring of light to be transmitted. These quasi-Bessel or Bessel-Gauss beams maintain an invariant profile over much greater distances than the Rayleigh range of a Gaussian beam with equivalent NA . And for the sake of simplicity, we refer to them as Bessel beams. The central core of a Bessel beam has radius r_0 and a maximum propagation-invariant range z_{\max} defined as:

$$r_0 = \frac{2.405}{k_r} \quad (1.15)$$

and

$$z_{\max} = \frac{R}{\arctan(r_A/f)} \quad (1.16)$$

where R is the effective radius of the lens, f is its focal length, and r_A is the radius of the annulus corresponding to a radial wavevector k_r .

A Bessel beam can be crafted with the pupil function [22]:

$$P_{\text{Bessel}}(u, v) = \frac{1}{\sqrt{\pi\beta(2 - \beta)}} H(1 - \mathbf{u}_r) H(\mathbf{u}_r - 1 + \beta), \quad (1.17)$$

where u and v are the normalized pupil coordinates corresponding to the z - and y - axes, respectively; $\mathbf{u}_r = \sqrt{u^2 + v^2}$, normalized so that $\mathbf{u}_r = 1 \equiv f_r = 2NA/\lambda$; and β is the fractional width of the annulus (width of annulus/radius).

The resulting cross-sectional intensity profile of a Bessel beam is shown in Fig. 1.5. The narrow main peak and extended focal zone make them attractive for a wide range of applications, ranging from optical trapping [38] to microscopy [39–43]. The side lobes can give the main lobe an improved ability to propagate through optically heterogenous media, even after distortion, by continuously “reconstructing” the main lobe after a characteristic propagation distance [37, 38, 40]. We engineer Bessel-like foci in Chapter 3 to extend the depth-of-field of a high NA detection system. Note that the primary pupil plane is inside the objective barrel and thus inaccessible. A $4f$ system (the distance between pairs of lenses are equal to the sum of their focal lengths) is commonly used to optically relay a conjugate pupil plane that makes the microscope’s angular spectrum accessible.

1.2 Volumetric imaging

Life is intrinsically three-dimensional and dynamic. Thus, high-speed volumetric imaging of biological processes has been a long-standing goal of optical microscopy. The most popular volumetric imaging technique today is confocal laser scanning microscopy. Confocal microscopy builds a 3D image from intensity information collected one voxel at a time [4, 44]. The sample is illuminated with a focused beam, point-by-point. This is achieved with a set of scanning galvanometer (galvo) mirrors that raster scans the excitation beam across

the sample. Detection with a photomultiplier tube or avalanche photodiode is performed through a pinhole, which is positioned in a conjugate plane to the focal plane. The pinhole rejects out-of-focus and scattered light, ensuring that only ballistic emitted photons in the

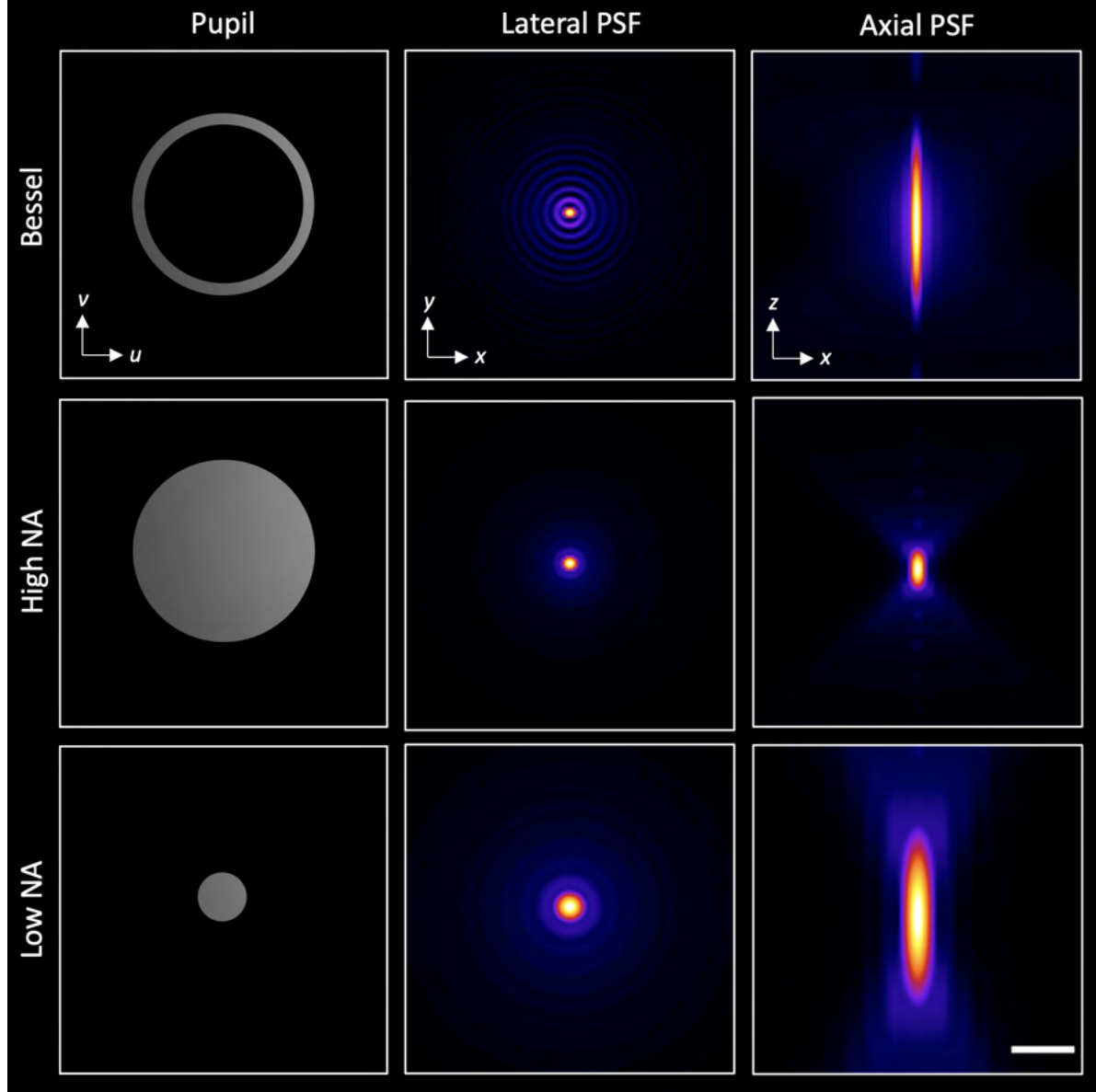


Figure 1.5: Bessel beam properties. Bessel beam (top row; $NA = 0.8$) propagating along z , with high-NA (middle row; $NA = 0.8$) and low-NA (bottom row; $NA = 0.41$) Gaussian beams for comparison. The Bessel beam has a main peak (lateral PSF, middle column) near-equivalent to the high-NA Gaussian beam, but with an equivalent axial extent (axial PSF, right column) to the low-NA beam. The cross-sectional intensity profile (lateral PSF) also shows concentric rings surrounding the main core of the Bessel beam, and the characteristic Airy disk in the Gaussian beams. Scale bar, $5 \mu\text{m}$.

vicinity of the focus are detected. Reducing the pinhole size (detection PSF) can improve the resolution up to a factor of $\sqrt{2}$, assuming sufficient fluorescent signal [45]. The elimination of out-of-focus light that bears little useful information provides excellent optical sectioning in thick specimens. For these reasons, confocal microscopy stands as the workhorse of bioimaging.

Two-photon laser scanning microscopy, as mentioned above, is the gold standard for deep-tissue imaging. Thanks to the quadratic dependence of the fluorescence signal on the excitation intensity, background is significantly minimized, yielding high SNR even without the use of a pinhole. The nonlinearity in the excitation means that all the signal from the diffraction-limited focus can be collected, making it extremely photon efficient. The nonlinearity also means photobleaching outside the focus is reduced. Further, the use of near-infrared illumination light greatly reduces scattering at increased penetration depth. These features together make two-photon microscopy remarkably adept at imaging neuronal activity in scattering tissue, like the mammalian rodent brain [8–10, 46].

The drawback to these point-scanning microscopes is the relatively low temporal resolution, due to the time required to scan over the volume. While the speed of galvo mirrors (and hence scan points) are fundamentally limited by mechanical inertia, advances in beam scanning optics has put the time required to drive a point and acquire signal in the sub-ms range, with the time required to acquire a cube of side s scaling as s^3 . This stands opposed to epifluorescence microscopy, where a 2D image is recorded in a snapshot, reducing the cubic acquisition scaling factor to just s . The caveat is that the wide-field illumination strategy lights up out-of-focus emitters and results in very low contrast. Spinning-disk confocal microscopy rapidly scans an array of foci across a plane in the sample that can be imaged simultaneously [4], which can help speed imaging. For fixed samples, small volumes or slow dynamics these common methods may be acceptable, but for live, large-volume or fast biological imaging they are insufficient.

This thesis explores two families of optical microscopy techniques for fast volumetric imaging. Both families parallelize image acquisition with a wide-field camera and selectively excite the sample. The first is light-sheet microscopy, also known as selective-plane illumination microscopy (SPIM) [47, 48]. As the name suggests, illumination is delivered in the form of a thin sheet of light. Detection leverages the benefits of a wide-field microscope (Section 1.1.4). Light confinement is achieved with a second optical path aligned orthogonally to the detection path to deliver single-plane illumination (Fig. 2.1). As a result, light-sheet microscopes permit an entire 2D plane of fluorophores to be excited and detected with high SNR, minimal light exposure to the sample, and speeds limited only by the available signal and detector. As an example, we have performed imaging of thick cancer organoids and thousands of individual functioning neurons interacting with each other across the entire brain of a behaving animal [49].

Our second approach to volumetric imaging, selective-volume illumination microscopy (SVIM), harvests the high contrast of light-sheet microscopy and the 3D snapshot ability of light-field microscopy (LFM). LFM optically encodes 3D intensity information onto a 2D detector synchronously (Section 1.2.1) [50, 51]. Because each 3D snapshot is captured in a single exposure, *volumetric* acquisition rates are now limited only by the available signal and detector. Taking inspiration from light-sheet microscopy, we confine excitation to only the volume of interest, reducing extraneous background and dramatically enhancing the image contrast. As a result, SVIM is particularly well-suited to imaging 3D volumes with rapid temporal dynamics. We have applied this technology to perform synchronous, large-volume, cellular resolution imaging of the embryonic beating heart and bacterial flows, at rates up to two orders of magnitude faster than standard light-sheet approaches [52].

1.2.1 Light fields

To lay the foundation for our SVIM work, it is worth describing how the light-field PSF arises, as it is different than the PSF introduced in Section 1.1.4, used in light-sheet microscopy.

The goal of a light-field microscope is to record volumetric information synchronously, and thus it must collect information from all locations in the volume simultaneously. Unlike existing volumetric imaging methods, it does not temporally multiplex or optically section the specimen volume. Instead, a light-field microscope uses an optical coding strategy. It works by positioning a lenslet array in place of the camera at the image plane, and moving the camera one focal length behind the lenslets (Fig. 1.6) [50, 51, 53]. The lenslet array samples both the lateral and angular distribution of light emitted from the specimen volume. This spatioangular information—the light-field—can be computationally reconstructed into a full 3D volumetric image stack (Fig. 1.6c). The angular information is what permits volumetric reconstruction, so there is a tradeoff in spatial resolution for angular sampling. How do we reconstruct a 3D volume from a single 2D image? We need to solve the inverse problem. Following Broxton [51], we aim to invert the discrete linear forward imaging model:

$$\mathbf{D} = H\mathbf{F}, \quad (1.18)$$

where the vector \mathbf{D} represents the light field, H is a discrete linear measurement matrix modeling the forward imaging process, and the vector \mathbf{F} is the discrete volume being reconstructed. The coefficients of H are determined by the light-field PSF.

A light-field microscope focuses light into an intensity pattern on the camera that is different for each position in the volume, illustrated in Fig. 1.6b. In contrast to the Airy disk formed by a diffraction-limited translation-invariant microscope, the light-field PSF varies in space. This means that each position in the volume must be uniquely calculated, and imaging cannot be modeled as a convolution (blurring) of the object intensity with the PSF of the system, as is done in wide-field fluorescence microscopy (Section 1.1.4). Rather, it is modeled as a general linear superposition integral [51]:

$$D(\mathbf{x}) = \int |H(\mathbf{x}, \mathbf{r})|^2 F(\mathbf{r}) d\mathbf{r}, \quad (1.19)$$

where \mathbf{r} is the position of the fluorescence emitter in the 3D volume $F(\mathbf{r})$ that gives rise to the continuous 2D wavefront $D(\mathbf{x})$ at the camera; the PSF $|H(\mathbf{x}, \mathbf{r})|^2$ is thus a function of both the position \mathbf{r} of the emitter in the sample volume and the position \mathbf{x} in the 2D wavefront at the camera sensor plane. Like all fluorescence microscopes, it assumes that emission signals from different parts of the sample add linearly to form an image. The model also adopts the first Born approximation [54], and assumes there is no (or weak) scattering in the volume.

In its current form, it is physically impossible to use light-field optics to “map” one diffraction-limited voxel to one pixel, so there is non-uniform spatio-angular sampling, where sampling is dense at some depths, but degenerate at others. As a result, there is a depth-dependence on spatial resolution, with the densest spatio-angular information and hence highest resolution near the native focal plane, which then gradually worsens with increasing distance. At the native focal plane, the maximum lateral resolution is determined by the diffraction-limited sampling rate of the lenslet array: the lenslet pitch divided by the effective magnification; here, resolution is weakest and reconstruction artifacts are also most prominent. The biggest drawback is that conventional wide-field illumination floods the entire specimen with light, creating extraneous out-of-volume background that reduces image quality and fidelity. In addition, the fact that almost every position in the volume must be calculated makes 3D deconvolution computationally demanding, though this is accelerated with GPU algorithms [51, 53]. Nonetheless, light-field microscopes stand out for their ability to image across large volumes synchronously at unmatched speeds. We address the issue of background in Chapters 4 and 5 with selective-volume excitation to achieve substantial gains in light-field SNR, contrast, and resolvability *in vivo*. We also develop a simple, easy-to-implement algorithm to alleviate common reconstruction artifacts in Section 5.6 of Chapter 5. These improvements to light-field imaging thus promises new insights into complex biological phenomena that are otherwise too fast or too 3D to be recorded with existing microscopes.

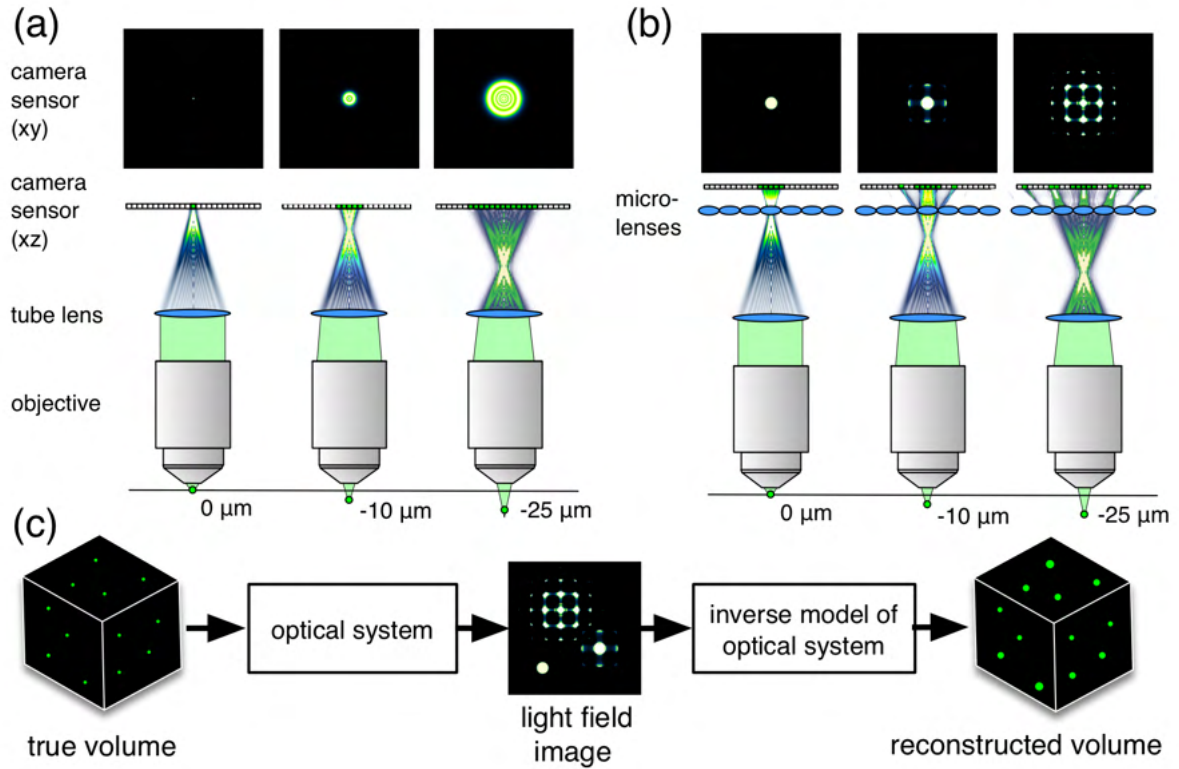


Figure 1.6: Overview of light-field microscopy. **(a)** In a conventional fluorescence microscope, a point source away from the focal plane creates an increasingly blurred image of the source, making it difficult to determine its 3D position. **(b)** In a light-field microscope, a lenslet array in the optical path refocuses the light, creating a pattern that is unique for each position in the volume. **(c)** A wave optics model of light propagating through the microscope can be used to solve the inverse problem, reconstructing a full volume from a single 2D light-field image. Adapted from [55].

1.3 The photon budget

Volumetric biological imaging poses unavoidable tradeoffs between spatial resolution, acquisition speed, penetration depth, and photodamage (Fig. 1.7). The central challenge is the limited photon budget from the sample: there are a finite number of fluorescently labeled molecules in a given voxel and each fluorophore emits only a finite number of photons before it is bleached [56]. Higher spatial resolution requires more measurements (voxels) and more photons collected within them, which requires more integration time to generate acceptable SNR. However, slowing the scan rate or averaging over many frames is not without cost, as the finite lifetime of fluorophores ($\sim 10^{-1} - 10^0$ s) yields $\sim 10^4 - 10^5$ photons before it is lost to photo-induced bleaching [57].

Higher acquisition speed requires more fluorophores in each voxel, since more of them will be expended at each time point. However, higher fluorophore concentration could increase phototoxicity. Excitation of fluorophores can generate reactive oxygen species that are unstable, short-lived, and can damage the chemical structure and function of the molecular environment inside the cell [58]. This can also lead to self-quenching of the fluorophore, resulting in a reduction of its fluorescence quantum yield (fraction of absorbed photons that yield fluorescence photons). Brighter fluorophores having a high extinction coefficient (the capacity to absorb light at a specific wavelength) and high quantum yield would in principle allow a reduction in illumination time to yield the same fluorescence emission, but tuning fluorophore brightness is technically challenging and not always possible.

Another issue is that the useful optical imaging depth in tissue is fundamentally limited by aberrations, absorption, and scattering. Multiphoton microscopy can help. In addition to the benefits of selective excitation via nonlinear optical effects, the longer wavelength of light scatters less and is generally less perturbing to multicellular specimens than high-energy, short-wavelength light. But again the volumetric imaging rate of point-scanning microscopy is relatively slow. Increasing the laser power to increase the probability of fluorophore excitation and hence the number of fluorescence photons is an option for some samples but it

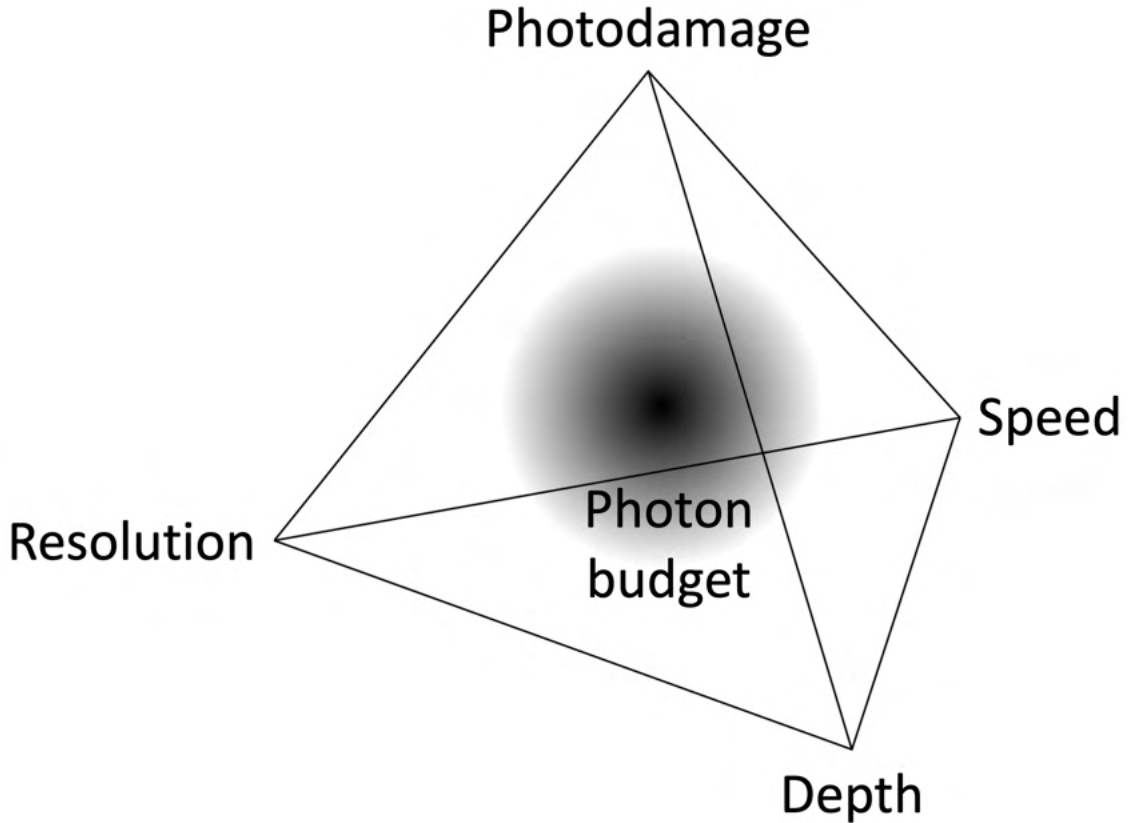


Figure 1.7: Biological imaging involves unavoidable tradeoffs between spatial resolution, temporal resolution, penetration depth, and noninvasiveness in the face of a limited photon budget from the sample.

is generally far from desirable, as high light doses on the specimen can lead to fluorophore saturation and worst yet increased photodamage (phototoxicity and photobleaching).

Sample health is the utmost important parameter in this thesis, and minimizing photodamage is a fundamental concern—it is the apex of our tetrahedron (Fig. 1.7). Manifestations of photodamage during imaging are seriously problematic, and can compromise the validity of conclusions drawn from an experiment. Photodamage often depends supra-quadratically on laser peak intensity [20, 59], so an effective management strategy we employ is to spread the illumination dose across space and time to minimize it. The overall goal of our research program is to use the excitation light as efficiently as possible and collect the emission photons as efficiently as possible while striking the optimal imaging compromises for whatever the application demands.

1.4 Overview

Recognizing the tradeoffs in spatial resolution, temporal resolution, imaging depth, and noninvasiveness, the aim of this thesis is to optimize the limited photon budget from the specimen for application-specific imaging that extends the reach of optical microscopy.

In Chapter 2, we present a versatile light-sheet imaging instrument that combines two independently controlled microscope-twins, built so that they can share the same multi-laser source, increasing the throughput and decreasing the cost. To permit a wide variety of specimens to be imaged, each microscope-twin provides flexible imaging parameters, including (i) operation in one-photon and/or two-photon excitation modes, (ii) delivery of one to three light-sheets via a trio of orthogonal excitation arms, (iii) sub-micron to micron imaging resolution, (iv) multicolor compatibility, and (v) upright (with provision for inverted) detection geometry. We offer a detailed description of the twin-microscope design to aid instrument builders who wish to construct and use similar systems. We demonstrate the instrument's versatility for biological investigation by performing fast imaging of the beating heart in an intact zebrafish embryo, deep imaging of thick patient-derived tumor organoids, and gentle whole-brain imaging of neural activity in behaving larval zebrafish.

In Chapter 3, we improve light-sheet microscopy by extending the depth-of-field of a high-numerical-aperture (NA) detection objective to match the light-sheet thickness used. We demonstrate instantaneous depth-of-field extension with a pupil phase mask increases total fluorescence emission (up to threefold) in light-sheet imaging through numerical simulations and bead phantoms. Compared to a low-NA system with an equivalent depth-of-field, our method increases signal collection nearly 5-fold and reduces the rate of photobleaching by over 15% in live vasculature-labeled zebrafish. Our new method improves the sensitivity in brain-wide imaging of neural activity in larval zebrafish, permitting us to capture $\sim 45\%$ more neurons over traditional high-NA light-sheet imaging.

In Chapter 4, we introduce light-field-based selective-volume illumination microscopy (SVIM), where illumination is confined to only the volume of interest, removing the background generated from the extraneous sample volume, and dramatically enhancing the image contrast. We demonstrate the capabilities of SVIM by capturing cellular-resolution 3D movies of flowing bacteria in seawater as they colonize their squid symbiotic partner, as well as of the beating heart and brain-wide neural activity in larval zebrafish. These applications demonstrate the breadth of imaging applications that we envision SVIM will enable, in capturing tissue-scale 3D dynamic biological systems at single-cell resolution, fast volumetric rates, and high contrast to reveal the underlying biology.

In Chapter 5, we advance SVIM to a single-objective geometry, using an oblique one-photon illumination path or two-photon illumination to accomplish selective-volume excitation. The elimination of the second orthogonally oriented objective to selectively excite the volume of interest simplifies specimen mounting; yet, this single objective approach still reduces out-of-volume background, resulting in improvements in image contrast, effective resolution, and volume reconstruction quality. We validate our new approach through imaging live developing zebrafish, demonstrating the technology’s ability to capture imaging data from large volumes synchronously with high contrast, while remaining compatible with standard microscope sample mounting.

2

A versatile, multi-laser twin-microscope system
for light-sheet imaging

2.1 Introduction

Over the past decade, there have been a series of important developments in light-sheet microscopy, a century-old technique [47] (also known as selective-plane illumination microscopy; SPIM) [48]. SPIM decouples the illumination and detection paths by using separate optics to excite and detect fluorescence: a cylindrical illumination lens is used to project a static,

thin, two-dimensional (2D) sheet of light coincident to the focal plane of a detection objective lens. In contrast to confocal laser scanning microscopy and other point-scanning techniques that acquire volumetric information one voxel at a time, light-sheet excitation permits an entire 2D plane of fluorophores to be excited and detected with high signal-to-noise ratio, high imaging speed, and minimal light exposure to the sample. Developments in light-sheet microscopy techniques [60–67] have led to cutting-edge applications across a range of fields [60–63, 66, 68, 69] from developmental biology [61, 70] to neuroscience [66, 68, 71–73]. Each of these modifications of light-sheet imaging has involved their own tradeoffs in performance, complexity and expense of the microscope optics, and expenditure of the photon budget. Comprehensive reviews of light-sheet development can be found elsewhere (see Ref. [61])—we highlight below several key developments that address the experimental demands that motivate the development of our instrument.

A key development was to create light-sheets by dynamically scanning a focused Gaussian beam, generated via a low-numerical-aperture (NA) lens, across the plane (Fig. 2.1) [74]. This scanned Gaussian-beam light-sheet approach (also termed digital scanned laser light-sheet fluorescence microscopy; DSLM) [74] provides better spatial illumination uniformity, higher light throughput, and more precise spatial control over the selected plane of interest compared to a static 2D light-sheet at the cost of replacing the simple cylindrical lens with the expense and complexity of a scanning galvanometer (galvo) mirror and associated optics and electronics. This task has been simplified by the commercial availability of integrated electro-optical galvo scanning modules.

The penetration depth of one-photon excitation light-sheet microscopy (1P-SPIM) was improved in two-photon light-sheet microscopy (2P-SPIM), where nonlinear excitation was added to the DSLM implementation [75]. 2P-SPIM has proven successful in relatively thick or optically dense samples, imaging up to twofold deeper than DSLM/1P-SPIM, and more than tenfold faster and 100-fold lower peak intensity than conventional 2P point-scanning microscopy. In addition, the near-infrared (NIR) light used for 2P excitation is invisible to

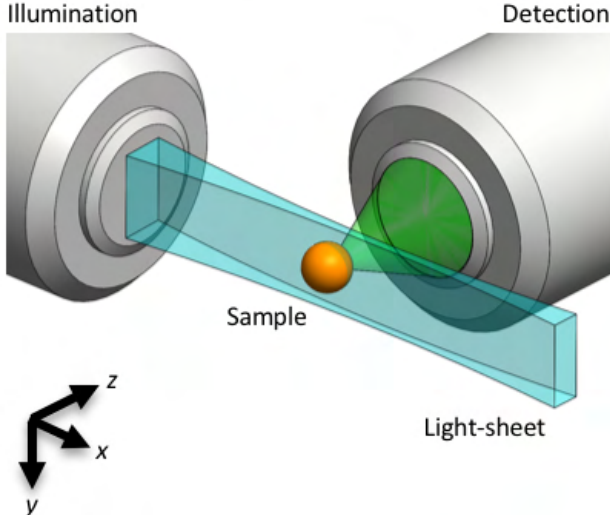


Figure 2.1: Light-sheet microscopy principle. A light-sheet (blue) can be created by dynamically scanning, along the y direction, a focused Gaussian beam that propagates in the x direction. The focusing is achieved via a low numerical aperture illumination lens. The fluorescence generated by the illuminated ($x-y$) plane is imaged (green) by an orthogonally positioned wide-field microscope. Axial ($x-y$) sections of the 3D sample are captured either by scanning the sample (orange) through the stationary focal plane or by scanning the light sheet and detection focal plane through the stationary sample.

many animals, which avoids unintended visual stimulation [76]. The disadvantages of 2P excitation are the extra laser cost, lower fluorophore absorption cross section (leading to lower maximum imaging speed), and less amenability to multicolor imaging compared to 1P excitation [61, 65]. Thus, for the best flexibility to handle a wide variety of samples, both 1P and 2P excitation modes are desirable. Because both use a low-NA illumination lens to generate an axially extended Gaussian focus, they can be conveniently carried out on the same light-sheet instrument. [75, 77].

A major expense of SPIM imaging setups is the laser source used for excitation, especially given that multiple lasers are used for multicolor imaging. For 2P-SPIM the ultrafast laser can more than double the equipment cost, which has limited its adoption, despite its superior performance in optically challenging samples. Even for well-funded laboratories, laser sources tied to a single microscope are not cost-effective. Since there is an upper limit to the

amount of laser power that can be delivered to any specimen without perturbing it, most implementations waste well more than half of the total laser power available.

Another practical challenge comes from the often dual need of continuously imaging to generate time-lapses and of imaging a large number of samples to obtain statistically significant results. While the low photodamage of SPIM allows biological processes to be imaged for a duration of several hours or days, a tradeoff exists between such prolonged imaging sessions and the number of samples that can be imaged in a given day using a single instrument.

Here, we describe the flex-SPIM, which combines two independently controlled light-sheet microscope-twins that share an ultrafast NIR laser and a bank of continuous-wave (CW) visible lasers. This permits two specimens to be imaged simultaneously for far less than the cost of two multi-laser microscopes. Each microscope-twin has built-in modularity for tailoring its use on diverse samples and scientific questions. In Chapter 2.2, we describe the flex-SPIM design in detail for those who wish to construct and use a similar instrument. In Chapter 2.3, we test the performance against our design objectives by imaging three challenging specimens: the beating larval zebrafish heart, patient-derived tumor organoids, and whole-brain neural dynamics in behaving zebrafish. The results demonstrate the ease of adapting the flex-SPIM for application-specific light-sheet imaging.

2.2 Instrument design, integration, and configuration

The flex-SPIM draws on lessons learned from proof-of-principle studies [75, 77] with a new imaging technology to meaningful scientific results; [78–80] several years of interactions with end users at advanced imaging centers (at the California Institute of Technology and the University of Southern California), the 2P-SPIM inventors, and other instrument builders; and thus integrates the following combination of improvements:

- Two independent microscope-twins share the same multi-laser source (Fig. 2.2), dramatically reducing instrument cost—a more than 30% savings.
- The twin architecture doubles the 1P- and 2P-SPIM imaging throughput, and increases the variety of specimens or imaging modes, when compared to a single microscope.
- The system is “flexible” by design, with an opto-mechanical configuration that is both open and modular, providing a straight-forward path to instrument evolution and customization for different samples and applications. Three orthogonal illumination arms offer easy matching to different specimens, enhancing illumination uniformity or increasing optical coverage for larger and more opaque samples [81]. Switching from high lateral spatial resolution (sub-micron) to a lower spatial resolution (\sim micron) with a larger field-of-view requires only a simple adjustment to the detection subsystem. Each twin can be configured in upright and/or inverted detection geometries to accommodate a diversity of specimens (Fig. 2.2).

The flex-SPIM consists of four functional subsystems (Fig. 2.2) and two modules 2.1 and sits on a 5×10 ft², anti-vibration optical table (Fig. 2.3). The schematic diagram of the integrated illumination paths is shown in Fig. 2.4; the corresponding 3D opto-mechanical model is shown in Fig. 2.2 and the complete computer-aided design (CAD) is available upon request. Whenever possible, commercially available hardware components are used; however, both basic machining of off-the-shelf parts and the fabrication of custom components are required (Table A1 in Appendix A). Most standard optical elements are mounted in Thorlabs 30 mm or 60 mm cage components. Beam steering mirrors shared by both the ultrafast and CW lasers (illumination-scanning optics) have protected silver coatings, whereas those used by the ultrafast or CW lasers alone have broadband dielectric coatings.

Table 2.1: flex-SPIM functional subsystems and modules. CW: continuous-wave; polarization beamsplitting optics: half-wave plate and polarizing beamsplitter; AOTF: acousto-optic tunable filter; galvo: galvonometer; LED: light-emitting diode.

Subsystem/module	Description	Main components
Multi-laser	Laser modulation and beam routing	CW lasers; beam expander; dichroic mirrors; polarization beamsplitting optics; AOTFs; mirrors Ultrafast laser; polarization beamsplitting optics; beam expander; Pockels cells; mirrors
Illumination-scanning optics	Generating the light-sheet	Scanning galvo mirrors and optics; mirrors; objectives
Detection	Image capture	Scientific camera; tube lens; filter wheel; filters; objective
Sample mounting and motion control	Holding and imaging the 3D sample	Custom sample chamber/holder; motion stages; piezoelectric z-stage
Instrument control	Control and timing of components	Acquisition computer; National Instruments PXI; system mainframe and scaling amplifiers
Auxiliary	Illumination masks and view-finding	Camera; LED; filter; aluminum masks

The main parts for each subsystem and module used to build the flex-SPIM are listed in Table A1 in Appendix A.

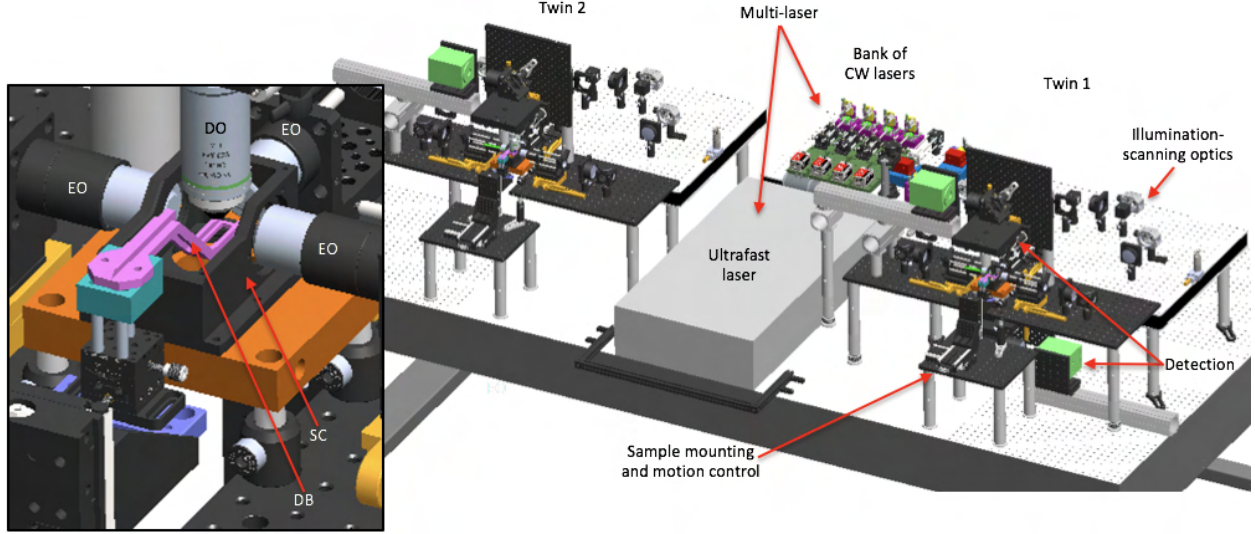


Figure 2.2: 3D opto-mechanical model of the twin-microscope system mounted on a $5 \times 10 \text{ ft}^2$ anti-vibration optical table. Model shows the multi-laser subsystem shared between microscope-twin-1 (right) and microscope-twin-2 (left). Twin-1 has the four functional subsystems labeled and features an implementation of both upright and inverted detection. Brief descriptions of each functional subsystem are provided in Table 2.1. The inset shows a detailed view of the sample chamber (SC); the dive bar (DB) used to hold the sample; three excitation objectives (EO) to deliver excitation light-sheets to the sample; and the detection objective (DO) to collect emitted fluorescence from the sample.

2.2.1 Multi-laser subsystem

CW visible light used for single- and multi-color imaging via linear excitation is provided by a bank of CW lasers (445 nm, 488 nm, 561 nm, and 647 nm), collimated and expanded to a $1/e^2$ diameter of 1.5 mm, and combined into a co-linear beam using broadband and dichroic mirrors (see Table A1 in Appendix A) [42]. The combined beam is then split into two paths of equal length and power through polarization beamsplitting optics (consisting of a half-wave plate mounted on a rotation mount and polarizing beamsplitter (PBS)), delivering light to each microscope-twin. Each light path passes through acousto-optic tunable filters (AOTFs), which are used to select the wavelengths and adjust the power independently for each twin. The AOTFs (Table A1) require the input laser beam polarization to be linearly orthogonal to the baseplate (s-polarization) to maximize the diffraction efficiency and ensure chromatic co-linearity of the modulated beam. Alternatively, the input beam

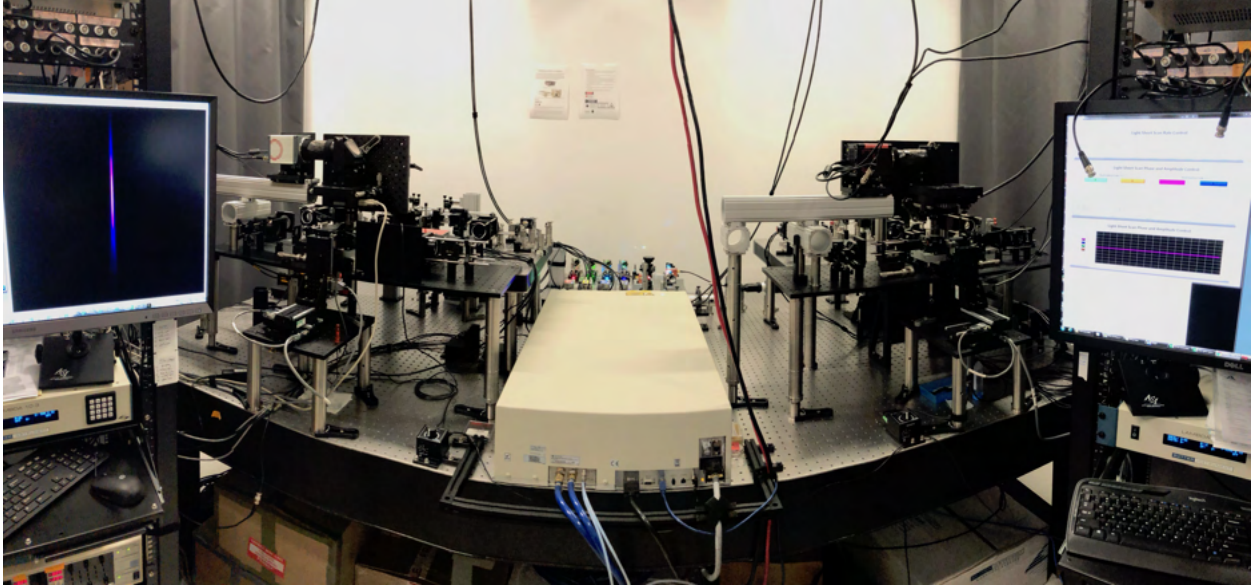


Figure 2.3: Panoramic photograph of the assembled twin-microscope system, showing the multi-laser subsystem shared between microscope-twin-1 (right) and microscope-twin-2). The corresponding electronic and instrument control racks are shown beside each microscope-twin.

can be p-polarized if the AOTF crystal output face is used as the “input” face due to the Helmholtz reciprocity principle [54]. Because of the upstream polarizing beamsplitter used, the beams are p-polarized for the twin-1 path and s-polarized for the twin-2 path. As such, the AOTF in the twin-1 path is mounted so that the p-polarized beam enters the AOTF through its output face; the AOTF in the twin-2 path is mounted conventionally. A half-wave plate can be placed in front of the AOTF to fine-tune the polarization direction of the beam entering the AOTF and thereby maximize the diffraction efficiency by the AOTF when more excitation energy is required at the sample, as we have implemented in the twin-2 path (Fig. 2.4). Note that alternatively, similar performance could be achieved by placing a half-wave plate in front of the AOTF in the twin-1 path to rotate the beam’s polarization so that it enters the AOTF conventionally.

The tunable NIR ultrafast mode-locked laser used for single- and multi-color imaging via nonlinear excitation is split into two paths of equal length and power through polarization beamsplitting optics, delivering NIR light to both microscope-twins. Note that the linear

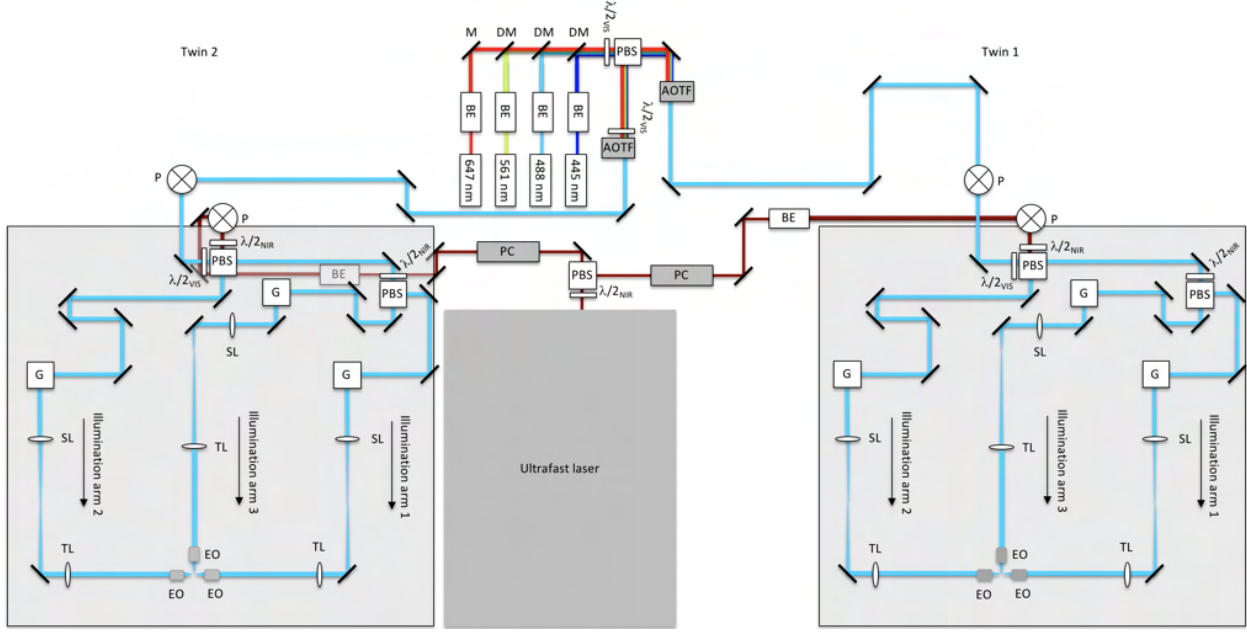


Figure 2.4: Schematic diagram of multi-laser and illumination-scanning optics subsystems of the instrument. Visible light from the continuous-wave laser bank is fed into microscope-twin 1 (right) and microscope-twin 2 (left) via polarization beamsplitting optics (consisting of a polarizing beamsplitter (PBS) and half-wave plate). Acousto-optic tunable filters (AOTFs) are used to select the visible wavelengths and adjust the power independently for each twin. The near-infrared (NIR) light from the ultrafast laser is routed similarly using Pockels cells (PCs) to adjust the NIR power independently for each twin. The visible and NIR beams are raised onto 24×36 in 2 optical breadboards by using periscopes (P). Polarization beamsplitting optics are used both to combine the visible and NIR beams and to split the combined beam into two paths (illumination arms 1 and 2). Illumination arm 1 is further split into two paths through polarization beamsplitting optics, creating a total of three illumination arms. Each illumination arm directs light to the sample through the excitation objectives (EO). BE—beam expander, M—mirror, DM—dichroic mirror, $\lambda/2$ —half-wave plate, where the subscripts VIS and NIR refer to the visible and near-infrared wavelengths, respectively, G—2D scanning galvo mirrors, SL—scan lens, and TL—tube lens. BE in the NIR twin-2 path appears gray because it is underneath the optical breadboard.

polarizations of the beams for the twin-1 path and the twin-2 path are orthogonal to each other. Each path passes through a Pockels cell to control the power independently for each twin (Fig. 2.4). Each Pockels cell is rotated to match its input polarization requirement and hence maximize its extinction ratio, removing the need for additional half-wave plates and power losses from their imperfections. Following the Pockels for each path, the beams are expanded to a $1/e^2$ diameter of 2.2 mm. A long-pass filter (800-nm cutoff) is mounted upstream of the beam expander to block any undesired residual wavelengths from the ultrafast laser source.

2.2.2 Illumination-scanning optics subsystem

Visible and NIR beams from the multi-laser subsystem are each raised onto a pair of 24×36 in² optical breadboards, one for each twin, by periscopes (Fig. 2.4). Polarizing beamsplitters are used to both combine the visible and NIR beams into a co-linear beam and to split the combined beam into two paths (illumination arms 1 and 2). Visible and NIR half-wave plates, each mounted in manual rotation mounts, are used to adjust the laser power (splitting ratio) delivered to illumination arms 1 and 2. Illumination arm 1 is further split into two paths through polarization beamsplitting optics, creating a total of three illumination paths. Rotation of the NIR half-wave plates before the polarizing beamsplitter can be used to adjust the relative laser power into illumination arms 1 and 3 (Fig. 2.4). The path lengths of all three illumination arms are routed so that they are equal.

The beams from each illumination arm are sent to a 2D scanning galvo mirror positioning system. The first galvo mirror rapidly scans the beam laterally to synthesize the light-sheet (in the x - y plane), and the second galvo mirror, which is conjugate to the back pupil of the excitation objective lens, translates the virtual light-sheet along the (z) detection axis. Following the scanning system, each illumination beam passes through a scan lens (achromatic doublet; see Supplementary Note 2.6.1); a tube lens, and a low magnification, low-NA, long-working-distance excitation objective lens. The distances between pairs of

lenses form a $4f$ arrangement (the distance between pairs of lenses are equal to the sum of their focal lengths).

Three excitation objective lenses, mounted orthogonally to each other, direct the illumination light toward the sample (Fig. 2.4). Depending on the sample properties, any combination of the excitation objectives can be used, either sequentially or simultaneously. Small and/or transparent samples, for example, may benefit from single-sided illumination with 1P excitation, whereas relatively large and thick samples may benefit from the uniform illumination coverage offered by using all three objectives with 2P excitation.

The illumination NA for 1P and 2P is ~ 0.02 and 0.03 , respectively, yielding fluorescence Gaussian-beam light-sheets of $\sim 10 \mu\text{m}$ in average thickness across an extent of $\sim 400 \mu\text{m}$, as shown in Fig. 2.8D. Note that to produce similar nominal fluorescence light-sheet thicknesses and extents, different NAs are needed for 1P vs 2P due to the difference in laser wavelength and the linear (1P) vs quadratic (2P) dependence of the fluorescence on the laser intensity[75]. Scanning of the first galvo yields an effective (x - y) field-of-view of $\sim 400 \times 1000 \mu\text{m}^2$. The chosen light sheet thickness ensures that we are able to resolve single neurons (6–8 μm in size) throughout the entire $\sim 400 \times 800 \times 250$ (x - y - z) μm^3 brain of zebrafish larva at 5 days-post-fertilization (dpf) [76, 82].

Light throughput for each twin, defined as the total measured laser power at the sample from the three illumination arms divided by 50% of the measured power at the laser output (for 1:1 split into each twin) for the ultrafast laser (taken at $\lambda = 900 \text{ nm}$) is $\sim 60\%$. Light throughput in the visible regime, taken by throughput measurements across each CW laser line is $\sim 6\%$. The lower visible light throughput is expected since most of the illumination-scanning optics were selected to optimize NIR throughput and maximize 2P excitation efficiency (Table A1). Both the ultrafast and CW laser sources are able to simultaneously run experiments on both twins with independent power control.

2.2.3 Detection subsystem

The sheet of fluorescence signal generated at the sample is collected by an orthogonally positioned water-immersion detection objective lens ($20\times$, 1.0 NA; see Table A1), mounted to a piezoelectric (piezo) collar. The high-NA objective, with low intrinsic magnification, not only enables high-resolution imaging across large volumes but also importantly maximizes light-collection, which is critical for maintaining acceptable signal-to-noise while minimizing the excitation laser power to reduce photodamage to live samples. The fluorescence signal passes through a filter wheel equipped with emission filters to block the excitation light and transmit the fluorescence signal emitted by the sample; the emission filters are optimized for the transmission of common fluorophores spanning the visible spectrum (Table A1). A tube lens forms the primary image of the fluorescence signal onto a scientific complementary metal-oxide-semiconductor (sCMOS) camera.

Different magnifications are achieved with the same detection objective by using tube lenses of different focal lengths, with the rail-mounted fluorescence camera providing the necessary distance adjustments (Figs. 2.2 and 2.5). Generally, tube lenses need to have a large enough diameter to capture the detection optical aperture and good performance to minimize chromatic and geometric aberrations [4]. Lower or higher magnification requires lenses with shorter or longer focal lengths, potentially exacerbating aberrations or making the instrument footprint larger, respectively. We find that the practical range of magnification is between $44\times$ and $11\times$ for our instrument (Table A1), given the available off-the-shelf double achromats (used as tube lenses), the size constraint of standard opto-mechanical components, and the desire to keep our instrument reasonably compact.

Our detection subsystem design choices described above represent a balanced compromise to achieve an economical light-sheet instrument with adjustable magnification, maximizing resolution while maintaining a large field-of-view. As will be shown later, the instrument provides cellular to sub-cellular resolution, sufficient for a wide range of applications. We note that the maximum diffraction-limited resolution, as determined theoretically by the NA

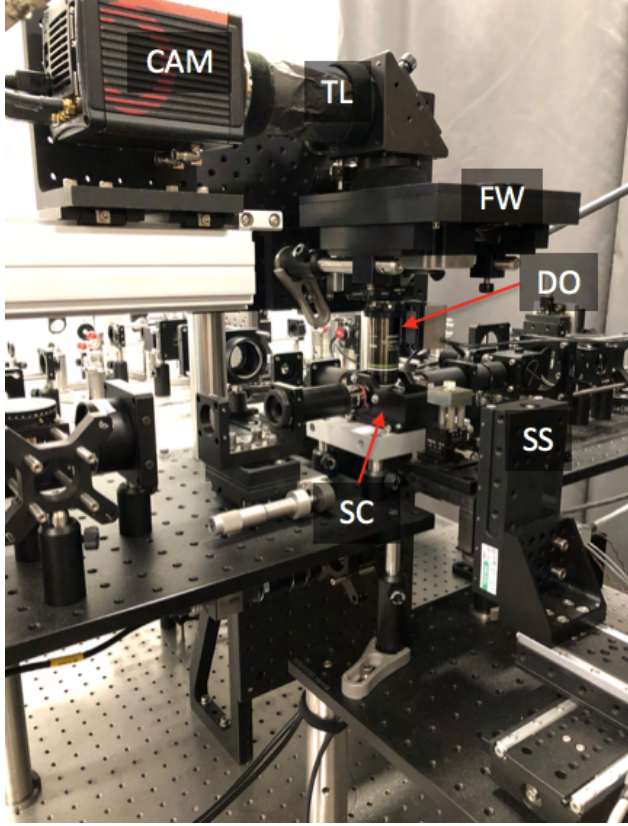


Figure 2.5: Photograph of an assembled microscope-twin with upright detection. SC—sample chamber, SS—3D stage stack-up, DO—detection objective, FW—filter wheel, TL—tube lens, and CAM—camera.

of the detection objective, is not expected to be achieved, given the practical design choices that we have made. First, at the magnifications used, the camera pixel size is not small enough to provide diffraction-limited spatial sampling according to the Nyquist criterion [4]. Second, independent of the magnification used, we do not expect our detection path to be fully aberration-free due to our choice of using economical off-the-shelf double-achromats as tube lenses, rather than more expensive specialized tube lenses (which often only exist with limited focal lengths). If higher resolution is desired with our system, a detection objective with higher NA and/or higher intrinsic magnification could be used in combination with the matched tube lens from the same manufacturer.

Depending on the sample properties, the detection subsystem can be arranged for upright and/or inverted configurations. We have experimentally implemented an upright configuration (Fig. 2.5), as it is the most optimized for the biological samples presented here. We implemented an inverted configuration in the CAD model shown in Fig. 2.2, where the same detection subsystem was designed to be mounted in either an upright or inverted configuration. Owing to the system’s arrangement of opto-mechanical components (Figs. 2.2, 2.4, and 2.5), switching between detection geometries or changing the overall magnification is relatively straightforward.

2.2.4 Sample mounting and motion control subsystem

The sample chamber has three side windows for the excitation objectives as well as a bottom window to provide an additional view of the specimen. The sample chamber is open at the top and is filled with imaging buffer; the open-top allows the detection objective to be liquid-immersed and the sample holder to be inserted. The sample chamber sits on a custom heat exchanger that has circulatory channels for temperature regulated fluid flow, which can be used to keep the medium-filled sample chamber at a specific temperature.

The sample holder is comprised of two parts: (i) a caddy that holds the specimen and (ii) a “dive bar” that holds the caddy and connects it to the stack-up of motion-control stages. Caddies can be used for agarose embedding of the sample or adapted to specific applications. For example, the caddy for imaging neural activity in behaving zebrafish (Fig. 2.6B) immobilizes the specimen’s head with 1.5% low-melting agarose gel (to record cellular resolution whole-brain neural activity), leaving the tail free to move (to record swimming behavior). With one end of the dive bar holding the caddy immersed in the imaging buffer, the other end is mounted to a dual-axis goniometer, providing rotational motions around the x - and y -axes (Fig. 2.6B). The goniometer is in turn mounted on a 3D stack-up of motorized linear stages (see Table A1), with each stage providing ± 25 mm of travel range. The combination of the two-axis goniometer and 3D stage stack-up allows fine sample positioning so that the

illuminated region of interest can be overlapped with the detection objective focal plane. The two-part design of the sample holder allows for the flexibility of designing different caddies to be best suited for specific types of specimens while still using the same dive bar to connect the caddy to the motion-control stages.

The flex-SPIM has two different modes of capturing volumetric information from a 3D sample: either by sample-scanning or by objective-scanning.

- Sample-scanning mode: the excitation light-sheet and detection objective remain stationary; the sample is moved via the z -stage of the 3D stage stack-up along the optical axis of the detection subsystem and images are sequentially collected. As the z -stage is already a necessary part of sample positioning, this approach is the simplest and most economical to implement. The motion range of z -stages is typically tens of mm; hence, sample-scanning enables volumetric imaging of large samples with depths up to the working distance of the detection objective (several mm or more). However, the imaging speed is limited by mechanical inertia of the stage and sample holder and by the communication overhead between the acquisition computer and the z -stage controller. Furthermore, the translational motion of the specimen can compromise normal biology.
- Objective-scanning mode: the movement of the detection objective piezo collar is synchronized with the second galvo mirror of each illumination arm—the light-sheet and piezo collar are scanned axially in concert (with a travel range of $\pm 500 \mu\text{m}$ set by the piezo collar) and images are sequentially collected (further details are described in [2.2.5](#)). This approach, notwithstanding the additional cost of the piezo collar and its limited range of motion, enables fast volumetric imaging without moving the specimen and is preferred for our whole-brain functional imaging and simultaneous behavioral observation studies with zebrafish.

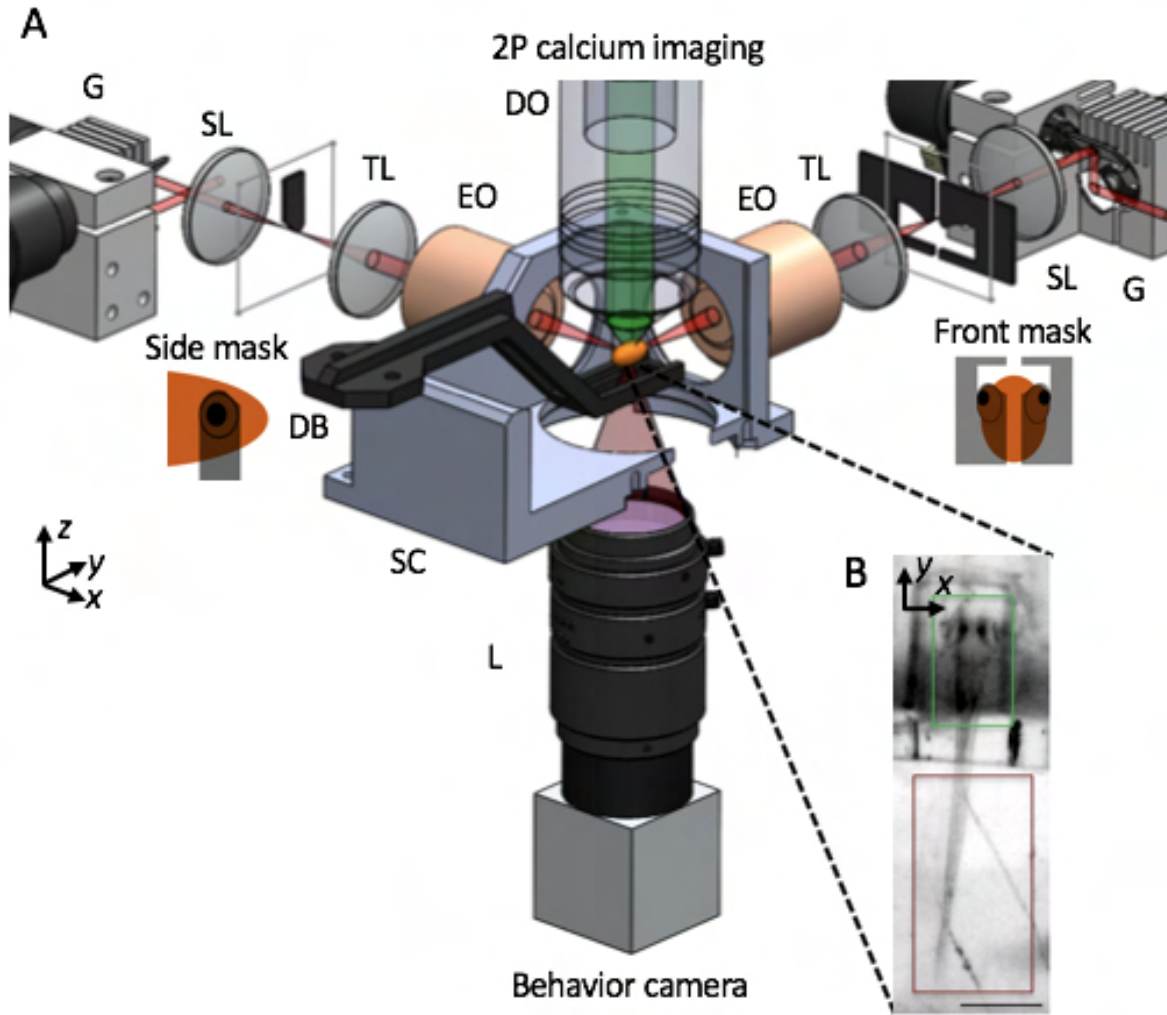


Figure 2.6: SPIM imaging of intracellular calcium for capturing neuronal activity. **(A)** Schematic of apparatus for imaging of neural activity during various behaviors in the larval zebrafish. Sheets of laser light are synthesized by quickly scanning the pulsed illumination beam (red) with galvo mirrors (G). 2P light-sheets are delivered to the agarose-embedded head of the animal with excitation objectives (EO) from the side and front arms. The side masks cover each eye on the sides of a horizontally oriented zebrafish, while the front mask covers both eyes, enabling access to neurons between the eyes. 2P-excited calcium fluorescence signal is collected through an upright detection objective (DO) and onto a scientific CMOS camera. A triggerable wide-field camera is positioned below the sample chamber (SC) to provide a wide- field, low-resolution view of the sample, as shown in **(B)**. During a typical neural imaging experiment, the zebrafish larva is mounted in a caddy, which in turn is mounted to the dive bar (DB) underneath the DO. Within the caddy, the zebrafish's head is immobilized in agarose, while the tail is free, permitting the monitoring of zebrafish behavior through tail movement. SL—scan lens, TL—tube lens, SC—sample chamber, and L—camera lens. The third illumination arm, emission filter, detection TL, scientific camera, light-emitting diode, and filter for behavior channel are not shown. Insets in **(B)** highlight that the calcium fluorescence channel (green) is recorded from the zebrafish brain, while the behavioral channel (dark red) monitors the tail movement of the animal. Scale bar **(B)**, 400 μ m.

2.2.5 Instrument control module

Each twin is independently controlled with a computer equipped with two Xeon E5-2650 v4 processors and 128 GB of 2400 MHz DDR4 RAM and seven PCIe slots, enough space for all the control cards. Instrument control and image acquisition are done through Micro-Manager [83]. Custom software developed in LabVIEW (National Instruments) is used to independently control each of the 2D scanning galvo mirror systems and allows precise alignment (size and swept-rate control) of the excitation light-sheet relative to the sample (software available upon request). Collected images are written directly to a dual-disk array consisting of eight 7200 rpm, 4-TB disks.

In the objective-scanning mode, the piezo collar's controller serves as the master timing source. The analog position-readout of the piezo collar triggers a PicoScope, which is used to generate control signal sequences to synchronize the camera(s) with image capture. The position-readout of the piezo collar is also used to drive the position of the z -galvos. The waveform from the timing output of the scientific CMOS camera controls the AOTF and Pockels so that the sample is not illuminated during the camera readout. Analog control signals for the galvos and Pockels are appropriately conditioned by individual scaling amplifiers. A schematic of the control signal sequences is shown in (Fig. 2.7).

2.2.6 Auxiliary module

Illumination can be selectively blocked with masks to avoid photosensitive regions or auto-fluorescent features in samples. For example, to avoid illuminating the zebrafish eyes while imaging neural activity, the excitation light is physically blocked with a pair of masks on each side of a horizontally positioned zebrafish and another mask for the front that covers both eyes (Fig. 2.6A). These masks, fabricated out of black anodized aluminum, are mounted at the image planes of the illumination-scanning optics, each on 2D translational stages to permit their accurate positioning for different specimens or their complete removal from the illuminated field. A far-red light-emitting diode and a wide-field camera, positioned to view

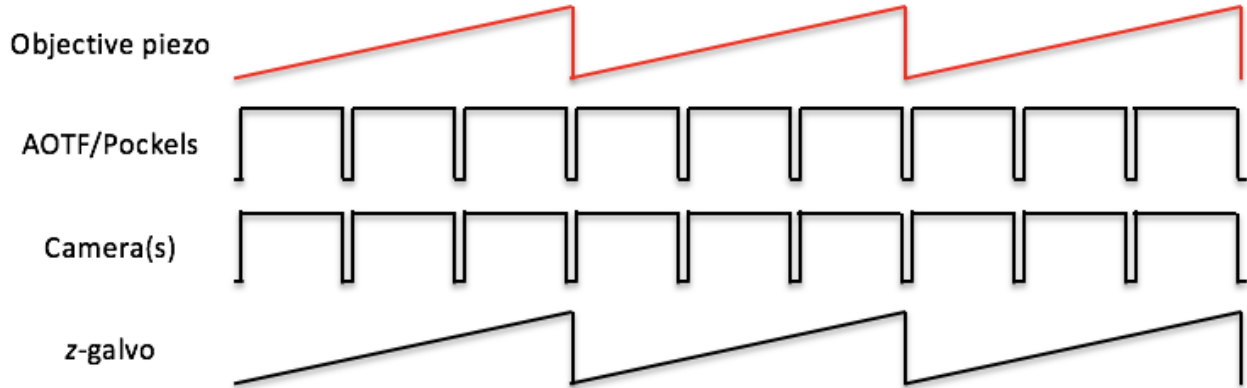


Figure 2.7: Schematic of control signal sequences for objective-scanning mode. The analog signal representing the position of the objective piezo collar is used as the master timing signal to generate control signals for the imaging cameras (both the fluorescence camera and behavior camera). The timing output of the fluorescence camera controls the AOTF/Pockels. The number of pulses driving the cameras, shown as 3 in the schematic here, determines the number of individual z -plane images to be recorded during a single z -scan cycle over the sample. The position signal of the objective piezo collar, appropriately scaled by a scaling amplifier, is also used to drive the z -galvo.

the sample from the bottom, enable view-finding and monitoring the tail behavior during neural imaging of the zebrafish (Fig. 2.6).

2.3 Instrument performance

We characterized the 3D resolution of the flex-SPIM by measuring the point-spread function (PSF) with sub-diffraction fluorescent beads and then demonstrated the utility of the instrument for investigating biological systems by imaging the beating embryonic zebrafish heart, thick patient-derived tumor organoids, and neural activity in behaving zebrafish.

2.3.1 Resolution characterization

We measured the system PSF with sub-diffraction (175 ± 5 nm diameter) fluorescent beads (PS-Speck Microscope Point Source Kit, P7220, Molecular Probes) embedded in 1.5% agarose, using the same detection objective ($20\times$, NA = 1.0) with different tube lenses to yield two different magnifications of $44\times$ and $11\times$ (Table A1). Representative bead images

and quantitative values of the PSF are presented in Fig. 2.8. On the whole, the instrument achieved $\sim 0.5 \mu\text{m}$ and $1 \mu\text{m}$ lateral resolution, for $44\times$ and $11\times$, respectively, and $\sim 1.8 \mu\text{m}$ axial resolution at both magnifications. This performance comes close to but does not achieve the full theoretical resolution limit determined by the NA of the detection objective, which is expected due to the practical compromises that we have made with the detection subsystem, as discussed previously in 2.2.3. Overall, the demonstrated resolution is quite suitable for a variety of imaging applications and represents the practical compromise between achieving a high resolution while maintaining a large field-of-view.

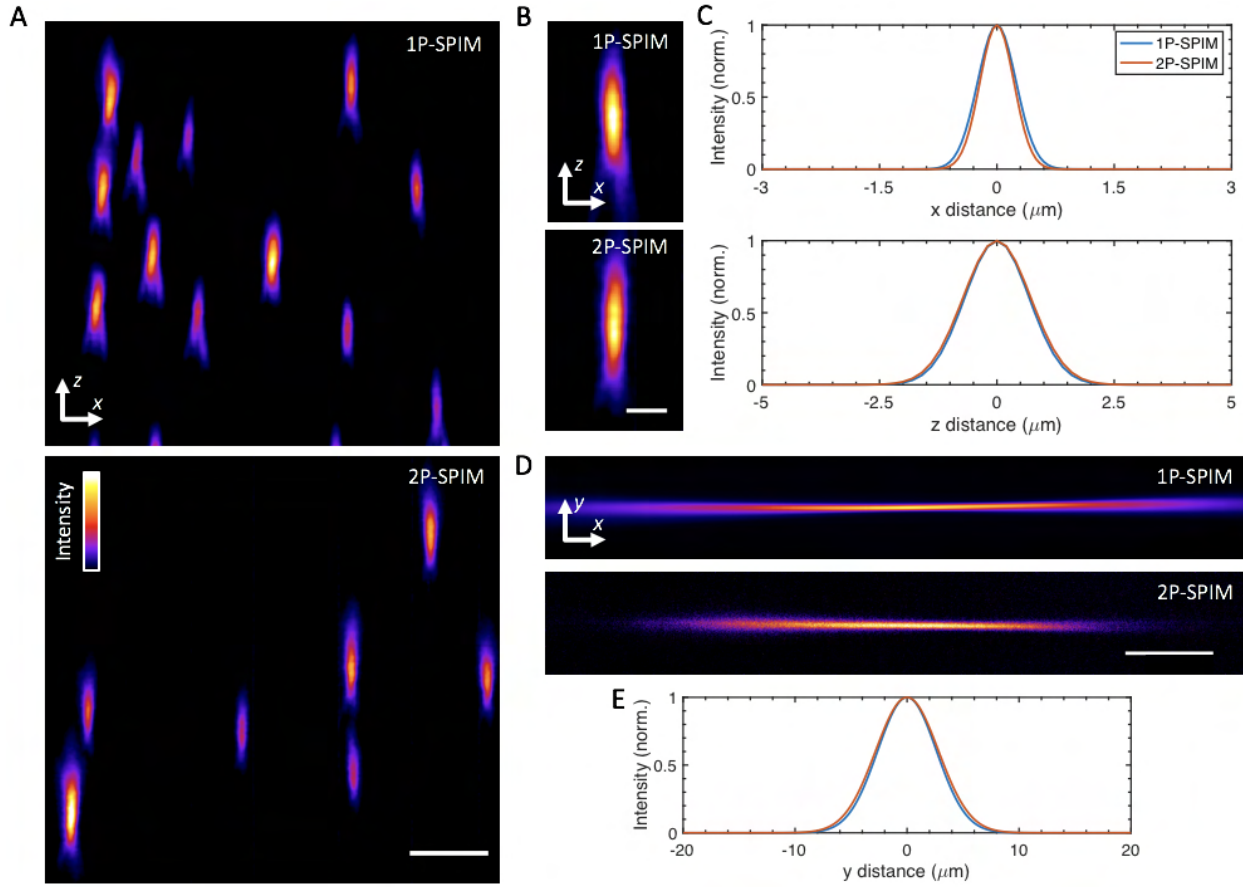


Figure 2.8: System imaging performance and characterization.

(A) y maximum-intensity projections of agarose-embedded 175 nm fluorescent beads imaged at 44 \times magnification in 1P (top) and 2P excitation mode (bottom). A false-color (fire) lookup table was used to enhance visualization.

(B) Selected y maximum-intensity projections of sub-diffraction fluorescent beads in 1P (top) and 2P mode (bottom).

(C) Averaged lateral (top) and axial (bottom) full-width at half-maximum (FWHM) extents for the imaged beads, determined by Gaussian fits of 7 bead intensity profiles. The averaged lateral and axial FWHM \pm SD values are 1P, 579 $\mu\text{m} \pm$ 15 nm and 1.67 $\mu\text{m} \pm$ 118 nm, respectively, and 2P, 528 $\mu\text{m} \pm$ 50 nm and 1.78 $\mu\text{m} \pm$ 183 nm, respectively. Similar measurements at 11 \times magnification yield 1P, 1.2 $\mu\text{m} \pm$ 86 nm and 1.73 $\mu\text{m} \pm$ 387 nm and 2P, 1.17 $\mu\text{m} \pm$ 232 nm and 1.81 $\mu\text{m} \pm$ 370 nm for lateral and axial directions, respectively.

(D) Experimental images of fluorescence excited by 1P (top) and 2P (bottom) Gaussian focused beams, which are scanned in the y direction to create virtual light-sheets. Images were acquired by illuminating a solution of rhodamine in the sample chamber.

(E) Intensity line profiles for the focused beams in (d), taken at the center of focus, with approximate FWHM values: 1P, 6.2 μm and 2P, 6.6 μm . These FWHM values yield an averaged light-sheet thickness of $\sim 10 \mu\text{m}$ across the 400 μm extent along the x direction, centered around the Gaussian focus.

Scale bars: **(A)** 5 μm , **(B)** 2.5 μm , and **(D)** 150 μm .

2.3.2 Light-sheet imaging of the beating zebrafish heart

The vertebrate heart is a highly dynamic organ that starts to take its form and function early on during development [84]. To gain insight into how the heart develops, studies of cells in their native dynamic and 3D context in the intact heart are needed. While the zebrafish is an ideal model system because of its optical and genetic accessibility [85], imaging is challenged by the heartbeat motion at 2–4 Hz and over tens of micrometers in amplitude [86]. Retroactive synchronization techniques can align the 2D images by taking advantage of the quasi-periodicity of the heart motion [77, 87–89]. We acquired 2D images of the beating heart at a high-spatiotemporal resolution in a 5-dpf transgenic larval zebrafish with the vasculature fluorescently labeled. The 1P excitation ($\lambda = 488$ nm) light-sheet was parked in z to optically section through the beating heart of the agarose-embedded sample as we acquired images at 85 frames/s, 11 \times magnification, and subcellular resolution (Fig. 2.10 and Movie 2.9), showing that the flex-SPIM is fully compatible with existing retroactive synchronization techniques [77, 87–89].

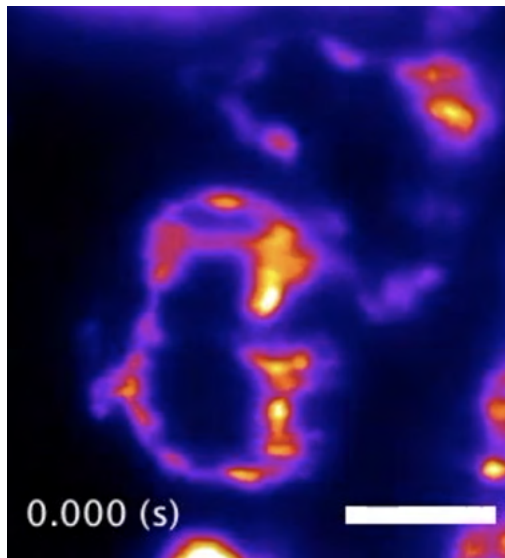


Figure 2.9: Light-sheet imaging of the dynamic motion of the beating heart of a 5-dpf transgenic larval zebrafish. Same dataset as presented in Fig. 2.10. Frames were captured at 85 Hz. Scale bar, 50 μ m. Movie: https://aip.scitation.org/doi/video_original/10.1063/1.5144487/1.5144487.mm.original.v1.mp4 (0.5 MB).

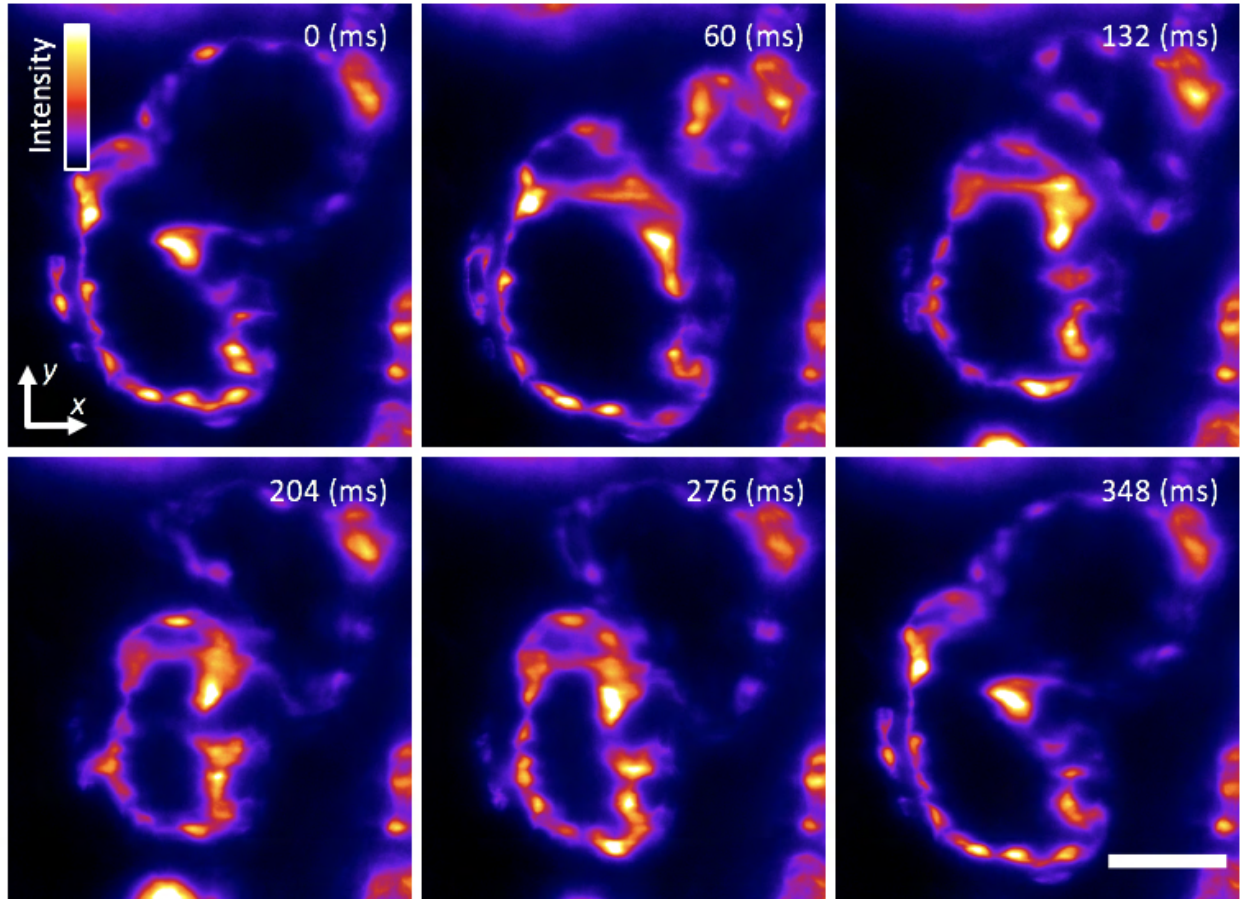


Figure 2.10: Cardiac light-sheet imaging. Single-plane SPIM recording of the beating heart in a live 5-dpf larval zebrafish with the endocardium fluorescently labeled (GFP), showing six distinct time points during the cardiac beating cycle. These subcellular 2D images are comparable to our previous efforts [77] as well as recent work by others [87]. A false-color (fire) lookup table was used to enhance visualization. Frames were captured with a magnification of $11\times$ and 5 ms exposure time at a rate of 85 frames/s. Fig. 2.9 (movie) shows a movie of the same data. Scale bar, $50\ \mu\text{m}$.

2.3.3 Imaging of thick, patient-derived tumor organoids

3D cell culture systems, such as spheroids or organoids, recapitulate the native physiology of multicellular tissues much better than 2D culture systems [90]. Multicellular cancer organoids permit the study of disease development and patient-specific response to therapy [91, 92]. Unfortunately, such multicellular systems are scattering and aberrating, making them challenging to image with conventional instruments.

To show the advantages of the flex-SPIM for such opaque and optically heterogeneous samples, we imaged, at $11\times$ magnification, chemically fixed, agarose-embedded organoids differentiated from cells derived from a colorectal cancer patient that had been engineered to transgenically express nuclear-localized H2B-GFP (Fig. 2.11A and Movie 2.12). 2P-SPIM provides better contrast throughout the imaged volume because the reduced scattering at the longer wavelength ($\lambda = 900$ nm) enables better-preserved light-sheet shape over longer propagation distances compared to 1P (Fig. 2.11B, C, and E). Even when the excitation light scatters, the fluorescence signal is still spatially restricted mainly to the central part of the light-sheet (where intensity is the highest) because of the quadratic dependence of the 2P-excited fluorescence signal on the excitation intensity. Thus, by mitigating the scattering-induced thickening of the light-sheet, 2P excitation with the flex-SPIM yields better effective 3D resolution than 1P (Fig. 2.13) and captures better images of labeled cells deep in the specimen (Figs. 2.11D and F).

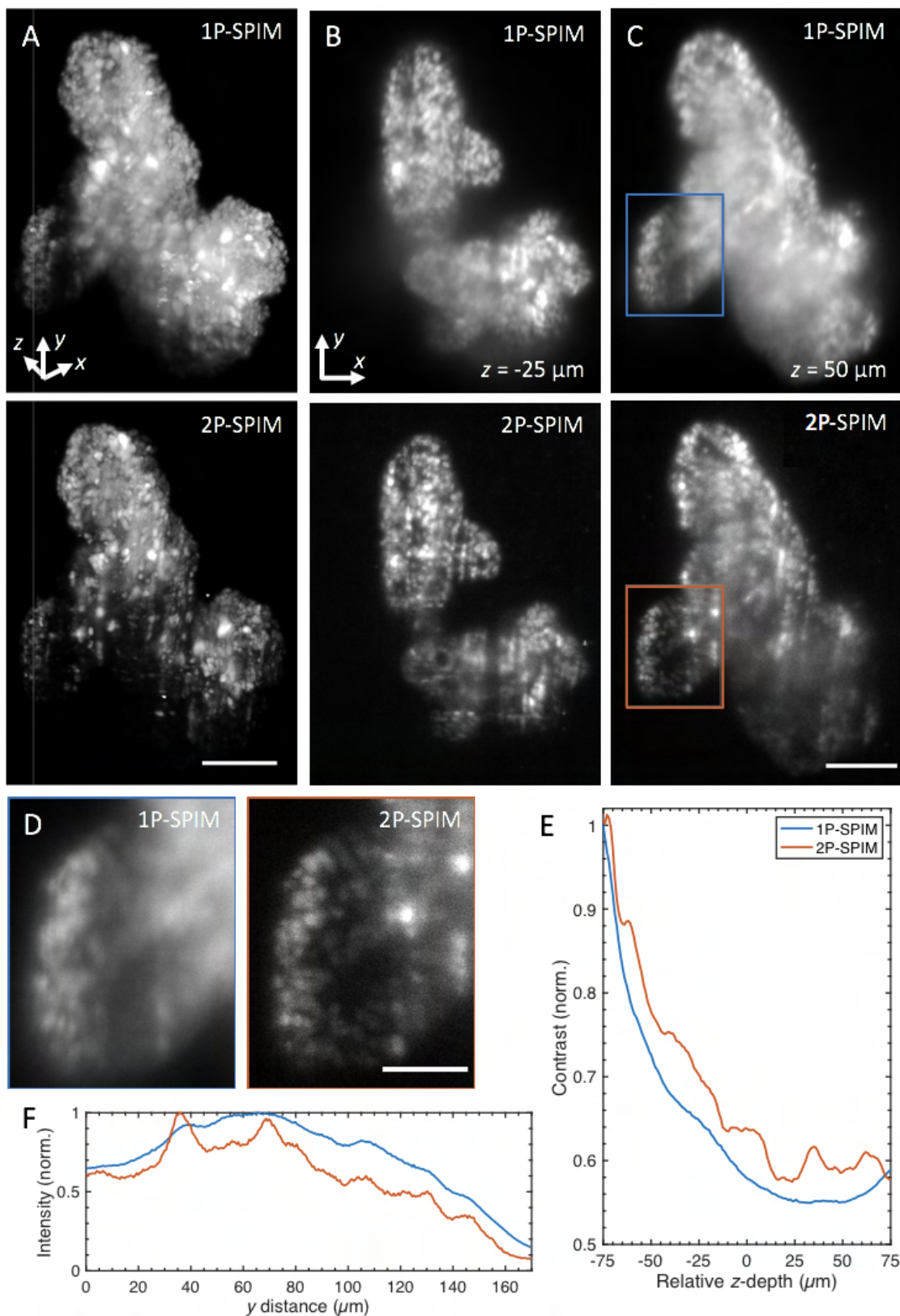


Figure 2.11: Continued on next page.

Figure 2.11: (Continued from previous page.) 1P- and 2P-SPIM imaging of thick tumor organoids derived from a patient with colorectal cancer.

(A) Volume rendering of fixed patient-derived tumor organoids expressing nuclear-localized H2B-GFP recorded in 1P (top) and 2P mode (bottom). Renderings show that the reduced background of 2P-SPIM enables better contrast throughout the imaged volume compared to 1P-SPIM. 3D organoid volume of $\sim 400 \times 55 \times 150$ ($x-y-z$) μm^3 captured with a magnification of $11\times$, $1\text{-}\mu\text{m}$ z -steps, and 150 ms exposure time. Figure 2.12 (movie) rotates the 3D-rendered volume of the same datasets.

(B) and (C) are $x-y$ image slices of (A) at $z = -25$ μm (50 μm from the surface) and $z = 50$ μm (125 μm from the surface), respectively. (D) Magnified images of the boxed regions in (C) for 1P (left) and 2P (right) mode revealing that 2P-SPIM resolves more cells than 1P-SPIM deep in the sample.

(E) Quantification of image contrast as a function of z -depth. This plot shows quantitatively the improved contrast of 2P-SPIM over 1P-SPIM throughout the imaged volume in (A). Contrast calculated from the standard deviation of the pixel intensities from each $x-y$ image slice and then normalized by the corresponding average image intensity. Each slice (from both modalities) is normalized against the surface slice ($z = -75$ μm) of 1P-SPIM to show the degradation of performance as a function penetration depth.

(F) Plot shows sum intensity along the x direction of images in (D) as a function of light-sheet propagation distance y . The longer NIR wavelength used in 2P-SPIM minimizes the scattering-induced degradation of the excitation light-sheet over longer propagation distances compared to the visible light used in 1P-SPIM. In both intensity profiles, intensity values were normalized by the global maximum.

Scale bars: (A) 100 μm and (B) 50 μm .

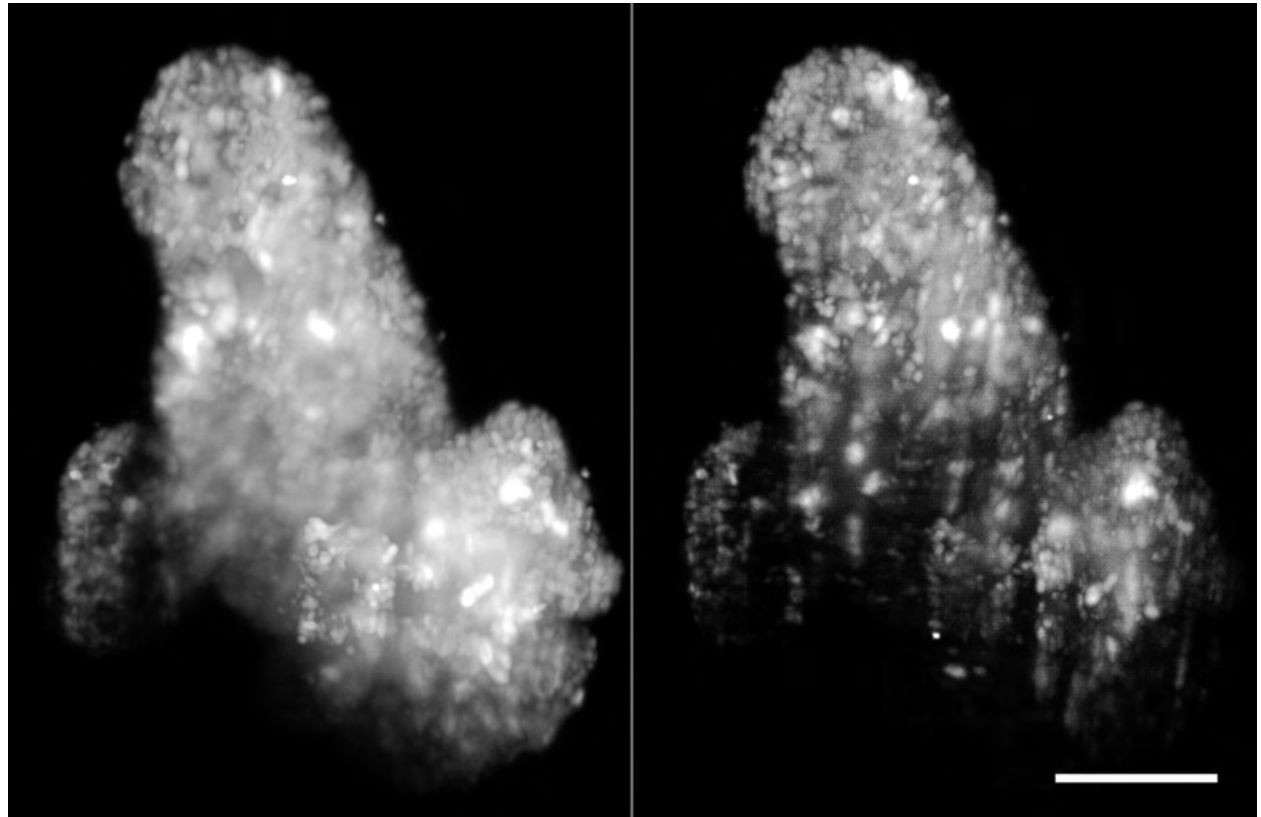


Figure 2.12: Volume rendering of fixed patient-derived tumor organoids expressing H2B-GFP, comparing images taken with 1P- (left) and 2P-SPIM (right). Volumes are rotated around the y and x axes. Same datasets as presented in Fig. 2.11. Scale bar, 100 μm . Movie: https://aip.scitation.org/doi/video_original/10.1063/1.5144487/1.5144487.mm.original.v2.mp4 (18.8 MB).

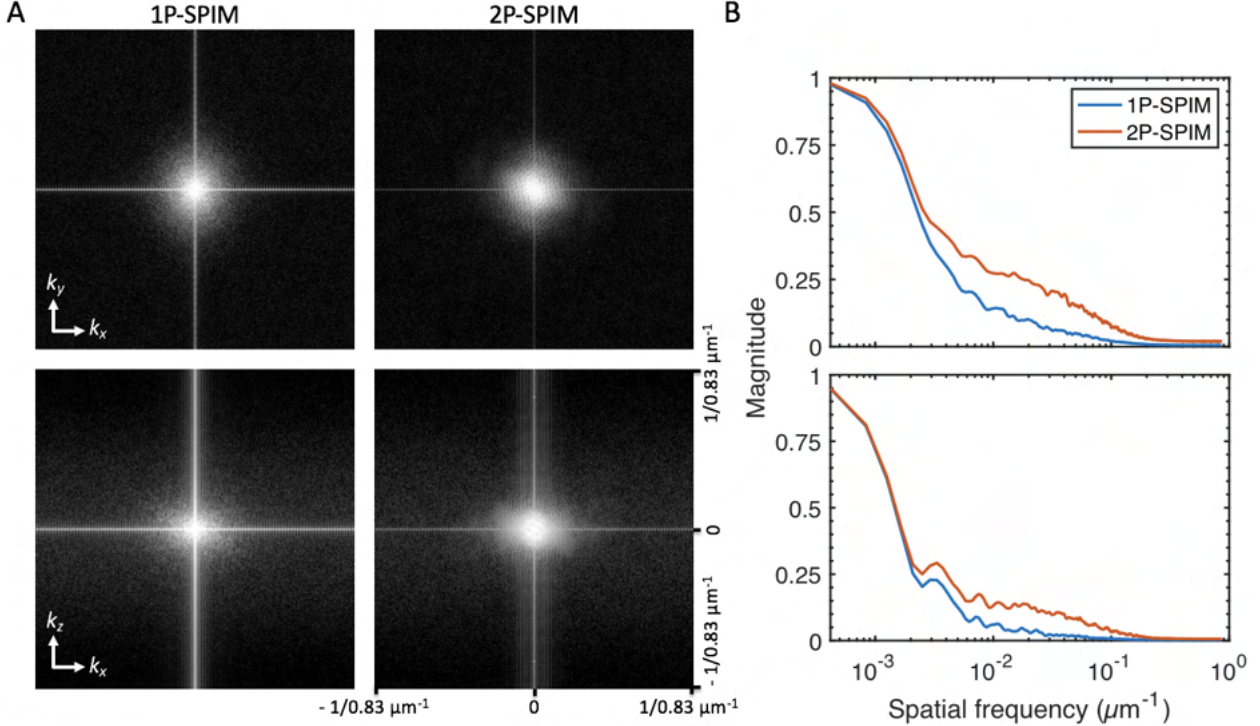


Figure 2.13: Optical transfer function (OTF) comparisons of patient-derived tumor organoids.

(A) Maximum intensity projections along z (x - y OTF, top row) and y (x - z OTF, bottom row) of the OTF showing higher spatial frequencies are transmitted with 2P-SPIM (right column), due to the sheet being more resistant to light scattering compared to 1P-SPIM (left column).

(B) Quantitative comparison of x - y (top row) and x - z OTFs (bottom row), demonstrating the slower spatial frequency roll-off for 2P-SPIM, both laterally and axially, and hence improved effective 3D resolution over 1P-SPIM. Plot shows average amplitudes along the k_y and k_z direction of top and bottom images in (A), respectively. The magnitudes for each OTF were normalized by the corresponding DC component.

2.3.4 Whole-brain functional imaging of behaving zebrafish

SPIM enables recording of whole-brain neural activity in transgenic larval zebrafish [71, 72]. These implementations, however, potentially stimulate the photoreceptors and other photosensitive cells in the retina with the visible excitation wavelengths used during acquisition. Such illumination can reduce visual sensitivity to stimuli and interfere with visually driven processes [76]. NIR ($\lambda = 930$ nm) 2P-SPIM overcomes this problem [76], achieving a recording depth of $120 \mu\text{m}$ at a 1 Hz volume rate (sampled by nine z -planes) [73].

We push the depth of 2P light-sheet functional imaging further with the flex-SPIM: more than doubling the volume size while maintaining high spatiotemporal performance (Fig. 2.14 and Movie 2.15). By employing a trio of 2P excitation arms with masks to avoid direct laser illumination to the animal’s eyes, we imaged the entire ($400 \times 800 \times 250 \mu\text{m}^3$) brain of a 5-dpf zebrafish expressing a pan-neural calcium indicator (elavl3:H2B-GCaMP6s) [72] at a 0.5 Hz volume rate (sampled by 52 z -planes) with single-neuron resolution and simultaneously monitored swimming behavior with a wide-field camera (Fig. 2.6). The temporal and spatial resolution of the time-series were sufficient to visualize individual active neurons across the brain (Fig. 2.14A and B) and capture single-neuron activity traces by calculating the relative fluorescence variation ($\Delta F/F$) as a function of time (Fig. 2.14C). Imaging was carried out for 30 min continuously with 490 mW of total average laser power delivered to the sample from the three illumination arms. We observed no apparent signs of phototoxicity from the animal’s macroscopic behavior (Fig. 2.14E), cellular structure (Figs. 2.14A and B), or calcium dynamics (Fig. 2.14C). Furthermore, the total fluorescence signal decreased by less than 0.5% after the 30-min, 900- z -stack acquisition (Fig. 2.14D), indicating that photobleaching was negligible. In future work, systematic analysis of the 4D functional imaging data acquired by the flex-SPIM, aided by state-of-the-art analysis pipelines such as CaImAn [93], will enable quantification of whole-brain single-cell activity patterns to gain insights into the neural basis of behavior.

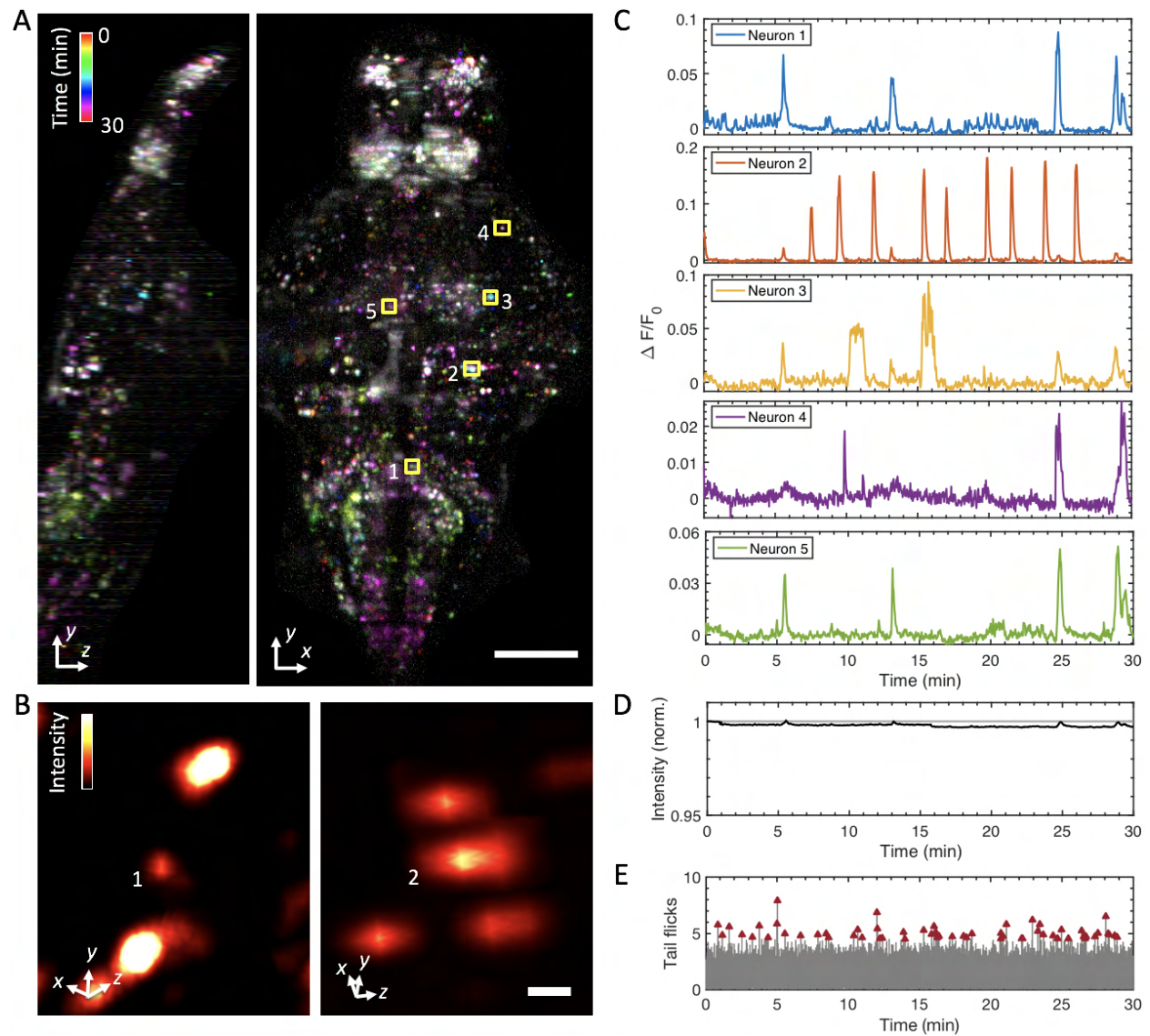


Figure 2.14: Continued on next page.

Figure 2.14: (Continued from previous page.) Whole-brain functional imaging at single-cell resolution in behaving 5-dpf transgenic larval zebrafish expressing nuclear-localized calcium indicator elavl3:H2B-GCaMP6s.

- (A) Maximum-intensity projections of calcium activity are color-coded in time over the 30-min recording window. Active neurons that exhibit fluorescence change during the recording appear as colored dots. Volume of $400 \times 800 \times 250$ ($x-y-z$) μm^3 was sampled by 52 z -planes (4.8 μm z -steps) at 0.5 Hz and 11 \times magnification. Figure 2.15 (movie) shows a 3D rendered movie of the same specimen.
- (B) Magnified volume renderings of neuron 1 (left) and neuron 2 (right) outlined in the $x-y$ projection in (A), demonstrating cellular resolution in whole-brain 2P-SPIM imaging. The standard deviation projection along the temporal axis was used to generate the renderings, and a false-color (hot) lookup table was used to aid visualization.
- (C) Representative single-neuron activity traces extracted from the whole-brain recordings, calculated as $\Delta F/F$ from the manually selected neurons in (A).
- (D) Plot shows the total sum intensity of the entire imaged volume as a function of time, normalized to the average intensity of the first 5 min of acquisition (gray line at $y = 1$). Total intensity exhibits less than a 0.5% decrease in magnitude after the 30-min recording window, indicating that photobleaching is negligible.
- (E) Analysis of tail flick behavior as a function of time. Tail flicks (movements) obtained by taking the absolute difference in the pixel intensities from the tail region of the wide-field view of the sample, as shown in Fig. 2.6, normalized by the average image intensity corresponding to when there is no tail movement (gray lines). A threshold was applied to classify tail flicks and subsequently confirmed by manual inspection. Tail flicks (red arrowheads), indicating intended swimming behavior, occur throughout the recorded time window (average of ~ 9 flicks ± 2.2 every 5 min), thus suggesting minimal stress from the imaging conditions used. Scale bars: (A) 100 μm and (B) 5 μm .

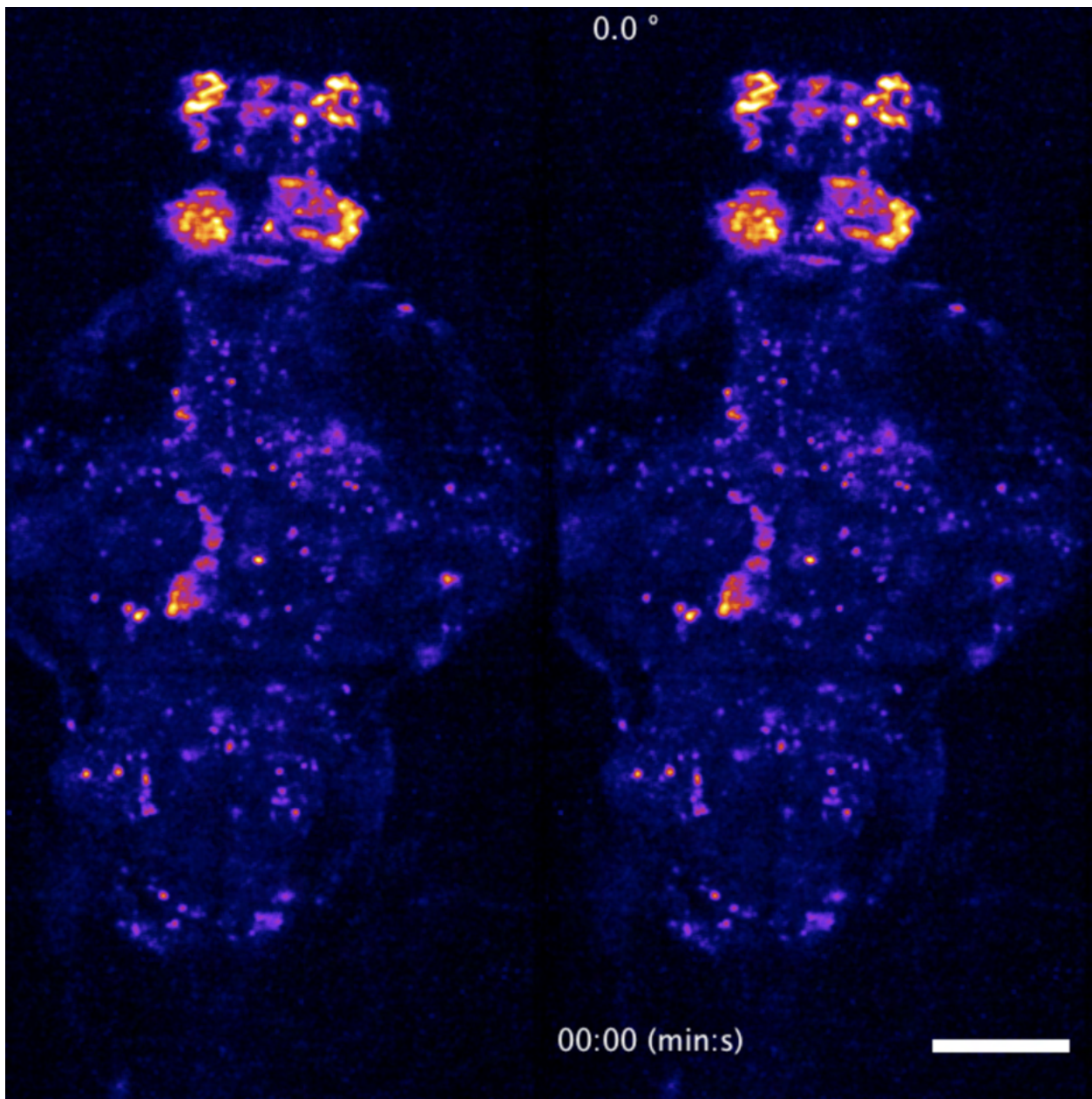


Figure 2.15: Dorsoventral (left) and rotating (right) maximum-intensity projections of a time-lapse recording of the whole-brain of a 5-dpf transgenic larval zebrafish. 2P whole-brain functional light-sheet imaging was performed at a volumetric rate of 0.5 Hz. The video loops a 5-min recording as part of the data presented in Fig. 2.14. Scale bar, 100 μ m. Movie: https://aip.scitation.org/doi/video_original/10.1063/1.5144487/1.5144487.mm.original.v3.mp4 (11.1 MB).

2.4 Discussion

We present the design and construction of the flex-SPIM, an instrument with two independently controlled light-sheet microscope-twins sharing the same multi-laser source, dramatically cutting the cost of the system. We demonstrate instrument versatility and application-specific customization by imaging a variety of specimens. In the same spirit as the OpenSPIM project [94], we offer a blueprint for optical developers to build and/or modify the flex-SPIM to serve user needs. Our design choice of upright (or inverted) detection, combined with our sample-mounting scheme using the caddy and the dive bar, allows for the flexibility in mounting different types of samples, from fixed tissues to live zebrafish embryos, but makes our instrument not easily amenable to multiview imaging [95], where the sample is imaged from multiple directions to improve axial resolution and coverage. On the other hand, a number of other modifications and enhancements could be implemented on the flex-SPIM to further optimize its performance for specific applications. Incoherent structured-illumination from intensity-modulated illumination patterns generated by the AOTF and/or Pockels cell would enhance contrast in more scattering specimens but would require additional exposures and post-processing [96]. Confocal line detection using the rolling shutter of the sCMOS camera is an efficient alternative to structured-illumination and would allow rejection of non-ballistic photons [97]. Designing a sample chamber rig with both temperature and CO₂ control in conjunction with inverted detection would allow for optimized live imaging of cultured tissues as well as organoids.

Light-field microscopy could be readily deployed on the flex-SPIM, enabling high-contrast, synchronous volumetric imaging with SPIM-inspired selective-volume illumination [52]. In addition, implementing multispectral imaging would improve signal multiplexing, either on the illumination path by rapid multispectral excitation [98] or on the detection path by de-scanned detection via a confocal slit and diffraction grating [99]. Further improvement is possible with our hyperspectral phasor software (HySP) for unmixing multiple spectrally overlapping fluorophores, even in the face of low signal-to-noise [100]. The combination of

HySP with a multispectral flex-SPIM design could thus enable dynamic visualization and quantitative analysis of many more important components and their interactions in intact specimens at high-resolution over extended durations.

2.5 Ethical approval statement

All zebrafish raising and handling procedures followed guidelines established in the Guide for the Care and Use of Laboratory Animals by the University of Southern California, where the protocol was approved by the Institutional Animal Care and Use Committee (IACUC). All zebrafish lines used are available from ZIRC (zebrafish.org).

2.6 Supplementary Material

2.6.1 Simulations of scan performance using an achromatic doublet

We chose an achromatic doublet lens as a scan lens, instead of using specially-designed scan lenses which are more expensive. This decision was based on computer-aided optical modeling (Zemax, Radiant Zemax LLC) of commercially available lenses, showing that the achromatic doublet lenses have sufficient performance for our needs. We considered $1/e^2$ Gaussian beam diameters ≥ 1.5 mm and ≤ 4 mm; excitation wavelengths corresponding to 445 nm, 448 nm, 561 nm, 647 nm, 910 nm, and 1040 nm; and a maximum scan angle of $\pm 4^\circ$, which is equivalent to sweeping out a 2.56 mm^2 illuminated plane at the sample (given the illumination tube lens and excitation objective described above)—far exceeding the desired $\sim 0.5 \times 1\text{ mm}^2$ illuminated field. Being ultra-conservative about the maximum field angle ensured minimal aberrations as well as the flexibility to illuminate even larger areas ($> 0.5 \times 1\text{ mm}^2$), if desired. The chosen achromatic doublet does a surprisingly good job of broadband (445-1040 nm) diffraction-limited performance over a large field angle, as illustrated in Fig. 2.16. Further optimization could be achieved with the use of custom [101]

or more sophisticated lens design [102, 103] such as the Plössl (a pair of symmetric achromatic doublets opposing each other) [102]; however, the cost would scale proportionally with each scan lens.

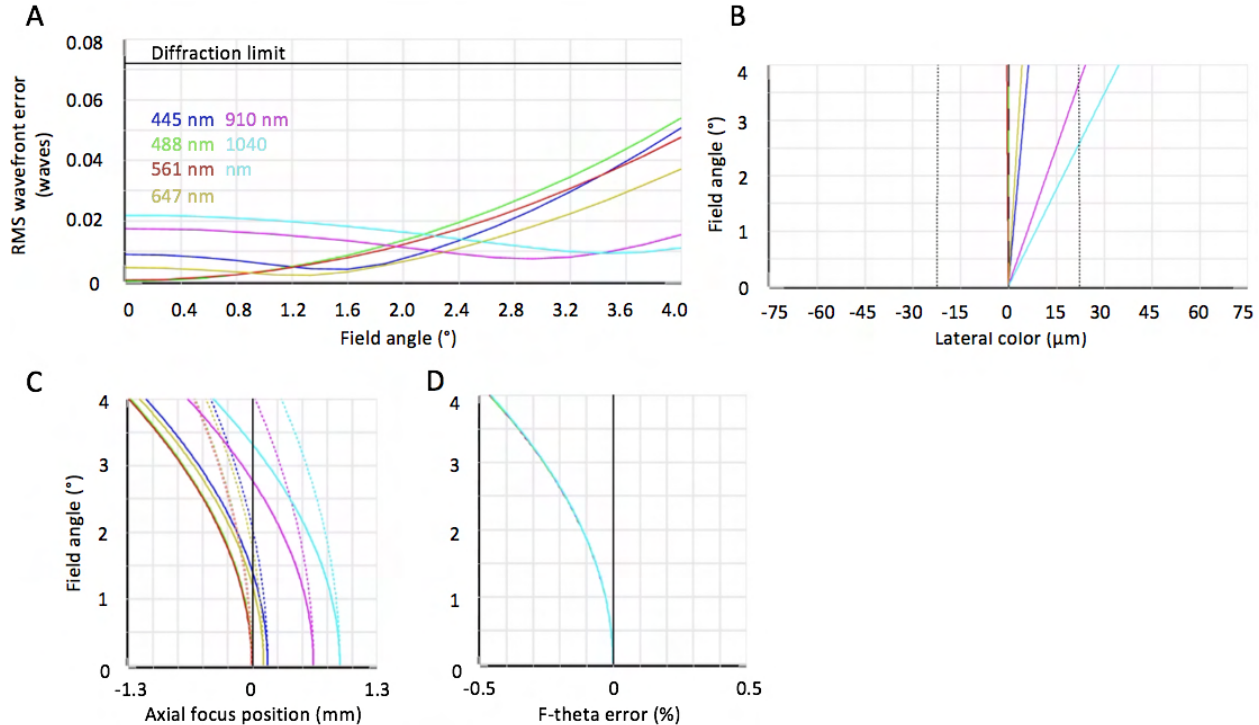


Figure 2.16: Simulations of the performance of the scan lens used, achromatic doublet ($f = 150$ mm, 50 mm diameter, VIS-NIR 49-391, Edmund Optics) using a $1/e^2$ beam diameter of 4 mm. (A) Transmitted wavefronts (measured by root mean squared (RMS) wavefront error) remain diffraction-limited, well beyond the desired scan range (for reference, $\pm 2^\circ$ is equivalent to a 1.25 mm^2 illuminated field at the sample). (B) Using a 1000 nm Airy disk as reference, lateral color remains diffraction-limited for the desired $\pm 2^\circ$ scan range; for scan angles $> 2.5^\circ$, chromatic aberrations occur at 910 nm and 1040 nm. (C) Field curvature for the tangential and sagittal beam components, respectively represented by the solid and dashed lines. At the maximum scan angle of $\pm 4^\circ$, the field curvature is 1.3 mm for the tangential and 0.52 mm for the sagittal components; at the sample, this curvature translates to $\sim 0.9 \mu\text{m}$ for the tangential and $\sim 0.4 \mu\text{m}$ for the sagittal components, both of which are minor deviations relative to the illuminated field. (D) F-theta distortions are minimal: $< 0.5\%$ at the largest scan angle.

2.7 Acknowledgements

We are grateful to Sara Madaan for custom LabView software, Matt Jones for electronics help, Peter Luu for zebrafish sample preparations, Seungil Kim and Shannon Mumenthaler (Lawrence J. Ellison Institute for Transformative Medicine of USC) for providing the organoid samples, and Jon Daniels (Applied Scientific Instruments, Inc.) for valuable thoughts on beam-scanning in light-sheet microscopy. Special thanks to Andrey Andreev and the other members of the Translational Imaging Center for insightful discussions and staff at the Viterbi/Dornsife Machine Shop for technical assistance. We acknowledge the loaning of some equipment used in our work as part of the Innovation Partnership in Multiscale Bioimaging between Olympus Corp. and USC's Ellison Institute and Translational Imaging Center. This work was supported, in part, by the National Institutes of Health (Grant No. 1R01MH107238-01) and the Human Frontier Science Program (Grant No. RGP0008/2017). K. Keomanee-Dizon was supported, in part, by the Alfred E. Mann Doctoral Fellowship.

2.8 Manuscript information

2.8.1 Previously published as

A previous version of this chapter appeared in [49]:

Keomanee-Dizon, K., Fraser, S. E. & Truong, T. V. A versatile, multi-laser twin-microscope system for light-sheet imaging. *Review of Scientific Instruments* **91**, 053703 (2020)
DOI: <https://doi.org/10.1063/1.5144487>

2.8.2 Author contributions

K.K.D designed, built, and performed all experimental characterization of the twin-microscope system with input from T.V.T and S.E.F. K.K.D. acquired, processed, and performed quantitative analysis of all optical image data, and produced all figures and movies, with input

from T.V.T. T.V.T. and S.E.F. supervised the project. K.K.D., S.E.F., and T.V.T. wrote the manuscript.

3

Extended depth-of-field improves light-sheet
microscopy at high numerical aperture

3.1 Introduction

From molecules to a cellular function, or from a collection of cells to an organism, the most striking phenomena of life emerges from spatially complex, dynamic interactions among millions of components over time. Optical imaging of such dynamics is needed to advance the fundamental understanding of their interrelationships—and by extension, the treatment of human disease—but is challenged by the multiple spatial, temporal, and energetic

scales in which they take place. Although various light-sheet microscopy (also known as selective-plane illumination microscopy; SPIM) techniques have been applied to this multiscale bioimaging problem [61], SPIM remains difficult to use in many specimens because the cellular dynamics encountered are fast and extend over a large, optically heterogenous volume, thereby creating a low signal-to-noise (SNR) regime within the specimen.

Photon flux from the sample sets the fundamental limit on temporal resolution: even an ideal detector with infinite speed and zero noise must wait for enough photoelectrons to form an image with acceptable SNR [4, 104]. In practice, photodamage sets the budget on the number of photons that can be captured from the specimen. Increasing the excitation intensity above the specimen’s photodamage-threshold (maximum tolerable excitation dosage) will not yield more useful signal but will induce unwanted bleaching and toxicity. Thus, the use of a high-numerical-aperture (NA) objective lens for detection is generally desirable, because it enables high spatial resolution as well as high light collection, which is critical for maximizing SNR while minimizing photodamage to living specimens.

The penalty for high-NA optics is the short depth-of-field (DOF), typically \sim 1-2 μm , since the DOF is inversely proportional to the NA squared. While this provides high axial resolution, this is often much more than is needed for cellular imaging across large tissue volumes (on the order of hundreds of cubic microns). To image such volumes with SPIM, a focused beam of light that spans several hundreds of microns in its propagation direction is ideally suited to rapidly achieve a large field-of-view (the confocal parameter). Due to diffraction, such a Gaussian focus generates an excitation light-sheet that has a full-width at half-maximum (FWHM) thickness of several microns or more. This is sufficiently thin to optically section and resolve single cells in tissue [49, 71, 74, 76]; however, much of the light-sheet FWHM thickness lies beyond the finite detection DOF of the high-NA objective. As a result, fluorescence signal photons from illumination outside the DOF detection optics

are lost or show up as low-contrast background that corrupts the recorded image. Consequently, the achievable SNR, useful contrast, imaging speed, and photon budget are greatly compromised.

To eliminate the oft overlooked tradeoff between the thin DOF of high-NA detection optics and the thicker light-sheets inherent to large field-of-view excitation beams, we have developed a method to sufficiently capture the entire light-sheet thickness used (Fig. 3.3). We began by modifying the detection path of our SPIM setup [105], adding a layer-cake phase mask [106] conjugate to the pupil plane of the high-NA detection objective (Fig. 3.1). The layer-cake phase mask divides the full back-pupil of the detection objective into multiple sub-apertures by breaking the coherence of the fluorescence waves traveling to the camera, creating an axially elongated point-spread function (PSF) through the incoherent superposition of all the different sub-apertures (Fig. 3.2a). Unlike existing SPIM techniques that elongate the DOF by hundreds of microns [52, 107–109], our method simply extends the DOF by several microns (Fig. 3.3), sacrificing little light collection or resolution (Fig. 3.4) and requiring no post-processing—images can be read out and interpreted directly. We call our method ExD-SPIM.

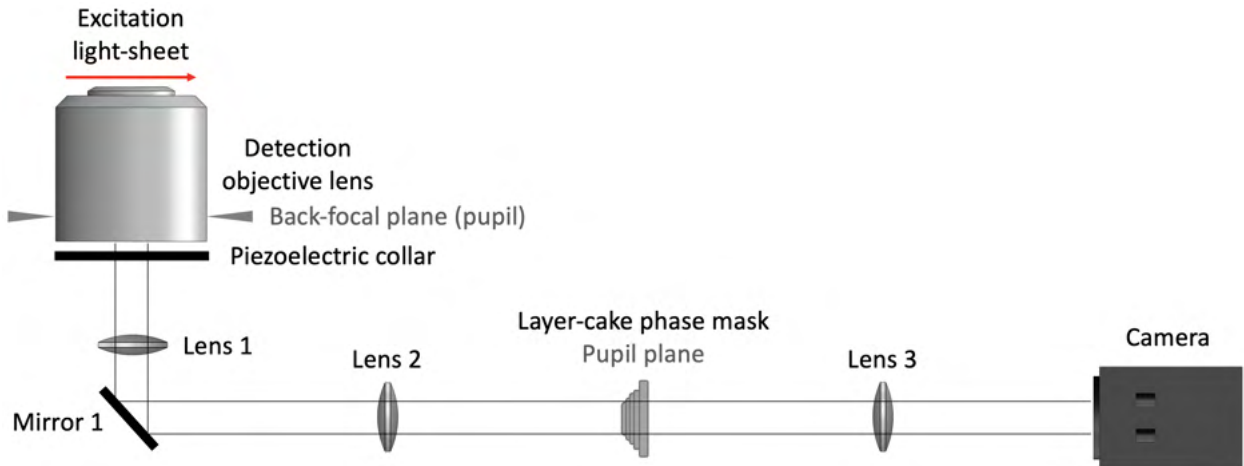


Figure 3.1: Simplified schematic of extended depth-of-field light-sheet microscope, illustrating the detection light path of the system. A layer-cake phase mask is positioned in a conjugate pupil plane to enable instantaneous depth-of-field extension to match the light-sheet thickness. See also Methods Section 3.4.2 and Fig. 3.2.

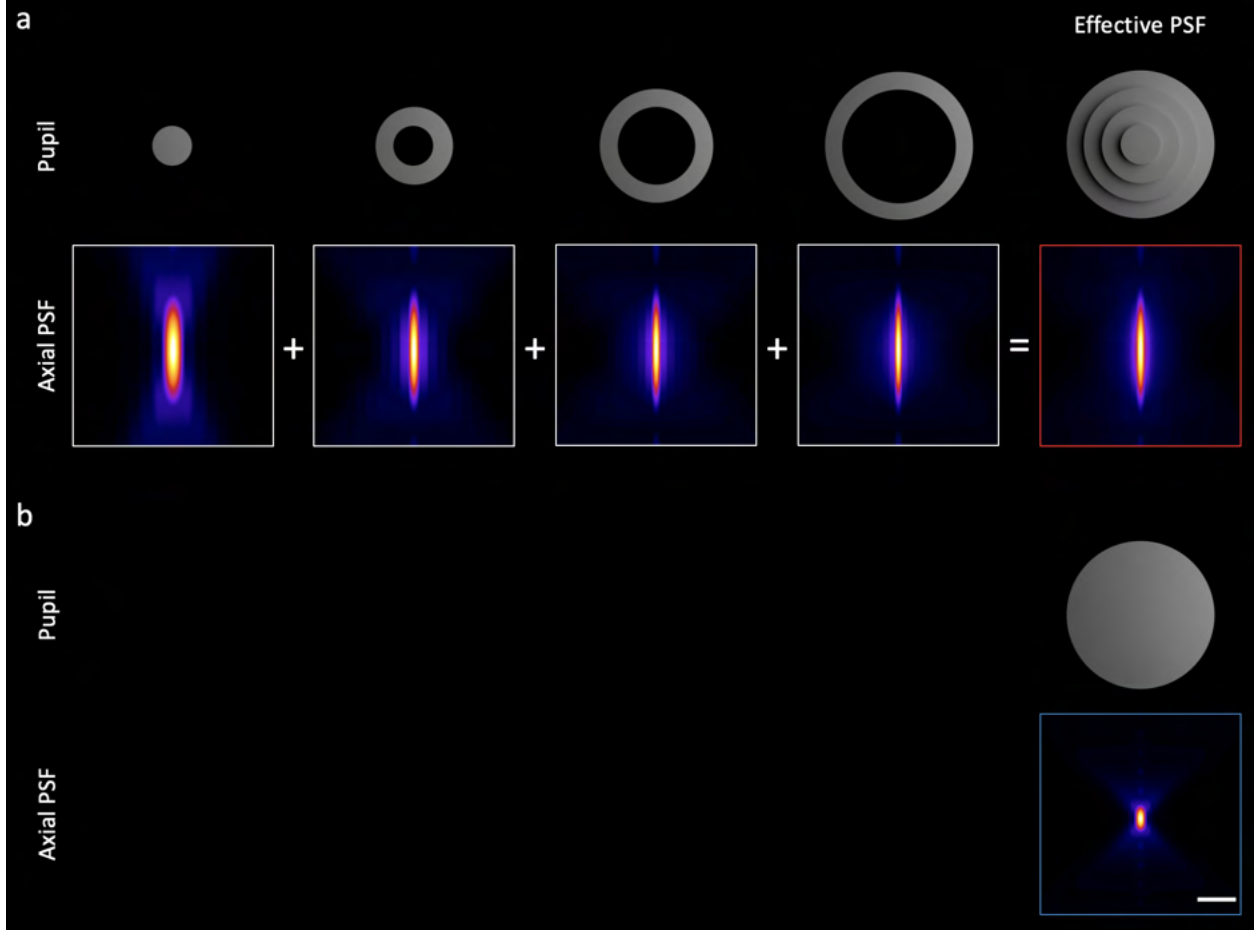


Figure 3.2: Theoretical principle and simulations of extended detection point-spread functions. **(a)** A series of apertures at the pupil (top row), each of different diameter, produce the same axial extent (second row). The (left column) aperture produces a Gaussian-like focus, whereas the annular apertures (middle columns) produce a Bessel-like focus. A layer-cake phase mask (right column) segments the full back-pupil of a high-NA detection objective into multiple sub-apertures, such that each sub-aperture is mutually incoherent [106]. The phase mask consists of multiple concentric glass disks, each of which is $\sim 400 \mu\text{m}$ thick and thereby breaks the short coherence length of the detected light, forming independent apertures that add together to produce an axially elongated focus, without compromising light collection. The amount of DOF scales linearly to the number of layers in the mask, and can thus be adjusted to the light sheet thickness. **(b)** A conventional high-NA detection objective, where different wavevectors interfere and add coherently to produce a tight focus, for comparison. Gamma was adjusted (to 0.85) in all PSF images to enhance contrast of weak features such as side lobes. Scale bar, $5 \mu\text{m}$.

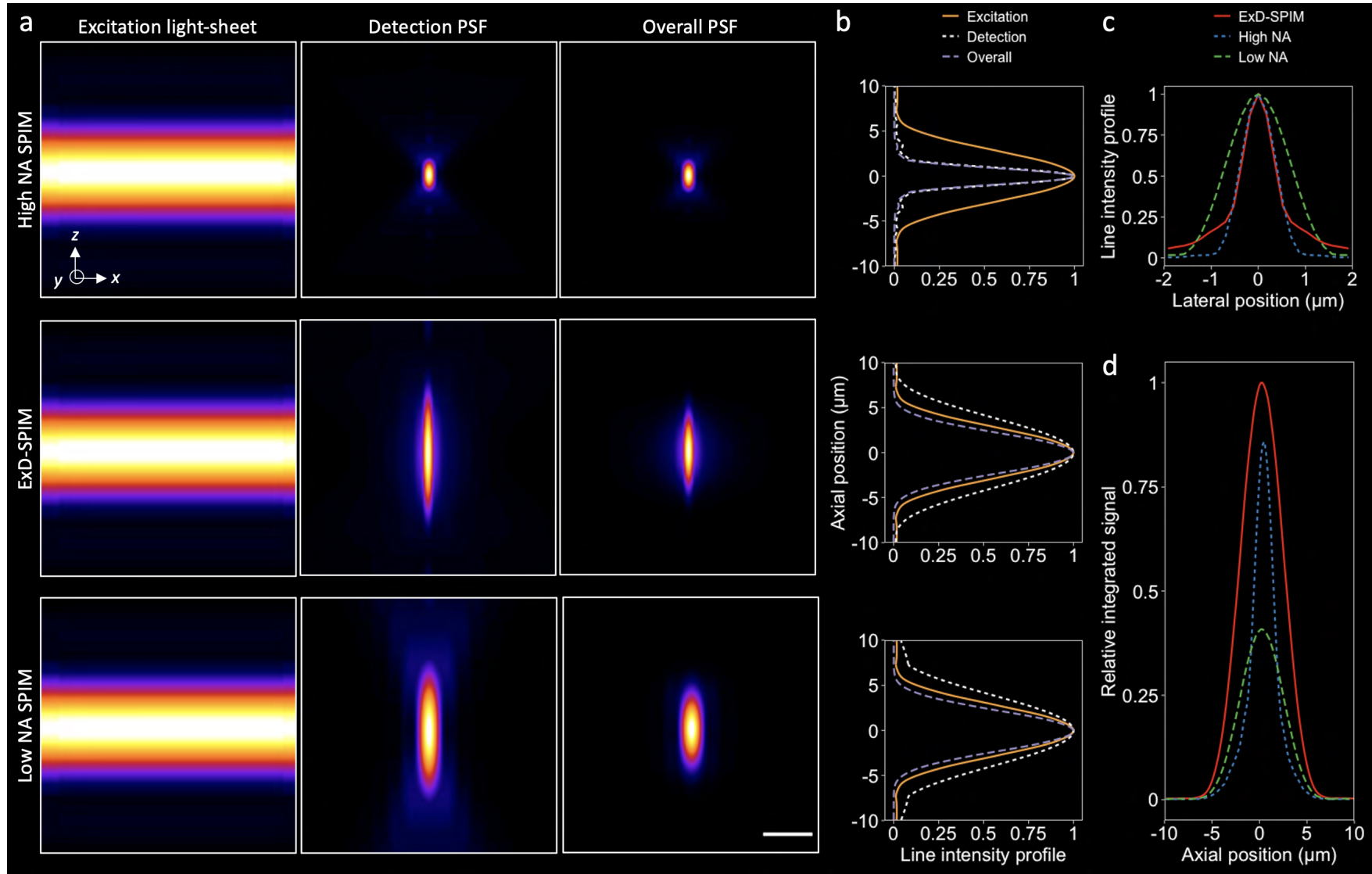


Figure 3.3: Continued on next page.

Figure 3.3: (Continued from previous page.) Extended depth-of-field light-sheet microscopy at high numerical aperture.

(a) Simulated $6 \mu\text{m}$ thick light-sheets (left column) and detection PSFs (middle column) for conventional high-NA SPIM (top row; $NA = 0.8$), ExD-SPIM (middle row; $NA = 0.8$), and low-NA SPIM (bottom row; $NA = 0.41$). Overall PSFs (right column) are calculated by multiplying the excitation PSF with the detection PSF. Scale bar, $5 \mu\text{m}$.

(b) x - z cross-sectional intensity profiles of the excitation, detection, and overall PSFs. High-NA SPIM (top row) provides maximal axial confinement of the overall PSF, despite the thicker light-sheet used. As a result, however, only a fraction of the excitation light-sheet is not used. ExD-SPIM (middle row) captures the entire light-sheet thickness by extending the DOF of the high-NA detection objective lens, just like a low NA system (bottom row), but without degrading the lateral extent.

(c) Lateral (x - y) line intensity profiles of the overall PSFs of the modalities shown in (a).

(d) Plot shows the relative integrated signal intensities of imaging a point source for each modality. Intensities were summed along the x direction of the images. ExD-SPIM extends the DOF without compromising the high-NA light gathering ability, yielding an increase in total integrated signal. See also Fig. 3.4.

3.2 Results

3.2.1 Simulations of imaging performance

We performed numerical simulations of three different imaging scenarios for comparison: ExD-SPIM ($NA_{\text{det}} = 0.8$), conventional SPIM at high NA ($NA_{\text{det}} = 0.8$) and SPIM at low NA ($NA_{\text{det}} = 0.41$). The PSFs are computed using the Debye approximation, as described by Chen, Chakraborty *et al.* [110], with the overall PSF of each case calculated as the product of the detection PSF and a Gaussian-beam light-sheet 6 μm in FWHM thickness. Because the amount of DOF extension scales linearly to the number of annular sub-apertures when the full pupil of the detection objective is utilized, we chose a 4-layer-cake phase mask to capture the entire light-sheet thickness across the field-of-view, so that all illuminated molecules are in focus and unwasted. We simulated the effect this would have on imaging by convolving the overall PSF with a sub-diffractive spherical object (Methods Section 3.4.1). While we observed an overall drop in peak intensity in ExD-SPIM near the focal plane, we also found a 2.4-fold increase in total collected signal over an extended axial volume compared to the conventional high NA system (Fig. 3.4d). In principle, the signal gain would be even greater at higher NA ($NA_{\text{det}} = 1.0$) and paired with a 7-layer-cake phase mask: over threefold more total fluorescence emission compared to a conventional high NA system (Fig. 3.4h). This may not be surprising, as the intrinsic DOF is inversely proportional to the NA squared, yielding much higher axial resolution and thus tight signal confinement in z at high NA.

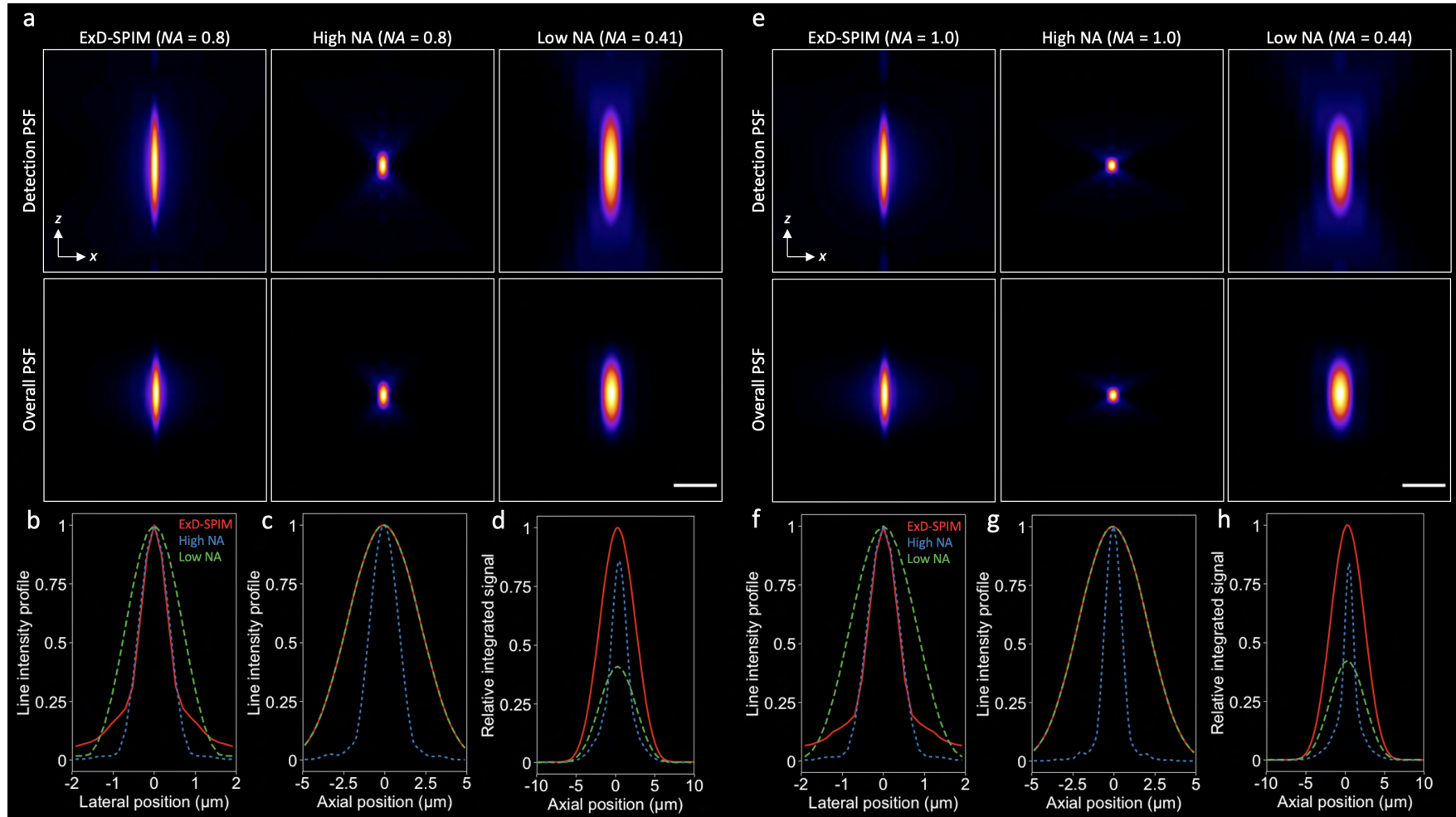


Figure 3.4: Continued on next page.

Figure 3.4: (Continued from previous page.) Numerical simulations of ExD-SPIM imaging.

(a) Simulated detection PSFs (top row) and overall PSFs (second row) for ExD-SPIM (left column; $NA = 0.8$), high-NA SPIM (middle column; $NA = 0.8$), and low-NA SPIM (right column; $NA = 0.41$).

(b) and (c) Lateral and axial line intensity profiles through the center of the overall PSFs of the modalities shown in (a), indicating little loss in lateral resolution with ExD-SPIM while its axial extent is equivalent to the low-NA system.

(d) Plot shows the relative integrated signal intensities of imaging for each modality (Methods Section 3.4.1). Images were simulated by convolving the overall PSFs in (a) with a sub-diffractive (170 nm) spherical object. Signal intensities were then summed along the x direction and plotted as a function of z position. Integrating along both the x and z directions, ExD-SPIM yielded a 2.4-fold increase in total signal over high-NA SPIM, and a 2.15-fold increase over low-NA SPIM.

(e-c) Same as in (a-d), except $NA = 1.0$ for ExD-SPIM and high-NA SPIM, and $NA = 0.44$ for low-NA SPIM. At these NAs, ExD-SPIM provided over threefold more total signal over high-NA SPIM, and 2.3-fold more than low-NA SPIM.

Scale bars, (a) and (e) 5 μm .

3.2.2 Experimental imaging performance

We experimentally tested ExD-SPIM performance by measuring the PSF with sub-diffractive fluorescent beads embedded in a mixture of 1.5% agarose and 10% Iodixanol [111]. As expected, we see only a $\sim 30\%$ increase in lateral blurring with ExD-SPIM, whereas a low NA system degraded lateral resolution by $\sim 80\%$ (Fig. 3.5a and b). Axially, we see a ~ 2.4 -fold extension for both ExD-SPIM and the low NA system compared to SPIM at high NA. The mean lateral and axial FWHM \pm s.d. values ($n = 8$) are ExD-SPIM, $0.71 \mu\text{m} \pm 0.04 \mu\text{m}$ and $5.25 \pm 0.66 \mu\text{m}$, respectively; high NA, $0.54 \pm 0.05 \mu\text{m}$ and $2.21 \pm 0.14 \mu\text{m}$, respectively; low NA, $0.96 \pm 0.06 \mu\text{m}$ and $5.26 \pm 0.8 \mu\text{m}$, respectively (Fig. 3.5c). These measurements are in good agreement with theoretical simulations (Fig. 3.4b and c). Most important, we see more than a twofold increase in the integrated signal of beads measured over a $\sim 375 \times 555 \times 150 \mu\text{m}^3$ field with ExD-SPIM compared to conventional high-NA SPIM, and a ~ 4.75 -fold increase compared to SPIM at low NA (Fig. 3.5d).

3.2.3 ExD-SPIM reduces photobleaching *in vivo*

To compare rates of photobleaching between ExD-SPIM and SPIM at high NA and low NA, we recorded single-plane intensities of GFP-labeled vasculature in live larval zebrafish (4-5 days post-fertilization, dpf) over time. The laser power was adjusted for each modality to reach similar SNR while keeping the exposure time and other imaging conditions identical over multiple samples (Methods Section 3.4.3). As ExD-SPIM preserves the high light collection efficiency of a high NA objective, rates of photobleaching were similar to a high NA system: even after 4 hours of continuous imaging (70,760 images), $\sim 95\%$ of the initial fluorescence intensity remained (Fig. 3.6). In contrast, after imaging the vasculature at low NA, we observed faster photobleaching, with the fluorescence dropping to $\sim 80\%$ of its original value. This highlights the importance of the twin goals of minimizing light exposure and maximizing signal collection for long-term *in vivo* imaging, especially since it is likely that phototoxicity has long since emerged once photobleaching is apparent.

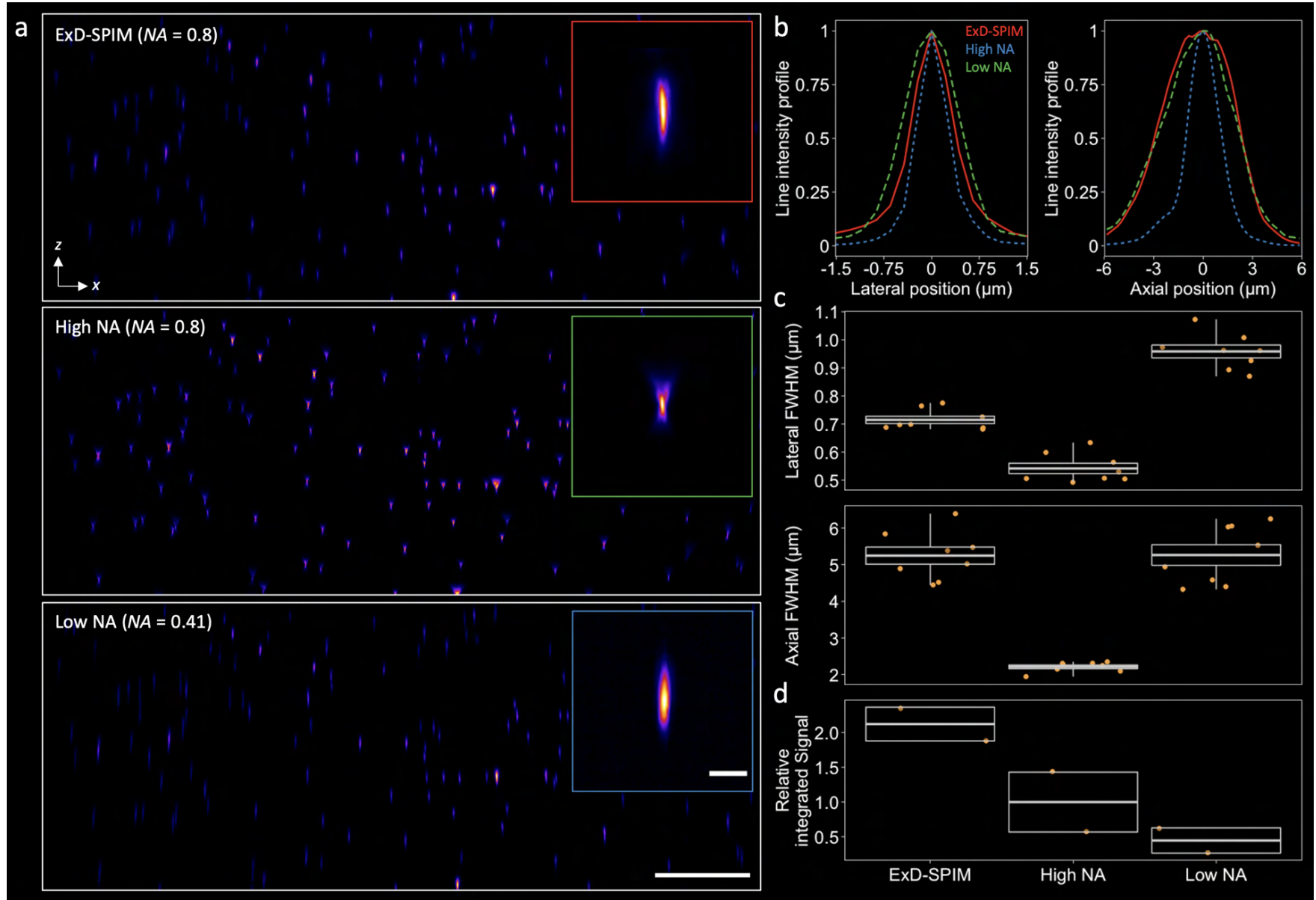


Figure 3.5: Continued on next page.

Figure 3.5: (Continued from previous page.) Experimental demonstration of improving light-sheet collection with depth-of-field extension.

(a) x - z maximum intensity projection of a $375 \times 555 \times 150$ (x - y - z) μm^3 beads field captured with ExD-SPIM (top row), high-NA SPIM (middle row), and low-NA SPIM (bottom row). Inset: Representative PSFs computed by averaging over four beads for each modality. Scale bar, 50 μm and (inset) 5 μm .

(b) Lateral (left) and axial (right) line intensity profiles through the PSFs in the insets of (a). ExD-SPIM shows an axial extent equivalent to the low-NA system with slight lateral blurring.

(c) Lateral (top) and axial (bottom) FWHM measurements; for each modality, the same eight beads were chosen from (a).

(d) Quantification of the total integrated signal intensity (along both the x and z directions) of multiple beads from (a). ExD-SPIM shows over a twofold signal enhancement compared to high-NA SPIM, and a 4.75-fold enhancement over low-NA SPIM.

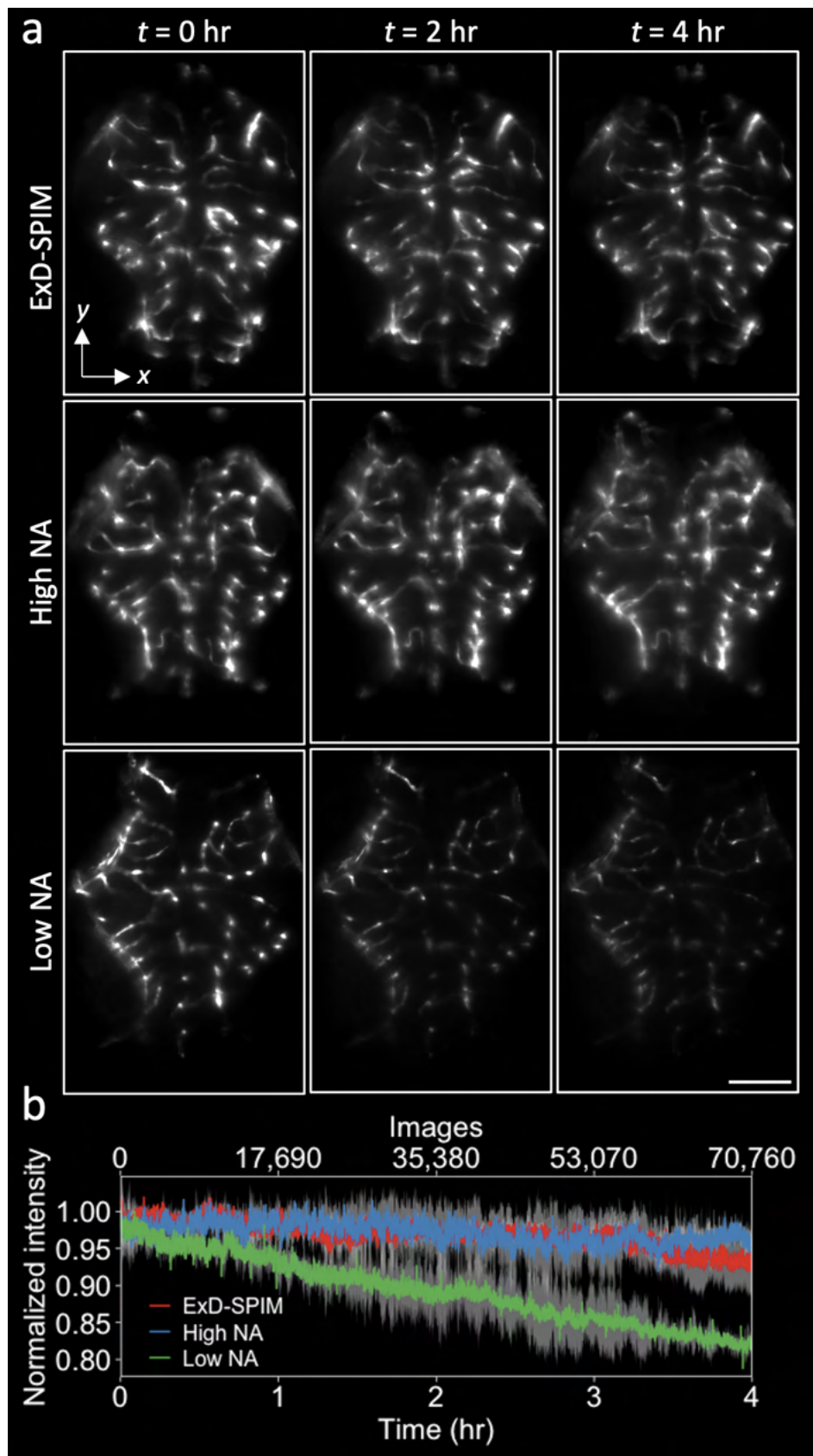


Figure 3.6: Continued on next page.

Figure 3.6: (Continued from previous page.) ExD-SPIM offers low photodamage *in vivo*.

- (a) Time-lapse images of GFP-vasculature-labeled larval zebrafish, with time points numbered above, acquired continuously over 4 hours (70,760 total images) for ExD-SPIM (top), high-NA SPIM (middle), and low-NA SPIM (bottom). Photobleaching is apparent in the low NA system at $t = 4$ hr. Scale bar, 100 μm .
- (b) Plot shows the total sum intensity of the entire imaged plane as a function of time for each modality. Total intensity of ExD-SPIM and SPIM at high NA exhibit similar rates of photobleaching, decreasing by only 5% of its initial intensity. The total intensity of the low NA system however decreases by 20% in magnitude from its initial intensity, suggesting the onset of photodamage, which is a concern for prolonged imaging.

3.2.4 ExD-SPIM improves brain-wide imaging of neural activity

The improved signal collection of ExD-SPIM makes it well suited to functional imaging. We tested its performance by imaging brain-wide dynamics in a 5-dpf transgenic larval zebrafish expressing the nuclear-calcium indicator GCaMP6s. We recorded single-plane images at 10 Hz and directly compared its abilities against conventional high-NA SPIM. The extended DOF of ExD-SPIM provided an overall increase in total signal: a $\sim 25\%$ increase on average over time compared to the high NA system (Fig. 3.7). This in turn allowed us to detect $\sim 45\%$ more neurons in time-lapse imaging, intracellular calcium transients that otherwise would have gone undetected with conventional high-NA optics (Fig. 3.7a). This example highlights how ExD-SPIM can enable the recording of increasingly transient dynamics to probe interactions at cellular resolution in living systems.

3.3 Discussion

ExD-SPIM improves light collection by extending the detection DOF to match the light-sheet thickness used. This general approach makes optimal use of the photon budget from the fluorescent distribution of the sample. Although there is a drop in peak intensity due to the slight laterally blurring of the layer-cake phase mask used here, we have shown how this is markedly offset by the total integrated signal collected axially through numerical simulations, bead phantoms, and *in vivo*. This improvement in signal collection increases with increasing NA, as the intrinsic DOF is inversely proportional to the NA squared. Our method outperforms other low-NA light-sheet methods[108]; these require substantially more laser excitation power to generate the same SNR, significantly increasing photodamage, and thus are limited in their utility for studying cellular dynamics over long time scales. More generally, we stipulate that light-sheet microscopes tailored towards large-volume imaging that currently operate at moderate-to-low NA [66, 112, 113] would benefit from improved

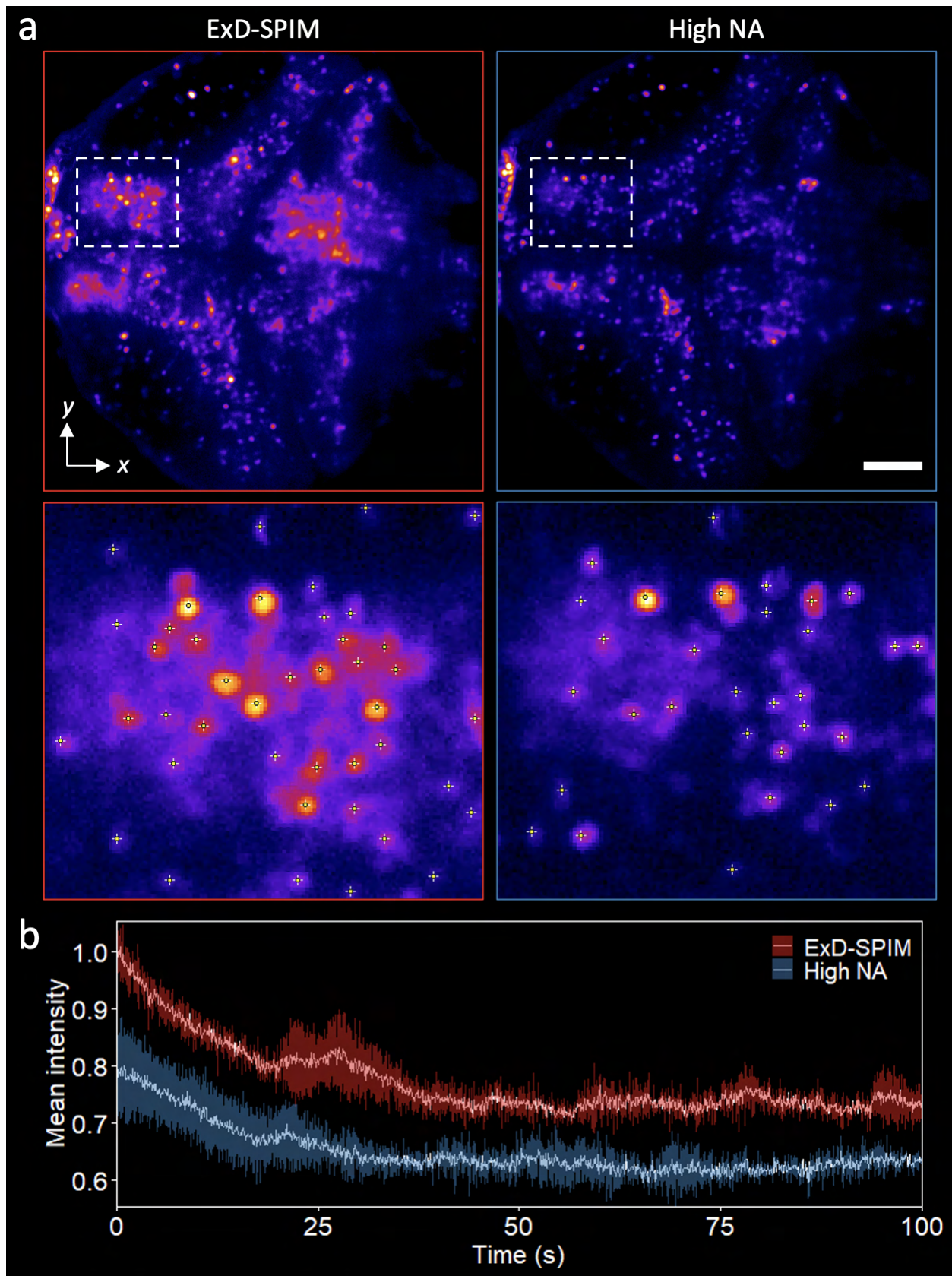


Figure 3.7: Continued on next page.

Figure 3.7: (Continued from previous page.) ExD-SPIM improves brain-wide imaging of neural activity.

(a) Temporal standard-deviation projections of neural activity in transgenic larval zebrafish (*Tg(elavl3:H2b-GCaMP6s)*) at 5-dpf. Projections depict the standard deviation over a 100-s period for each pixel, highlighting active neurons captured by each modality. Second row shows enlarged views of the boxed regions in the top row, indicating more neurons detected with ExD-SPIM than conventional high-NA SPIM (neuron count, ExD-SPIM: 42; high-NA SPIM: 29). Neurons were semi-automatically segmented and quantified in FIJI followed by manual verification. Imaging performed at 10 Hz (Methods Section 3.4.3). Scale bar, 100 μm .

(b) Plot shows the mean intensity of the entire imaged plane as a function of time for the data shown in (a) and from two other similarly acquired datasets ($n = 3$). The mean intensity of ExD-SPIM is on average $\sim 25\%$ greater than high-NA SPIM. The means (solid white lines) and standard deviations (color shadings) are shown.

photon efficiency with an extended DOF at high NA, especially in very dim regimes where every photon counts.

The signal gain in ExD-SPIM could in principle be translated into faster imaging speeds. In addition, the extended DOF relaxes sampling in z , enabling faster volumetric speeds compared to a high NA system, as well as the benefit of reduced rates of photodamage from less exposures. Finally, our implementation of ExD-SPIM with a transmission phase mask is simple and does not require extensive optical redesign or wavelength-dependent phase modulation, making it easily adaptable to multicolor fluorescence microscopy and scalable for high-throughput imaging.s

3.4 Methods

3.4.1 Theory and numerical simulations

The electromagnetic focus field of an objective was simulated using the vectorial Debye diffraction integral with the Fourier transform method [114] given in Chen, Chakraborty *et al.* [110]. Briefly, we ensure that each sub-aperture of the layer-cake phase mask produces the same axial extent. To do this, we consider the spread of wavevectors passed through an

objective; these lie on a spherical cap and have a magnitude $k = n\lambda$, where n is the refractive index and λ is wavelength. We map the spatial extent of features laterally (x - y) and axially (x - z) to the spread of wavevectors along k_x and k_z . The full spread of k_x components is given by $2k \sin(\alpha_2)$. The spread of k_z wavevectors is defined as $k(\cos(\alpha_1) - \cos(\alpha_2))$. For a full spherical cap, $\alpha_1 = 0$ and

$$d_z = \frac{\lambda}{n(1 - \cos(\alpha_2))}. \quad (3.1)$$

We can now begin to map sub-apertures of the phase mask to wavevector sets. The central layer consists of a typical Gaussian-like focus so that the axial extent follows Equation 3.1. The other sub-apertures produce Bessel-like foci, where $\alpha_1 \neq 0$, so we must write

$$d_z = \frac{\lambda}{n(\cos(\alpha_1) - \cos(\alpha_2))}. \quad (3.2)$$

Since $\alpha = \arcsin(\frac{NA}{n})$, we can rewrite Equation 3.2 in terms of NA:

$$d_z = \frac{\lambda}{n \left[\cos \left(\arcsin \left(\frac{NA_1}{n} \right) \right) - \cos \left(\arcsin \left(\frac{NA_2}{n} \right) \right) \right]}. \quad (3.3)$$

Given the back pupil of the objective is $2 \cdot f \cdot NA$, where f is the back focal length of the objective lens, we can convert NAs to physical mask dimensions. From the above expressions, we determine the required aperture diameter for a given DOF, calculating the inner most sub-aperture NA that will produce a Gaussian-like focus with the desired DOF. Then, we calculate the first annular sub-aperture to have an inner NA equivalent to the NA of the central, low-NA, Gaussian focus, with an outer-ring NA such that the Bessel-like focus has the same DOF using Equation 3.3. This is repeated iteratively for the outer and inner NAs of the annular sub-apertures until all annuli are considered or the maximum available NA is filled. The number of annular layers scales linearly to the amount of DOF extension. Each annular sub-aperture produces independent 3D PSFs which are assumed mutually incoherent

to the other sub-apertures and can thus be summed to form the effective detection PSF [106, 110]. Theoretical simulations, where possible, match experimental parameters.

ExD-SPIM detection PSF: $\lambda_{\text{em}} = 525 \text{ nm}$, $NA_{\text{det}} = 0.8$, $n = 1.33$, and $L = 4$, where L is the number of annular sub-apertures in the layer-cake phase mask. This yielded a DOF of $8 \mu\text{m}$. We similarly simulated $NA_{\text{det}} = 1.0$ and $L = 7$, yielding a DOF of $7 \mu\text{m}$.

High-NA detection PSF: $\lambda_{\text{em}} = 525 \text{ nm}$, $NA_{\text{det}} = 0.8$, and $n = 1.33$; this yielded a DOF of $2 \mu\text{m}$. We similarly simulated $NA_{\text{det}} = 1.0$, yielding a DOF of $1 \mu\text{m}$.

Low-NA detection PSF: $\lambda_{\text{em}} = 525 \text{ nm}$, $NA_{\text{det}} = 0.41$, and $n = 1.33$; this yielded a DOF of $8 \mu\text{m}$. We similarly simulated $NA_{\text{det}} = 0.44$, yielding a DOF of $7 \mu\text{m}$.

Excitation light-sheet: $\lambda_{\text{em}} = 525 \text{ nm}$, $NA_{\text{det}} = 0.02$, $n = 1.33$; this yielded a $6\text{-}\mu\text{m}$ -thick Gaussian light-sheet.

Overall PSFs were calculated by multiplying the detection PSF with the light-sheet PSF. To simulate the total signal captured from the different detection modes, we assumed the same laser light-sheet intensity and detector exposure time, and scaled the intensity of the overall low-NA PSF by $\left(\frac{\text{Low NA}}{\text{High NA}}\right)^2$, given that the collection efficiency is proportional to the NA squared [23]. We scaled down the overall ExD-SPIM PSF by 20% to account for losses through the imperfect pupil phase mask. The overall PSF of each modality was then convolved with a sub-diffractive spherical object 170 nm in diameter (see Section 1.1.4).

3.4.2 Microscope optics

The optical microscope was based on an existing light-sheet setup [105], with modifications to provide extension of the detection focal zone. The light-sheet module is described in detail in Section 5.5 of Chapter 5. We replaced the illumination lens with a $5\times$, 0.1 NA , long-working distance objective lens (LMPLN5XIR, Olympus).

The detection module consisted of a $40\times$, 0.8 NA , water-immersion objective lens (N40X-NIR, Nikon), mounted on a piezoelectric collar; a set of tube lenses (200 mm focal length,

TTL200, Thorlabs; 200 mm focal length, 49-286b, Edmund Optics) that relayed the back-pupil of the detection objective to the layer-cake phase mask (10 mm diameter aperture, 5 layers, A12802-35-040, Hamamatsu Photonics) used to extend the DOF. We under-filled the phase mask and used only 4 of the layers, extending the DOF accordingly (Methods Section 3.4.1). A bandpass filter (525 nm \pm 50) follows the phase mask to separate the excitation light, and a tube lens (150 mm focal length, AC-508-150-A, Thorlabs) that forms the primary image at an sCMOS camera (Zyla 5.5, Andor).

For neural activity imaging, we used a 20 \times , 1.0 NA, water-immersion objective lens (XLUMPLFLN-W, Olympus). In this configuration, a different set of tube lenses (150 mm focal length, AC508-150-A, Thorlabs; 75 mm focal length, AC508-075-A-ML, Thorlabs) were used to relay the back-pupil of the detection objective to the layer-cake phase mask. Following the bandpass filter, the fluorescence was imaged onto the camera with a different tube lens (100 mm focal length, 49390, Edmund Optics).

The high NA mode was achieved simply by removing the phase mask. To switch to the low NA mode, the aperture of an iris positioned at the conjugate pupil plane was closed down to an NA of ~ 0.41 .

3.4.3 Sample preparation and imaging conditions

Sub-diffractive fluorescent beads (175 \pm 5 nm diameter; PS-Speck Microscope Point Source Kit, P7220, Molecular Probes) were diluted (1:1000) and embedded in a mixture of 2% agarose, using the caddy-dive bar system described in Chapter 2 and Ref. [49]. The beads were then submerged in an imaging chamber filled with 60 mL of distilled water. A concentration of 10% Iodixanol was added to the imaging chamber and left to diffuse throughout the agarose-embedded beads and imaging chamber for 24 hours, prior to imaging. Iodixanol helped alleviate the index of refractive mismatch between the agarose and water [111].

Zebrafish were raised and maintained as described in Ref. [115], in strict accordance with the recommendations in the Guide for the Care and Use of Laboratory Animals by University of Southern California, where the protocol was approved by the Institutional Animal Care and Use Committee (IACUC). All zebrafish lines used are available from ZIRC (<http://zebrafish.org>). Zebrafish embryos were collected from mating of appropriate adult fish (AB/TL strain) and raised in egg water ($60 \mu\text{g L}^{-3}$ of stock salts in distilled water) at 28.5°C . At 20 hpf, 1-phenyl-2-thiourea (PTU) (30 mg L^{-1}) was added to the egg water to reduce pigmentation in the animals.

The imaging chamber was filled with 30% Danieau solution (1740 mM NaCl, 21 mM KCl, 12 mM MgSO $^4 \cdot 7\text{H}_2\text{O}$, 18 mM Ca(NO 3) 2 , 150 mM HEPES). Fish were embedded in 2% agarose as described in Chapter 2 and Ref. [49]. To measure photobleaching rates, cranial vasculature 4-5-dpf *Tg(kdrl:eGFP)* larvae were used. The laser power was adjusted to reach similar signal levels (maximum and mean intensities) for each modality. Generally, this required 3- to 5-fold more laser power at low NA to reach the same SNR as the high NA systems, depending on the fish. Typical laser powers used for ExD-SPIM and high-NA SPIM ranged from 160 to 180 μW ; low-NA SPIM ranged from 0.45 to 0.75 mW. Exposure time was fixed at 200 ms for all experiments. We searched for similar features within the sample and acquired $n = 2$ datasets for each modality.

For neural activity imaging, 5-dpf zebrafish larvae expressing the nuclear-localized pan-neuro fluorescent calcium indicators, *Tg(elavl3:H2B-GCaMP6s)*, were used. Triplets of 100-s imaging was performed with 77 ms exposure and 200 μW of laser power for both ExD-SPIM and high-NA SPIM. Each acquisition was spaced at least 3 minutes apart.

3.5 Acknowledgements

We thank S. Madaan for early development of the light-sheet module, and the D. Prober Lab (California Institute of Technology) for many inspiring discussions that sharpened the

technology presented here. We also thank R. Kershaw (Hamamatsu Photonics) for allowing us to test the cake phase mask.

3.6 Manuscript information

3.6.1 Author contributions

The authors for this work: Kevin Keomanee-Dizon, Matt Jones, Peter Luu, Scott E. Fraser, and Thai V. Truong.

T.V.T. and K.K.D. conceived the idea, with further refinement from S.E.F. K.K.D. performed the simulations with input from T.V.T. K.K.D designed, built, and performed all experimental characterization of the optical detection module with input from T.V.T and S.E.F; M.J. helped build the light-sheet module. P.L. provided transgenic zebrafish. K.K.D. acquired, processed, and performed quantitative analysis of all optical image data with input from TVT. K.K.D. produced all figures with input from T.V.T. and S.E.F; T.V.T. helped quantify the neurons in Fig. 3.7. T.V.T. and S.E.F. supervised the project. K.K.D. and T.V.T. wrote the manuscript, which is still in preparation.

4

High-contrast, synchronous volumetric imaging
with selective-volume illumination microscopy

4.1 Introduction

Understanding dynamic biological processes requires volumetric imaging tools that can faithfully image across hundreds of microns in 3D with cellular resolution within time scales as short as milliseconds. Conventional imaging approaches based on sequentially collecting signal from one point (confocal microscopy), one line (line-confocal), or one plane (light-sheet) at a time [4, 10] are often not fast enough to faithfully capture the relevant dynamics without

distortion, as different parts of the 3D sample are observed at different times. Light-field microscopy (LFM; Fig. 4.1a) meets this challenge by capturing an extended sample volume in a single snapshot, enabling synchronous volumetric imaging [50, 51, 53]. LFM records the extended light field coming from the sample space on a 2D camera by positioning a micro-lens array at the image plane, and moving the camera to the focal plane of the micro-lens array. This permits the camera to capture information from the volume that extends above and below the native focal plane. Computational reconstruction is used to solve the inverse problem, reconstructing the image of the 3D sample volume from the recorded 2D image, sacrificing resolution for dramatically enhanced z -depth coverage [50, 51, 53]. LFM conventionally employs wide-field illumination, exciting sample regions beyond the volume of interest (Fig. 4.1b), thus generating background signal that reduces the contrast of both the recorded 2D image and the final reconstruction. The limited contrast of conventional LFM has substantially limited its utility for imaging dynamic 3D biological tissues.

Taking inspiration from selective-plane illumination microscopy (SPIM; also known as light-sheet microscopy) [48], which achieves low-background and high-contrast imaging by illuminating only the optical plane of interest (Fig. 4.1b), we reasoned that we could enhance the contrast of LFM by illuminating only the volume of interest. We thus created selective-volume illumination microscopy (SVIM) by preferentially illuminating the volume of interest and then capturing the resulting fluorescence with light-field detection. SVIM reduces background, increases contrast, and produces an overall higher-quality reconstruction of the sample, while preserving the synchronous volumetric imaging capability of LFM.

4.2 Results

4.2.1 Overview of SVIM instrument

Our SVIM instrument combined selective-volume illumination and LFM modules with an existing custom-built SPIM [77], permitting direct comparison between SVIM, conventional

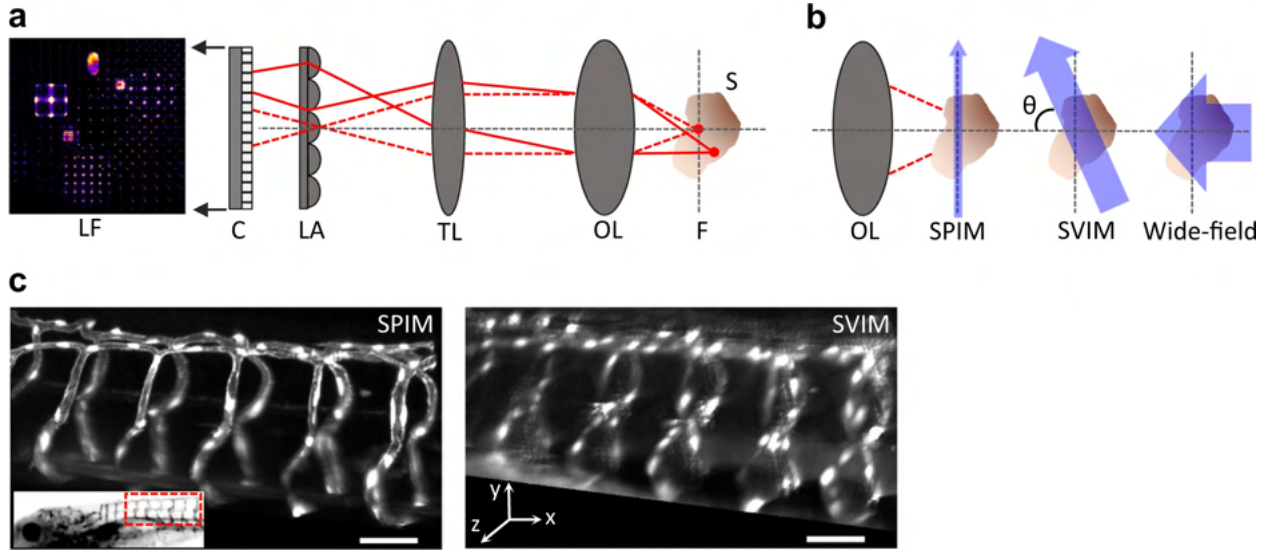


Figure 4.1: Selective-volume illumination microscopy enhances LFM for the synchronous imaging of 3D samples.

(a) LFM is a simple extension of a conventional microscope, which produces a magnified image of the sample (S) from the native focal plane (F) to the image plane (IP) using an objective lens (OL,) and tube lens (TL). LFM places a micro-lens array (LA) at the IP, encoding 3D image information into a 2D light-field image (LF), which is captured by a planar detection camera. This permits LFM to synchronously capture information at z -positions above and below F; the 3D image of the sample is reconstructed from the LF image, based on knowledge of the optical transformation.

(b) SVIM improves LFM by selectively illuminating the volume of interest within the sample. This decreases background and increases contrast when compared to wide-field illumination of the entire sample. SVIM was implemented through the use of light-sheet (SPIM) illumination that is scanned axially, so that the thin sheet of excitation is extended into a slab. In our work, the SVIM illumination axis was orthogonal to the detection axis ($\theta=90^\circ$), but the benefits of reduced background can be obtained by using illumination from a different angle, and/or by employing non-linear optical effects to selectively excite the volume of interest.

(c) SPIM and SVIM 3D images of the trunk vasculature of 5 dpf zebrafish larva reveal the compromises between resolution and volumetric imaging time. SPIM offers higher resolution but requires the collection of 100 sequential images to cover the 100- μm -depth z -stack; SVIM captures the same 3D volume in a single snapshot, two-orders-of-magnitude faster, but with lower resolution. Transgenic animal, *Tg(kdr:GFP)*, had its vasculature fluorescently labeled with GFP. Inset shows the approximate location of the imaged volume along the trunk of the zebrafish larva.

Scale bars, 50 μm .

wide-field LFM, and SPIM imaging of the same specimen (Methods Section 4.4.1, Fig. 4.17, Table A2 in Appendix B). SPIM provided slower, but higher-resolution, “ground truth” images against which to judge the other imaging modalities. To achieve selective-volume illumination, in either 1P or 2P excitation, we implemented galvanometer-based rapid scanning of the specified volume multiple times within a single camera exposure time [74, 75], providing micron-level control over the spatial extent of the selected volume (Methods Section 4.4.1, Supplementary Note 4.5.1). Our design of the light-field detection module drew upon previous efforts [50, 51, 53], and the light-field image reconstruction followed the 3D deconvolution approach [51] using publicly available software [53]. Table A3 in Appendix C provides imaging and reconstruction parameters for all presented results. As previously described theoretically and experimentally [50, 51], LFM image reconstructions are affected by non-uniform resolution and grid-like artifacts centered around the native focal plane, both of which were present in our results. SVIM performed as expected from the optical parameters used [51], achieving a nominal maximum resolution of $\sim 3 \mu\text{m}$ laterally and $\sim 6 \mu\text{m}$ axially, as approximated by the full-width half-maximum (FWHM) of sub-diffractive fluorescent beads, over a volume of $440 \times 440 \times 100 (x, y, z) \mu\text{m}^3$ (Fig. 4.2). Our SVIM implementation provides a simple path for conventional SPIM instruments to be upgraded to SVIM.

4.2.2 SVIM imaging performance

The capabilities and compromises of SVIM are demonstrated by its single-snapshot capture of the entire depth of the trunk vasculature of a live larval zebrafish (Fig. 4.1c). Compared to the z -stack assembled from ~ 100 higher-resolution SPIM snapshots, SVIM captured faithfully the 3D structure of the green fluorescent protein (GFP)-labeled vasculature. SVIM demonstrated modest reductions in resolution, but its single-snapshot acquisition offered two-orders-of-magnitude greater z -depth coverage and enhanced imaging speed, even after

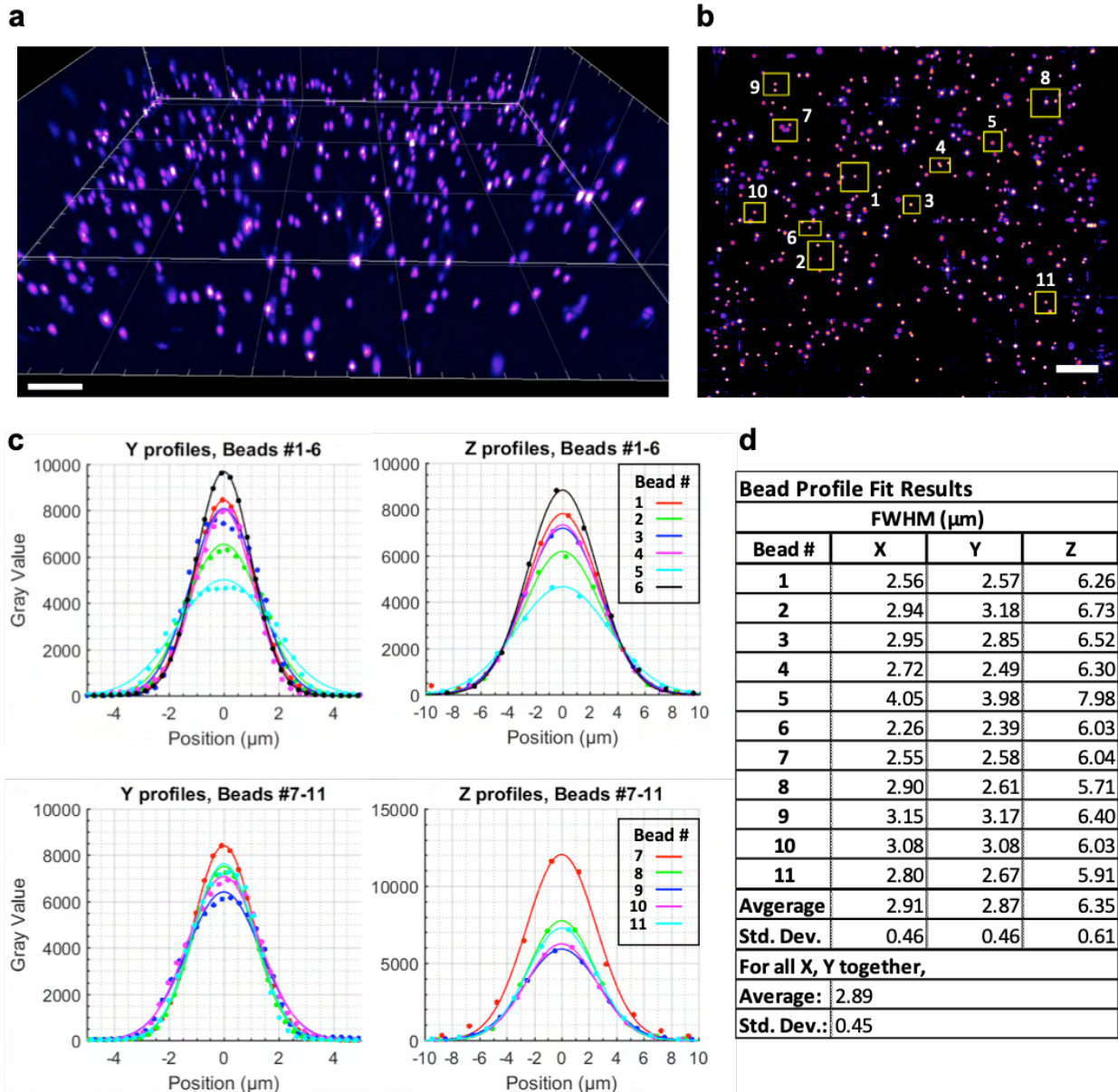


Figure 4.2: Imaging of sub-diffractive fluorescent beads to characterize resolution of SVIM. Resolution performance of SVIM was characterized by imaging sub-diffractive fluorescent beads (diameter = 175 nm, PS-Speck, ThermoFisher) embedded in low-melting agarose. **(a)** 3D-rendered and **(b)** maximum projection view of the reconstructed volume of beads, spanning $\sim 400 \times 400 \times 100$ (x, y, z) μm^3 . We sampled the point-spread-function (PSF) of multiple beads across the field of view as indicated by the yellow boxes shown in **(b)**. Line profiles along the lateral and axial directions **(c)** show a nominal Gaussian-fitted fullwidth-half-maximum (FWHM) resolution of 3 μm laterally and 6 μm axially **(d)**. This resolution performance was as expected for the optical parameters used. Scale bars, 50 μm .

normalization for the number of resolvable voxels captured (Table A3, Supplementary Note 4.5.2).

SVIM enhances image quality compared with wide-field LFM, as seen in the 3D images of the cranial vasculature of the same live zebrafish larva, with the illuminated volumes varying from 100- μm axial extent to wide-field illumination of the entire animal (Figs. 4.3a and 4.4). Wide-field LFM produced the lowest-quality image with the highest background. SVIM produced progressively better-quality and higher-contrast images as the z -extent was reduced, approaching the ground truth images achieved by SPIM when the SVI was 100 μm (Fig. 4.4g). Measurements of the quantitative image contrast (Methods Section 4.4.5) show SVIM’s progressively increased performance as the illumination extent was confined to smaller volumes (Fig. 4.3b). The decreased contrast from background is consistent with our simulations (Fig. 4.5), where increased levels of Poisson noise applied to the raw light-field images resulted in decreased contrast in the reconstructions. The higher contrast of SVIM mitigates against resolution-degrading effects of background noise, resulting in a better effective resolution even though SVIM and wide-field LFM utilize the same detection optics. This was demonstrated in imaging $\sim 5\text{-}\mu\text{m}$ -diameter blood vessels where SVIM achieved up to $\sim 35\%$ improved FWHM over wide-field LFM (Fig. 4.6).

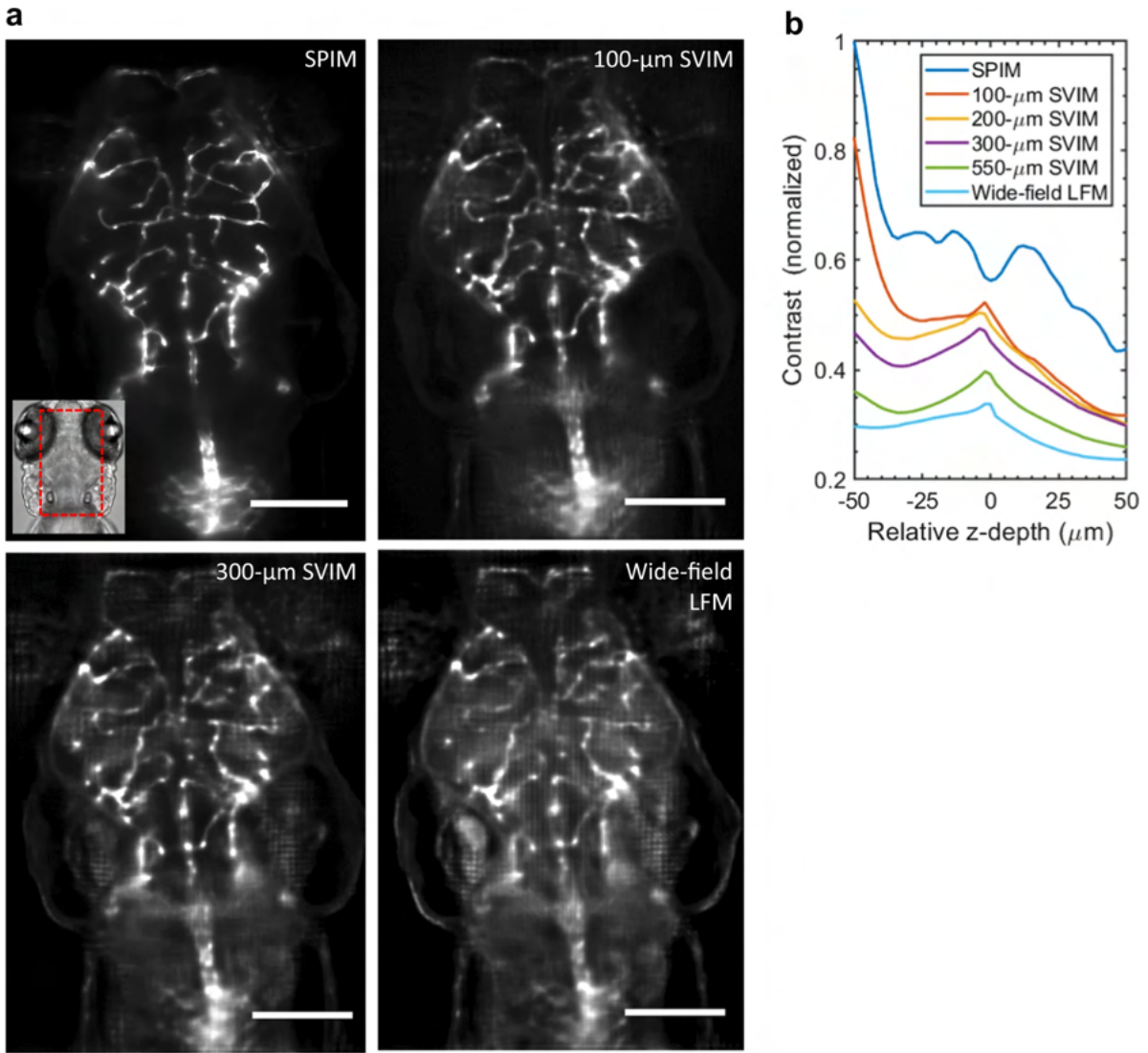


Figure 4.3: Higher contrast achieved by SVIM

(a) SVIM images of the cranial vasculature improve in contrast as the depth (axial extent) of the illumination volume is decreased. Images are averaged-intensity z -projections of the same 40- μm thick sub-volume, centered at $\sim 170 \mu\text{m}$ into the head of a 5 dpf zebrafish larva. The SVIM image quality progressively approaches the performance of SPIM as the axial extent of the illumination is reduced to 300 μm or 100 μm , far exceeding the image contrast obtained with wide-field LFM. Inset shows the approximate location of the imaged volume, in context of the zebrafish head.

(b) Quantitative comparison of image contrast, defined as the normalized standard deviation of the pixel values (Methods Section 4.4.5), comparing LFM, SPIM, and SVIM of different SVI extents from **(a)**. SVIM of smaller extents yielded increasingly better contrast, approaching the performance of SPIM. The contrast of SPIM showed the intrinsic contrast variation of the 3D sample, coupled with the expected contrast decay for increasing imaging depth. The local increase in contrast seen for the SVIM cases around $z = 0 \mu\text{m}$ came from grid-like artifacts from the light-field reconstruction centered around the native focal plane, a known feature of LFM in general [50, 51].

Scale bars, 100 μm .

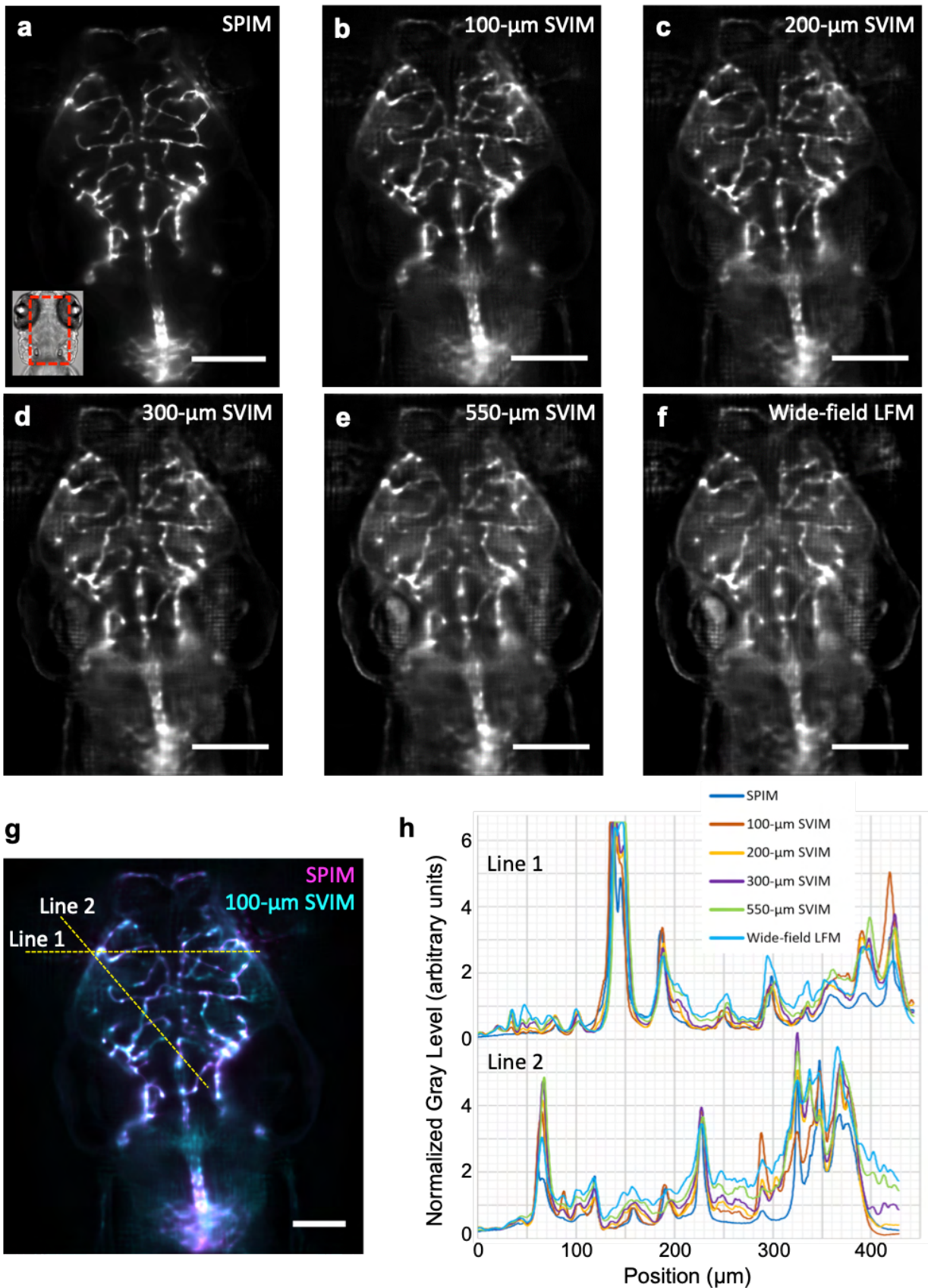


Figure 4.4: Continued on next page.

Figure 4.4: (Continued from previous page.) SVIM offers improved contrast over conventional wide-field LFM.

Images of the same sub-volume of the GFP-labeled vasculature of a 5-dpf, *Tg(kdrl:eGFP)*, zebrafish larva captured with **(a)** SPIM, and **(b-e)** SVIM with *z*-extents of 100, 200, 300, and 550- μm , respectively, and **(f)** wide-field LFM. A subset of images in **(a-e)** are shown in Fig. 4.3a. See Fig. 4.3b for quantitative analysis of the contrast obtained with SVIM of increasingly smaller *z*-extents having increasingly higher contrast, approaching the performance of SPIM, and far exceeding the image quality obtained with wide-field illumination. The images shown are each averaged-intensity *z*-projections of the same 40- μm thick sub-volume, centered at approximately 170 μm into the specimen, with the image intensity normalized to full scale with 0.4% saturation.

In **(g)** and **(h)** we demonstrate that the lower background and higher contrast achieved with SVIM helped to produce reconstructed images that were more similar to the “ground-truth” SPIM images. The *z*-projected images shown in **(a-e)** were overlaid in the lateral plane, as shown in **(g)** for the 2 cases of SPIM and 100- μm SVIM, and intensity line profiles were compared between all the imaging modalities, along two representative lines that cross multiple blood vessels **(h)**.

Overall, we found good semi-quantitative correspondence between SPIM and SVIM in capturing the vascular structures. Importantly, this correspondence was generally better for SVIM as compared to conventional wide-field LFM; the correspondence improved as the illumination extent was reduced. Full quantitative correspondence between the light-field reconstructed images and SPIM is not expected, due to SVIM’s inherent lower and non-uniform resolution, and artifacts/limitations in the computational nature of LFM in general [50, 51]. Active research efforts are on-going to fully characterize and improve the correspondence between LFM and image ground truth [116, 117].

Scale bar, 100 μm .

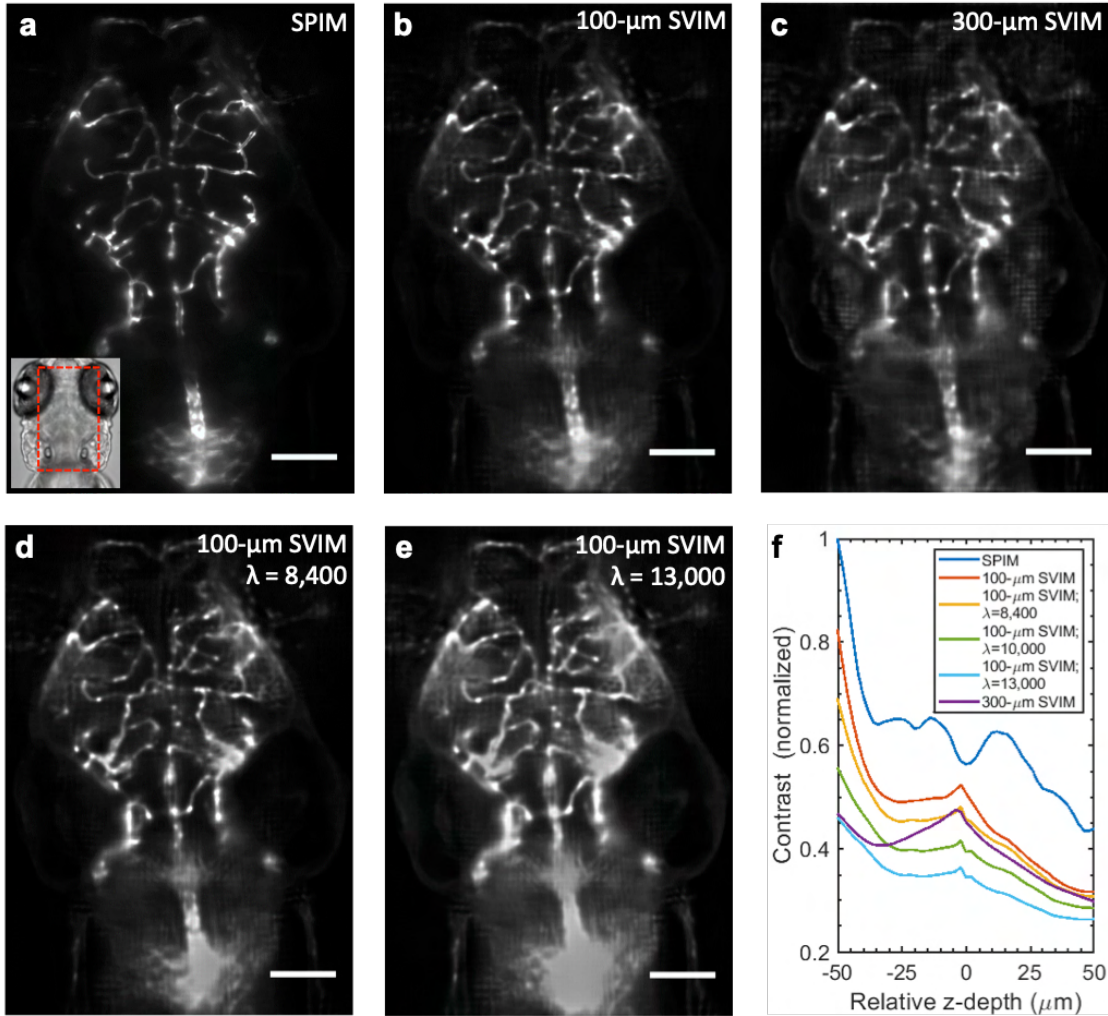


Figure 4.5: Simulation of SVIM contrast degradation with increased background noise. Averaged-intensity z -projection images of the same $40\text{ }\mu\text{m}$ -thick sub-volume of GFP-labeled vasculature of a 5-dpf zebrafish larva, centered at approximately $170\text{ }\mu\text{m}$ into the specimen (as in Fig. 4.3a), comparing (a) SPIM, (b) $100\text{-}\mu\text{m}$ SVIM, (c) $300\text{-}\mu\text{m}$ SVIM, and (d) and (e) $100\text{-}\mu\text{m}$ SVIM with different levels of Poisson noise applied to the raw light-field images before reconstruction, to simulate the extra background signal that would be expected to come from larger illumination extents ($\lambda = 8,400$ corresponds to the mean photon number per pixel of the raw light-field image of $300\text{-}\mu\text{m}$ SVIM; $\lambda = 10,000$ and $13,000$ simulates even larger illumination extents). See Methods Section 4.4.5. The images in (a-e) show that applying noise to $100\text{-}\mu\text{m}$ SVIM led to both increased background and artifacts in the reconstructed volumes, which was consistent with our empirical results (Fig. 4.3a and 4.4). Comparison of the quantitative contrast of the 3D images is shown in (f), similar to the comparison shown in Fig. 4.3b. For each modality, contrast was measured at every available z -plane and normalized against the top plane ($z = -50\text{ }\mu\text{m}$) of SPIM. As expected, $100\text{-}\mu\text{m}$ SVIM with increasing levels of noise applied ($\lambda = 8,400, 10,000$, and $13,000$) had poorer contrast than $100\text{-}\mu\text{m}$ SVIM. Note that when $\lambda > 10,000$, $100\text{-}\mu\text{m}$ SVIM exhibited even lower contrast than $300\text{-}\mu\text{m}$ SVIM. [50, 51].

Scale bars, $100\text{ }\mu\text{m}$.

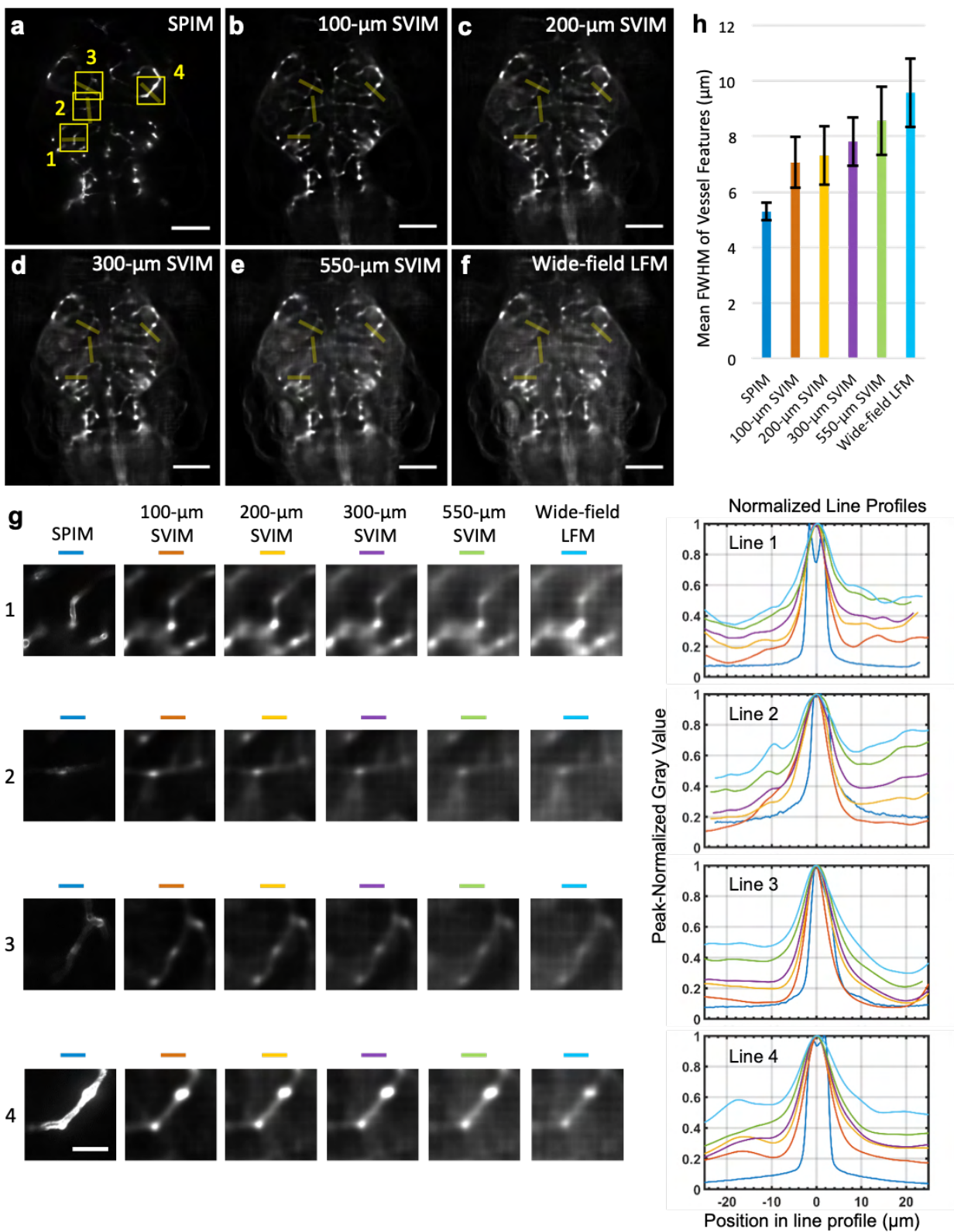


Figure 4.6: Continued on next page.

Figure 4.6: (Continued from previous page.) Enhanced effective resolution enabled by the higher contrast of SVIM.

(a) To compare the effective resolution achieved with the various imaging modalities, we quantified the FWHM diameter of the same blood vessels captured by each modality. Starting in the SPIM 3D dataset, we selected a single z -slice that had four well-imaged blood vessels of approximately the same size. We then found the matched z -slices in the SVIM and LFM datasets. Shown in (a-f) are the corresponding single z -slice images, selected at z -depth = 150 μm into the sample (50 μm above the native focal plane) across all modalities. Similar to all presented results, SPIM images were background-subtracted to account for camera dark-counts and SVIM images were background-adjusted within the reconstruction process. Four rectangular regions-of-interest (ROI), labeled 1-4, were generated by a MATLAB script to traverse orthogonally the respective blood vessels, whose zoomed-in images are shown in (g). Each rectangular ROI had length of $\sim 50 \mu\text{m}$ and width of $\sim 10 \mu\text{m}$, and the line profiles were calculated as averages across the width extent. All line profiles were normalized to peak value equal to 1, from which the mean FWHM and standard deviation values were measured and quantified in (h). SPIM, as expected, exhibited the best resolution, establishing the ground-truth mean FWHM diameter of $\sim 5 \mu\text{m}$ for the analyzed blood vessels. With SVIM, smaller selectively-illuminated volume extents yielded decreased background and increased effective resolution, represented by the achieved mean FWHM diameter of the blood vessels, showing an improvement of $\sim 35\%$ between 100- μm SVIM and wide-field LFM.

Scale bars, (a-f) 100 μm , (g) 30 μm .

4.2.3 SVIM enhances imaging of biological components moving in 3D

The synchronous volumetric imaging capability and enhanced contrast of SVIM is ideal for imaging dynamic systems, where components undergo fast motion in 3D space. We employed SVIM to image the bacterial flows in seawater, surrounding the light organ of a Hawaiian bobtail squid, *Euprymna scolopes*, while it was selectively colonized by the bacteria *Vibrio fischeri* [118]. The squid–bacteria symbiosis is an important model for understanding the effects of fluid flow during interactions between bacteria and epithelial surfaces [119]. Previous 2D measurements of the bacterial flow field [120] inadequately captured the 3D flows around the light organ. SVIM offered dramatically better image quality as compared to wide-field LFM (Fig. 4.7a and b). SVIM removed most of the background that severely compromised wide-field LFM, which came from the excitation of nearby auto-fluorescent tissues. In SVIM, the fluorescence of individual bacteria could be clearly imaged and tracked (Fig. 4.7 and Movies 4.8, 4.9, and 4.10), yielding the position (Fig. 4.7c) and speed (Supplementary Fig. 4.18c) of each bacterium, and a full quantitative description of the flow field in 3D.

We further tested the performance of SVIM by imaging the motions of the live beating heart of an intact zebrafish larva (Fig. 4.7d-g and Movies 4.11 and 4.12), important for understanding how dynamic cellular and fluid motions contribute to the heart development [56, 84]. SVIM captured the beating motion of the heart walls and the trajectories of blood cells, with single blood cell resolution, at $90 \text{ volumes s}^{-1}$ over the entire heart (Fig. 4.7d and e, and Movies 4.11 and 4.12). This represents a volume coverage rate five times larger than an optimized plane illumination approach could achieve [121]. Compared to wide-field LFM, SVIM achieved images with 50% and 10% better contrast of the heart wall and blood cells, respectively (Fig. 4.13). SVIM synchronously captures dynamic cardiac behaviors, free of potential artifacts that could arise in other beating heart imaging methods that rely on specific presumptions about the nature of the heart motions [77, 88, 89, 122]. Thus SVIM

could be ideally suited for 3D imaging of arrhythmias and other transient, non-periodic heart beating behavior in studies involving genetic, physical, or pharmacological perturbations.

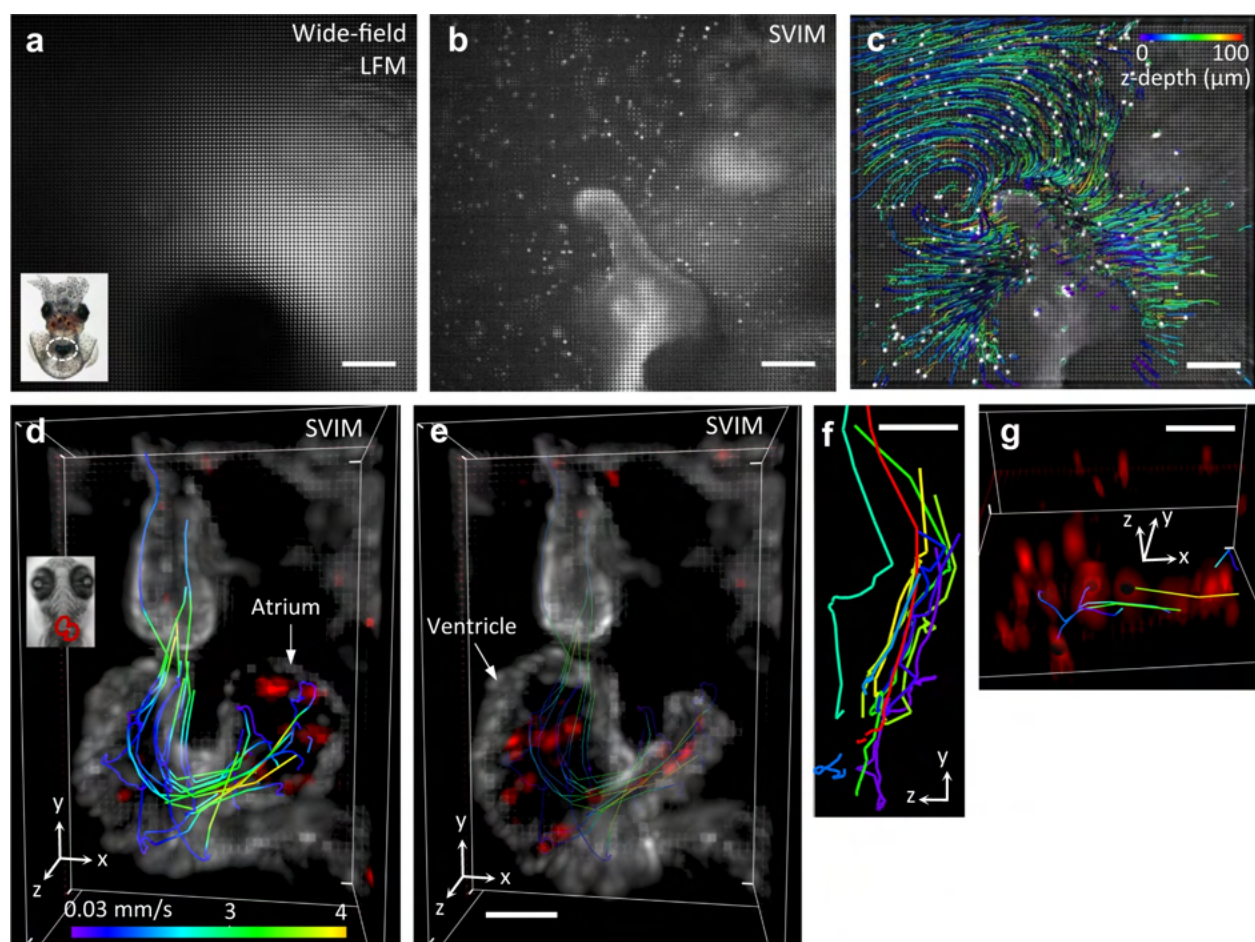


Figure 4.7: Continued on next page.

Figure 4.7: (Continued from previous page.) SVIM enables fast, high-contrast, volumetric imaging of live biological systems.

(a-c) Imaging the bacterial flow around the light organ of a juvenile squid. Raw light-field images recorded with conventional wide-field illumination yielded excessive background **(a)**, whereas SVIM, with a selectively-illuminated volume of $100 \mu\text{m}$, reduced this background and enhanced the contrast to allow localization of individual bacteria **(b)**. Inset shows squid with the light organ region highlighted by the dashed oval. **(c)** Quantitative flow trajectories tracked from the reconstructed SVIM data, color-coded for z -depth. Non-uniform 3D flow patterns were observed throughout the imaged volume. Images were collected at 20 volumes s^{-1} , with a volume $\sim 600 \times 600 \times 100$ (depth) μm^3 .

(d-g) Imaging the motions of the beating heart wall and moving blood cells. A volume of $\sim 250 \times 50 \times 150$ (depth) μm^3 in a live 5-dpf zebrafish larva was captured at 90 volumes s^{-1} . Transgenes labeled the endocardium (rendered white) and blood cells (rendered red), *Tg(kdrl:eGFP, gata1:dsRed)*. Inset in **(d)** highlights the position of the heart within the animal. The captured beating heart is shown in 3D-rendered views at two representative time points during the cardiac cycle: **(d)** the atrium was at its fullest expanded extent, followed by **(e)** when the blood had been pumped into the enlarged ventricle. Representative blood-cell flow trajectories were manually tracked and quantified (color of the trajectories in **(d-g)** depicts blood-cell speed) (Methods Section 4.4.4). **(f)** Maximum projection image along the x -axis of several representative flow trajectories highlights the substantial component of blood flow along the z -direction. To aid visualization, clipping planes in the yz plane were used to cut out the atrium and parts of the ventricle. Color-coding of the blood-cell tracks in **(f)** is only for visual identification. **(g)** Perspective view of the blood cells demonstrates the achieved single-cell resolution, notably along the z direction. Circular voids within several blood cells mark the cells whose trajectories were tracked and quantified.

Scale bars, **(a-c)** $100 \mu\text{m}$, **(d-g)** $30 \mu\text{m}$.

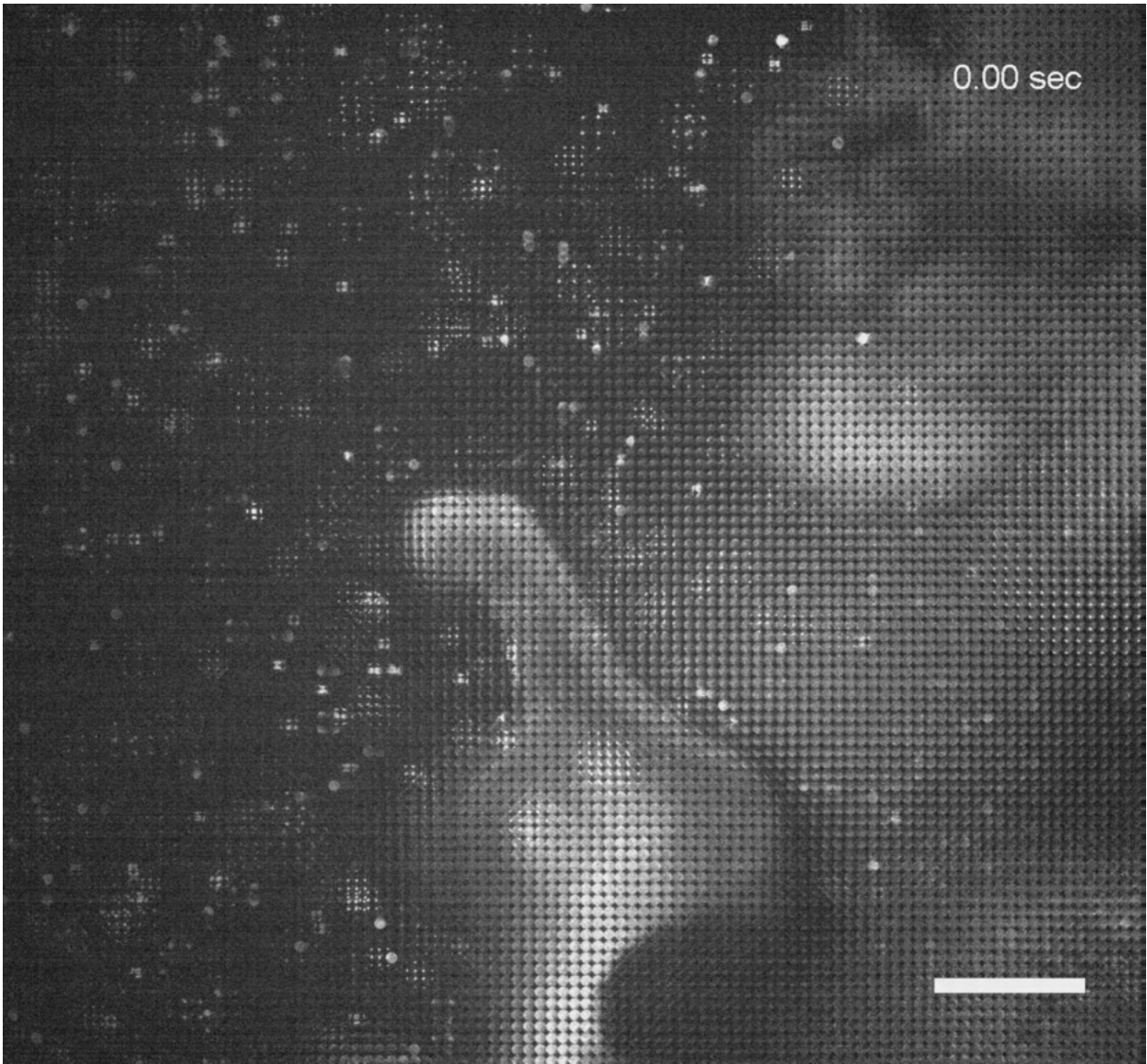


Figure 4.8: Raw light-field-image movie of the bacterial flow around the squid light organ, recorded with SVIM. Movie depicts the raw, unprocessed 2D-light-field images of the flow of fluorescently-labeled *Vibrio fischeri* bacteria around the light organ of the Hawaiian bobtail squid *Euprymna scolopes*, during early stage of colonization. Time series were acquired at 20 frames s^{-1} , and the movie playback frame rate was set at the same rate. Note the high contrast and resolution achieved in these raw light-field SVIM images, which enabled following the 3D motion of individual bacterium. A single frame of the movie was shown in Fig. 4.7b. Scale bar, 100 μm . Movie: https://static-content.springer.com/esm/art%3A10.1038%2Fs42003-020-0787-6/MediaObjects/42003_2020_787_MOESM1_ESM.mp4 (76 MB).

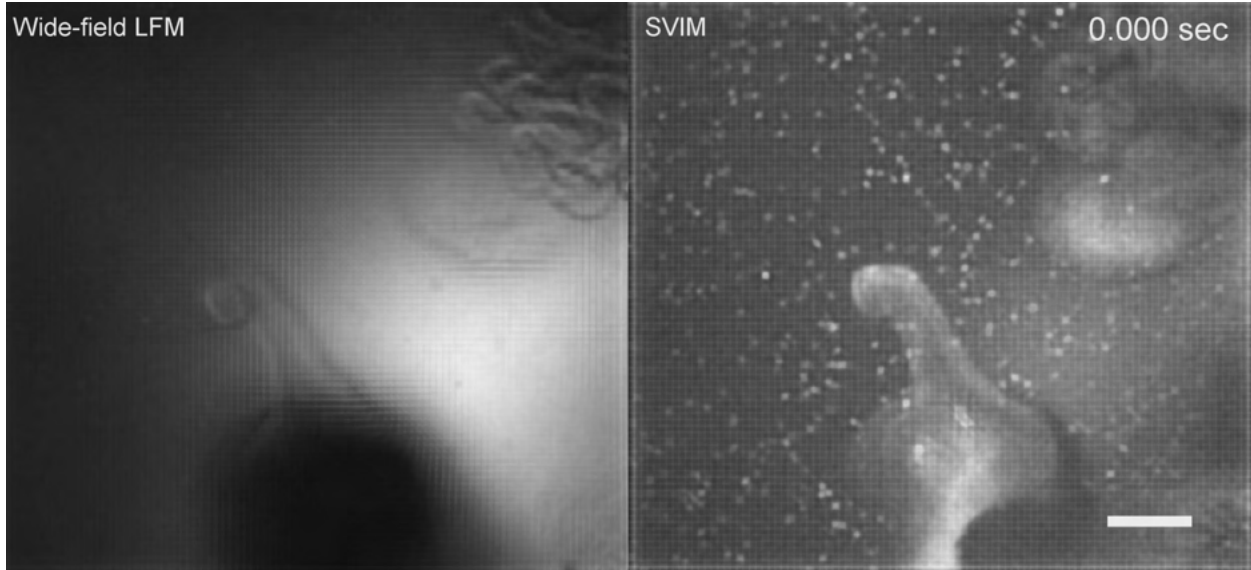


Figure 4.9: Comparison of reconstructed movie of the bacterial flow around the squid light organ, recorded with wide-field LFM versus with SVIM. Movie depicts the side-by-side comparison of the reconstructed movies recorded with wide-field LFM versus with SVIM, of the flow of fluorescently-labeled *Vibrio fischeri* bacteria around the light organ of the Hawaiian bobtail squid *Euprymna scolopes*, during early stage of colonization. Each 4D dataset (time-series, z-stack) was reconstructed with the same parameters from the raw data (Methods Section 4.4.3), then normalized in intensity levels with 0.4% pixel saturation for display purposes here, and finally a *z*-projection was taken based on average values. Time-series were acquired at 20 frames s^{-1} , and movie playback frame rate was set at the same rate. Raw time-series for the two modalities were recorded sequentially in time, and frame-matched here to facilitate comparison. Note the high contrast and single-bacterium resolution achieved with SVIM, compared with the low contrast of the wide-field LFM reconstruction. Scale bar, $100 \mu\text{m}$. Movie: https://static-content.springer.com/esm/art%3A10.1038%2Fs42003-020-0787-6/MediaObjects/42003_2020_787_MOESM2_ESM.mp4 (4.5 MB).

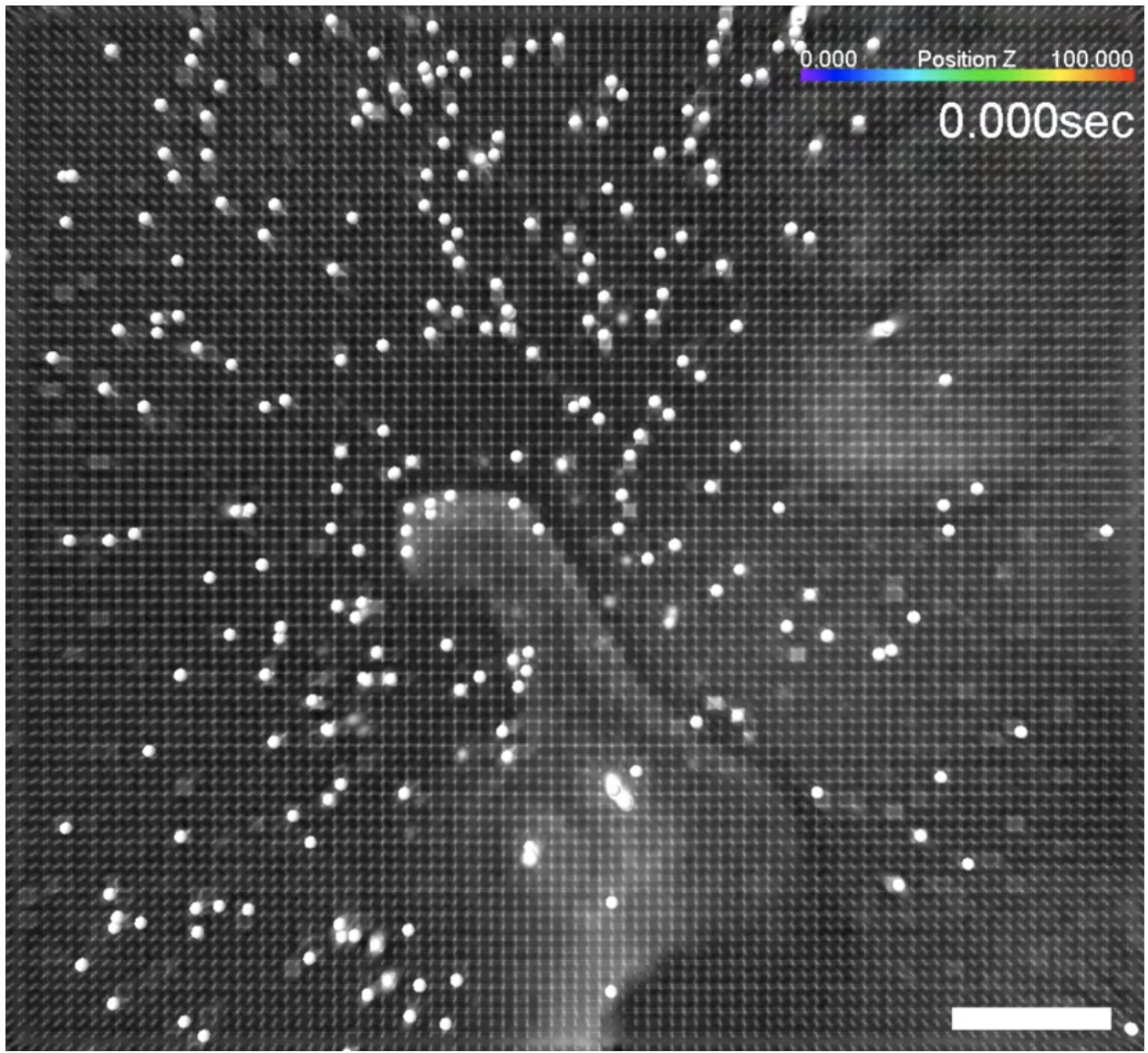


Figure 4.10: 3D flow fields of bacteria around the squid light organ, recorded with SVIM. Movie depicts the flow fields of fluorescently-labeled *Vibrio fischeri* bacteria around the light organ of the Hawaiian bobtail squid *Euprymna scolopes*, tracked from the 3D-reconstructed light-field rendering. Light-field images were acquired at 20 frames s^{-1} , yielding 3D volumetric rate of $20 \text{ volumes s}^{-1}$ after reconstruction, of volume $\sim 600 \times 600 \times 100$ (depth) μm^3 . Movie playback frame rate was set to 20 frames s^{-1} . Gray-scale image in the background is the average intensity projection of the 3D reconstruction. Individual fluorescent bacterium was computationally tracked, and tracks are shown color-coded by z position. Analysis of the tracks provided a quantitative description of the 3D bacterial flow fields, as shown in Fig. 4.7c and Supplementary Fig. 4.18c and d. Scale bar, $100 \mu\text{m}$. Movie: https://static-content.springer.com/esm/art%3A10.1038%2Fs42003-020-0787-6/MediaObjects/42003_2020_787_ESM.mp4 (19.3 MB).

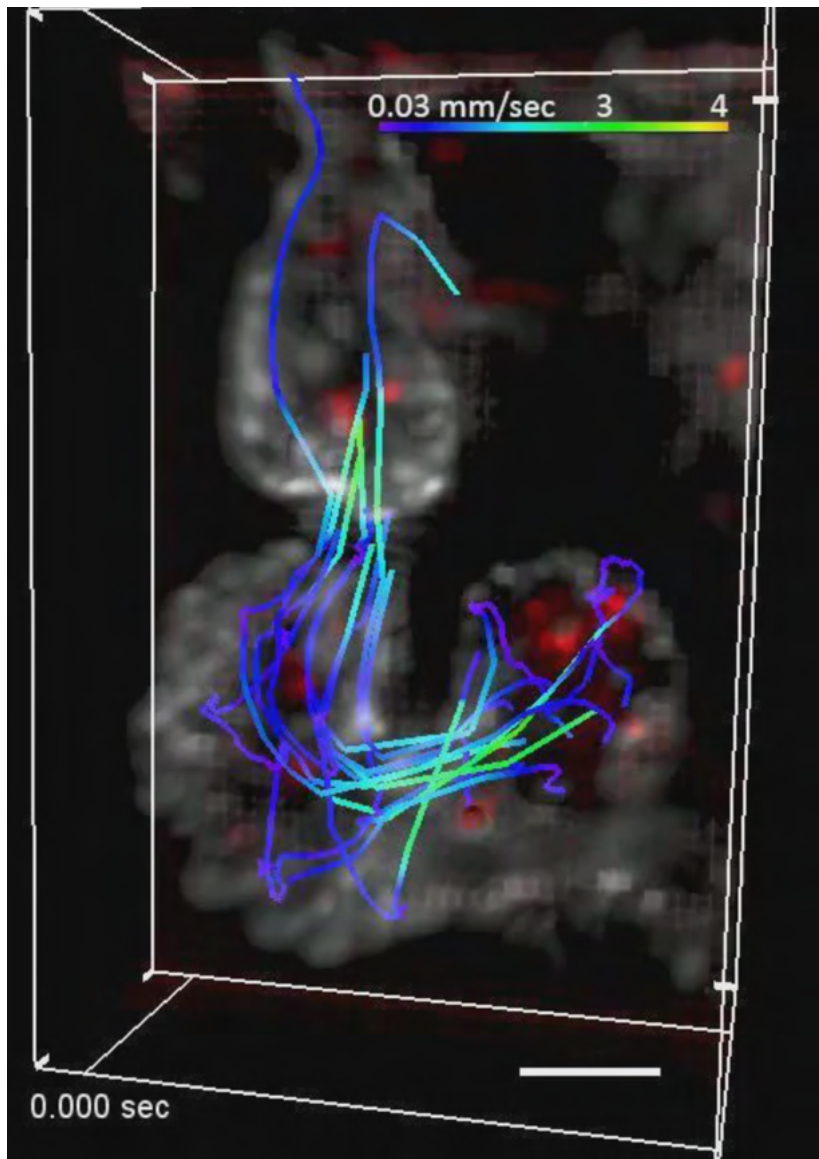


Figure 4.11: 3D blood flow and endocardium motion of the entire larval zebrafish beating heart. Movie of fluorescently-labeled endocardium (white) and blood cells (red) in a beating heart of a live 5-dpf zebrafish larva, 3D-rendered following the light-field reconstruction. Acquisition was at $90 \text{ volumes s}^{-1}$, and movie playback frame rate was slowed by 5.5 times. Representative blood cells' trajectories through the heart were manually tracked and quantified (color of the trajectories depicts speed). During the movie, the endocardium channel was turned off at several time points to aid visualization of the blood cells. The high synchronous volumetric imaging rate and volume coverage enabled imaging and tracking of the 3D blood flow, at single-blood-cell resolution throughout the cardiac beating cycle, which was about 450 ms. Still frames from the movie were depicted in Fig. 4.7d-g. Scale bar, $50 \mu\text{m}$. Movie: https://static-content.springer.com/esm/art%3A10.1038%2Fs42003-020-0787-6/MediaObjects/42003_2020_787_ESM.mp4 (1.1 MB).

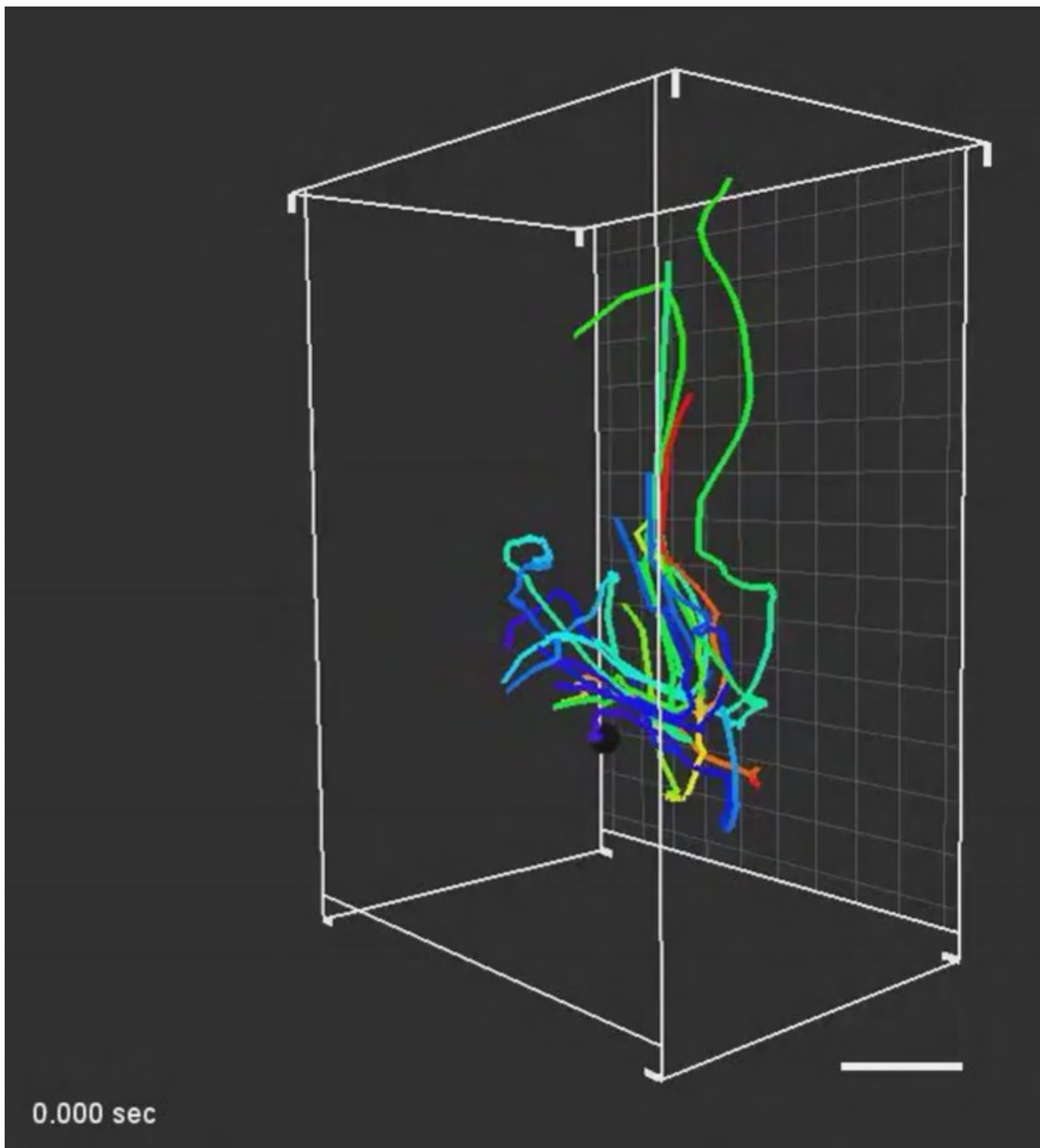


Figure 4.12: 3D blood flow and endocardium motion of the entire larval zebrafish beating heart. Movie depicts the representative trajectories of blood cells flowing through the larval zebrafish beating heart, as seen while rotating the imaged cardiac volume about the y -axis. Note the substantial extent of the motion along the z direction, and the non-uniform 3D trajectories, of the blood cells. Acquisition was at $90 \text{ volumes s}^{-1}$, and movie playback frame rate was slowed by 5.5 times. Centroids of blood cells are shown as black-colored spheres. Each individual blood cell trajectory is represented in a single color to aid visualization. A 3D-cropped still frame of the movie was shown in Fig. 4.7f. Scale bar, $50 \mu\text{m}$. Movie: https://static-content.springer.com/esm/art%3A10.1038%2Fs42003-020-0787-6/MediaObjects/42003_2020_787_MOESM5_ESM.mp4 (1.2 MB).

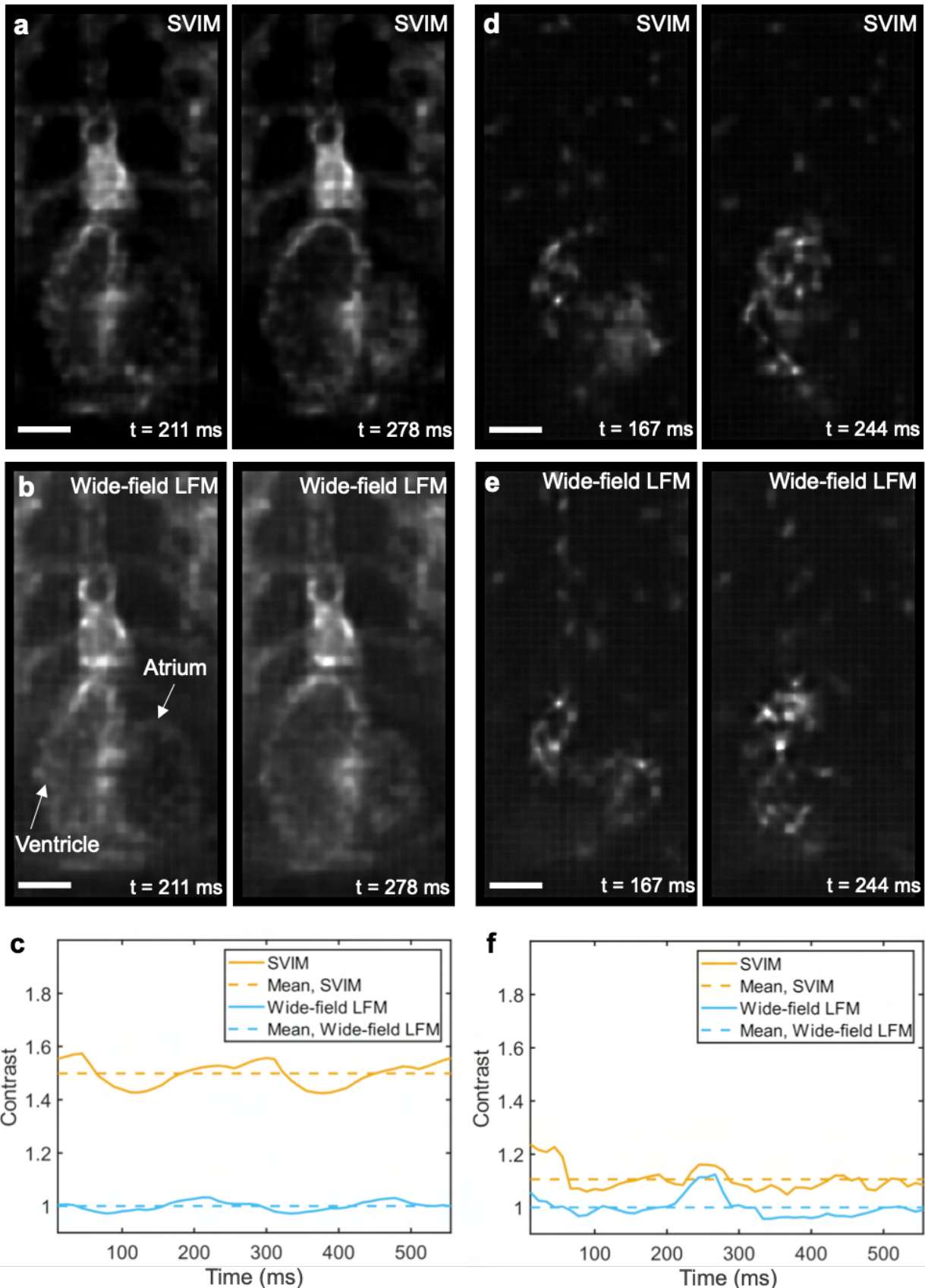


Figure 4.13: Continued on next page.

Figure 4.13: (Continued from previous page.) Contrast enhancement of SVIM in imaging the zebrafish beating heart and blood flow. Comparison of image reconstructions acquired with SVIM and wide-field LFM, of fluorescently-labeled endocardium and blood cells in the beating heart of a 5-dpf zebrafish larva, captured at 90 volumes/s. See Table A3 in Appendix C for details on imaging and reconstruction parameters. Taking advantage of the periodic nature of the beating heart, movies taken with SVIM and wide-field LFM were frame-synchronized to depict a similar sequence of the beating motion, to facilitate frame-to-frame comparison of image quality. Shown in (a-e) are the averaged-intensity z -projections of the 3D reconstructed z -stack at the time points as labeled, where $t = 0$ ms corresponded to when the atrium was maximally contracted. See Movies 4.11 and 4.12 for the full temporal sequences that spanned several heart beats. Comparison of the quantitative contrast in imaging the endocardium and blood cells were shown in (c) and (f), respectively. Image processing and contrast analysis were carried out with procedure similar to that used for the vasculature results, Fig. 4.3b (Methods Section 4.4.5). The contrast was calculated for the averaged-intensity z -projection images as shown in (a-e), for each time point of the 50-frame beating cycle, and normalized to the averaged value of the wide-field LFM case. SVIM achieved approximately 50% and 10% higher contrast than wide-field LFM over the entire beating cycle, in imaging the endocardium and blood cells, respectively. Scale bar, 50 μm .

4.2.4 SVIM enhances brain-wide functional neuroimaging

Many recent developments of LFM have focused on functional neuroimaging [53, 55, 116, 117, 123–125] despite the challenges presented by the relatively slow image reconstruction algorithms, and the reduced image quality of LFM compared with state-of-the-art neuroimaging techniques [10]. This is because the extraordinary imaging rate possible with LFM could be game changing for the simultaneous recording of large number of spatially distributed neurons. We tested if the enhanced contrast of SVIM would improve the recording of neural activity in larval zebrafish, as assayed through a genetically encoded calcium indicator expressed in all of its neurons (Figs. 4.14, 4.15, and 4.16). The enhanced contrast from the reduced background of SVIM, in both 1P and 2P excitation modes (Fig. 4.15), enabled better performance than wide-field LFM in recording the calcium transients that reflect the firing of single neurons across the zebrafish brain, capturing up to fourfold more neurons during spontaneous brain activity (Methods Section 4.4.4; Fig. 4.14d–f). While both 1P and 2P excitation SVIM offered improved contrast, they present different compromises. Excitation with 1P offers simplicity and fast volumetric imaging rates, as demonstrated with LFM in general [53, 55, 116, 117, 123–125]. The lower 2P excitation cross section limits the imaging rate of 2P-SVIM; however, we found that 2P excitation led to better contrast and a larger number of resolved active neurons (Fig. 4.14e and f, and Fig. 4.15). This detection of more active neurons, enabled by the improved contrast, results not only from the reduced tissue autofluorescence of 2P excitation, but also from additional mechanisms specific to our application. First, 2P laser light preserves its spatial profile better than 1P light as it penetrates deeper into the sample [75], due to the reduced scattering at longer wavelengths. Thus, the scanned selectively illuminated volume is more precisely defined spatially with 2P, leading to less extraneous background coming from outside of the illuminated region. Furthermore, the invisible near-infrared light used for 2P excitation avoids the visual responses triggered in the zebrafish by the visible 1P excitation [76], eliminating the “always-on” visually activated neurons that would otherwise yield background fluorescence that suppresses

the detection of neurons undergoing spontaneous activity. This last point suggests that 2P-SVIM is best suited for studies of visually sensitive behaviors, such as brain-wide responses to visual stimuli (Fig. 4.16) or sleep [80].

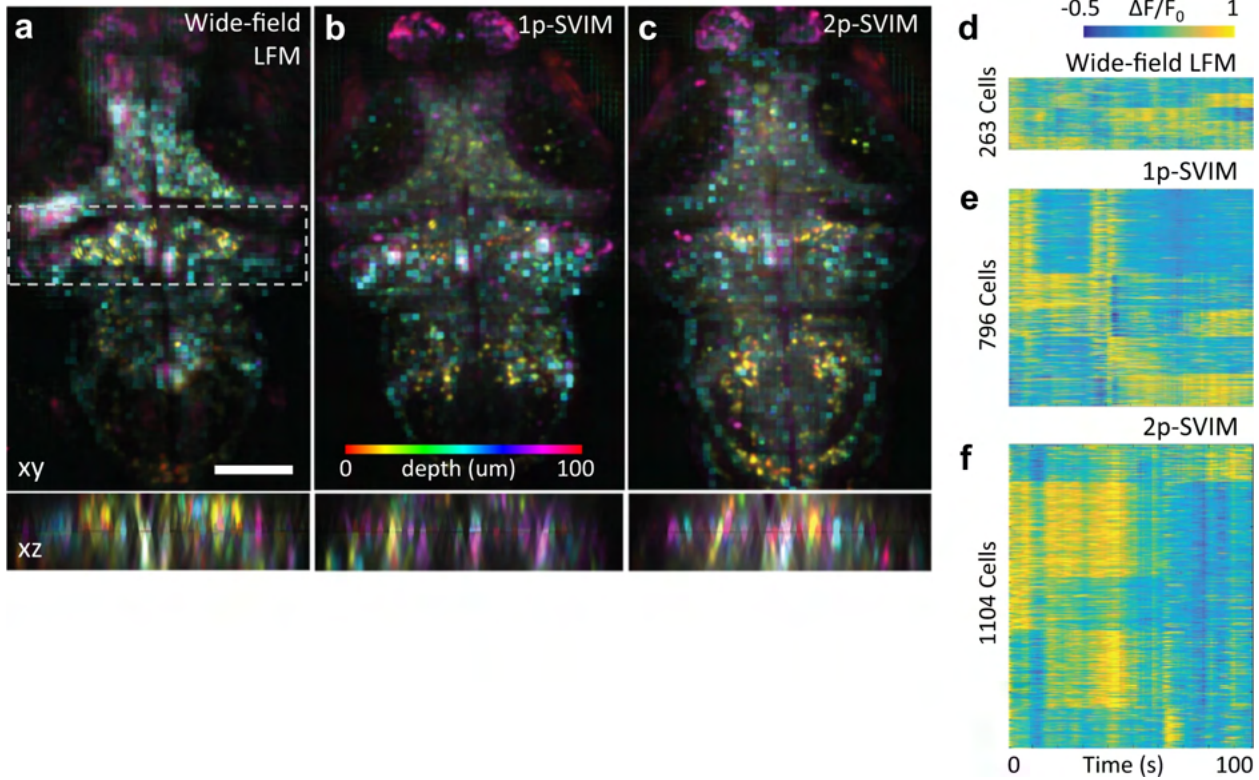


Figure 4.14: Functional neuroimaging with SVIM. Functional imaging of a 5-dpf larval zebrafish with pan-neuronal fluorescent calcium indicators, *Tg(elavl3:H2b-GCaMP6s)*. Spontaneous brain activity, over volume $\sim 600 \times 600 \times 100$ (depth) μm^3 , was recorded at 1 volume s^{-1} , with SVIM, in either 1- or 2-photon excitation mode (1P-SVIM or 2P-SVIM, respectively), or conventional 1P wide-field LFM. Cellular resolution representations of active neurons were found with standard methodology based on spot segmentation of the time-domain standard deviation of the 3D time series data (Methods Section 4.4.4).

(a-c) Images shown are depth color-coded *xy*- or *xz*-projections, of the time-domain standard-deviation-projection of the recorded brain activity over a time window of 100 s. Colored ellipsoids represent active neurons. Dashed box in the *xy*-projection image represent the region that produces the corresponding *xz*-projection image. Activity traces of segmented neurons are shown in **(d-f)**, revealing that the most number of neurons were found with 2P-SVIM (1104 cells), then with 1P-SVIM (796 cells), both of which were several-fold higher than with conventional wide-field LFM (263 cells).

Scale bar, 100 μm .

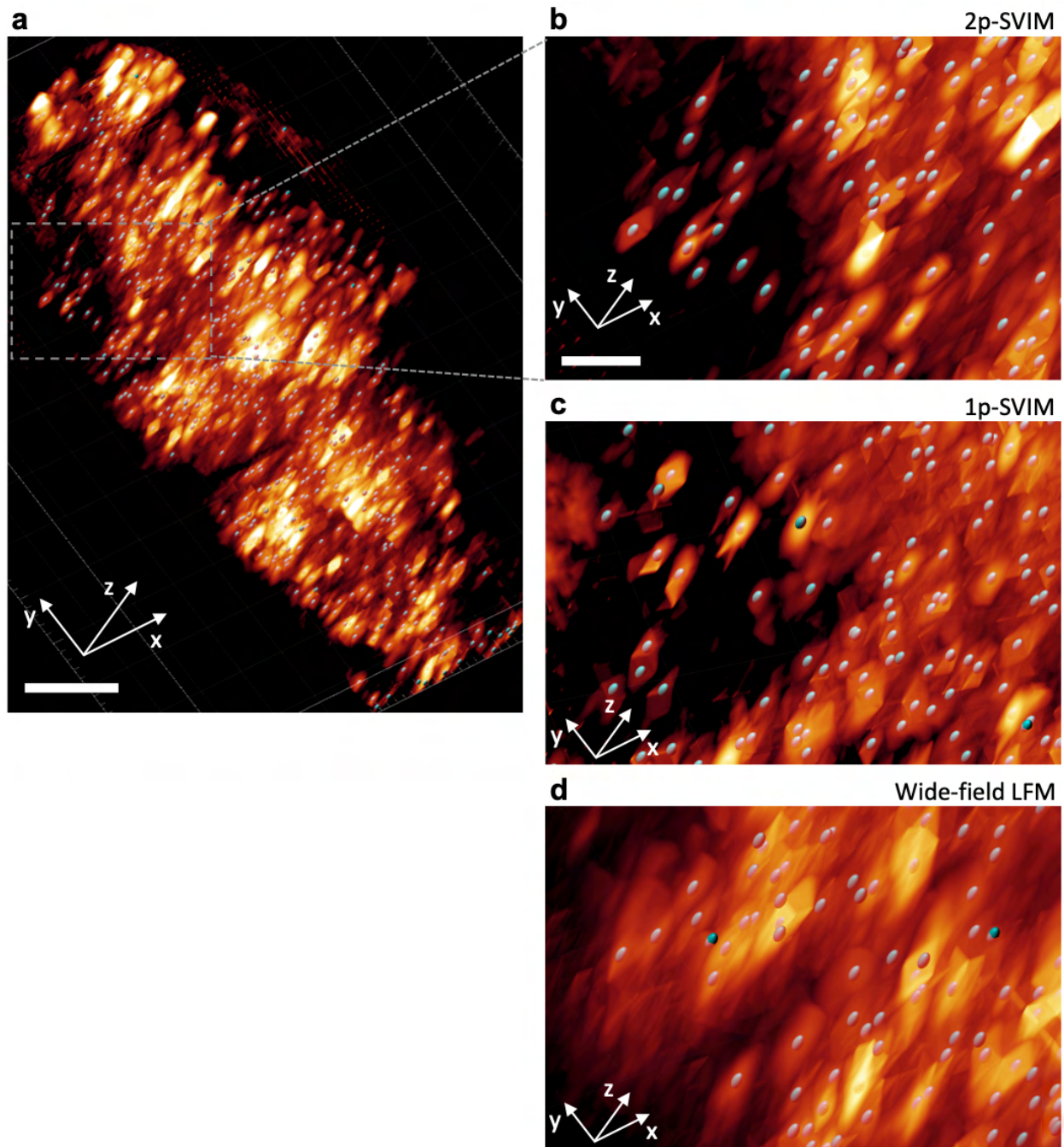


Figure 4.15: Continued on next page.

Figure 4.15: (Continued from previous page.) Zoomed-in, 3D-rendered views of the zebrafish spontaneous brain activity.

Higher magnification, 3D-rendered views from the functional imaging of a 5-dpf zebrafish's spontaneous brain activity (same results as in Fig. 4.14a-c). Shown in **(a)** is the 3D-rendered view of the time-domain standard-deviation-projection of spontaneous brain activity over a time window of 100 s, of the entire imaged volume, captured with 2P-SVIM.

(b-d) Zoomed-in views of approximately the same region of the zebrafish brain for 2P-SVIM, 1P-SVIM, and wide-field LFM, respectively. Spot segmentation of the time-domain standard-deviation-projections was carried out to identify neurons that were active during the experimental time window (see Methods Section 4.4.4 for full details on the processing and analysis of the neuroimaging results). The segmented active neurons are depicted as cyan-colored ellipsoids in the image panels. Image contrast has been manually adjusted for each image panel to improve visualization of individual neurons.

Scale bars, **(a)** 100 μm , **(b-d)** 20 μm .

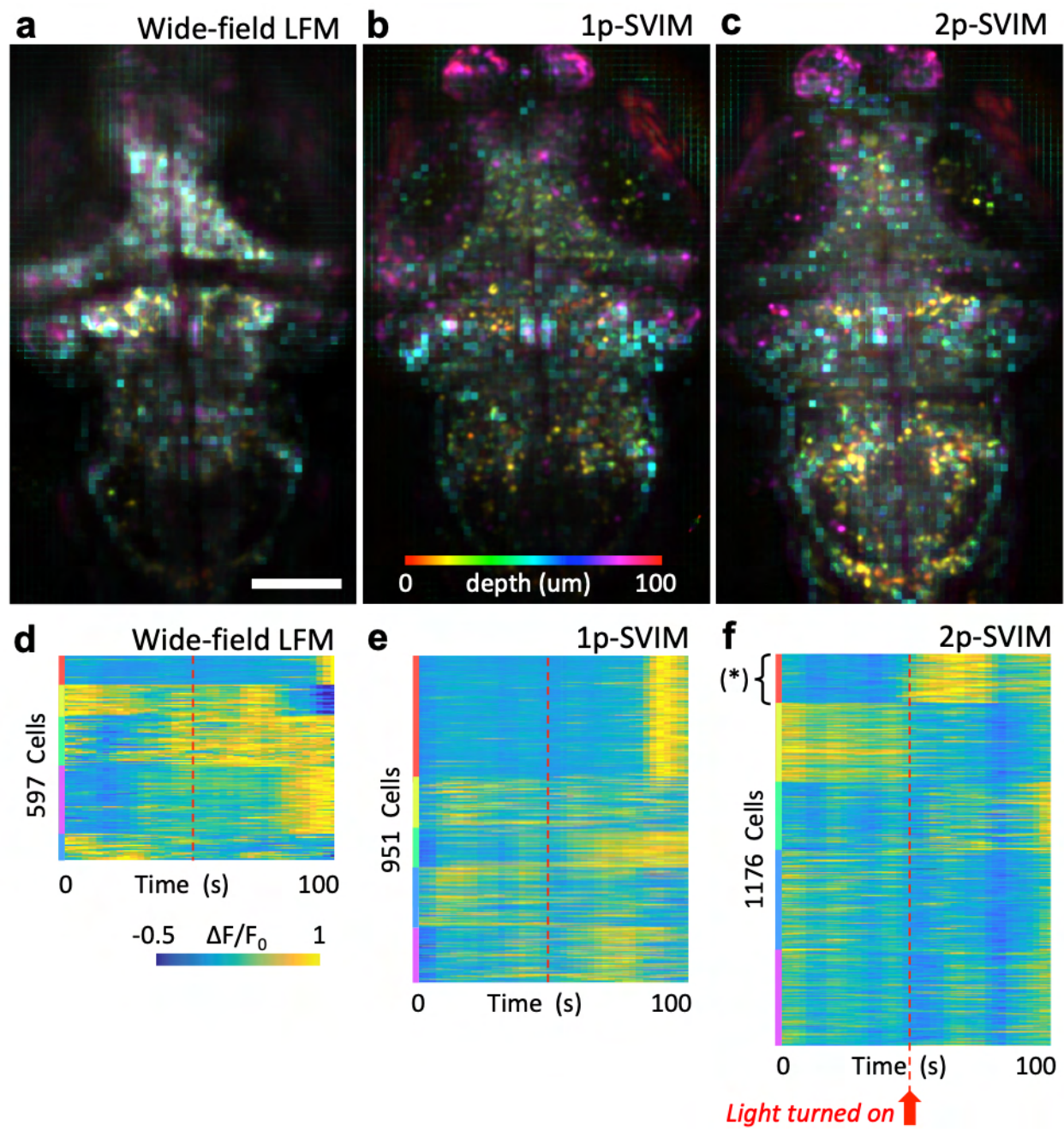


Figure 4.16: Continued on next page.

Figure 4.16: (Continued from previous page.) Light-evoked brain response captured by 2P-SVIM. Functional imaging of a 5-dpf larval zebrafish with pan-neuronal fluorescent calcium indicators, *Tg(elavl3:H2b-GCaMP6s)*, across a time window of 100 s with a LED light turned on at the midpoint. Analysis and presentation of the imaged results are similar to the spontaneous activity window shown in Fig. 4.14. Cellular resolution representations of active neurons were found with standard methodology based on spot segmentation of the time-domain standard deviation of the 3D time series data (Methods Section 4.4.4). Images shown in (a-c) are depth color-coded of the time-domain standard-deviation-projection of the light-field reconstructed 3D time series data, where colored puncta represent active neurons. Activity traces of segmented neurons shown in (d-f) were further grouped by k-means clustering. Only the results recorded with 2P-SVIM revealed a group of neurons (marked by *), that exhibited a clear response to the LED light turning on at $t = 50$ s. Scale bar, 100 μm .

4.3 Discussion

The results presented here demonstrate that, by combining the strengths of SPIM and LFM, SVIM provides a powerful tool for high-contrast, synchronous volumetric imaging of dynamic systems. By optimizing the illumination pathway, SVIM offers single-cell resolution, with improved contrast over wide-field LFM. The SVI principle was implemented in a recent work [126], where the sample was illuminated with a beam having a large cross-sectional area that filled up the volume of interest. This volume-filling strategy, compared with our volume-scanning strategy, is simpler to implement but gives up spatial precision in defining the volume of interest (Supplementary Note 4.5.1). SVIM is compatible and synergistic with recent innovations in LFM that optimize the detection pathway for more spatially uniform resolution and reduced grid-like artifacts in the reconstructions. These include implementation of multi-view light-field detection [126], and methods that capture and process light-field information through phase masks [127], diffusers [128], or in the Fourier domain [116, 129]. SVIM could also be further optimized by approaches that speed up the image reconstruction or information extraction pipeline [55, 123, 124]. Together, these latest refinements of LFM and the high contrast of SVIM may enable LFM-based techniques to become the next-generation tools for imaging tissue-scale 3D dynamic biological systems. LFM-based methods belong to an emerging class of diverse computational imaging techniques [130, 131] that harness the power of physical modeling, signal processing, and computation to enable new performance spaces beyond conventional microscopy. The selective volume illumination strategy of limiting the illuminated sample volume, in improving the contrast of the acquired image data, is positioned to play a key role in optimizing a variety of computational imaging approaches for a wide range of biological applications.

4.4 Methods

4.4.1 Microscopy setup and implementation

The optical setup was based on an existing SPIM apparatus [77], with modifications to provide the selective-volume illumination and light-field detection (Fig. 4.17, Table A3 in Appendix C). Briefly, collimated beams from 1P excitation CW and 2P excitation femtosecond-pulsed lasers were combined and directed at the sample through a pair of galvanometer scanners and scanning optics. The fluorescence signal was collected in the direction orthogonal to the illumination axis, through appropriate spectral optical filters, and directed to a detection module that allowed imaging in either SPIM or SVIM mode. For SVIM mode, a micro-lens array was placed at the conventional image plane to capture the light field coming from the sample, which was subsequently recorded by the detection camera [50, 51]. Computer-controlled motorized stages were used to allow reproducible switching between SPIM and SVIM modes. To provide selective-volume illumination, the galvos controlling the illumination light were adjusted to paint out the desired illuminated volume multiple times within a single camera exposure. Image acquisition was through the software Micro-Manager [83] and custom software written in LabVIEW (National Instruments). See Fig. 4.17 and its caption for more detailed descriptions, and Table A2 in Appendix B for a list of key components of the microscopy setup. Supplementary Note 4.5.1 provides further discussion on the advantages and disadvantages of our volume-scanning implementation of SVIM.

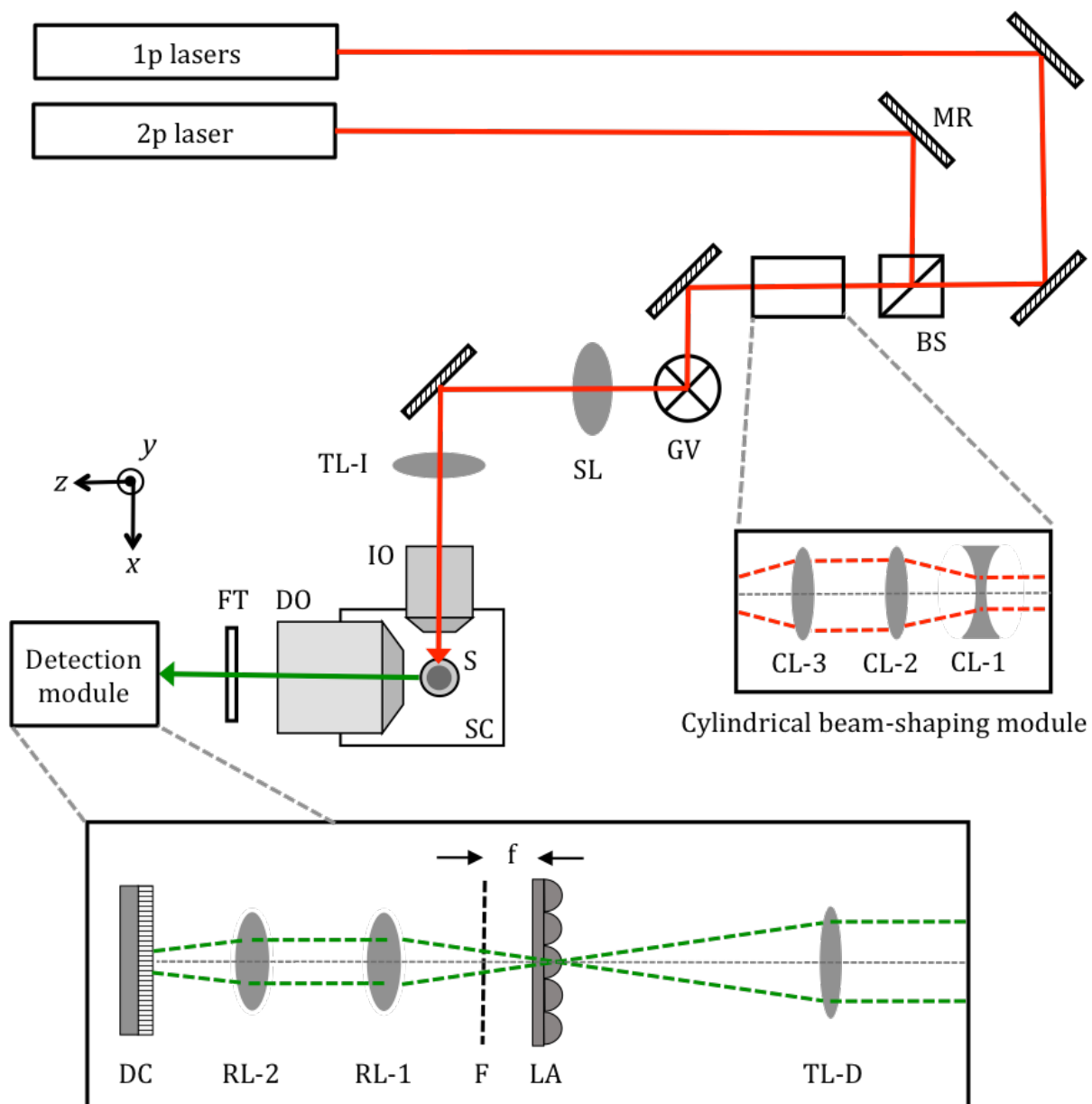


Figure 4.17: Continued on next page.

Figure 4.17: (Continued from previous page.) Schematic of the SVIM/SPIM optical setup, and description of operation procedure. Top-view of the optical setup, depicting only the key components. (See Table A2 for specific part numbers of the key components.) Laser beams, for 1P and 2P excitation, were directed by silver mirrors (MR) and combined into the same optical path by a polarizing beamsplitter (BS). The laser light was routed into a 2D scanning galvos module (GV), then through the scan lens (SL) and illumination tube lens (TL-I), and into the illumination objective (IO). Sample (S) was suspended from the top of the liquid-filled sample chamber (SC), and the detection objective (DO) collected the fluorescence light generated at the sample. The y direction of the experimental coordinate system is anti-parallel to gravity. The beam at GV was imaged to the back focal plane of IO by SL and TL-I, so adjusting the rotational positions of the galvos enabled translating the illumination beam at the sample in the y and z directions.

Fluorescence signal collected by the DO passed through the appropriate interference bandpass filters (FT) to block the laser light and select for the right detection colors. The fluorescence was recorded by a detection module that allowed imaging in either SVIM or SPIM mode. In SVIM mode, as depicted in the figure, detection tube lens (TL-D) formed the image of the sample at its focal plane, where the micro-lens array (LA) was placed. The desired light-field image was formed at focal plane F, at a distance f away from the LA (where $f =$ focal length of the micro-lens). A pair of identical photographic lenses (RL-1 and RL-2), configured in 4f mode, relayed the light-field image at F to be recorded at detection camera (DC). The optical parameters of the LA and the DO and TL-D, for the different imaging magnifications of $32\times$ and $20\times$ (see Table A3 in Appendix C), were chosen to ensure that the spatial-angular bandwidth of the light-field collected by the DO was matched to that of the LA [50, 51]. To operate in SPIM mode, LA was moved entirely out of the optical path, and the entire block of (RL-1, RL-2, and DC) was moved by distance f closer to the TL-D (along the $-z$ direction). Computer-controlled motorized translational stages (not shown) were used to allow convenient and reproducible switching between SVIM and SPIM modes.

Not shown was an imaging module looking at the sample from opposite to the IO, which allowed observation of the laser illuminated sample region in the yz plane. This imaging module was used to verify and calibrate the galvos scanning parameters to achieve the desired SVI. Also not shown was a separate beam path that directed the illumination laser light toward the sample along the $+z$ direction—this path was used for wide-field illumination of the sample.

Continued on next page.

Figure 4.17: (Continued from previous page.) For $32\times$ (& $20\times$) imaging with 1P excitation, the illumination beam size was adjusted to achieve an NA of ~ 0.04 (& 0.03), which following Gaussian-beam optics [75] yielded excitation depth of focus of $\sim 250\ \mu\text{m}$ (& $470\ \mu\text{m}$) and FWHM focused beam waist of $\sim 5\ \mu\text{m}$ (& $6\ \mu\text{m}$). For $20\times$ imaging with 2P excitation, the NA was ~ 0.04 , yielding excitation depth of focus of $\sim 500\ \mu\text{m}$ and FWHM focused beam waist of $\sim 6\ \mu\text{m}$.

During SPIM imaging, the illumination beam was scanned in the y direction, resulting in a scanned light sheet transecting the sample in the xy plane, and the sample was moved along z to achieve 3D imaging. During SVIM imaging with 2P excitation, the beam was scanned in both the y and z directions, with appropriate amplitudes, to paint out the desired selectively-illuminated volume at the sample (galvo line scan rate = 1 kHz along y , and galvo stepping along z). During SVIM imaging with 1P excitation, a removable cylindrical beam-shaping module was put in place, up-stream of the GV, where cylindrical lenses (CL-1) and (CL-2) expanded the beam along y -direction by $2\times$, and cylindrical lens (CL-3) focused the beam along the y -direction at the GV. This focusing resulted in a static illumination light sheet (in the xy plane) at the sample, and the beam only needed to be scanned along one direction, z , to enable painting out the desired selectively-illuminated volume (galvo line scan rate = 1.5 kHz). A custom-written LabView program, in conjunction with the software Micro-Manager [83], coordinated the galvos scanning and camera triggering to ensure that within one camera exposure the volume of interest was illuminated an integer number of times, or that it was illuminated > 10 times, to ensure that the excitation intensity was uniform to better than 10% from frame to frame. Alternative selective-volume illumination approaches are discussed in Supplementary Note 4.5.1.

4.4.2 Sample handling and imaging procedure

Zebrafish experiments: fish were raised and maintained as described in Ref. [115], in strict accordance with the recommendations in the Guide for the Care and Use of Laboratory Animals by University of Southern California, where the protocol was approved by the Institutional Animal Care and Use Committee (IACUC). All zebrafish lines used are available from ZIRC ([urlhttp://zebrafish.org](http://zebrafish.org)). Zebrafish embryos were collected from mating of appropriate adult fish (AB TL strain) and raised in egg water ($60 \mu\text{g L}^{-3}$ of stock salts in distilled water) at 28.5°C . At 20 hpf, 1-phenyl-2-thiourea (PTU) (30 mg L^{-1}) was added to the egg water to reduce pigmentation in the animals. For imaging experiments, the samples were embedded in a 1 mm-diameter cylinder of 1.5% low-melting agarose (Sea Plaque) for imaging in the SPIM/SVIM setup, as described in Ref. [77].

The imaging chamber was filled with 30% Danieau solution (1740 mM NaCl, 21 mM KCl, 12 mM MgSO $^4 \cdot 7\text{H}_2\text{O}$, 18 mM Ca(NO 3) 2 , 150 mM HEPES) at 28°C . Anesthetic was used (buffered Tricaine, 100 mg L^{-1}) during the mounting procedure and imaging, except for during neural functional imaging. For structural imaging of the cranial vasculature, 5-dpf *Tg(kdrl:eGFP)* larvae were used. At this age, zebrafish larvae have not undergone sex differentiation. For heart imaging, transgenic adults, *Tg(kdrl:eGFP)* and *Tg(gata1:dsRed)*, were crossed to produce offspring with fluorescent labels in both the blood cells (dsRed) and endocardium (eGFP). Samples, at 5 dpf, were selected for heterozygous expression in gata1:dsRed as this reduced the density of fluorescent blood cells. Two-color imaging of the blood cells and endocardium were carried out sequentially, at a rate of $90 \text{ volumes s}^{-1}$. For neural functional imaging, 5-dpf zebrafish larvae expressing the nuclear-localized pan-neuro fluorescent calcium indicators, *Tg(elavl3:H2B-GCaMP6s)*, were imaged at a rate of 1 volume s^{-1} . Each bout of neural activity imaging lasted 150 s, with a visual stimulus, provided by a 625 nm LED (Thorlabs), turned on at $t = 100 \text{ s}$.

Squid-bacteria experiments: squid samples were procured as previously described [132]. Briefly, adult squids were collected in Oahu, Hawaii, and then housed and allowed to reproduce at a facility at the University of Wisconsin, Madison. Hatchling squid were shipped overnight to our laboratory, maintained in artificial seawater (Instant Ocean), and used for experiments within 3 days of arrival. A solution of 2% ethanol/artificial seawater was used to anesthetize the squid during mounting and imaging. Under a stereo dissection microscope, the mantle of the squid was carefully cut open and trimmed to expose the light organ of the animal. Then the animal was embedded in a cylinder of agarose (2% low melt agarose, 2% ethanol, in artificial seawater) using a procedure similar to that used for zebrafish. The cylinder and plunger unit were fashioned from a FEP tube (inside diameter \sim 2 mm) and glass rod (outside diameter \sim 2 mm), respectively, to accommodate the size of the squid. To allow direct interaction between the light organ and the surrounding fluid environment, the small volume of solidified agarose encasing the light organ was carefully removed with forceps. The agarose-embedded squid was mounted into the imaging chamber (containing 60 mL of the ethanol/seawater solution), and GFP-expressing *V. fischeri* ES114 carrying pVSV102 Ref. [133] was added to reach a concentration of 50,000 cfu L⁻³. The squid and bacteria were monitored using SPIM for \sim 2 h before imaging of the bacterial flow fields with SVIM was carried out.

4.4.3 Light-field image processing and 3D reconstruction

Reconstruction of light-field images was carried out using the wave-optics procedure, described in Refs. [51, 53] and the software package made available by Ref. [53]. Briefly, the rectifying parameters of the acquired light-field images, describing the geometrical relationships between the micro-lens array and the detection optical train, were found using the software LFDisplay [50]. Theoretical point spread functions (PSF) were calculated using the optical parameters of the entire imaging path, and the desired spatial sampling and coverage of the 3D reconstruction [53]. Then, the rectifying parameters and the PSF were used as

inputs into the 3D wave-optics reconstruction program from [53] to reconstruct the acquired 2D light-field images into 3D images. Two key parameters for the PSF calculation and the resulting 3D reconstruction are the z -extent of the volume to be reconstructed and the desired z -sampling (i.e. thickness of individual z -slice). Larger z -extent and finer z -sampling requires more onboard memory for the graphical processing unit (GPU) used in the 3D reconstruction program. With the GPU used here (Titan X, Nvidia), the largest z -extent that we could reconstruct was $400\ \mu\text{m}$, at z -sampling of $2\ \mu\text{m}$. Consequently, for results shown in Figs. 4.3, 4.4, and 4.6, the datasets of both $550\text{-}\mu\text{m}$ SVIM and WF-LFM were reconstructed with z -extent of $400\ \mu\text{m}$; all others were reconstructed with z -extent equal to their actual experimental illumination extent.

We used the same micro-lens array (pitch = $150\ \mu\text{m}$, focal length = $3\ \text{mm}$) for two imaging conditions of (i) $32\times$ magnification, $0.8\ \text{NA}$, and (ii) $20\times$ magnification, $0.5\ \text{NA}$. With these parameters, and the reconstruction parameters listed in Table A3 in Appendix C, following [51] we expect the $32\times$ magnification reconstructions to have ~ 3 (& 6) μm resolution laterally (& axially), and the $20\times$ magnification reconstructions to have ~ 4 (& 12) μm laterally (& axially).

4.4.4 Image analysis and presentation

Raw images were background-subtracted to account for camera dark-counts, for both SPIM (done manually) and SVIM (done automatically in the software LFDISPLAY). All SPIM and SVIM images were scaled to fill the full 16-bit dynamic range. For visualization in the figures, unless otherwise noted, image pixel intensities were further scaled to minimum and maximum display contrast with 0.4% saturation. Unless otherwise noted, 3D images are presented as 2D averaged-intensity, instead of maximum-intensity, projections as this method provides a more accurate way to represent the background of 3D data in 2D format. Image processing and analysis in 2D were done in Fiji [134], while 3D rendering and analysis were done in Imaris (Bitplane).

Zebrafish vasculature: For zebrafish vasculature images (Figs. 4.3, 4.4, 4.5, and 4.6), the 3D datasets were displayed as an averaged projection in z , for the same volume section extending from $z = -48$ to $-12 \mu\text{m}$, where $z = 0 \mu\text{m}$ is the native focal plane of the detection objective. This volume excludes the native focal plane of the imaged z -stack, where grid-like artifacts from the light-field reconstruction are most prominent. The native focal plane was experimentally set at approximately $200 \mu\text{m}$ into the zebrafish head from its dorsal surface for the datasets shown in Figs. 4.3, 4.4, 4.5, and 4.6.

Bacteria-squid: For squid-bacterial results (Fig. 4.7a-c, Supplementary Fig. 4.18, and Movies 4.8, 4.9, and 4.10), tracking and quantification of the bacterial flow field were carried out using the automatic spot segmentation and tracking functions in Imaris, followed by manual correction.

Zebrafish heart-blood: For results describing the zebrafish beating heart (Fig. 4.7d-g, Fig. 4.13, and Movies 4.11 and 4.12), the sequentially acquired light-field time-series data of the endocardium and blood flow were reconstructed separately. The reconstructed 4D datasets, each spanning approximately 4 heart beats, were then synchronized in time by renumbering the endocardium frames such that the time point at which the atrium is most contracted in the endocardium movie matches the time point when, in the blood flow movie, the flow into the ventricle from the atrium momentarily stops. After synchronization, the two movies were overlaid to create a composite 2-color movie. Tracking and quantification of twelve representative blood cells' flow trajectories in the zebrafish heart were carried out manually in Imaris. We analyzed and presented the flow trajectories as they were directly derived from the manual tracking, to mainly demonstrate the benefits of SVIM. Follow-up work that aims to draw biological and biophysical insights from the imaged beating heart and blood flow should take into account the nonuniform resolution and image-artifacts inherent with LFM in general.

Zebrafish brain activity: For the zebrafish brain activity results (Figs. 4.14, 4.15, and 4.16), we used an analysis pipeline based on spot segmentation of the time-domain standard

deviation of the 3D time series data to find active neurons [135]. First, from the light-field reconstructed 3D time series data we calculated the standard-deviation-projection along the temporal axis. The resulting time-projected 3D dataset was a spatial map of where the signal intensity changed substantially during the imaged time window, due to neuronal activity. Spot segmentation was then carried out on the time-projected 3D dataset using Imaris to find active neurons, with the constraint that neuronal nuclei appeared as ellipsoids with diameter of 5 and 10 μm in the lateral and axial direction, respectively, following the expected resolution of the light field imaging and reconstruction. Once found, segmented neurons were used as spatial masks to extract the $\Delta F/F_0$ neural activity traces from the original reconstructed 3D time series data. Spontaneous activity time window was from $t = 1$ to 100 s (Figs. 4.14 and 4.15), while the visually evoked activity time window was from $t = 51$ to 150 s with the LED evoking light turned on at $t = 100$ s (Fig. 4.16). For the latter case, k-means clustering of the activity traces was used to group the active neurons, identifying a subgroup that exhibited clear responses to the evoking light. Analysis was carried out using a combination of Fiji, Imaris, and MATLAB (MathWorks).

4.4.5 Image contrast, simulated noise, and effective resolution

Contrast: To compare image contrast between SPIM, SVIM, and wide-field LFM, we measured the relative standard deviation of the pixel intensities from the respective images. The standard deviation σ of an image, which is the same quantity as root-mean-square (RMS) contrast that appears in vision science [136, 137], is given by

$$\sigma = \sqrt{\frac{1}{N-1} \sum_{i=1}^N (x_i - \bar{x})^2}, \quad (4.1)$$

in which x_i is a normalized intensity-level value, so that $0 \leq x_i \leq 65,535$, and \bar{x} is the average intensity of all pixel values N in the image:

$$\bar{x} = \frac{1}{N} \sum_{i=1}^N x_i. \quad (4.2)$$

Putting the expressions above together, we have

$$Contrast = \frac{\sigma}{\bar{x}}. \quad (4.3)$$

This measure of image contrast is independent of the total pixel count N , and thus provides a concise metric for direct comparison of contrast between SPIM, SVIM with various SVI extents, and wide-field LFM. For the vasculature results (Figs. 4.3b and 4.5f), we calculated the contrast for individual z -slices of the static 3D reconstructions to provide a z -depth-dependent comparison between different imaging modalities. To match the intrinsically lower axial resolution of SVIM and LFM ($\sim 12 \mu\text{m}$), a moving average over twelve successive z -planes was applied to calculate the SPIM contrast curve. For the beating heart results (Fig. 4.13c and f), the 4D reconstructions involved dynamic motion of the 3D samples, with substantial motion along the z direction; therefore, we opted to calculate the contrast for the averaged-intensity z -projections at individual time points along the beating cycle. Analysis was performed in MATLAB.

Simulated noise: To simulate the extraneous background signal that would be expected from larger illumination extents, raw light-field images were corrupted with Poisson noise [138]. Simulated images were created by scaling up the raw $100\text{-}\mu\text{m}$ SVIM light-field image so that λ , the mean photon number of a pixel, would be equal to higher values. The raw $300\text{-}\mu\text{m}$ SVIM light field image has $\lambda = 8,400$, and larger illumination extents produce larger λ . Poisson noise was then applied to these scaled images on a per-pixel basis. The background noise produced is thus spatially correlated with the original raw $100\text{-}\mu\text{m}$ SVIM light field

image, which is a more realistic approximation than noise created from a uniform background. The resulting simulated images were then reconstructed and compared (Fig. 4.5).

Effective resolution: To evaluate the effective resolution achieved with the various imaging modalities, we quantified the full-width-half-maximum (FWHM) diameter of the same blood vessels captured by each modality (Fig. 4.6, see its caption for full details). Briefly, starting in the SPIM 3D dataset, we selected a single z -slice that had four well-imaged blood vessels of approximately the same size. Matched z -slices in the SVIM and LFM datasets were found, and a MATLAB script generated line regions-of-interests across the selected blood vessels. Intensity line profiles were produced, normalized to a peak value of 1, from which the mean FWHM was calculated.

4.4.6 Data availability

Data underlying the plots in Figs. 4.3b and 4.14d-f are available as Excel files.

Zebrafish vasculature data: https://static-content.springer.com/esm/art%3A10.1038%2Fs42003-020-0787-6/MediaObjects/42003_2020_787_MOESM9_ESM.xlsx (13 KB).

Zebrafish brain activity data: https://static-content.springer.com/esm/art%3A10.1038%2Fs42003-020-0787-6/MediaObjects/42003_2020_787_MOESM10_ESM.xlsx (1.7 MB).

All other relevant data are available from the authors upon request.

4.4.7 Code availability

All relevant custom-written LabVIEW and MATLAB scripts/codes are available from the authors upon request.

4.5 Supplementary Information

4.5.1 Discussion on implementations of selective-volume illumination

selective-volume illumination was implemented in our work by employing galvo-based beam scanning, to paint out the desired volume with Gaussian-focused laser light multiple times over the exposure time of each captured image (Methods Section 4.4.1, Fig. 4.17). For 1P excitation, a cylindrical beam-shaping module was used to create a static 2D “sheet” of light at the sample, and the light sheet needs only to be scanned in one direction to cover the volume of interest. For 2P excitation, to achieve optimal signal rate, we used a spherically-focused beam to excite the sample [75], and scanned the beam in 2D (y & z directions, in the lab reference frame depicted in Fig. 4.17), to achieve 3D volume coverage. In both implementations, the illumination focusing-NA was adjusted to be relatively low ($\sim 0.03 - 0.04$) to achieve axially-extended focus (depth of focus $\sim 500 - 250 \mu\text{m}$), so that volume coverage along the axial direction (x , in the lab reference frame) was “automatic”, i.e., without needing to scan the beam along that direction.

The main advantage of the galvo-based volume-scanning approach is the spatial precision with which we can achieve in defining the volume of interest. Just as the spatial precision of a painting is approximately given by the size of the brush, the scanned selectively-illuminated volume can be controlled to within the size of the focused illumination beam ($\sim 5 \mu\text{m}$ in our case), thus providing the necessary precision for our work in quantifying the difference in the images obtained with different selectively-illuminated volume extents.

An alternative to the volume-scanning approach is to illuminate the sample with a beam having a larger cross-sectional area, as large as to completely fill the volume of interest without the need to scan the illumination beam (while still minimizing illumination of the extraneous sample volume, to maintain the benefits of SVIM). This approach, implemented in a recent work [126], does give up the spatial precision with which one can achieve the

selectively-illuminated volume, as a larger “brush” is used to fill in the volume of interest. A large beam, with a cross-sectional diameter of $\sim 100\text{-}\mu\text{m}$ or more, in either a focused or collimated state, would necessarily have their boundaries less sharp than a focused beam with diameter of $5\text{-}\mu\text{m}$ as used in our case. Practically, such beams of diameter $\sim 100\text{-}\mu\text{m}$ or more would have their blurred boundaries extending over several tens of microns or more. While we deem this precision is not enough for our work presented here, we envision that for many biological imaging applications, the precision of \sim several tens of microns is adequate, and thus the volume-filling strategy to implement SVIM could be used in such scenarios.

The volume-scanning approach to implement SVIM has several disadvantages. First is its relative complexity and cost, due to the need for the galvo scanners and associated electronics and software to control the scanning. Second, the scanning could in principle restrict the volumetric imaging rate of the setup: the highest imaging rate would be limited to the fastest time needed to paint out the volume once. We consider this last issue with some back-of-envelope calculations below.

For the relatively small scanning angles of $< 2\text{-}3$ degrees employed in our SVIM setup, the galvo could reach a maximal line-scanning rate of 1.5 kHz, or line-scanning period of 0.67 ms. Thus, for the 1D scanning employed with 1P excitation, the entire volume, with a depth up to 1 mm, could be painted out within 0.67 ms, yielding ~ 1500 volumes/s as the fastest possible volumetric imaging rate. This rate is over one order of magnitude higher than the full-frame imaging rate of current state-of-the-art sCMOS cameras, which typically top out at 100 frames/s. For the 2D scanning employed with 2P excitation, a volume of depth $\sim 300\text{ }\mu\text{m}$ could be painted out with ~ 100 lines (with a nominal cross-sectional diameter of $6\text{ }\mu\text{m}$), thus achieving a single-volume scanning time of 67 ms, which is equivalent to ~ 15 volumes/s as the fastest volumetric imaging rate. If the galvo in our setup is replaced with a resonant scanner, which can scan ~ 10 times faster, the maximum volumetric rate could be as high as 150 volumes/s. Thus, we see that quite high imaging rates are still possible with the volume-scanning approach: 100 volumes/s for 1P (limited by camera speed), and

15-100 volumes/s for 2P excitation. Furthermore, higher imaging rates with lower exposure times require higher optical excitation intensities to maintain useful signal-to-noise ratios. However, concerns about photo-damage to the biological samples would often place a hard restriction on the light intensity that can be used. This is a particular concern with 2P excitation, given the substantially lower excitation cross-section for 2P absorption. Thus, in practice, the useful volumetric imaging rate of SVIM is restricted more by the threshold of photo-damage than by the constraints of the volume-scanning strategy.

4.5.2 Volumetric imaging rate normalized by the number of diffraction-limited voxels

In the comparison of the volumetric imaging rate of SVIM, and LFM in general, with SPIM, it is instructive to also consider the imaging rate normalized by the number of diffraction-limited voxels, due to the large difference in resolution of SVIM and SPIM. This exercise will provide insights into the trade-offs involved between high-resolution and high-speed imaging.

The diffraction-limited (DL) voxel is defined as the smallest useful rectangular volume unit that is captured, extending in each of the spatial directions by an amount, following Nyquist criterion, equal to half of the spatial resolution achieved along that direction. The spatial resolution is determined by either the optical resolution of the combined imaging and reconstruction pipeline, or the experimental spatial sampling during imaging (i.e., the lateral pixel size and μ slice thickness), whichever that is larger.

For concreteness, we calculated the normalized volumetric imaging rate for several representative imaging scenarios and present the results in Supplementary Table 4.1 (refer to Table A3 in Appendix C for the corresponding imaging and reconstruction parameters). For SPIM imaging of the vasculature (Fig. 4.3a), the expected optical resolution for detection $NA = 0.5$ is $\sim 0.51 \mu\text{m}$ laterally and $\sim 4.4 \mu\text{m}$ axially while the spatial sampling is lateral pixel = $0.325 \mu\text{m}$ and μ slice thickness = $1 \mu\text{m}$. Thus we arrived at the lateral extent =

$0.325\text{ }\mu\text{m}$ and axial extent = $2.2\text{ }\mu\text{m}$ for the DL voxel. (For the SPIM optical resolution calculation, we used the formulas: lateral resolution = $\lambda/(2\text{NA})$, axial resolution = $2\lambda/(\text{NA}^2)$, with $\lambda = 0.55\text{ }\mu\text{m}$.) For the SVIM/LFM imaging cases, following [51] and the experimental optical parameters, we estimated the resolution to be $4\text{ }\mu\text{m}$ laterally and $12\text{ }\mu\text{m}$ axially for the SVIM/LFM vasculature reconstruction (Fig. 4.3a), and $3\text{ }\mu\text{m}$ laterally and $6\text{ }\mu\text{m}$ axially for the SVIM heart-blood reconstruction (Fig. 4.7d). The latter case was experimentally confirmed (Fig. 4.2). For all SVIM/LFM cases, the DL voxel sizes were determined by the optical resolution, as they were larger than the spatial sampling (see Table A3).

From the sizes of the DL voxels, we straightforwardly calculated the DL-voxel-normalized volumetric imaging rate for the different imaging scenarios, shown in Supplementary Table 4.1. In our work, we did not push the experimental conditions to achieve the fastest possible imaging rate, for either SPIM or SVIM/LFM. However, the imaging rates shown in the table below could still be usefully compared to each other as “typical” performances, and more importantly to demonstrate the parameters and relationships that are involved in determining the normalized volume rate. The vasculature results shown for SPIM, $300\text{-}\mu\text{m}$ SVIM, and wide-field LFM cases (labeled as A, B, C in the table) were from imaging the same sample, so they can be directly compared with each other. The heart-blood SVIM result (labeled as D in the table) represents a scenario where SVIM enabled a high volumetric imaging rate, normalized by the number of DL voxels or not, that was not reachable with conventional SPIM, as discussed in the main text.

From the results shown in Supplementary Table 4.1, we can make a few observations concerning the trade-offs involved in choosing between high-resolution or high-speed imaging. First, the 3-orders of magnitude higher volume rate of SVIM/LFM compared to SPIM gets reduced to a factor of ~ 4 after the rates are normalized by the number of DL voxels captured (comparing A and B in the table). This is not surprising, since the higher resolution achieved with SPIM means that many more DL voxels are captured with SPIM than with SVIM/LFM. Thus, we see that SVIM/LFM achieves high imaging rate by trading away

resolution, capturing a reduced number of DL voxels while still covering the same sample volume. However, the speed advantage of SVIM/LFM does not come entirely from capturing a reduced number of DL voxels. It also comes from the fact that the entire volume is imaged in a single snapshot, eliminating the overhead time needed in SPIM to go from one imaged z -plane to the next (see note *(f)* of Table A3 in Appendix C). Thus, the larger the z -extent of the volume of interest, the better performance SVIM/LFM will have in terms of the normalized volumetric imaging rate (comparing A, B, and C in the table). This speed benefit of thicker- z extents of SVIM/LFM of course comes with a cost, namely larger z extents will have lower image contrast and effective resolution, depending on the sample properties, as we have shown in our work here.

Table 4.1: Volumetric imaging rate normalized by the number of diffraction-limited voxels. DL: diffraction-limited.

		A	B	C	D
		Vasculature			
	(Units)	SPIM (Fig. 4.3c)	300- μm SVIM (Fig. 4.3c)	Wide-field LFM (Fig. 4.3c)	SVIM (Fig. 4.7d)
Captured image plane	$\mu\text{m} \times \mu\text{m}$	300×600	300×600	300×600	200×400
Captured image depth	μm	300	300	400	150
Lateral extent of DL voxel	μm	0.325	2	2	1.5
Axial extent of DL voxel	μm	2.2	6	6	3
Number of captured DL pixels/plane		1.7×10^6	4.5×10^4	4.5×10^4	3.6×10^4
Number of captured DL z -planes		136	50	67	50
Number of captured DL voxels		2.3×10^8	2.2×10^6	3.0×10^6	1.8×10^6
Volume rate (*)	Volumes/s	0.023	10	10	90
Volume rate (normalized)	DL voxels/s	5.3×10^6	2.2×10^7	3.0×10^7	1.6×10^8

See Supplementary Note 4.5.2 for details. (*) Volume rate values are duplicated from Table A3 in Appendix C.

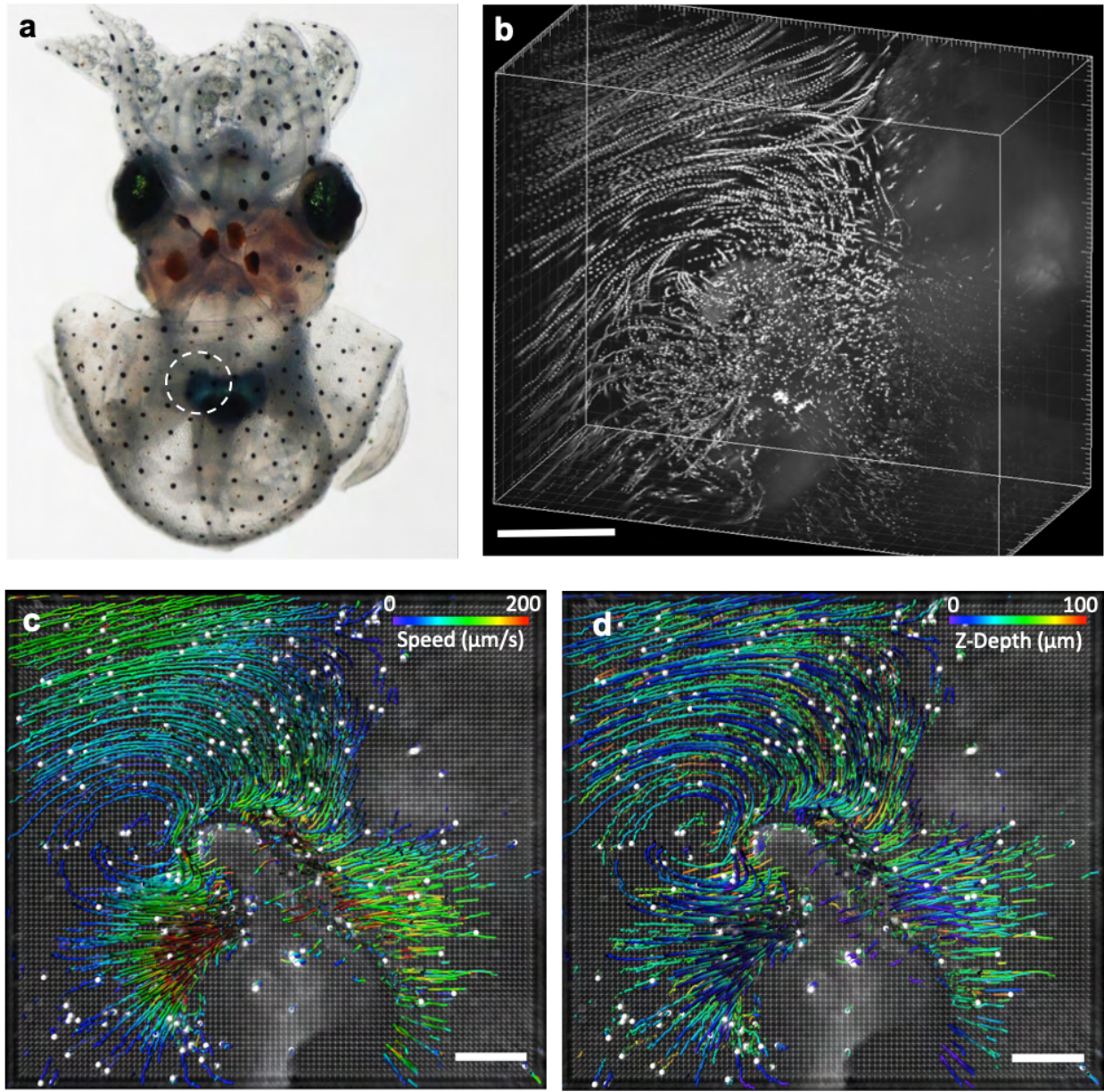


Figure 4.18: SVIM enabled single-bacterium-resolution imaging and quantification of 3D bacterial flow tracks around the squid light organ. (a) Photograph of a representative juvenile Hawaiian bobtail squid, *Euprymna scolopes*, with inset showing the light organ area, which will be selectively colonized by the bacteria *Vibrio fischeri* as part of the symbiosis between the two organisms. (b) 3D-rendered, maximum-intensity projection view of a 200- μm z -stack taken with SPIM, over the approximately same region of interest as captured with light-field imaging. SPIM imaging speed was at 6 z -slices/s or 0.035 volumes/s. SVIM allowed synchronous volumetric imaging speed of 20 volumes/s to capture more accurately the 3D flow field across the z -depth (c) (duplicated here from Fig. 4.7c), and enabling quantification of the speed of individual bacterium flow tracks (d). See Table A3 in Appendix C for full imaging and reconstruction parameters. Scale bar, 100 μm .

4.6 Acknowledgements

We thank E.G. Ruby (University of Hawaii-Manoa) for critical assistance and sharing of resources for the squid–bacteria experiments; Misha Ahrens (Janelia) for sharing of zebrafish lines; and Le Trinh for advice and support on zebrafish husbandry. Funding was provided for by the Gordon and Betty Moore Foundation grant #3396 (Ruby, McFall-Ngai and Fraser); National Institute of Health, grant #1R01MH107238-01 (Arnold, Kesselman, Fraser), grant #R37AI150661 (McFall-Ngai and Ruby), grant #R01OD11024 (Ruby and McFall-Ngai); National Science Foundation, grant #1650406 (Dickman, Fraser, Truong), and grant #1608744 (Kanso, Fraser). S.M. was supported by the USC Provost Fellowship; and K.K.D. by the Alfred E. Mann Doctoral Fellowship.

4.7 Manuscript information

4.7.1 Previously published as

A previous version of this chapter appeared in [52]:

Truong, T. V., Holland, D. B., Madaan, S., Andreev, A., Keomanee-Dizon, K., Troll, J., *et al.* High-contrast, synchronous volumetric imaging with selective volume illumination microscopy. *Communications Biology* **3**, 74 (2020)

DOI: <https://doi.org/10.1038/s42003-020-0787-6>

4.7.2 Author contributions

The authors for this work were: Thai V. Truong, Daniel B. Holland, Sara Madaan, Andrey Andreev, Kevin Keomanee-Dizon, Josh V. Troll, Daniel E. S. Koo, Margaret J. McFall-Ngai, and Scott E. Fraser.

T.V.T. conceived the idea, with further refinement from S.M., D.B.H., and S.E.F. T.V.T., D.B.H., S.M., A.A., J.V.T., M.J.M.N., and S.E.F. designed the experiments. T.V.T., S.M.,

D.B.H., and A.A. designed the microscopy setup. T.V.T. built the setup. T.V.T., D.B.H., S.M., A.A., and J.V.T. collected the data. S.M., D.B.H., D.E.S.K., A.A., and T.V.T. set up the light-field reconstruction pipeline. K.K.D. performed 3D reconstruction of the zebrafish brain activity, underlying Figs. 4.14, 4.15, and 4.16.

D.B.H., K.K.D., S.M., A.A., J.V.T., and T.V.T. analyzed the data and produced the figures; K.K.D., T.V.T. and D.B.H. developed the image contrast and resolution metrics (described in Methods Section 4.4.5), which were used to produce Figs. 4.3b, 4.4, 4.5f, 4.6, and 4.13c and f. K.K.D. performed the simulations of Poisson noise in Fig. 4.5.

T.V.T., K.K.D., and S.E.F. wrote the manuscript, with inputs from all authors. T.V.T. and S.E.F. supervised the work. T.V.T., D.B.H., and S.M. contributed equally. A.A. and K.K.D. contributed equally. This work lays the foundation for Chapter 5.

5

Single-objective selective-volume illumination
microscopy enables high-contrast light-field
imaging

5.1 Introduction

Biological processes often depend on the tight spatiotemporal coordination between cells across tissue-level length scales, extending over hundreds of microns in three-dimensions (3D). Functional understanding of such processes would be greatly aided by imaging tools

that offer the combined speed and sensitivity needed to observe 3D cellular dynamics without compromising the normal biology [104, 139]. Light-field microscopy (LFM) is a fast, synchronous 3D imaging technique [50, 51, 53]. Unlike existing volumetric imaging methods that reconstruct a 3D image from intensity information collected one voxel, one line, or one plane at a time, LFM captures both the 2D spatial and 2D angular information of light emitted from the sample (Fig. 5.1A, permitting computational reconstruction of the signal from a full volume in just one snapshot. Because lateral spatial resolution must be compromised to capture the angular distribution of the emitting light to yield the extended depth coverage, LFM sacrifices some resolution for its dramatically increased acquisition speed, achieving \sim 2 orders of magnitude improvement compared to existing volumetric imaging methods [50–53, 126, 140]. While 3D deconvolution can be used to enhance LFM performance [51, 53], out-of-volume fluorescence background, coming from parts of the sample outside of the volume of interest, limits signal detection, image contrast and resolution. Conventional wide-field illumination excites significant out-of-volume background (Fig. 5.1B), especially for volumes within thick or densely fluorescent samples, precluding LFM’s full potential in intact tissues.

Inspired by light-sheet microscopy, a.k.a. selective-plane illumination microscopy (SPIM), we recently introduced an improved light-field-based imaging approach, selective-volume illumination microscopy (SVIM), where confining excitation preferentially to the volume of interest reduces extraneous out-of-volume background, thereby sharpening image contrast, reducing unwanted photodamage, and improving the *effective* resolution in thick specimens (hundreds of microns or more) [52, 140]. SVIM was implemented with two objective lenses: one to selectively illuminate the volume of interest, and a second objective, orthogonally aligned, to acquire the fluorescent light-field (Fig. 5.1C). This two-objective geometry requires the sample to be mounted within the mutual intersecting volume defined by the perpendicular objectives, complicating sample mounting and limiting sample size. Here,

we implement SVIM in a single-objective geometry, eliminating the need for two orthogonally oriented objectives, greatly simplifying sample mounting and broadening its utility for biological research.

5.2 Axial single-objective selective-volume illumination microscopy

This new technique, termed axial single-objective SVIM (ASO-SVIM), selectively illuminates the sample volume through the same objective used for high-numerical-aperture (NA) detection (Section 5.5 and Fig. 5.12). The volume of interest is preferentially excited by either one-photon or two-photon processes (1P- or 2P-ASO-SVIM). 1P-ASO-SVIM is accomplished by using a 2D light-sheet oriented obliquely to the axial axis (26.5° ; Fig. 5.1D], created via a cylindrical lens with an effective NA of ~ 0.04 to 0.06 , yielding a Gaussian-beam waist of ~ 4 to $6 \mu\text{m}$ and ~ 150 to $230 \mu\text{m}$ confocal parameter; the sample is illuminated by sweeping this oblique sheet in 1D to excite fluorescence within the desired region of interest, multiple times within a single camera exposure. 2P-ASO-SVIM is accomplished using a low-NA (~ 0.055 to 0.08) focused Gaussian beam that is parallel to the axial axis (Fig. 5.1D), for opto-mechanical simplicity. Two-photon excitation defines the volume of interest axially (~ 150 to $230 \mu\text{m}$), owing to the quadratic dependence of the fluorescence signal on the excitation intensity [52, 75]; the beam is raster-scanned in 2D to excite the desired 3D sample volume. To capture fluorescence light-fields emitted from the excited volume, a lenslet array is placed at the native image plan [51]; the foci of the lenslets are imaged onto a camera sensor (Fig. 5.1A). To enable direct, quantitative comparison of our technique to more established methods, our microscope is designed to offer seamless switching to SPIM or wide-field LFM modes (Section 5.5, and Figs. 5.12 and 5.13).

We benchmarked ASO-SVIM performance by measuring the point-spread function (PSF) with 175-nm fluorescent beads suspended in agarose (Section 5.5.6). After 3D deconvolution

[51, 53], we obtained volumetric images with the expected maximum resolution, consistent with the optical design: $2.4 \pm 0.3 \mu\text{m}$ lateral full-width at half-maximum (FWHM); $5.7 \pm 0.2 \mu\text{m}$ axial FWHM (Fig. 5.2C). Due to diffraction and non-uniform sampling of the light-field volume [51, 53], the 3D resolution was depth-dependent (varying up to $\sim 46\%$ over a z range of -50 to 50 μm) (Fig. 5.2B), and reconstructions contained grid-like artifacts near the native focal plane, as previously reported [51]. To reduce such artifacts in the reconstructions presented here, we applied a low-pass filter in Fourier space (k -space), truncating spurious spatial frequencies beyond the resolution limit of the native focal plane (see Section 5.6 and Figs. 5.14 and 5.15). The simple process of k -space filtering across the nominal focus damped the artifacts and improved visualization of the 3D reconstructions, without any major loss of 3D resolution or spatial information (Figs. 5.15 and 5.16).

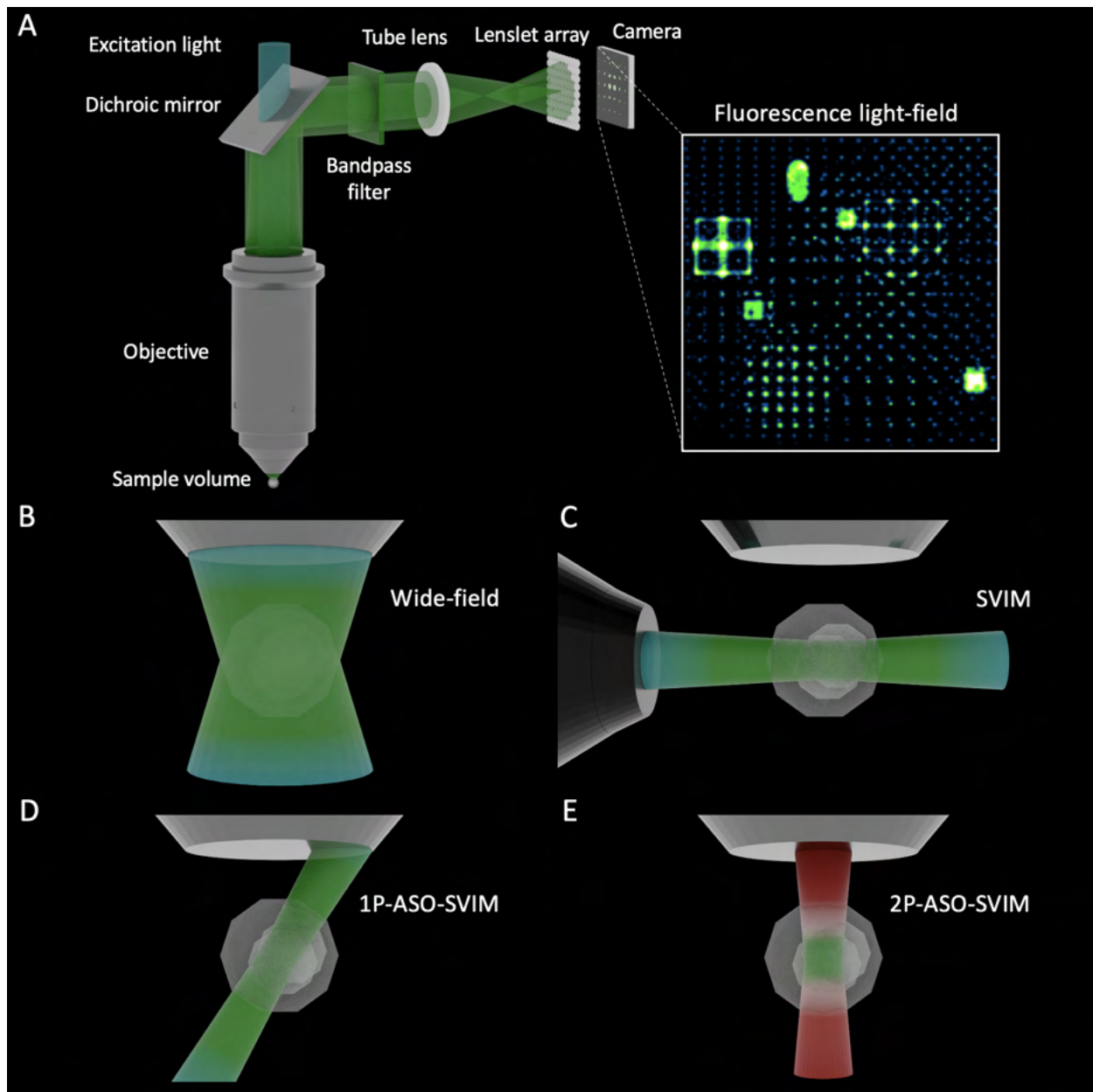


Figure 5.1: Continued on next page.

Figure 5.1: (Continued from previous page.) Axial single-objective selective-volume illumination (ASO-SVIM).

(A) Simplified schematic of light-field microscopy (LFM). Fluorescence light is collected from the sample volume by an objective lens, separated and filtered from the excitation light by the appropriate dichroic mirror and bandpass filter, and focused by a tube lens at an intermediate image plane where a lenslet array is positioned. The lenslet array refocuses the light onto a camera, so that each position in the 3D sample volume is mapped onto the camera as a unique light intensity pattern. The fluorescence light-field illustrated was captured with point-sources located at, above, and below the native focal plane. Such light-fields can be reconstructed to full volumes by solving the inverse problem [51].

(B) LFM with conventional wide-field illumination is compatible with standard forms of sample preparation but excites regions outside of the volume of interest (VOI).

(C) SVIM selectively illuminates the VOI using orthogonal illumination and detection objectives. Shown previously [52, 126, 140], SVIM reduces background fluorescence outside the VOI, increasing image resolution and contrast.

(D) and **(E)** ASO-SVIM preferentially excites the VOI and collects the fluorescence using a single objective lens, providing flexibility in sample mounting similar to traditional microscopy.

(D) 1P-ASO-SVIM uses an oblique light sheet (tilted 26.5° relative to the optical axis), that is scanned in 1D, to define the excitation volume.

(E) 2P-ASO-SVIM uses nonlinear excitation of a pulsed near-infrared (NIR) beam that is raster-scanned to define the VOI.

In each figure, 1P excitation is depicted in cyan (**A-D**) and 2P excitation in red (**E**); fluorescence emission is depicted in green.

See also Section 5.5, and Figs. 5.12 and 5.13.

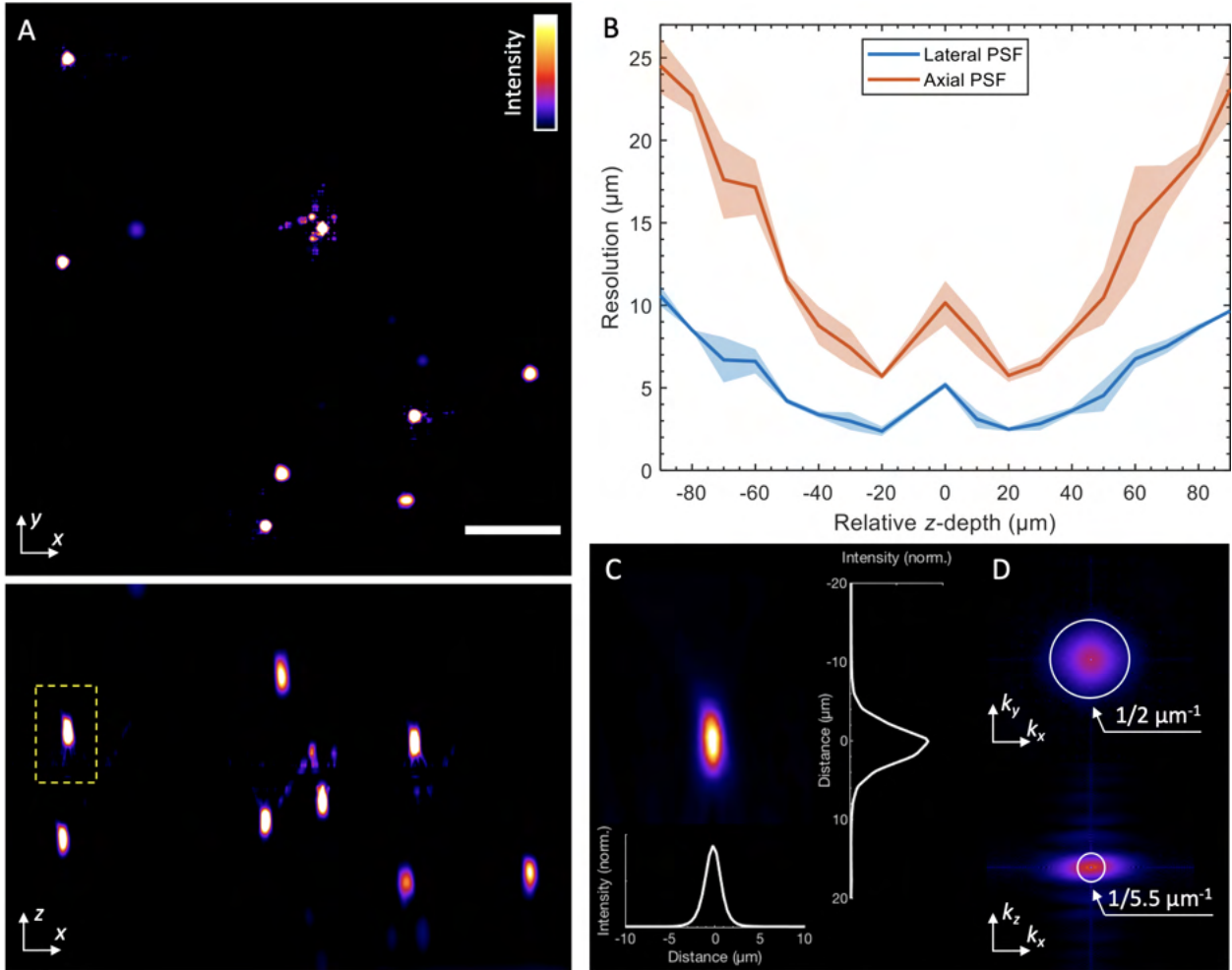


Figure 5.2: System resolution.

(A) x - y (top) and x - z (bottom) maximum-intensity projections (MIPs) of a 300- by 300- by 200- μm field of beads in agarose. Scale bar, 50 μm .

(B) Lateral (x - y) and axial (x - z) PSF measurements across the imaging volume, where $z = 0$ is the native focus ($N = 53$ FWHM bead images at different depths). Means (center lines) and standard deviations (shadings) are shown.

(C) Enlarged view of the x - z MIP of an exemplary bead from the image volume, denoted by dashed yellow rectangle (in A, bottom). Line profiles of the lateral (bottom) and axial (right) intensities through the center of the bead. Note that MIPs are contrast adjusted (0.4% of the pixels are saturated), separately for (C) and (A), so the image of the selected (dashed rectangle) bead may appear different.

(D) Same bead presented as lateral (top) and axial views of the optical transfer functions with resolution bands (white circles).

5.3 Results

5.3.1 ASO-SVIM improves image contrast and effective resolution *in vivo*

We compared ASO-SVIM with wide-field LFM in imaging the fluorescently-labeled vasculature of the same live larval zebrafish (Fig. 5.3). In the comparison, ground-truth images were provided by SPIM, which was recorded as a multi-plane z -stack and deconvolved, thus producing the best image quality at the cost of being slower than the light-field modalities, where the 3D volume was recorded in one snapshot (Section 5.5.4). ASO-SVIM, using either 1P or 2P excitation, came closer to SPIM than wide-field LFM, producing images with reduced out-of-volume background and higher contrast, (Fig. 5.3A), consistent with results we previously reported for SVIM [52, 140]. This is clearly revealed in an x - z slice through the 3D volume (Fig. 5.3A, bottom).

To obtain quantitative measures of the enhanced performance of 1P-ASO-SVIM and 2P-ASO-SVIM, we calculated the image contrast (defined as the standard deviation of the pixel intensities normalized to the mean intensity) for each x - y image plane (Fig. 5.3B): 1P-ASO-SVIM showed a modest improvement; 2P-ASO-SVIM showed more dramatic improvement over wide-field LFM. Intensity profiles of LFM images (along the dashed yellow line in Fig. 5.3A, bottom) documented the improved performance of ASO-SVIM (Fig. 5.3C), as did Fourier transforms of the images (Fig. 5.3D and E). Thus, the reduction in background fluorescence substantially boosts image contrast as well as effective spatial resolution, both laterally and axially (Figs. 5.3D and E, and 5.4). The enhanced contrast and effective resolution of the ASO-SVIM modalities are further demonstrated by comparing recorded images of single blood vessels, as well as measurements of the width of these vessels from the line profiles (Figs. 5.3F and G, and 5.5).

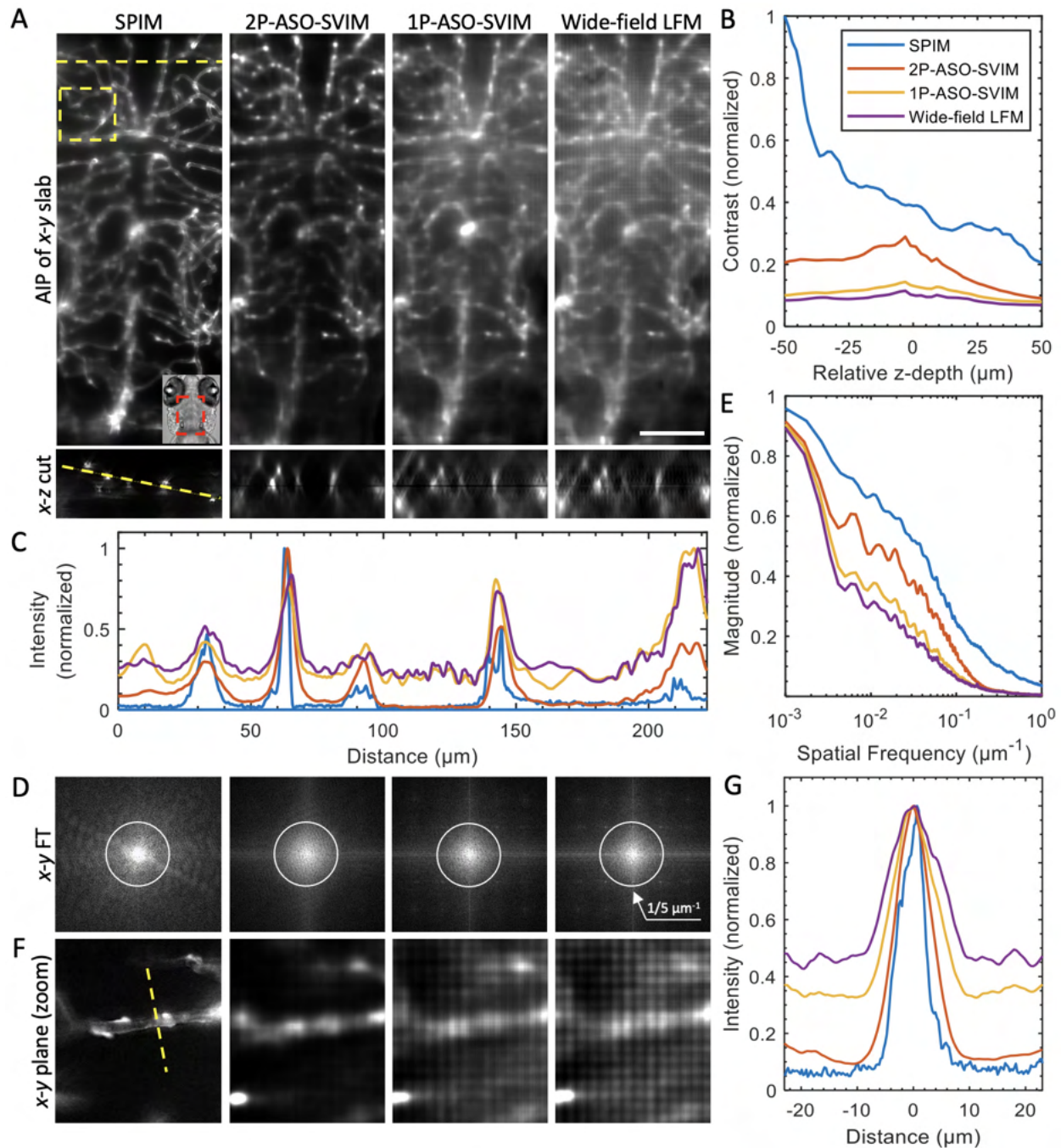


Figure 5.3: Continued on next page.

Figure 5.3: (Continued from previous page.) ASO-SVIM improves contrast and effective resolution in live imaging of zebrafish larvae.

(A, Top) Average-intensity projections (AIPs) of a 100- μm -thick 3D image stack from the same transgenic (*Tg(kdrl:GFP)*) 5-day post fertilization (dpf) zebrafish, where the vasculature was fluorescently labeled with green fluorescent protein (GFP), captured by different imaging modalities. (Inset) Transmitted light image of the zebrafish head, where the dashed red rectangle marks the $230 \mu\text{m} \times 600 \mu\text{m} \times 100 \mu\text{m}$ volume imaged. (Bottom) Cross-sectional (x - z) views at the location indicated by the dashed yellow line (top left, SPIM panel). The SPIM volume consisted of 67 optical sections (exposure time: 355 ms; excitation power at sample: 0.15 mW), collected serially over ~ 44 s; the LFM-based volumes were reconstructed from a single image with an exposure of 355 ms (excitation power, 2P-ASO-SVIM: 525 mW; 1P-ASO-SVIM: 1.5 mW; wide-field LFM: 4 mW). Scale bar, 100 μm .

(B) Quantification of image contrast versus z -depth, showing improvements of 1P-ASO-SVIM and 2P-ASO-SVIM over wide-field LFM. Image contrast, measured as the standard deviation of the pixel intensities divided by the mean intensity, is plotted for each x - y slice, normalized by the value of the deconvolved SPIM (blue trace) at $z = -50 \mu\text{m}$.

(C) Intensity profiles along the same line for all four modalities (dashed yellow line shown on the x - z cut in **A**, bottom, SPIM). The fluorescence intensities of ASO-SVIM better agree with the ground truth SPIM data than does wide-field LFM.

(D) Fourier transforms (FTs) of x - y MIPs through the 100- μm -thick slabs in **(A)**. Resolution bands (white circles) help show the increased spatial frequency content of ASO-SVIM compared to wide-field LFM, where more signal intensity at larger radial position designates higher resolution captured.

((E)) Average amplitudes along k_y direction of the FTs shown in **(D)**, showing that ASO-SVIM frequency spectra fall slower to the experimental noise floor, indicating better effective resolution than wide-field LFM. See also Fig. 5.4.

(F) Enlarged x - y slices to highlight single blood vessels, centered at $\sim 86 \mu\text{m}$ into the specimen, from the subregion indicated by dashed yellow box in **(A, top left)**.

(G) Intensity profiles, averaged from the dashed yellow line shown in **(F)** and from 2 other similar vessel structures (Fig. 5.5), demonstrate the improvements in effective resolution of ASO-SVIM over wide-field LFM, in measuring the width of blood vessels.

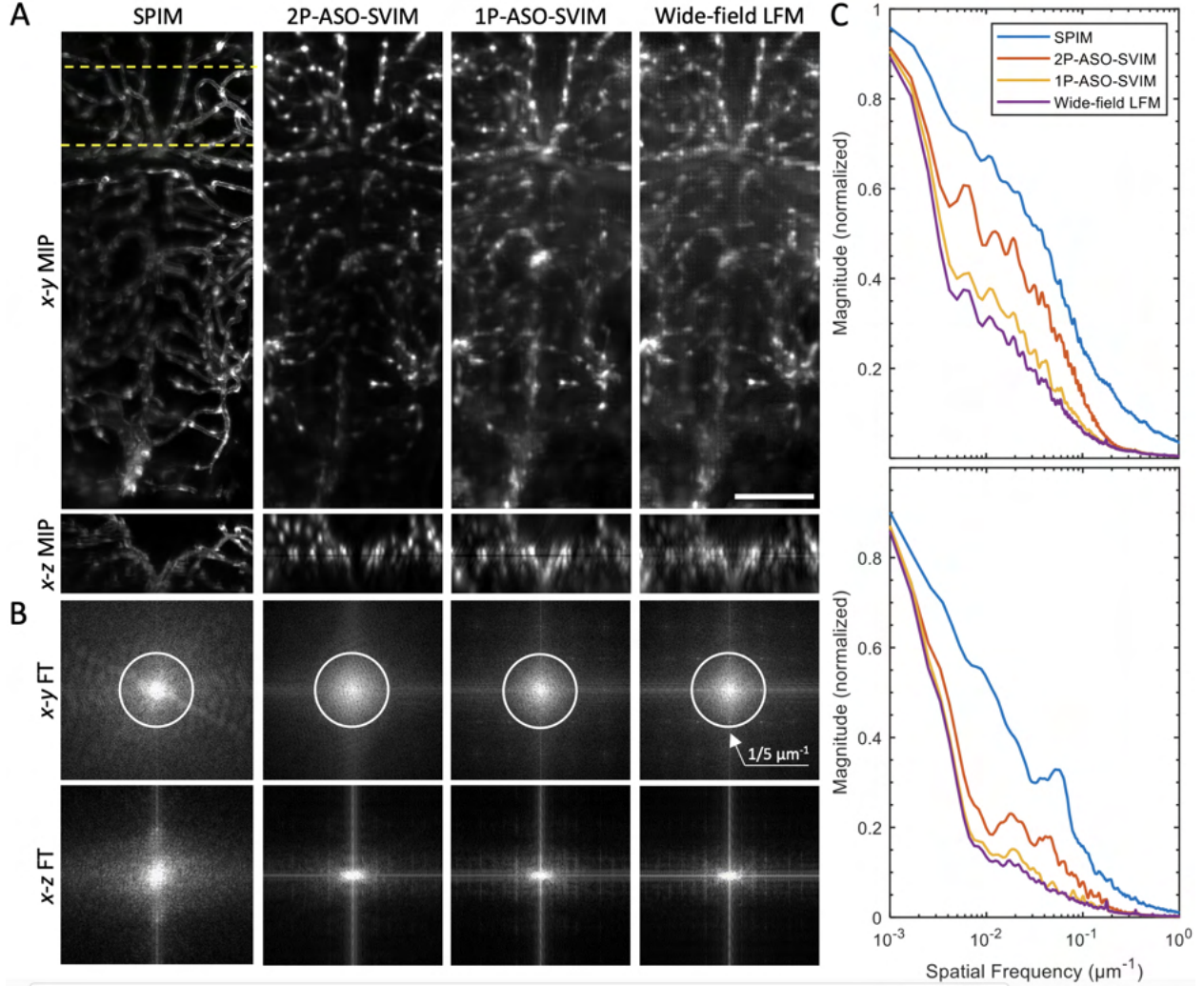


Figure 5.4: ASO-SVIM enhances effective resolution across large tissue volumes.

(A) x - y (top row) and x - z (bottom row) MIPs of a $100\text{-}\mu\text{m}$ thick slab (same dataset as Fig. 5.3), highlighting maximum attenuation for each modality shown. Scale bar, $100\text{ }\mu\text{m}$.

(B) Fourier transforms (FTs) of the MIPs in (A). Resolution bands (white circles) indicate increased spatial frequency content with ASO-SVIM compared to wide-field illumination, due to decreased out-of-volume background by selective excitation.

(C) Average amplitudes along the k_y (top) and k_z direction (bottom) of FTs in (B), respectively. Frequency spectra demonstrate the slower spatial frequency roll-off for ASO-SVIM, both laterally and axially, and hence improved effective 3D resolution over the conventional wide-field technique. See also Figs. 5.3 and 5.5.

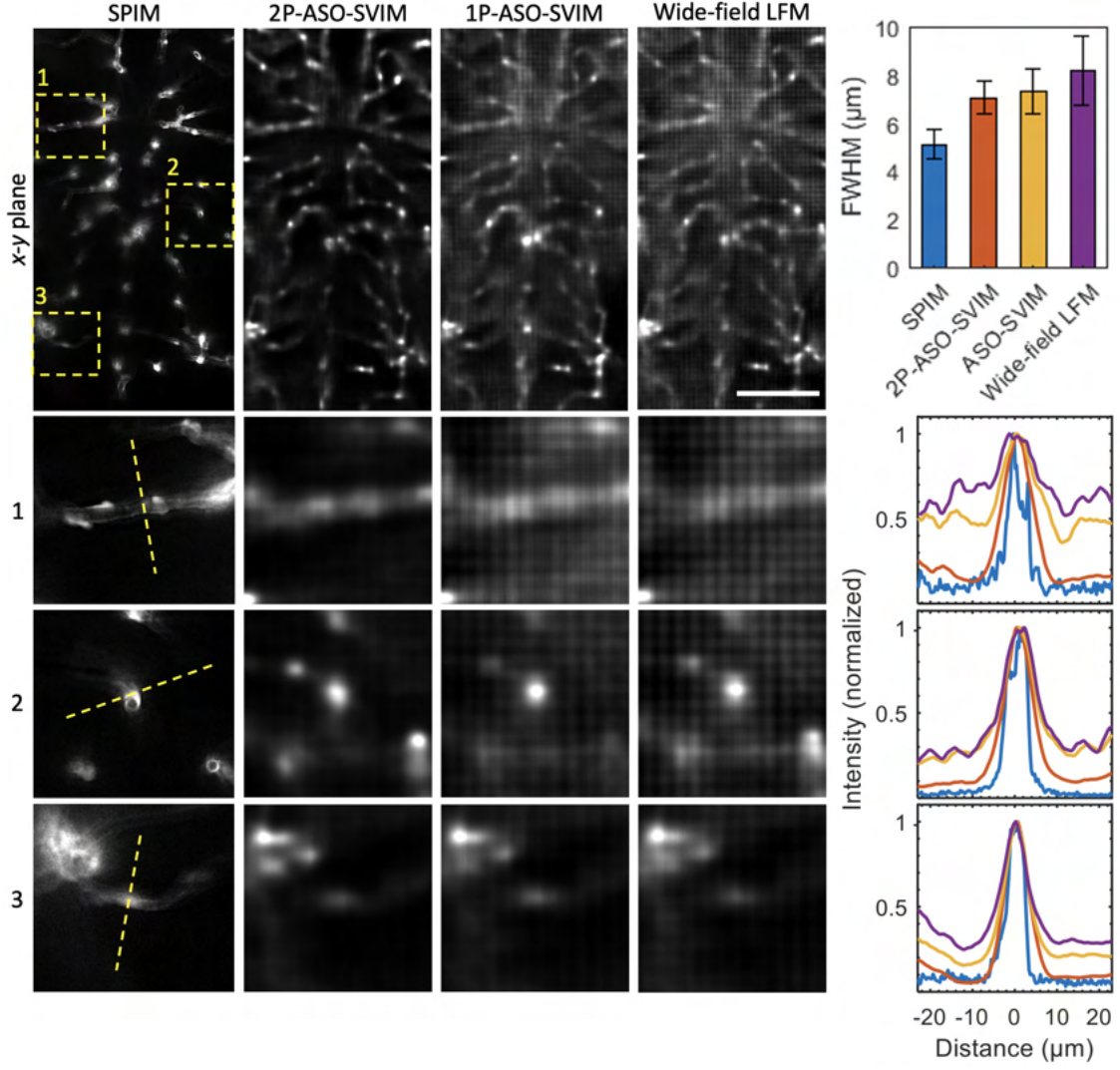


Figure 5.5: Comparison of line cuts through vessel structures *in vivo*. Top row: x - y slice from a 100- μm thick slab (same dataset as Fig. 5.3), centered at approximately 86 μm into the specimen ($z = -14 \mu\text{m}$), comparing the performance of the indicated modalities. Scale bar, 100 μm .

Remaining rows: Zoomed-in regions of structures in the yellow boxes in the x - y plane (top row), along with corresponding line intensity profiles (as shown by the 50- μm yellow line in the images) plotted on the right. Given the intrinsically higher spatial resolution of SPIM, full quantitative correspondence of the light-field-based images is not expected. All three line profiles were used to quantify the average FWHM and standard deviation for each modality (right column, top). Of the light-field-based methods, 2P-ASO-SVIM achieves the highest biological resolution (owing to nonlinear excitation as well as reduced background and scattering), approaching the performance of SPIM, followed by ASO-SVIM in 1P mode, and last, wide-field LFM. Note that this plane is not k -space filtered.

See also Figs. 5.3 and 5.4.

5.3.2 ASO-SVIM improves brain-wide activity imaging

To test ASO-SVIM on a more demanding application, we recorded the activity of large populations of neurons in larval zebrafish. LFM is an attractive technique to meet the neuroimaging challenge of recording the transient firings of a large number of spatially distributed neurons because it can synchronously capture large volumes; however, the high level of background fluorescence in wide-field LFM has remained an impediment to efforts aimed at capturing brain-wide activity with cellular resolution [53, 55, 116, 117, 123–125, 141]. We previously showed in Section 4.2.4 that the improved contrast and effective resolution of SVIM improved brain-wide functional imaging over conventional LFM [52]. We extended the demonstration and analysis to our new ASO-SVIM approach here.

We compared 1P-ASO-SVIM, 2P-ASO-SVIM, and wide-field LFM in imaging the spontaneous brain activity of the same zebrafish larva, labeled with a genetically encoded pan-neuronal fluorescent calcium indicator (Fig. 5.6). The reconstructed 4D recordings are compared by taking the standard deviation along the temporal axis (Fig. 5.6A), to highlight their capability in capturing active neurons, whose transient firings would produce voxels that have large intensity variation in time and thus appear as high-contrast puncta in the resulting projections. We calculated the image contrast of these temporal-standard-deviation projections: 2P-ASO-SVIM achieved the highest contrast, followed by the 1P ASO-SVIM, and then by wide-field LFM (Fig. 5.6B), suggesting that the ASO-SVIM modalities excel in capturing neuronal activity over wide-field LFM.

To quantitatively compare the performance of the different modalities in capturing brain activity at cellular resolution, we identified neurons in the 4D recordings by spot-segmenting the temporal-standard-deviation projections. This standard protocol (Methods Section 4.4.4) [52] produced spatial masks corresponding to neurons that were active during the time-lapse. These masks were then applied to the 4D datasets to extract temporal signals that represent single-neuron activity traces (Fig. 5.6C). The improved contrast of 2P-ASO-SVIM and 1P-ASO-SVIM allowed us to detect a greater number of active neurons in the brain compared to

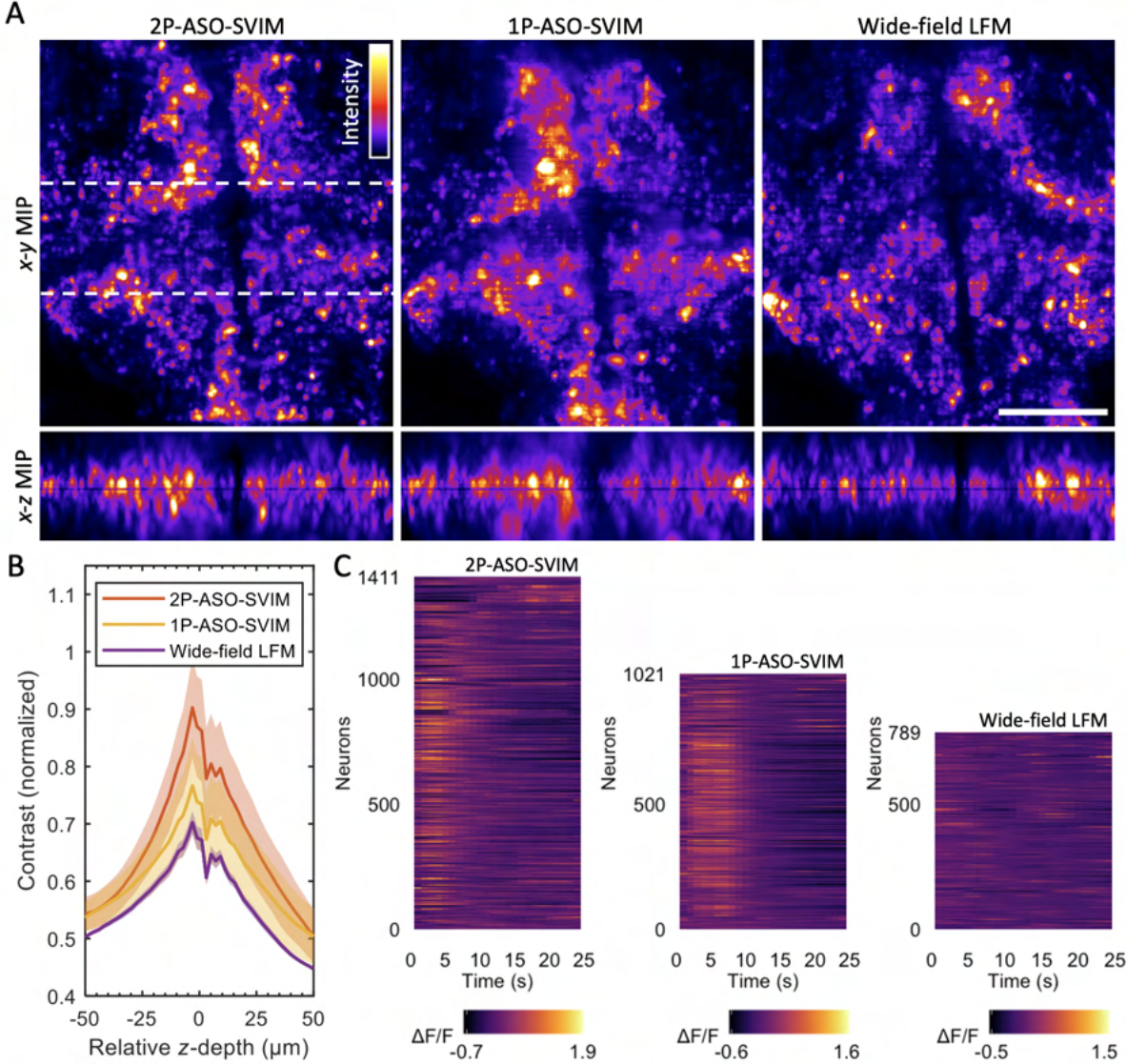


Figure 5.6: ASO-SVIM enhances large-scale *in vivo* recording of neural activity in a $320 \mu\text{m} \times 350 \mu\text{m} \times 100 \mu\text{m}$ volume in larval zebrafish, at 5-dpf, *Tg(elavl3:H2b-GCaMP6s)*. Volumetric rate of 1 Hz sufficiently captured the transient neuronal dynamics given the relatively slow temporal kinetics of the nuclear-localized calcium indicator GCaMP6s [142]. Excitation power, 2P-ASO-SVIM: 525 mW; 1P-ASO-SVIM: 0.4 mW; wide-field LFM: 0.5 mW.

(A) MIPs of *x-y* (top) and *x-z* (bottom) brain-wide 100- μm -thick volumes of the same zebrafish. These projections depict the standard deviation over a 25-s period for each voxel, highlighting active neurons. Scale bar, 100 μm . See Movie 5.7.

(B) Quantification of image contrast versus z-depth, showing progressive improvements of 1P-ASO-SVIM and 2P-ASO-SVIM over wide-field LFM. Means (center lines) and standard deviations (shadings) are shown.

(C) Single-neuron signal traces captured by the different modalities, extracted from the 4D datasets shown in (A). The greatest quantity of neurons were found with 2P-ASO-SVIM, followed by 1P-ASO-SVIM, and then wide-field LFM. Signal extraction protocol described in text.

conventional wide-field illumination (Fig. 5.6C). 2P-ASO-SVIM captured the largest number of active neurons, due not only to its higher contrast than its 1P counterpart (expanded below) but also because the NIR excitation light is invisible to the fish and thereby significantly reduces the response of the animal’s visual system to the illumination, which would otherwise cloud spontaneous activity [52]. 2P-ASO-SVIM is thus an optimal tool for studies of visually sensitive neural behaviors.

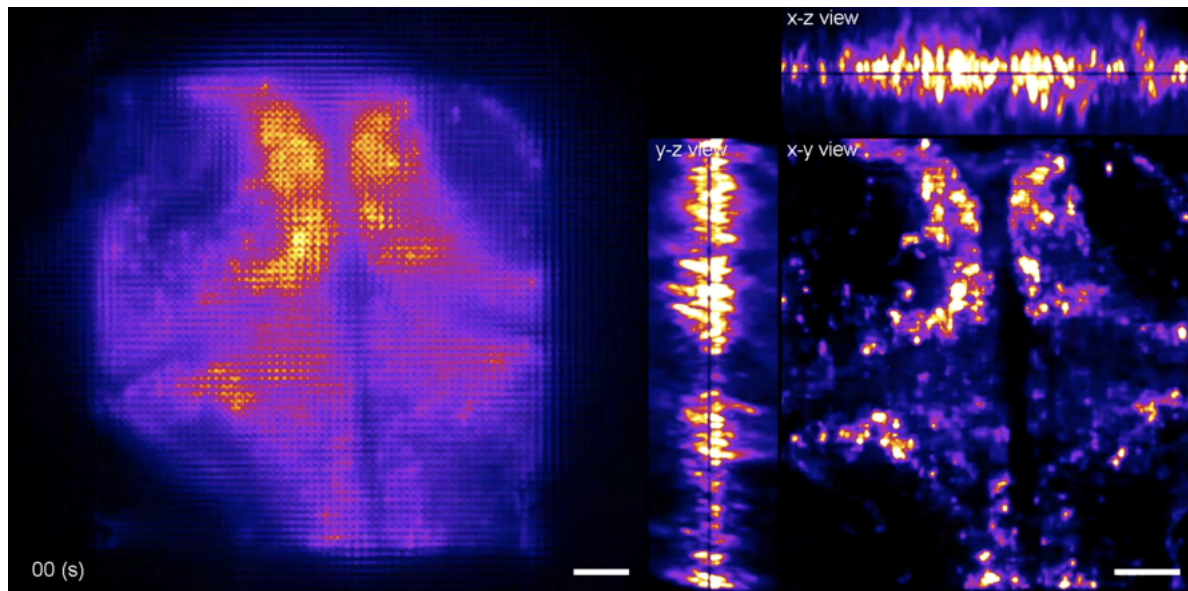


Figure 5.7: 2P-ASO-SVIM brain-wide activity imaging. Fluorescence light-field (left) and 3D reconstructed maximum-intensity projections along the indicated directions (right) of a time-lapse recording of brain-wide neural activity in a 5-dpf transgenic zebrafish. 2P-ASO-SVIM imaging was performed at a volumetric rate of 1 Hz. Same dataset as presented in Fig. 5.6. Scale bar (left), $150 \mu\text{m}$, (right) $50 \mu\text{m}$. Movie: <https://osapublishing.figshare.com/n downloader/files/25328621> (4.08 MB).

5.3.3 High-throughput imaging of whole-brain blood flow in zebrafish

As a final example of the combination of high-contrast, ultrahigh-speed volumetric imaging at cellular resolution and the sample-mounting flexibility of ASO-SVIM, we imaged 3D blood flow in nearly the entire larval zebrafish brain, covering a $670 \mu\text{m} \times 470 \mu\text{m} \times 200 \mu\text{m}$ volume at ~ 50 Hz, in 9 zebrafish mounted in a standard multi-well plate (Fig. 5.8, and Movies 5.9, 5.10, and 5.11).

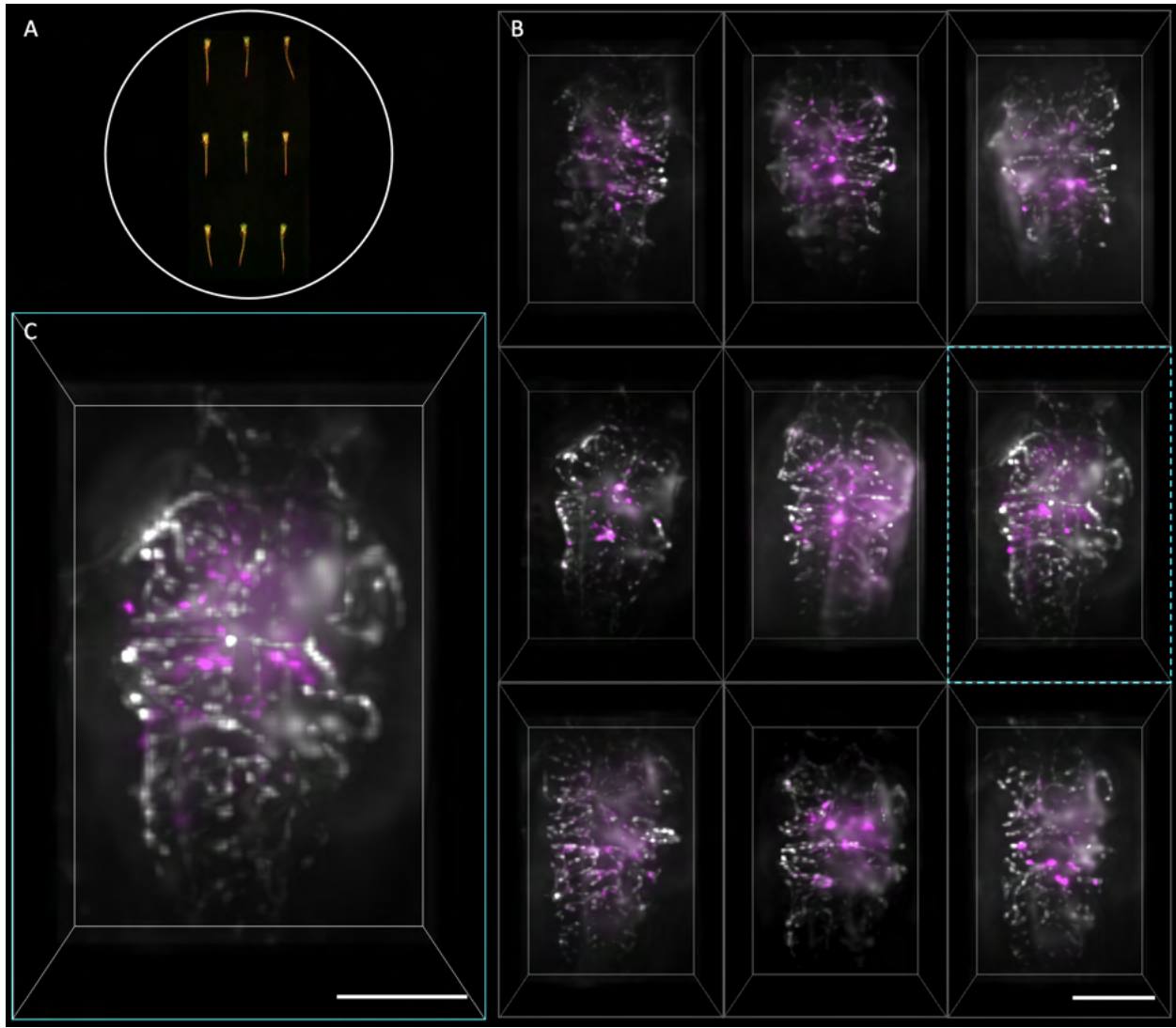


Figure 5.8: ASO-SVIM enables high-throughput imaging of whole-brain blood flow in zebrafish larvae.

(A) Nine 5-dpf zebrafish, with fluorescent labels in both the blood cells (*Tg(gata1:dsRed)*) and endocardium (*Tg(kdrl:eGFP)*), were mounted in a standard multi-well plate. Two-color imaging was performed over a synchronous 670- by 470- by 200- μm volume at ~ 50 Hz, per color, for each fish.

(B) MIPs of 50- μm -thick slabs axially-centered within the 9 dually-labeled zebrafish brains. Captured light-fields were reconstructed using ray optics [50] for increased computational speed. Blood cells and endocardium are represented in magenta and grayscale, respectively. Scale bar, 200 μm .

(C) Magnified MIP of the specimen highlighted by the cyan box in **(B)**. Scale bar, 100 μm . See Movies 5.9, 5.10, and 5.11.

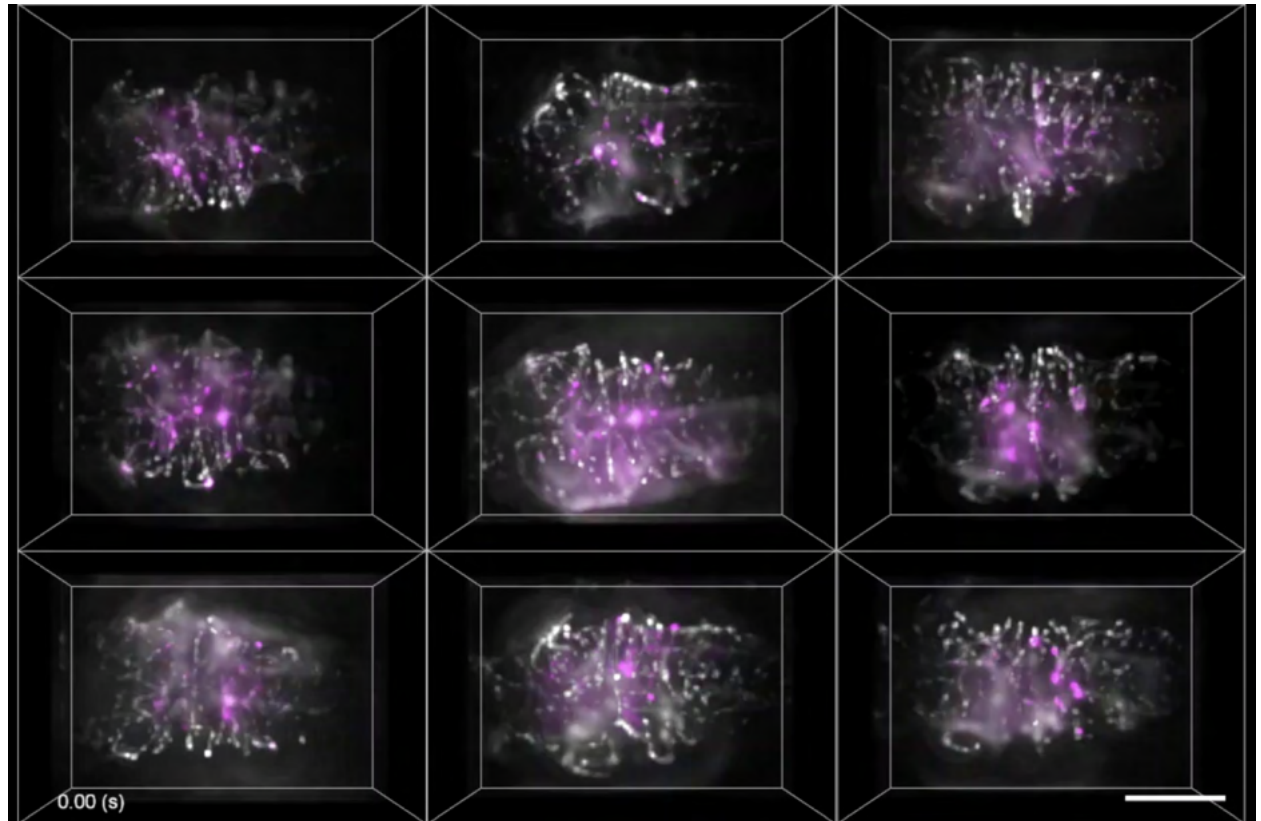


Figure 5.9: Multicolor, high-throughput imaging of nine zebrafish mounted in a standard multi-well plate. Maximum-intensity projections of nine 5-dpf zebrafish, with fluorescent labels in both the blood cells (*Tg(gata1:dsRed)*) and endocardium (*Tg(kdrl:eGFP*)), represented in magenta and grayscale, respectively. Samples were recorded serially, with each sample imaged with 1P-ASO-SVIM over a synchronous 670- by 470- by 200- μm volume at ~ 50 Hz. Same dataset as presented in Fig. 5.8. Scale bar, 200 μm . Movie: <https://osapublishing.figshare.com/ndownloader/files/25328624> (12.34 MB).

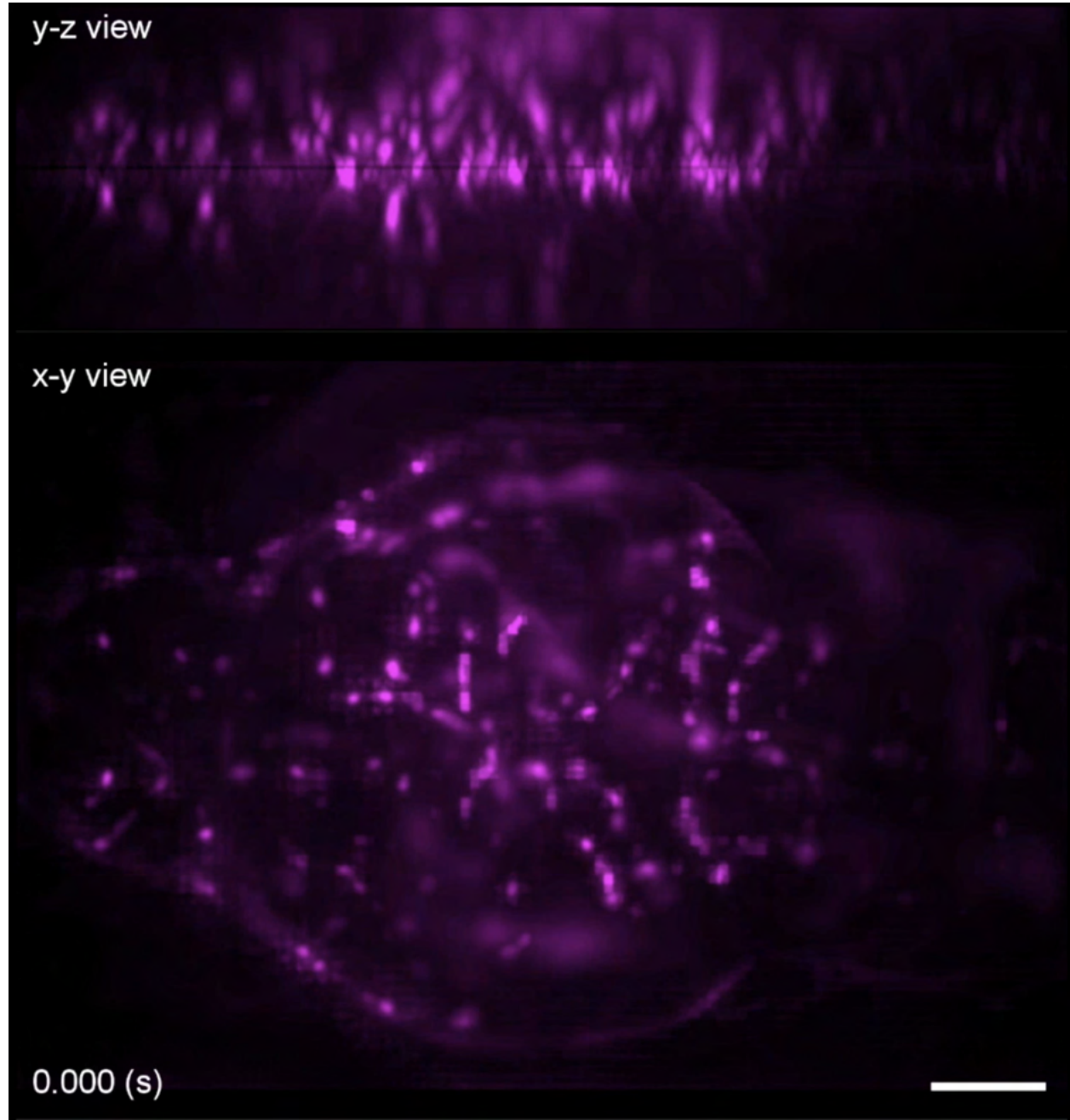


Figure 5.10: 1P-ASO-SVIM imaging of blood cells (*Tg(gata1:dsRed)*) flowing across the entire brain of a 5-dpf zebrafish. Cellular resolution imaging was performed over a 670- by 470- by 200- μm volume at ~ 50 Hz. Fluorescent light-fields were wave optics reconstructed. Animal is oriented anterior (left) to posterior (right). Scale bar, 50 μm . Movie: <https://osapublishing.figshare.com/n downloader/files/25328630> (9.48 MB).

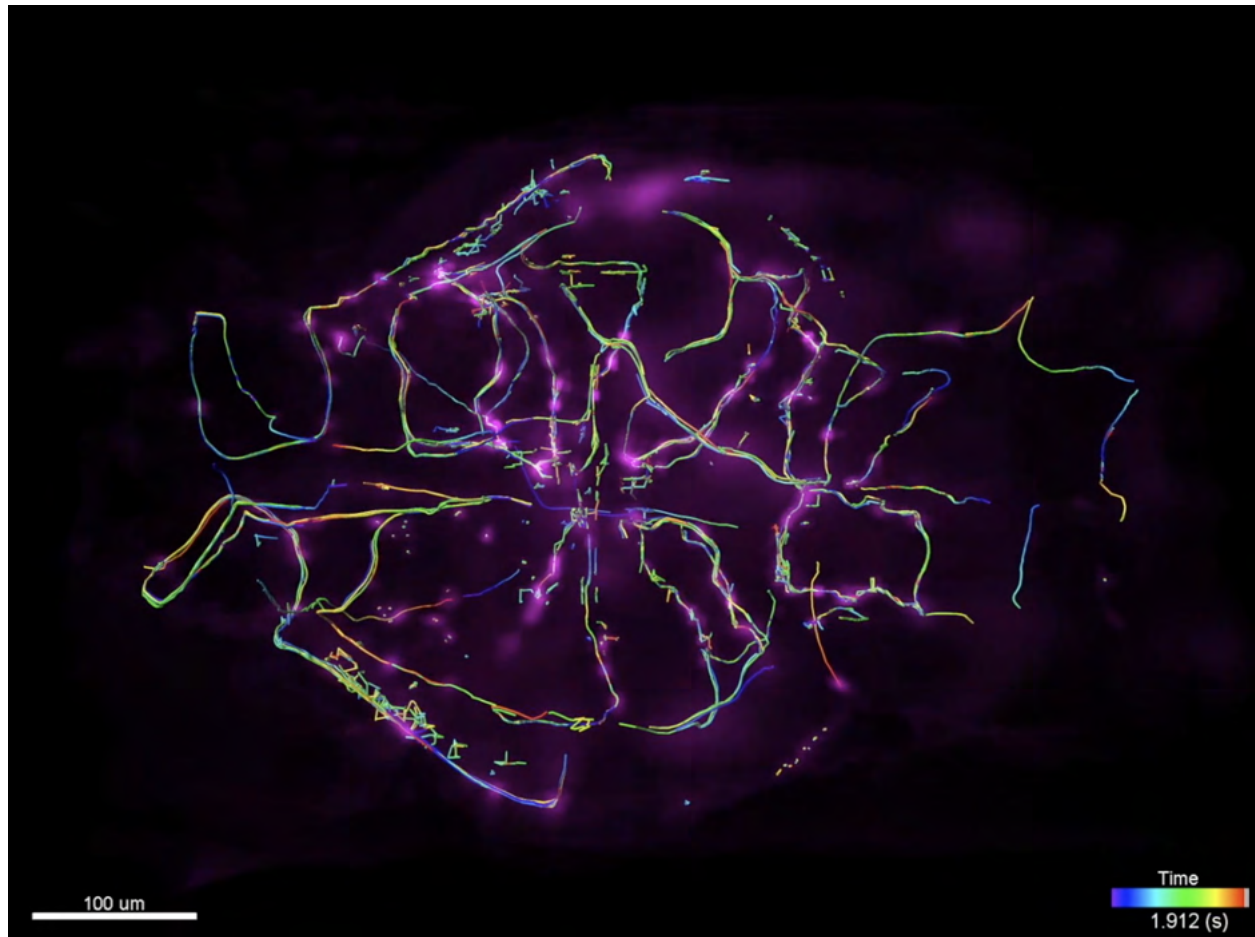


Figure 5.11: Volumetric view of whole-brain blood flow, with red blood cell tracks color-coded in time. Same dataset as presented Movie 5.10. Movie: <https://osapublishing.figshare.com/ndownloader/files/25328627> (13.88 MB).

5.4 Discussion

1P-ASO-SVIM and 2P-ASO-SVIM offer distinct strengths. 1P-ASO-SVIM commands lower laser costs, and offers optical simplicity and exceptionally high volumetric acquisition speed, limited largely by the rate of the camera [52]. However, the 1P excitation volume intersects the sample obliquely and is larger than the desired detection volume (Fig. 5.1D), making 1P-ASO-SVIM less efficient at reducing background than SVIM (Supplementary Note 5.7.2). Like all forms of linear excitation, visible 1P excitation light increasingly scatters with depth, resulting in unavoidable background from outside the volume of interest. 2P-ASO-SVIM effectively eliminates background from out-of-volume fluorescence (Fig. 5.3A) due to non-linear excitation: the quadratic dependence of 2P-excited fluorescence on the laser intensity restricts the excitation volume to near the focus [52, 75], resulting in negligible background even with single-objective designs. The NIR excitation light is scattered much less than visible wavelengths, allowing better penetration depth into biological tissue. Through the judicious selection of illumination NA and beam-scanning, it is straightforward to match the 2P excitation volume to the desired light-field region of interest (Section 5.5.2). This advantage is partially tempered by the reduced speed of 2P-ASO-SVIM, as the lower 2P excitation cross section yields lower fluorescence signal for a given laser intensity, which cannot be increased without bounds out of concern for photodamage.

Together, our results show that ASO-SVIM offers a convenient middle ground between SPIM and traditional wide-field LFM, offering improved contrast and effective resolution compared to LFM, while outperforming the 3D imaging speed of SPIM by approximately two orders of magnitude, as it requires only a single camera exposure to capture an extended volume. Compared to our earlier form of SVIM [52, 140], ASO-SVIM relaxes steric constraints by using only one objective, easing sample preparation and expanding the application space to multicellular systems that are impractical for a dual-objective design. Improvements of 1P-ASO-SVIM could include a detection objective with larger NA to enable a larger excitation tilt-angle, or a tilted detection path via a tertiary imaging module [64–66,

[143, 144] that maximizes the effective angle between excitation and detection, to further leverage the strengths of selective illumination (Supplementary Note 5.7.2). To improve the signal rate and hence the imaging speed of 2P-ASO-SVIM, measures that similarly improve the signal rate of multiphoton microscopy could be deployed, such as dispersion compensation [145], resonant scanning, and an optimal laser pulse repetition rate [19] (Supplementary Note 5.7.1). Finally, the simplicity of ASO-SVIM renders it compatible and synergistic with many recent refinements of LFM [55, 116, 123, 124], and we envision that together they will bring LFM-based imaging techniques into a wide range of biological systems and applications.

5.5 Microscope optics

We describe here the light-field-based selective-volume illumination microscope used in our work. Refer to Fig. 5.12 for the beam paths and key components.

5.5.1 ASO-SVIM: oblique-angled one-photon excitation and wide-field illumination modes

The illumination path for one-photon (1P) excitation, represented by the blue line, is provided by a bank of continuous-wave (CW) fiber lasers (Coherent OBIS LX, UFC Galaxy: 488 nm, 30 mW; 514 nm, 50 mW; 640 nm, 75 mW) and high-power CW lasers (488 nm, 300 mW, Coherent Sapphire LP; and 532 nm, 5 W, Coherent Verdi). Light from the CW laser bank is collimated and expanded by an objective (BE; Nikon, Plan Fluorite 10 \times , 0.3 NA, 16 mm WD), directed by a dichroic mirror (DC₁; FF750-SDi02-25x36, Semrock), and passed through a remote refocus module, which is composed of lens pair T₁₁ and T₁₂ (both 75-mm focal length, Thorlabs AC₂₅₄-075-A-ML). Adjusting the position of T₁₂ refocuses the beam waist so that it is coincident to the nominal detection focal plane at the sample. The illumination beam is then sent to a 2D (x - y) scanning galvo system (G; 6-mm aperture

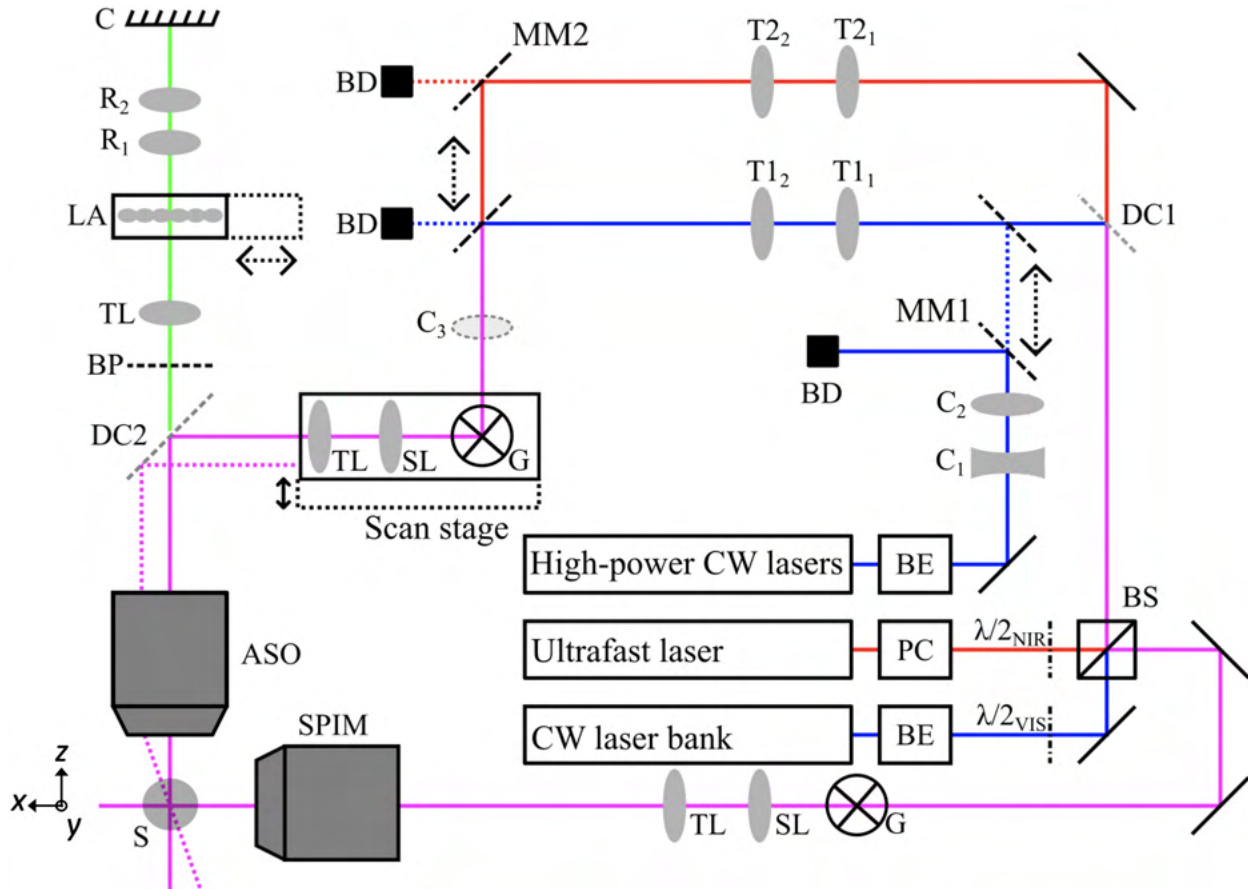


Figure 5.12: Simplified schematic diagram of ASO-SVIM. CW: continuous-wave; BE: beam expander; PC: Pockels cell; $\lambda/2$: half-wave plate, where the subscripts VIS and NIR refer to the visible and near-infrared wavelengths, respectively; BS: polarizing beamsplitter; DC: dichroic mirror, T1: VIS relay lens, T2: NIR relay lens, C: VIS cylindrical lens, MM: movable mirror, where the subscripts refer to the sequence of elements; BD: beam dump; G: 2D scanning galvo mirrors; SL: scan lens; TL: tube lens; ASO: ASO-SVIM objective; SPIM: light-sheet excitation objective; S: sample; BP: band-pass filter; LA: lenslet array; R: detection relay lens, where the subscripts refer to the sequence of lenses; C: camera sensor.

silver mirrors, Cambridge Technology H8363) before being passed through a scan lens (SL; 110-mm focal length, Thorlabs LSM05-BB), a tube lens (TL; 150-mm focal length, Thorlabs AC508-150-B), and a water-dipping objective (ASO; Nikon, CFI LWD Plan Fluorite 16 \times , 0.8 NA, 3 mm WD); G, SL, and TL are mounted on a computer-controlled motorized translational stage (Newport 436 and Newport LTA-HS) to control the inclination angle in ASO-SVIM mode (tilted 26.5° relative to the optical axis of ASO; purple dashed line), and easily port the beam back to the wide-field illumination mode. The illumination NA is adjusted to be \sim 0.04 to 0.06, depending on the selective illumination extent, yielding a fluorescence Gaussian-beam waist of \sim 4 to 6 μm with an axial (z) extent ranging from \sim 150 to 230 μm (measured as the confocal parameter of the focal volume). As G is conjugate to the back pupil of ASO, scanning along the x - and y -axes with the appropriate voltages selectively paints out the desired sample volume.

For fast volumetric 1P imaging, the high-power CW laser was used to provide the high laser intensity needed beyond what the CW laser bank could provide. Light from the high-power CW lasers are collimated and expanded by BE (Thorlabs BE052-A) and directed by mirrors to a cylindrical beam-shaping module, composed of a pair of cylindrical lenses C₁ and C₂ (-50-mm focal length, Thorlabs LK1662L1 or -30-mm focal length, Thorlabs LK1982L1; and 150-mm focal length, Thorlabs LJ1629L1) which expand the beam elliptically in the y -direction. This expanded beam is reflected by a mirror mounted on a motorized motion-control stage (MM1; Newport 436 and Newport LTA-HS), where it is directed through T₁₁ and T₁₂ and then focused into a 2D (y - z) sheet by C₃ (75-mm focal length, Thorlabs LJ703RM-A) onto G. Thus, G only needs to provide scanning along the x -axis to selectively paint out the desired volume at the sample. Note that C₃ is used only for 1D scanning, and omitted in the other imaging modes. All 1P imaging data were acquired with 1D scanning except for Fig. 5.6, where 2D scanning was employed to provide a more precise selectively-illuminated volume, in order to avoid direct illumination of the animal's eyes. An inspection camera (not shown; PCO pco.edge 5.5) conjugate to the sample volume and

coincident to the x - z plane aided in alignment and calibration of the illumination tilt angle and G scanning parameters. Tradeoffs associated with volume-scanning as well as alternative implementations of selective-volume illumination are discussed in Supplementary Note 4.5.1 of Chapter 4 and Ref. [52].

5.5.2 2P-ASO-SVIM: two-photon excitation mode

The illumination path for two-photon (2P) excitation begins in red. Near-infrared (NIR) pulsed illumination is provided by a Ti:Sapphire ultrafast laser (Coherent Chameleon Ultra II) and the illumination power is controlled by a Pockels cell (PC; Conoptics 350-80). A polarizing beamsplitter (PBS; Thorlabs PBS102) is used to combine the visible and NIR beams into a co-linear beam and to split the combined beam into two integrated excitation paths (towards ASO and SPIM objectives). Visible and NIR half-wave plates ($\lambda/2_{\text{VIS}}$ and $\lambda/2_{\text{NIR}}$; Thorlabs AHWP05M-600 and AHWP05M-980), each mounted in manual rotation mounts, are used to adjust the laser power delivered to ASO and SPIM as appropriate. In the ASO path, the NIR illumination beam is transmitted through DC₁ and then through lens pair T21 and T22 (75-mm focal length, Thorlabs AC₂54-75-B-ML and 100-mm focal length, Thorlabs AC₂54-100-B), used to expand and refocus the beam waist before being sent to the same illumination-scanning optics in the aforementioned 1P mode (G, SL, TL, and ASO). A mirror mounted on a motion-control stage (MM2) allows automated switching between 2P- and 1P-ASO excitation. The illumination NA is adjusted to be ~ 0.055 to 0.08 , yielding similar fluorescence Gaussian-beam characteristics as the 1P mode: ~ 4 to $5 \mu\text{m}$ waist and ~ 150 to $230 \mu\text{m}$ axial extent. For all 2P imaging experiments presented (Figs. 2-3), $\sim 525 \text{ mW}$ of average laser power was delivered to the specimen. Although we did not observe any photodamage in live imaging of zebrafish larvae, a quantitative assessment of the excitation laser power on photobleaching and sample health is needed for prolonged biological experiments.

5.5.3 Light-field detection and reconstruction

Excited fluorescence at the sample is collected by the ASO objective. A dichroic mirror (DC2; Di01-R488/561 or di01-R405/488/543/635-25x36) and a filter wheel (Sutter Instrument Lambda 10-3, 32 mm diameter) equipped with emission filters (FF01-470/28-32, FF03-525/50-32, FF01-609/54-32, and FF01-680/42-32) together block the excitation light and transmit the fluorescence signal emitted from the sample (green). An intermediate image at an overall magnification of $24\times$ is projected onto a lenslet array (LA; 2.06-mm focal length, 18x18 mm, 136 μm pitch, AR coated, OKO Technologies APO-Q-P192-F3.17; *f*-number matched to the NA of ASO) by a tube lens (TL; 300-mm focal length, Edmund Optics 88-597). With LA placed at the native image plane, an array of fluorescence focal spots is created, which encode 4D spatio-angular information for each position in the 3D volume—referred to as the light-field [50, 51]. The generated light-field is imaged onto an sCMOS camera (C; Andor Zyla 5.5) by a pair of photographic lenses R_1 and R_2 (both 50-mm focal length, Nikon NIKKOR f/1.4). These raw light-fields are reconstructed into full volumes as described in Refs. [52, 53] and Methods Section 4.4.3 of Chapter 4. Unless otherwise noted, all image stacks are further processed using a filtering algorithm described in Section 5.6.

5.5.4 SPIM: one-photon and two-photon light-sheet imaging modes

In order to operate in SPIM mode, either $\lambda/2_{\text{VIS}}$ or $\lambda/2_{\text{NIR}}$ is rotated so that enough excitation energy is transmitted through PBS and delivered at the sample. After PBS, the illumination beam is routed to a 2D (x - z) scanning galvo system (G; 5-mm aperture silver mirrors, Thorlabs GVSM002), and then passed through SL, TL, and an objective (SPIM; Olympus, LMPLN-IR 10 \times , 0.3 NA, 18 mm WD) to excite the sample with a scanned Gaussian-beam light-sheet. The SPIM objective is mounted on a manual translational stage to create more sample space for ASO-SVIM mode if needed.

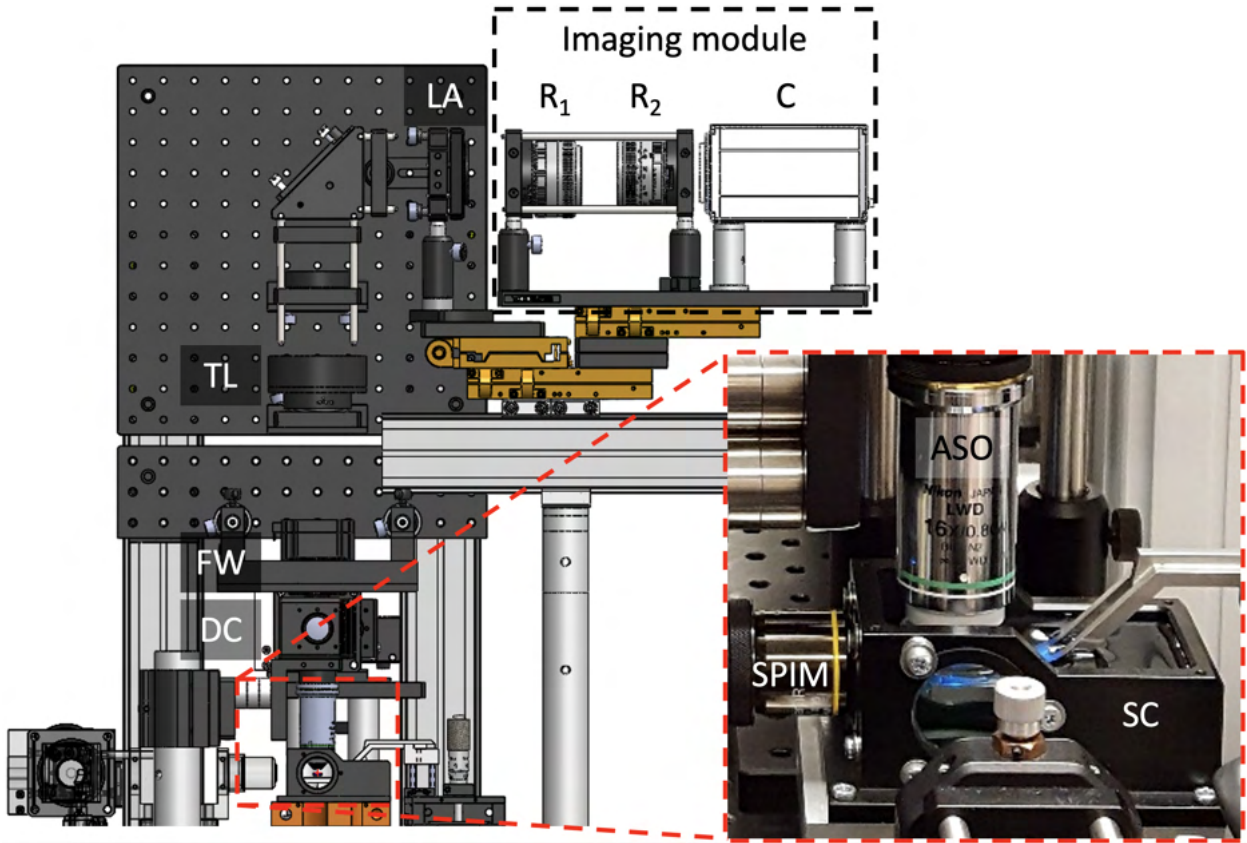


Figure 5.13: 3D opto-mechanical model of the ASO-SVIM light-field detection path. Inset shows a photograph of the sample chamber, the axial-single-objective (ASO) used to both deliver selective-volume illumination at the sample and collect the excited fluorescence, as well as the light-sheet excitation objective (SPIM). Owing to the ASO design, samples can be mounted using a caddy and dive bar system as described in Ref. [49] and Section 2.2.4 of Chapter 2 and are entirely compatible with standard sample preparation protocols (e.g., Fig. S9). Fluorescence collected from ASO passes through a dichroic mirror (DC), a filter wheel (FW), a tube lens (TL), a lenslet array (LA), and onto an imaging module. R: detection relay lens, where the subscripts refer to the sequence of lenses; C: camera.

In order to collect images in SPIM mode, LA is moved entirely out of the detection path, and the entire imaging module (R1, R2, and C) is moved in $-z$ by the focal length of LA. As shown in Fig. S2, LA and the imaging module are each mounted on motorized linear translational stages (Newport 436 and Newport LTA-HS), enabling high-precision positioning and seamless switching between light-field and conventional wide-field/SPIM detection via computer command. The stages also serve to aid in fine alignment. To assemble a 3D volume, 2D images are recorded in series by scanning the sample in z through the stationary light-sheet with a motorized stage (Newport 436 and Newport LTA-HS).

In the comparison of the imaging modalities presented in Fig. 5.3, where SPIM was used to provide the ground-truth images, the 3D volume was recorded with 67 z -slices, spaced 1.5 microns apart, with an exposure time of 0.355 s for each slice, yielding a total acquisition time of 44 s. Note that this final total time included the overhead time associated with the z -stack acquisition (such as stage moving and settling time, and communication overhead). For the corresponding 1P- and 2P-ASO-SVIM recordings, we used an exposure time of 0.355 s for the single snapshot required to capture the 3D volume. This single snapshot was then reconstructed to achieve the final 3D volume, where the z -step size was set to be 2 microns during the reconstruction process. The total time needed to record the 3D volume, 44 s and 0.355 s, for SPIM and ASO-SPIM, respectively, demonstrate that ASO-SVIM is 100 times faster than SPIM in volumetric imaging. A comprehensive comparison of the volumetric imaging speed between ASO-SVIM and SPIM would require additional details, such as adjusting the respective exposure times to equalize the signal-to-noise ratios, and considerations for the different resolutions between the two modalities. Such an in-depth comparison has been carried out in our previous report on SVIM in Supplementary Note 4.5.2 of Chapter 4 and Ref. [52]. Importantly, ASO-SVIM is expected to perform similarly to SVIM in terms of the volumetric imaging rate, as the main difference between them is in the illumination direction, which should not affect the imaging speed.

5.5.5 Instrument control

Instrument control is similar to our previous implementation (detailed in Methods Section 4.4.1 of Chapter 4 and Ref. [52]), with the primary changes concerning the coordination between the scanning system and camera triggering. In our new single-objective configuration, a combination of custom software developed in LabView (National Instruments), ScanImage [146], and Micro-Manager [83] synchronize the scanning system, laser intensity, and camera triggering so that the volume of interest is illuminated an integer number of times within one camera exposure and the excitation intensity is near-uniform frame-to-frame during acquisition. All the motorized linear translational stages used to switch between modes are controlled by an XPS Universal Motion Controller (Newport XPS-Q8). The 3D stage stack-up (Sutter MP-285) used for sample positioning is controlled with its corresponding controller; the sample-scanning z -stage (noted in Section 5.5.4) is controlled via Micro-Manager.

5.5.6 Characterizing system resolution

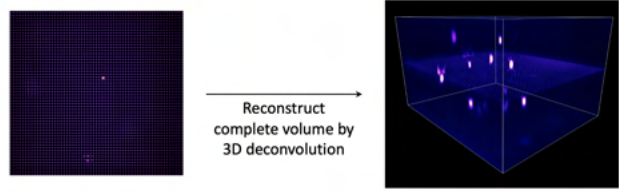
To quantify resolution in volumetric reconstructions of light-fields, we measured the point-spread function (PSF) with 175-nm fluorescent beads sparsely suspended in agarose (Fig. 5.2). We stepped the sparse bead sample in z by $2\text{ }\mu\text{m}$ over a $200\text{-}\mu\text{m}$ volume, imaging the same field of beads at different axial depths, and thereby facilitating multiple measurements of isolated beads throughout the light-field volume. The z -series of light-field images were then reconstructed to yield a series of 3D-stacks with overlapping z -extents, from which we calculated the resolution as a function of relative z -depth (Fig. 5.2B). The observed relation between relative z -depth and the PSF are consistent with results derived from wave optics theory [51]: at different axial depths, the PSF size is different, generally broadening away from the native focus symmetrically; on the other hand, bead-measured PSFs across reconstructed 2D (x - y) slices at each corresponding z -depth are nearly identical.

5.6 k -space filtering

We describe here our k -space filtering process to alleviate light-field microscopy (LFM) reconstruction artifacts. These grid-like artifacts are due to the degeneracy in spatio-angular sampling at the native focal plane, and have been described theoretically and experimentally [51]. Our method is motivated by two empirical observations. First, the grid-like artifacts are mainly composed of spatial frequencies beyond the theoretical resolution limit of the detection optics (Fig. 5.15A, left column). Second, the artifacts are most prominent at the native focal plane and the immediate axial range around it (Fig. 5.15B, left column and Fig. 5.16C). With these observations in mind, we devised the following filtering procedure that selectively removes the bulk of reconstruction artifacts without compromising the resolution of the 3D volume.

At the native focal plane, the theoretical maximum lateral resolution is determined by the diffraction-limited sampling rate of LA: the lenslet pitch divided by the effective magnification [51], which we experimentally confirmed (theory: $5.7 \mu\text{m}$; experiment: $5.2 \pm 0.2 \mu\text{m}$). This resolution limit sets a cutoff frequency in Fourier space (k -space) where we can impose a low-pass filter to remove high-frequency noise, the main source of the image artifacts (Fig. 5.15A, left column). We apply this low-pass filter to the native focal plane and adjacent planes extending across a $10\text{-}\mu\text{m}$ depth, a small subvolume defined by the experimental axial PSF (see dashed yellow rectangles in Fig. 5.15B). Image planes outside of this subvolume are not low-pass filtered. Note that in LFM the resolution changes as a function of depth, and maximum resolution is achieved at z positions away from the native focal plane [51], as experimentally shown in Fig. 5.2B. Because only the subvolume that extends across the focal plane (where artifacts are most prominent) is k -space filtered, higher resolution present elsewhere in the volume is unscathed. Experimental aberrations, background, scattering, and other sources of noise break the underlying assumptions in the reconstruction [51, 52], generally decreasing the highest non-zero spatial frequency achievable (i.e., the effective resolution limit)—or artificially increasing it—making our k -space filter a conservative approach. Our

Light-field reconstruction



k-space filtering

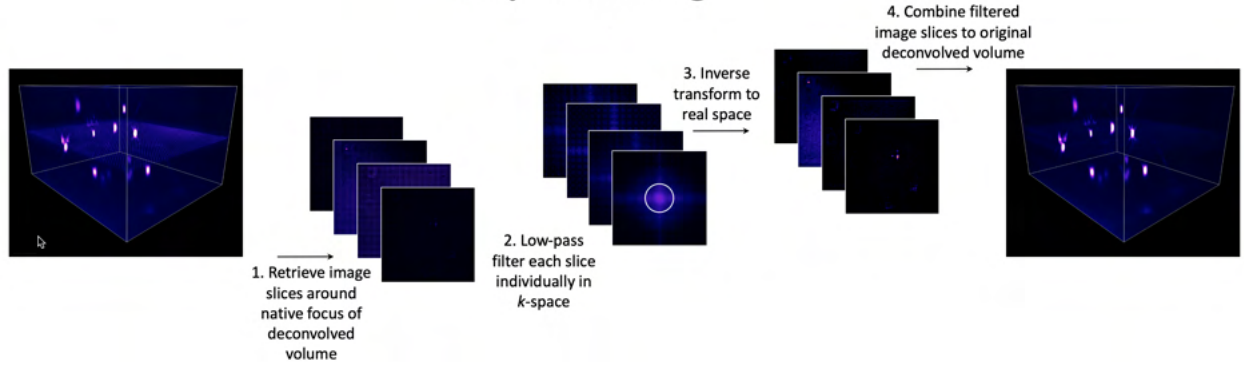


Figure 5.14: *k*-space filtering algorithm. LFM (top) reconstructs a complete 3D volume with depth-dependent resolution and artifacts near the native focal plane [51, 53]. Due to the non-uniform resolution across the entire volume, a single cutoff frequency cannot be applied without compromising peak resolution at other image planes. *k*-space filtering (bottom) splits the deconvolved volume into smaller subvolumes, and independently processes the subvolume that extends across the native focal plane. Retrieved image slices are low-pass filtered in Fourier (*k*) space, based on the experimental optical transfer function (OTF) bounds at that subvolume. Next, image slices are inverse transformed back into real space, and a median filter is applied to minimize ringing artifacts. The filtered image slices are then combined to assemble the final, denoised volume.

filtering process is outlined in Fig. 5.14 and can be combined with any LFM reconstruction algorithm.

To quantitatively assess how well *k*-space filtering mitigates reconstruction artifacts, we compared standard LFM and *k*-space filtered reconstructions of a 300- by 200- by 200- μm field of beads in agarose (Fig. 5.15). In large part the field of beads are similar, but it's clear that artifacts are visible both in lateral and axial maximum-intensity projection (MIP) views of the conventional reconstruction that are not apparent with *k*-space filtering (Fig. 5.15A). Even though the periodic artifacts are only concentrated at the native focus (Fig. 5.15B, left column), they persist and lift the noise floor throughout the lateral MIP view (Fig. 5.15A,

left column). High-frequency artifacts can swamp the signal intensity of weak point sources, making it difficult to differentiate artifacts from real signal; in contrast, the k -space filtered signal intensities are weighted as expected—where real point sources are located (Fig. 5.15D, line 2). In addition, filtering significantly decreases reconstruction artifacts without any loss of spatial resolution throughout the 3D volume, as measured by line cuts through several PSFs (Fig. 5.15D, line 1).

We further tested k -space filtering *in vivo*, where background and noise can critically affect the reconstruction quality [52]. We acquired volumetric data of transgenic zebrafish embryos expressing green fluorescent protein in the cranial vasculature by means of LFM and light-sheet microscopy (also known as selective-plane illumination microscopy; SPIM), which provided an additional ground truth (higher resolution) structural image to compare our filtering method against (same dataset as Fig. 5.3). When applied to living tissue, we observe a dramatic reduction in grid-like artifacts at the native focal plane compared to conventional LFM reconstruction (i.e., no filter), as shown in Fig. 5.16C. Comparing volumetric contrast in standard and k -space filtered reconstruction, we see a dip near the native focal plane (Fig. 5.16B). This is to be expected, as the grid-like patterns lead to an artificial increase in contrast. Similar to the experimentally measured PSFs, line intensity profiles along filtered blood vessels show an important decrease in spurious spatial signal without loss of resolution (Fig. 5.16D), alteration of structural features, or additional artifacts (Fig. 5.16F).

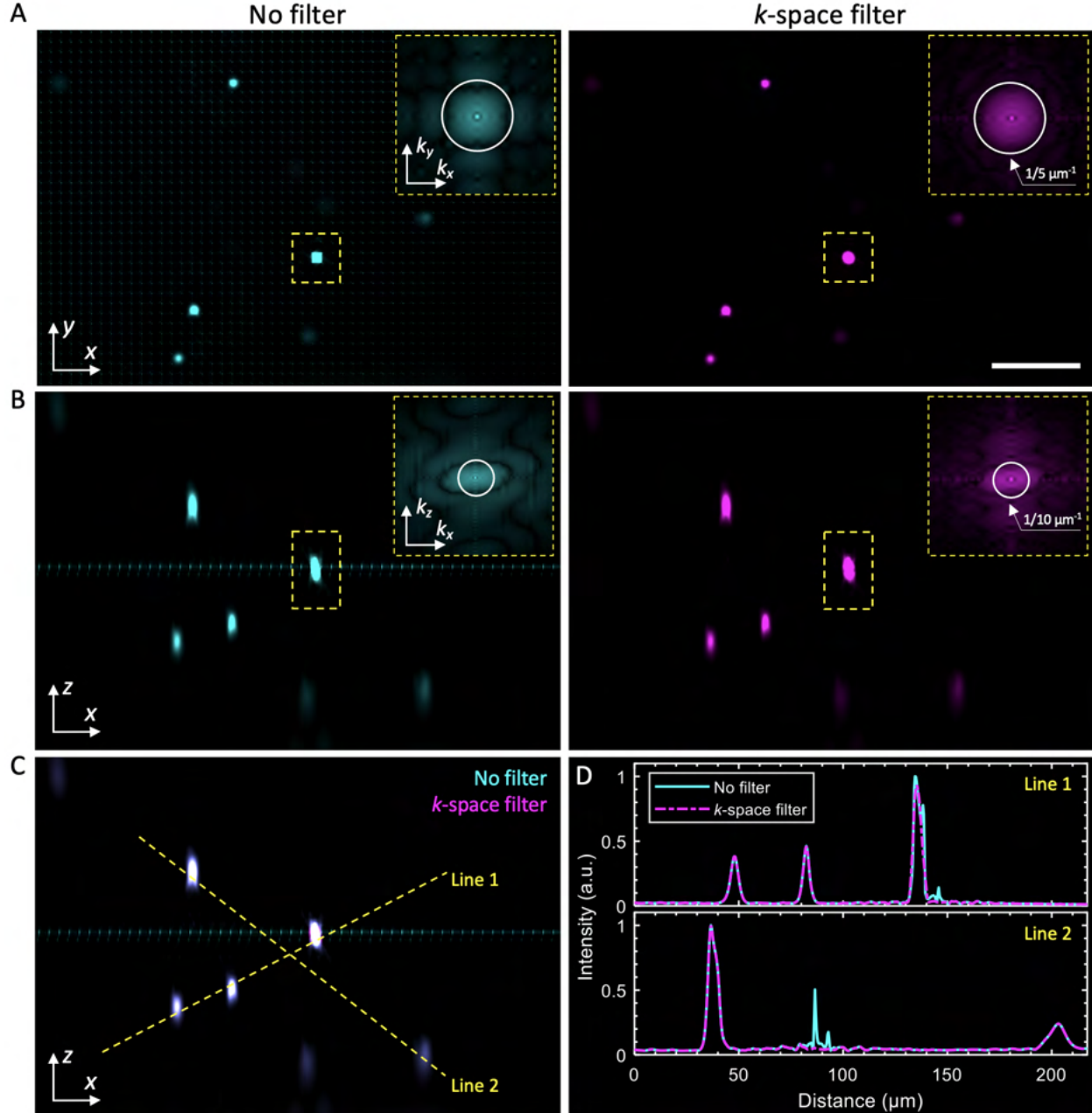


Figure 5.15: *k*-space filtering reduces artifacts and improves volume reconstruction with uncompromised resolution. Comparative *x*-*y* (A) and *x*-*z* (B) MIPs of a 300- by 200- by 200- μm sparse field of fluorescent beads before (left column) and after filtering in *k*-space (right column). Each inset shows the spatial frequency content of the corresponding axially-centered PSF at the native focus, as indicated by the dashed yellow rectangle in the image. Both real and frequency space representations show the ability of *k*-space filtering to reduce high-frequency artifacts, laterally and axially. OTF images were equally gamma-contrast-adjusted to aid in visualizing weak features. Scale bar, 50 μm . (C) Overlap of *x*-*z* MIPs show excellent spatial correspondence of PSFs before and after filtering. (D) Comparative line profiles as indicated by the yellow lines in (C). As expected, there is no appreciable loss of resolution by *k*-space filtering (line 1). Away from the native focus, bead-measured signal intensities show full quantitative correspondence, while at the native focal plane, periodic reconstruction artifacts are effectively suppressed (line 2).

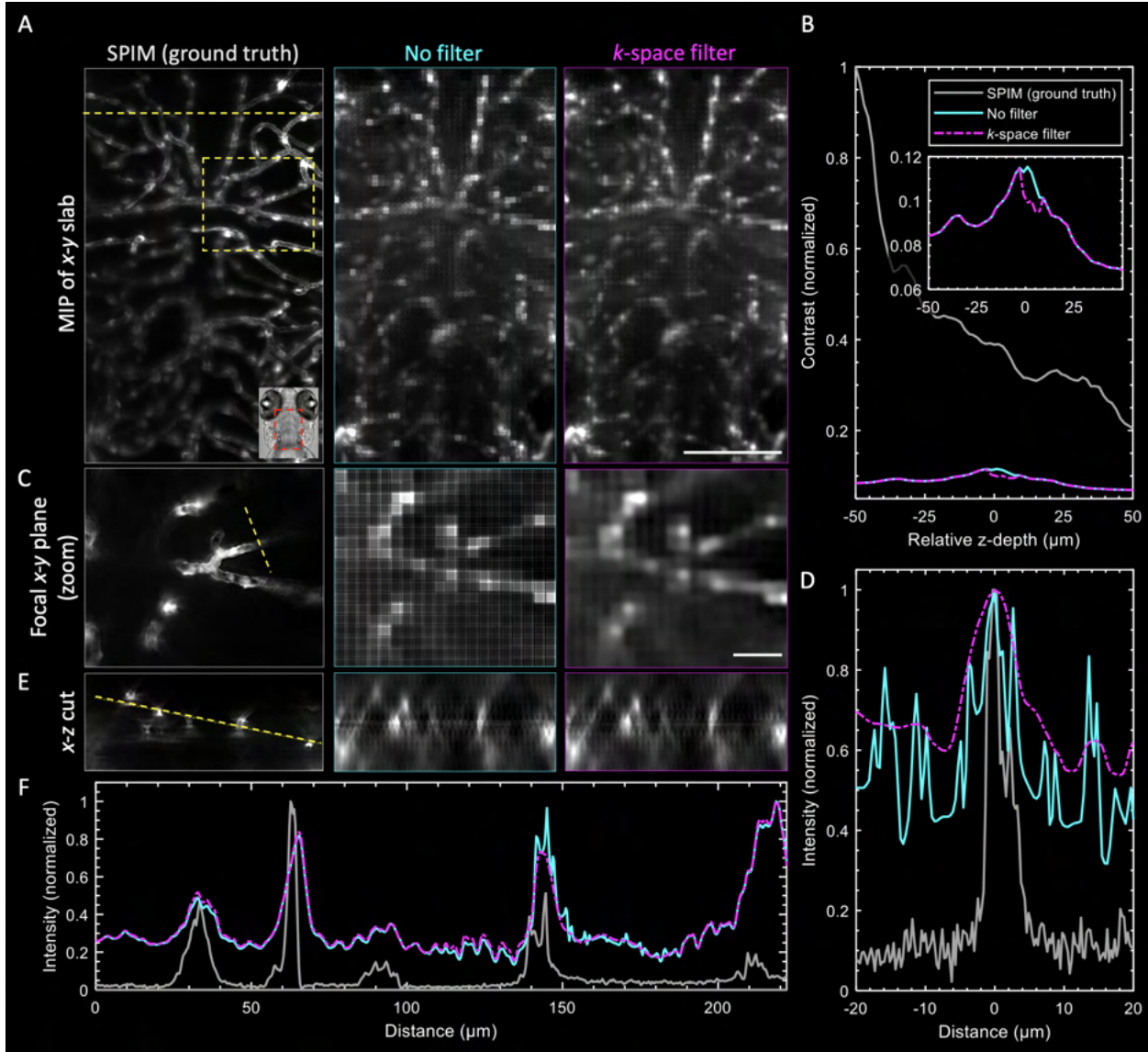


Figure 5.16: *k*-space filtering improves volume reconstruction quality *in vivo*. (A) *x*-*y* MIP of a 100-μm-thick slab (same dataset as Fig. 5.3), comparing each protocol as shown. Scale bar, 100 μm. (B) Quantification of image contrast versus z-depth; each *x*-*y* slice (from all protocols) was normalized against the deconvolved SPIM (gray) slice at $z = -50 \mu\text{m}$. Inset shows light-field protocols only, with the expected decrease in artificially high contrast by *k*-space filtering. (C) Focal *x*-*y* plane (zoom) of yellow boxed region in (A), showing a significant decrease in common reconstruction artifacts by *k*-space filtering (third column). Scale bar, 25 μm. (D) Comparative intensity profiles for each protocol, indicated by line cut in (C). (E) *x*-*z* slice, at the location indicated by the dashed yellow line in the MIP slab in (A). (F) Comparative intensity profiles for each protocol, indicated by the 225-μm yellow line in (E).

5.7 Supplementary material

5.7.1 Improving the signal rate and volumetric imaging speed of 2P-ASO-SVIM

In our work, we did not try to maximize the volumetric imaging rate of 2P-ASO-SVIM (or any of the other compared modalities), including for the neuro imaging demonstration in Section 5.3.2, as shown in Fig. 5.6. The main reason was that we would like to focus on comparing how the different background levels affect the image quality of the various modalities. Thus we have used exposure times generally longer than needed to ensure that the overall brightness of the images was not a limiting factor in the comparison. The second reason, specific to the neuro imaging, was that given the relatively slow dynamics of the nuclear-localized GCaMP6s calcium indicators ($\gtrsim 1$ s), the 1 vol/s imaging rate was adequate in capturing the relevant neuronal firings in the zebrafish brain, as demonstrated in Fig. 5.6C. Judging from the signal-to-noise ratio obtained in the 2P-ASO-SVIM data, we deem that the exposure could have been reduced by a factor of 2 or more, thus yielding a volumetric rate of 2 vol/s or more, and the resulting signal-to-noise would still have been sufficient. Despite the fact that our work is not aimed at maximizing the volumetric imaging rate of 2P-ASO-SVIM, it is useful to consider potential measures that could bring improvements toward that direction. We describe these measures below.

The optical train of our current 2P-ASO-SVIM setup leaves room for improvement, as there are a number of potentially dispersive optical elements, including the high-NA primary objective used for excitation/detection (Fig. 5.12). The resulting dispersion could broaden the ultrafast pulse width, reducing the signal for a given laser power (since the signal scales inversely with pulse width), thereby reducing the volumetric imaging rate. Thus, one future improvement would be to implement dispersion compensation to restore the ultrafast pulse back to its bandwidth-limited duration [145].

In 2P point-scanning microscopy, fast resonant scanners have been found to reduce photodamage when used in “time-averaged” mode, where the recorded image comes from the average signal of the sample being scanned multiple times, as compared to when the sample is scanned only once with a \sim 10-fold slower galvanometer scanner, both under identical average excitation power. This comes from the fact that the faster scanning allows the laser beam to illuminate a given voxel within the sample multiple times in accumulating the signal, increasing the illumination duty cycle, spreading the laser excitation out over time, and thus reducing photodamage. Since 2P-ASO-SVIM also employs beam scanning to illuminate the selective volume of interest, we expect that by using a resonant scanner, instead of the current galvanometer scanner currently used in our setup, we could reduce the photodamage, which in turn would allow us to increase the laser power to increase the signal rate and thus the volumetric imaging rate.

Finally, it has recently been shown that the signal rate of two-photon light sheet microscopy (2P-SPIM), a modality that 2P-ASO-SVIM shares the beam-scanning illumination strategy with, can be increased by an order of magnitude by lowering the ultrafast laser pulse repetition rate to 1-40 MHz, in contrast to the standard 80 MHz of lasers typically used in multiphoton microscopy [19]. The low repetition rate permits higher peak intensity at a constant average power, leading to a higher signal rate due to the squared-dependence of the signal on the peak intensity, while limiting thermal toxicity from linear absorption. Note that since both 2P-SPIM and 2P-ASO-SVIM use a low-numerical-aperture focused beam for illumination, the peak intensity is typically \sim 100 times lower than conventional 2P point-scanning microscopy, and therefore there is significant overhead room for the peak intensity to be increased, with the lower repetition rate, before nonlinear photodamage starts to become a problem. Thus, we envision that similar to the results shown for 2P-SPIM in [19], a lower ultrafast laser repetition rate would enhance the signal rate and volumetric imaging speed of 2P-ASO-SVIM.

5.7.2 Tradeoffs associated with light-field detection in ASO-SVIM

For opto-mechanical convenience and simplicity, we designed our light-field detection arm in an upright epi-configuration (Figs. 5.1A and 5.13). In 2P-ASO-SVIM, we illuminate the sample volume axially with a low NA Gaussian beam (Fig. 5.1E), capturing the full cone of light from the ASO objective: maximizing spatio-angular information, sensitivity, and the usable volume. Axial 2P illumination has the additional benefit of defining the volume of interest axially, owing to the quadratic dependence of the signal on the laser intensity, greatly suppressing extraneous background and providing exceptional contrast. In 1P-ASO-SVIM, we obliquely illuminate the sample volume at a tilt angle of 26.5° to the optical axis (Fig. 5.1D). This similarly captures the full cone of light admitted by the ASO objective as 2P-ASO-SVIM, but does not fully eliminate out-of-volume background because the illuminated volume is larger than the desired detection volume, resulting in residual background above and below the volume of interest, thus leading to 1P-ASO-SVIM performing less well in enhancing the contrast than the ideal performance of the previously reported orthogonal SVIM of Chapter 4 and Ref. [52], which of course requires two orthogonal microscope objectives.

In future work, to enhance the background-elimination of 1P-ASO-SVIM, we generally want to increase the inclination angle between the illumination and detection axes, toward the orthogonal condition of being equal to 90° , to more fully leverage the geometry for selective illumination. A simple way to achieve this would be to use an ASO objective with higher NA to enable a larger inclination angle between the illumination and detection axes, which then would reduce the illuminated z -extent above and below the desired detection volume, and thus lead to lower extraneous out-of-volume background. Another way to increase the angle between the illumination and detection axes is by borrowing a strategy from single-objective implementations of light-sheet microscopy, where a tertiary imaging module is employed to tilt the detection axis so that it is $\sim 90^\circ$ to the illumination beam [64, 66, 143]. Nonetheless, while the tilted detection path would indeed produce less background,

the usable field of view and light collection efficiency of the primary objective would be compromised, limiting resolution and sensitivity. Recent developments in single-objective light-sheet microscopy have shown promise in preserving much of the full NA of the primary objective by compressing the light cone angle between an index-mismatched pair of objectives in a tilted tertiary imaging module [65, 144, 147]. This concept could certainly be combined with ASO-SVIM to circumvent the reduced NA in a tilted light-field detection configuration and extend the improvements in contrast.

5.8 Acknowledgements

D. Holland, A. Andreev, and F. Cutrale, for discussion and technical assistance.

5.8.1 Funding

US National Science Foundation (1608744, 1650406, 1828793); US National Institutes of Health (1R01MH107238-01); Human Frontier Science Program (RGP0008/2017); Jet Propulsion Laboratory Research Subcontract (1632330); Alfred E. Mann Doctoral Fellowship (to K.K.D.).

5.9 Manuscript information

5.9.1 Previously published as

A version of this chapter appeared in [105]:

Madaan, S., Keomanee-Dizon, K., Jones, M., Zhong, C., Nadtochiy, A., Luu, P., *et al.* Single-objective selective-volume illumination microscopy enables high-contrast light-field imaging. *Optics Letters* **46**, 2860 (2021)

DOI: <https://doi.org/10.1364/OL.413849>

5.9.2 Author contributions

The authors for this work were: Sara Madaan, Kevin Keomanee-Dizon, Matt Jones, Chenyang Zhong, Anna Nadtochiy, Peter Luu, Scott E. Fraser, and Thai V. Truong.

T.V.T. conceived the idea, with further refinement from S.M. and S.E.F. S.M. designed the optical microscope with input from T.V.T. S.M., M.J., and K.K.D. built the microscope with input from T.V.T. S.M., M.J., and K.K.D. performed all microscope characterization. S.M. created the galvo-scanning control software. S.M. and M.J. acquired all biological data with co-authors. S.M., C.Z., K.K.D., and A.N. setup the light-field reconstruction pipeline and performed reconstructions.

K.K.D. processed and performed quantitative analysis of all optical image data, and developed the k -space filtering algorithm (Section 5.6). K.K.D. produced all figures and movies with input from T.V.T., except for Fig. 5.12, which was produced by M.J.; and S.M. and A.N. assisted in rendering Movie 5.9.

K.K.D., T.V.T., and S.E.F. wrote the manuscript with input from S.M. S.E.F. and T.V.T. supervised the work. S.M. and K.K.D. contributed equally.

References

1. Galilei, G. *Sidereus Nuncius* (Thomas Baglioni, 1610).
2. Hooke, R. *Micrographia: or, Some physiological descriptions of minute bodies made by magnifying glasses* 1st ed. (J. Martyn and J. Allestry, London, 1665).
3. Cremer, C. & Cremer, T. Considerations on a laser-scanning-microscope with high resolution and depth of field. *Microscopica Acta* **81**, 31 (1978).
4. Pawley, J. B. *Handbook of Confocal Microscopy* 3rd ed. (Springer Science and Business Media, 2006).
5. Göppert-Mayer, M. Über Elementarakte mit zwei Quantensprüngen. *Annals of Physics* **401**, 273 (1931).
6. Diaspro, A., Chirico, G. & Collini, M. Two-photon fluorescence excitation and related techniques in biological microscopy. *Quarterly Reviews of Biophysics* **38**, 97 (2006).
7. Denk, W., Strickler, J. H. & Webb, W. W. Two-photon laser scanning fluorescence microscopy. *Science* **248**, 73 (1990).
8. Zipfel, W. R., Williams, R. M. & Webb, W. W. Nonlinear magic: multiphoton microscopy in the biosciences. *Nature Biotechnology* **21**, 1369 (2003).
9. Helmchen, F. & Denk, W. Deep tissue two-photon microscopy. *Nature Methods* **2**, 932 (2005).
10. Yang, W. & Yuste, R. In vivo imaging of neural activity. *Nature Methods* **14**, 349 (2017).
11. Wang, T., Ouzounov, D. G., Wu, C., Horton, N. G., Zhang, B., Wu, C.-H., et al. Three-photon imaging of mouse brain structure and function through the intact skull. *Nature Methods* **15**, 789 (2018).
12. Shimomura, O., Johnson, F. H. & Saiga, Y. Extraction, Purification and Properties of Aequorin, a Bioluminescent Protein from the Luminous Hydromedusan, Aequorea. *Journal of Cellular and Comparative Physiology* **59**, 223 (1962).
13. Chalfie, M., Tu, Y., Euskirchen, G., Ward, W. W. & Prasher, D. C. Green fluorescent protein as a marker for gene expression. *Science* **263**, 802 (1994).
14. Tsien, R. The Green Fluorescent Protein. *Annual Review of Biochemistry* **67**, 509 (1998).
15. Zhan, H., Stanciuaskas, R., Stigloher, C., Keomanee-Dizon, K., Jospin, M., Bessereau, J.-L., et al. In vivo single-molecule imaging identifies altered dynamics of calcium channels in dystrophin-mutant *C. elegans*. *Nature Communications* **5**, 1 (2014).
16. Zhang, J., Campbell, R. E., Ting, A. Y. & Tsien, R. Y. Creating new fluorescent probes for cell biology. *Nature Reviews Molecular Cell Biology* **3**, 906 (2002).
17. Maimon, T. Stimulated optical radiation in ruby. *Nature* **187**, 493 (1960).

18. Kaiser, W. & Garrett, C. G. B. Two-Photon Excitation in CaF₂:Eu²⁺. *Physical Review Letters* **7**, 229 (1961).
19. Maioli, V., Boniface, A., Mahou, P., Ortas, J. F., Abdeladim, L., Beaurepaire, E., *et al.* Fast in vivo multiphoton light-sheet microscopy with optimal pulse frequency. *Biomedical Optics Express* **11**, 6012 (2020).
20. Ji, N., Magee, J. C. & Betzig, E. High-speed, low-photodamage nonlinear imaging using passive pulse splitters. *Nature Methods* **5**, 197 (2008).
21. Svelto, O. *Principles of Lasers* 4th ed. (Plenum Press, 1998).
22. Nylk, J. & Dholakia, K. *Neurophotonics and Biomedical Spectroscopy* (eds Alfano, R. R. & Shi, L.) (William Andrew, 2018).
23. Hect, E. *Optics* 5th ed. (Pearson Education, 2017).
24. Ploem, J. S. The use of a vertical illuminator with interchangeable dichroic mirrors for fluorescence microscopy with incidental light. *Zeitschrift für wissenschaftliche Mikroskopie* **68**, 129 (1967).
25. Brumberg, E. M. & Krylova, T. N. O fluoreschentnykh mikroskopopak. *Zhurnal Obshchei Biologii* **14**, 461 (1953).
26. Gustafsson, M. G. L., Shao, L., Carlton, P. M., Wang, C. J. R., Golubovskaya, I. N., Cande, W. Z., *et al.* Three-Dimensional Resolution Doubling in Wide-Field Fluorescence Microscopy by Structured Illumination. *Biophysical Journal* **94**, 4957 (2008).
27. Li, D., Shao, L., Chen, B.-C., Zhang, X., Zhang, M., Moses, B., *et al.* Extended-resolution structured illumination imaging of endocytic and cytoskeletal dynamics. *Science* **349**, aab3500 (2015).
28. Abbe, E. Beiträge zur Theorie des Mikroskops und der mikroskopischen Wahrnehmung. *Archiv für Mikroskopische Anatomie* **9**, 413 (1873).
29. Rayleigh, L. Investigations in optics, with special reference to the spectroscope. *he London, Edinburgh, and Dublin Philosophical Magazine and Journal of Science* **8**, 261 (1879).
30. Goodman, J. W. *Introduction to Fourier Optics* 3rd ed. (Roberts and Company Publishers, 2005).
31. Agard, D. A. & Sedat, J. W. Three dimensional architecture of a polytene nucleus. *Nature* **302**, 676 (1983).
32. McNally, J. G. & Conchelloc, T. K. J. C. J. A. Three-Dimensional Imaging by Deconvolution Microscopy. *Methods* **19**, 373 (2002).
33. Boyle, W. S. & Smith, G. E. Charge Coupled Semiconductor Devices. *Bell System Technical Journal* **49**, 587 (1970).
34. Inoue, S. Video Image Processing Greatly Enhances Contrast, Quality, and Speed in Polarization-based Microscopy. *The Journal of Cell Biology* **89**, 346 (1981).
35. Durnin, J., Jr., J. J. M. & Eberly, J. H. Diffraction-Free Beams. *Physical Review Letters* **58**, 1499 (1988).
36. Durnin, J., Jr., J. J. M. & Eberly, J. H. Comparison of Bessel and Gaussian beams. *Optics Letters* **13**, 79 (1988).
37. McGloin, D. & Dholakia, K. Bessel beams: Diffraction in a new light. *Contemporary Physics* **46**, 15 (2005).

38. Garcés-Chávez, V., McGloin, D., Melville, H., Sibbett, W. & Dholakia, K. Simultaneous micromanipulation in multiple planes using a self-reconstructing light beam. *Nature* **419**, 145 (2002).
39. Botcherby, E. J., Juškaitis, R. & Wilson, T. Scanning two photon fluorescence microscopy with extended depth of field. *Optics Communication* **268**, 253 (2006).
40. Fahrbach, F. O., Simon, P. & Rohrbach, A. Microscopy with selfreconstructing beams. *Nature Photonics* **4**, 780 (2010).
41. Planchon, T., Gao, L., Milkie, D. E., Davidson, M. W., Galbraith, J. A., Galbraith, C. G., *et al.* Rapid three-dimensional isotropic imaging of living cells using Bessel beam plane illumination. *Nature Methods* **8**, 417 (2011).
42. Chen, B.-C., Legant, W. R., Wang, K., Shao, L., Milkie, D. E., Daniel, E., *et al.* Lattice light-sheet microscopy: Imaging molecules to embryos at high spatiotemporal resolution. *Science* **346**, 1257998 (2014).
43. Lu, R., Sun, W., Liang, Y., Kerlin, A., Bierfeld, J., Seelig, J. D., *et al.* Video-rate volumetric functional imaging of the brain at synaptic resolution. *Nature Neuroscience* **20**, 620 (2017).
44. Minsky, M. *Microscopy Apparatus* U.S. Patent No 3,013,467. 1961.
45. Hewlett, S. J. & Wilson, T. Resolution enhancement in three-dimensional confocal microscopy. *Machine Vision and Applications* **4**, 232 (1991).
46. Weisenburger, S. & Vaziri, A. A Guide to Emerging Technologies for Large-Scale and Whole-Brain Optical Imaging of Neuronal Activity. *Annual Review of Neuroscience* **41**, 431 (2018).
47. Siedentopf, H. & Zsigmondy, R. On visualization and sizing of ultramicroscopic particles, with particular application to gold ruby glasses. *Annalen der Physik* **315**, 1 (1902).
48. Huisken, J., Swoger, J., Bene, F. D., Wittbrodt, J. & Stelzer, E. Optical Sectioning Deep Inside Live Embryos by Selective Plane Illumination Microscopy. *Science* **305**, 1007 (2004).
49. Keomanee-Dizon, K., Fraser, S. E. & Truong, T. V. A versatile, multi-laser twin-microscope system for light-sheet imaging. *Review of Scientific Instruments* **91**, 053703 (2020).
50. Levoy, M., Ng, R., Adams, A., Footer, M. & Horowitz, M. Light field microscopy. *ACM Transactions on Graphics* **25**, 924 (2006).
51. Broxton, M., Grosenick, L., Yang, S., Cohen, N., Andalman, A., Deisseroth, K., *et al.* Wave optics theory and 3-D deconvolution for the light field microscope. *Optics Express* **21**, 25418 (2013).
52. Truong, T. V., Holland, D. B., Madaan, S., Andreev, A., Keomanee-Dizon, K., Troll, J., *et al.* High-contrast, synchronous volumetric imaging with selective volume illumination microscopy. *Communications Biology* **3**, 74 (2020).
53. Prevedel, R., Yoon, Y.-G., Hoffmann, M., Pak, N., Wetzstein, G., Kato, S., *et al.* *Nature Methods* **11**, 727 (2014).
54. Born, M. & Wolf, E. *Principles of Optics* 7th ed. (Cambridge University Press, 1999).
55. Grosenick, L., Broxton, M., Kim, C. K., Liston, C., Poole, B., Yang, S., *et al.* Identification of cellular-activity dynamics across large tissue volumes in the mammalian brain. *bioRxiv* **132688** (2017).

56. Vermot, J., Forouhar, A. S., Liebling, M., Wu, D., Plummer, D., Gharib, M., *et al.* Reversing Blood Flows Act through klf2a to Ensure Normal Valvulogenesis in the Developing Heart. *PLOS Biology* **7**, e1000246 (2009).
57. Fraser, S. E. Crystal gazing in optical microscopy. *Nature Biotechnology* **21**, 1272 (2003).
58. Laissue, P. P., Alghamdi, R. A., Tomancak, P., Reynaud, E. G. & Shroff, H. Assessing phototoxicity in live fluorescence imaging. *Nature Methods* **14**, 657 (2017).
59. Donnert, G., Eggeling, C. & Hell, S. W. Major signal increase in fluorescence microscopy through dark-state relaxation. *Nature Methods* **4**, 81 (2006).
60. Gao, L., Shao, L., Chen, B.-C. & Betzig, E. 3D live fluorescence imaging of cellular dynamics using Bessel beam plane illumination microscopy. *Nature Protocols* **9**, 1083 (2014).
61. Power, R. M. & Huisken, J. A guide to light-sheet fluorescence microscopy for multi-scale imaging. *Nature Methods* **14**, 360 (2017).
62. Glaser, A. K., Reder, N. P., Chen, Y., McCarty, E. F., Yin, C., Wei, L., *et al.* Light-sheet microscopy for slide-free non-destructive pathology of large clinical specimens. *Nature Biomedical Engineering* **1**, 0084 (2017).
63. Liu, T., Upadhyayula, S., Milkie, D. E., Singh, V., Wang, K., Swinburne, I. A., *et al.* Observing the cell in its native state: Imaging subcellular dynamics in multicellular organisms. *Science* **360**, eaaq1392 (2018).
64. Kumar, M., Kishore, S., Nasenbeny, J., McLean, D. L. & Kozorovitskiy, Y. Integrated one- and two-photon scanned oblique plane illumination (SOPi) microscopy for rapid volumetric imaging. *Optics Express* **26**, 13027 (2018).
65. Yang, B., Chen, X., Wang, Y., Feng, S., Pessino, V., Stuurman, N., *et al.* Epi-illumination SPIM for volumetric imaging with high spatial-temporal resolution. *Nature Methods* **16**, 501 (2019).
66. Voleti, V., Patel, K. B., Li, W., Campos, C. P., Bharadwaj, S., H. Yu, C. F., *et al.* Real-time volumetric microscopy of *in vivo* dynamics and large-scale samples with SCAPE 2.0. *Nature Methods* **16**, 1054 (2019).
67. Fiolka, R. Resolution upgrades for light-sheet microscopy. *Nature Methods* **16**, 813 (2019).
68. Hillman, E. M. C., Voleti, V., Li, W. & Yu, H. Light-Sheet Microscopy in Neuroscience. *Annual Review of Neuroscience* **42**, 295 (2019).
69. Cutrale, F., Fraser, S. E. & Trinh, L. A. Imaging, Visualization, and Computation in Developmental Biology. *Annual Review of Biomedical Data Science* **2**, 223 (2019).
70. McDole, K., Guignard, L., Amat, F., Berger, A., Malandain, G., Royer, L. A., *et al.* In Toto Imaging and Reconstruction of Post-Implantation Mouse Development at the Single-Cell Level. *Cell* **175**, 859 (2018).
71. Ahrens, M. B., Orger, M. B., Robson, D. N., Li, J. M. & Keller, P. J. Whole-brain functional imaging at cellular resolution using light-sheet microscopy. *Nature Methods* **10**, 413 (2013).
72. Vladimirov, N., Mu, Y., Kawashima, T., Bennett, D. V., Yang, C., Looger, L. L., *et al.* Light-sheet functional imaging in fictively behaving zebrafish. *Nature Methods* **11**, 883 (2014).

73. Wolf, S., Dubreuil, A. M., Bertoni, T., Böhm, U. L., Bormuth, V., Candelier, R., *et al.* Sensorimotor computation underlying phototaxis in zebrafish. *Nature Communications* **8**, 651 (2017).
74. Keller, P. J., Schmidt, A. D., Wittbrodt, J. & Stelzer, E. H. K. Reconstruction of Zebrafish Early Embryonic Development by Scanned Light Sheet Microscopy. *Science* **322**, 1065 (2008).
75. Truong, T. V., Supatto, W., Koos, D. S., Choi, J. M. & Fraser, S. E. Deep and fast live imaging with two-photon scanned light-sheet microscopy. *Nature Methods* **8**, 757 (2011).
76. Wolf, S., Supatto, W., Debrégeas, G., Mahou, P., Kruglik, S., Sintes, J. M., *et al.* Whole-brain functional imaging with two-photon light-sheet microscopy. *Nature Methods* **12**, 379 (2015).
77. Trivedi, V., Truong, T. V., Trinh, L. A., Holland, D. B., Liebling, M. & Fraser, S. E. Dynamic structure and protein expression of the live embryonic heart captured by 2-photon light sheet microscopy and retrospective registration. *Biomedical Optics Express* **6**, 2056 (2015).
78. Reeves, G. T., Trisnadi, N., Truong, T. V., Nahmad, M., Katz, S. & Stathopoulos, A. Dorsal-Ventral Gene Expression in the Drosophila Embryo Reflects the Dynamics and Precision of the Dorsal Nuclear Gradient. *Developmental Cell* **22**, 544 (2012).
79. Bower, D. V., Lansdale, N., Navarro, S., Truong, T. V., Bower, D. J., Featherstone, N. C., *et al.* SERCA directs cell migration and branching across species and germ layers. *Biology Open* **6**, 1458 (2017).
80. Lee, D. A., Andreev, A., Truong, T. V., Chen, A., Hill, A. J., Oikonomou, G., *et al.* Genetic and neuronal regulation of sleep by neuropeptide VF. *eLife* **6**, e25727 (2017).
81. Huisken, J. & Stainier, D. Even fluorescence excitation by multidirectional selective plane illumination microscopy (mSPIM). *Optics Letters* **32**, 2068 (2007).
82. Naumann, A., Kampff, A. R., Prober, D. A., Schier, A. F. & Engert, F. Monitoring neural activity with bioluminescence during natural behavior. *Nature Neuroscience* **13**, 513 (2010).
83. Edelstein, A. D., Tsuchida, M. A., Amodaj, N., Pinkard, H., Vale, R. D. & Stuurman, N. Advanced methods of microscope control using Micro-Manager software. *Journal of Biological Methods* **1**, 10 (2015).
84. Hove, J. R., Köster, R. W., Forouhar, A. S., Acevedo-Bolton, G., Fraser, S. E. & Gharib, M. Intracardiac fluid forces are an essential epigenetic factor for embryonic cardiogenesis. *Nature* **421**, 172 (2003).
85. Stainer, D. Y. Zebrafish genetics and vertebrate heart formation. *Nature Reviews Genetics* **2**, 39 (2001).
86. Forouhar, A. S., Liebling, M., Hickerson, A., Nasiraei-Moghaddam, A., Tsai, H. J., Hove, J. R., *et al.* The Embryonic Vertebrate Heart Tube Is a Dynamic Suction Pump. *Science* **312**, 751 (2006).
87. Weber, M., Scherf, N., Meyer, A. M., Panáková, D., Kohl, P. & Huisken, J. Cell-accurate optical mapping across the entire developing heart. *eLife* **6**, e28307 (2017).
88. Liebling, M., Forouhar, A. S., Gharib, M., Fraser, S. E. & Dickinson, M. E. Four-dimensional cardiac imaging in living embryos via postacquisition synchronization of nongated slice sequences. *Journal of Biomedical Optics* **10**, 054001 (2005).

89. Taylor, J. M. Optically gated beating-heart imaging. *Frontiers in Physiology* **5**, 481 (2014).
90. Strobl, F., Schmitz, A. & Stelzer, E. H. K. Improving your four-dimensional image: traveling through a decade of light-sheet-based fluorescence microscopy research. *Nature Protocols* **12**, 1103 (2017).
91. Pampaloni, F., Chang, B.-J. & Stelzer, E. H. K. Light sheet-based fluorescence microscopy (LSFM) for the quantitative imaging of cells and tissues. *Cell and Tissue Research* **360**, 129 (2015).
92. Takahashi, T. Organoids for Drug Discovery and Personalized Medicine. *Annual Review of Pharmacology and Toxicology* **59**, 447 (2019).
93. Giovannucci, A., Friedrich, J., Gunn, P., Kalfon, J., Brown, B. L., Koay, S. A., *et al.* CaImAn an open source tool for scalable calcium imaging data analysis. *eLife* **8**, e38173 (2019).
94. Pitrone, G., Schindelin, J., Stuyvenberg, L., Preibisch, S., Weber, M., Eliceiri, K. W., *et al.* OpenSPIM: an open-access light-sheet microscopy platform. *Nature Methods* **10**, 598 (2013).
95. Tomer, R., Khairy, K., Amat, F. & Keller, P. J. Quantitative high-speed imaging of entire developing embryos with simultaneous multiview light-sheet microscopy. *Nature Methods* **9**, 755 (2012).
96. Keller, P. J., Schmidt, A. D., Santella, A., Khairy, K., Bao, Z., Wittbrodt, J., *et al.* Fast, high-contrast imaging of animal development with scanned light sheet-based structured-illumination microscopy. *Nature Methods* **7**, 637 (2010).
97. Baumgart & Kubitscheck, U. Scanned light sheet microscopy with confocal slit detection. *Optics Express* **20** (2012).
98. Valm, A. M., Cohen, S., Legant, W. R., Melunis, J., Hershberg, U., Wait, E., *et al.* Applying systems-level spectral imaging and analysis to reveal the organelle interactome. *Nature* **546**, 162 (2017).
99. Jahr, W., Schmid, B., Schmied, C., Fahrbach, F. O. & Huisken, J. Hyperspectral light sheet microscopy. *Nature Communications* **6**, 7990 (2015).
100. Cutrale, F., Trivedi, V., Trinh, L. A., Chiu, C.-L., Choi, J. M., Artiga, M. S., *et al.* Hyperspectral phasor analysis enables multiplexed 5D in vivo imaging. *Nature Methods* **14**, 149 (2017).
101. Negrean, A. & Mansvelder, H. D. Optimal lens design and use in laser-scanning microscopy. *Biomedical Optics Express* **5**, 1588 (2014).
102. Nagler, A. *Plossl type eyepiece for use in astronomical instruments* U.S. Patent No. 4,482,217. 1984.
103. Tsai, P., Mateo, C., Field, J. J., Schaffer, C. B., Anderson, M. E. & Kleinfeld, D. Ultra-large field-of-view two-photon microscopy. *Optics Express* **23**, 13833 (2015).
104. Supatto, W., Truong, T. ., Débarre, D. & Beaurepaire, E. Advances in Multiphoton Microscopy for Imaging Embryos. *Current Opinion in Genetics & Development* **21**, 538 (2011).
105. Madaan, S., Keomanee-Dizon, K., Jones, M., Zhong, C., Nadtochiy, A., Luu, P., *et al.* Single-objective selective-volume illumination microscopy enables high-contrast light-field imaging. *Optics Letters* **46**, 2860 (2021).

106. Abrahamsson, S., Usawa, S. & Gustafsson, M. *A new approach to extended focus for high-speed high-resolution biological microscopy* in *Three-Dimensional and Multidimensional Microscopy: Image Acquisition and Processing XIII* (2006), 60900N.
107. Olarte, O. E., Artigas, J. A. D. & Loza-Alvarez, P. Decoupled illumination detection in light-sheet microscopy for fast volumetric imaging. *Optica* **2**, 702 (2015).
108. Tomer, R., Lovett-Barron, M., Kauvar, I., Andelman, A., Burns, V. M., Sankaran, S., *et al.* SPED Light Sheet Microscopy: Fast Mapping of Biological System Structure and Function. *Cell* **163**, 1796 (2015).
109. Quirin, S., Vladimirov, N., Yang, C.-T., Peterka, D. S., Yuste, R. & Ahrens, M. B. Calcium imaging of neural circuits with extended depth-of-field light-sheet microscopy. *Optics Letters* **41**, 855 (2016).
110. Chen, B., Chakraborty, T., Daetwyler, S., Manton, J. D., Dean, K. & Fiolka, R. Extended depth of focus multiphoton microscopy via incoherent pulse splitting. *Biomedical Optics Express* **11**, 3830 (2020).
111. Boothe, T., Hilbert, L., Heide, M., Berninger, L., Huttner, W. B., Zaburdaev, V., *et al.* A tunable refractive index matching medium for live imaging cells, tissues and model organisms. *eLife* **6**, e27240 (2017).
112. Vettenburg, T., Dalgarno, H. I. C., Nylk, J., Coll-Lladó, C., Ferrier, D. E. K., Čižmár, T., *et al.* Light-sheet microscopy using an Airy beam. *Nature Methods* **11**, 541 (2014).
113. Hosny, N. A., Seyforth, J. A., Spickermann, G., Mitchell, T. J., Almada, P., Chesters, R., *et al.* Planar Airy beam light-sheet for two-photon microscopy. *Biomedical Optics Express* **11**, 3927 (2020).
114. Leutenegger, M., Rao, R., Leitgeb, R. A. & Lasser, T. Fast focus field calculations. *Optics Express* **14**, 11277 (2006).
115. Westerfield, M. *The Zebrafish Book*. (University of Oregon Press, 2000).
116. Cong, L., Wang, Z., Chai, Y., Hang, W., Shang, C., Yang, W., *et al.* Rapid whole brain imaging of neural activity in freely behaving larval zebrafish (*Danio rerio*). *eLife* **6**, e28158 (2017).
117. Skocek, O., Nöbauer, T., Weilguny, L., Traub, F. M., Xia, C. N., M. I. Molodtsov A. Grama, M. Y., *et al.* High-speed volumetric imaging of neuronal activity in freely moving rodents. *Nature Methods* **15**, 429 (2018).
118. McFall-Ngai, M. J. Divining the essence of symbiosis: insights from the squid-vibrio model. *PLOS Biology* **12**, e1001783 (2014).
119. Nyholm, S. V., Stabb, E. V., Ruby, E. G. & McFall-Ngai, M. J. Establishment of an animal–bacterial association: Recruiting symbiotic vibrios from the environment. *Proceedings of the National Academy of Sciences of the United States of America* **97**, 10231 (2000).
120. Nawroth, J. C., H. Guo, E. K., Heath-Heckman, E. A. C., Hermanson, J. C., Ruby, E. G., Dabiri, J. O., *et al.* Motile cilia create fluid-mechanical microhabitats for the active recruitment of the host microbiome. *Proceedings of the National Academy of Sciences of the United States of America* **114**, 9510 (2017).
121. Fahrbach, F. O., Voigt, F. F., Schmid, B., Helmchen, F. & Huisken, J. Rapid 3D light-sheet microscopy with a tunable lens. *Optics Express* **21**, 21010 (2013).

122. Mickoleit, M., Schmid, B., Weber, M., Fahrbach, F. O., Hombach, S., Reischauer, S., *et al.* High-resolution reconstruction of the beating zebrafish heart. *Nature Methods* **11**, 919 (2014).
123. Pégard, N. C., Liu, H.-Y., Antipa, N., Gerlock, M., Adesnik, H. & Waller, L. Compressive light-field microscopy for 3D neural activity recording. *Optica* **3**, 517 (2016).
124. Nöbauer, T., Skocek, O., P.-A., A. J., Weilguny, L., Traub, F. M., Molodtsov, M. I., *et al.* Video rate volumetric Ca²⁺ imaging across cortex using seeded iterative demixing (SID) microscopy. *Nature Methods* **14**, 811 (2017).
125. Aimon, S., Katsuki, T., Jia, T., Grosenick, L., Broxton, M., Deisseroth, K., *et al.* Fast near-whole-brain imaging in adult *Drosophila* during responses to stimuli and behavior. *PLOS Biology* **17**, e2006732 (2019).
126. Wagner, N., Norlin, N., Gerten, J., Medeiros, G. D., Balázs, B., Wittbrodt, J., *et al.* Instantaneous isotropic volumetric imaging of fast biological processes. *Nature Methods* **16**, 497 (2019).
127. Cohen, N., Yang, S., Andalman, A., Broxton, M., Grosenick, L., Deisseroth, K., *et al.* Enhancing the performance of the light field microscope using wavefront coding. *Optics Express* **22**, 24817 (2014).
128. Antipa, N., Kuo, G., Heckel, R., Mildenhall, B., Bostan, E., Ng, R., *et al.* DiffuserCam: lensless single-exposure 3D imaging. *Optica* **5**, 1 (2018).
129. Guo, C., Liu, W., Hua, X., Li, H. & Jia, S. Fourier light-field microscopy. *Optics Express* **27**, 25573 (2019).
130. Zheng, G., Horstmeyer, R. & Yang, C. Wide-field, high-resolution Fourier ptychographic microscopy. *Nature Photonics* **7**, 739 (2013).
131. Adams, J. K., Boominathan, V., Avants, B. W., Vercosa, D. G., Ye, F., Baraniuk, R. G., *et al.* Single-frame 3D fluorescence microscopy with ultraminiature lensless FlatScope. *Science Advances* **3**, e1701548 (2017).
132. Troll, J. V., Adin, D. M., Wier, A. M., Paquette, N., Silverman, N., Goldman, W. E., *et al.* Peptidoglycan induces loss of a nuclear peptidoglycan recognition protein during host tissue development in a beneficial animal-bacterial symbiosis. *Cellular Microbiology* **11**, 1114 (2009).
133. Dunn, A. K., Millikan, D. S., Adin, D. M., Bose, J. L. & Stabb, E. V. E. V. New rfp- and pES213-Derived Tools for Analyzing Symbiotic *Vibrio fischeri* Reveal Patterns of Infection and lux Expression In Situ. *Applied and Environmental Microbiology* **72**, 802 (2006).
134. Schindelin, J., Arganda-Carreras, I., Frise, E., Kaynig, V., Longair, M., Pietzsch, T., *et al.* Fiji: an open-source platform for biological-image analysis. *Nature Methods* **9**, 676 (2012).
135. Muto, A., Ohkura, M., Abe, G., Nakai, J. & Kawakami, K. Real-Time Visualization of Neuronal Activity during Perception. *Current Biology* **23**, 307 (2013).
136. Peli, E. Contrast in complex images. *Journal of the Optical Society of America A* **7**, 2032 (1990).
137. Bex, P. J. & Makous, W. Spatial frequency, phase, and the contrast of natural images. *Journal of the Optical Society of America A* **19**, 1096 (2002).
138. Taylor, M. A. & Bowen, W. P. Quantum metrology and its application in biology. *Physics Reports* **615**, 1 (2016).

139. Cutrale, F., Fraser, S. E. & Trinh, L. A. Imaging, Visualization, and Computation in Developmental Biology. *Annual Review of Biomedical Data Science* **2**, 223 (2019).
140. Truong, T. V., Holland, D. B., Madaan, S., Andreev, A., Troll, J. V., Koo, D. E. S., *et al.* Selective volume illumination microscopy offers synchronous volumetric imaging with high contrast. *bioRxiv* **403303** (2018).
141. Lin, Q., Manley, J., Helmreich, M., Schlumm, F., Li, J. M., Robson, D. N., *et al.* Cerebellar Neurodynamics Predict Decision Timing and Outcome on the Single-Trial Level. *Cell* **180**, 536 (2020).
142. Chen, T. W., Wardill, T. J., Sun, Y., Pulver, S. R., Renninger, S. L., Baohan, A., *et al.* Ultrasensitive fluorescent proteins for imaging neuronal activity. *Nature* **499**, 295 (2013).
143. Dunsby, C. Optically sectioned imaging by oblique plane microscopy. *Optics Express* **16**, 20306 (2008).
144. Sapoznik, E., Chang, B. J., Huh, J., Ju, R. J., Azarova, E. V., Pohlkamp, T., *et al.* A versatile oblique plane microscope for large-scale and high-resolution imaging of subcellular dynamics. *eLife* **9**, e57681 (2020).
145. Chauhan, V., Bowlan, P., Cohen, J. & Trebino, R. Single-diffraction-grating and grism pulse compressors. *Applied Optics* **27**, 619 (2010).
146. Pologruto, T., Sabatini, B. & Svoboda, K. ScanImage: flexible software for operating laser scanning microscopes. *Biomedical Engineering OnLine* **2**, 13 (2003).
147. Millett-Sikking, A. & York, A. High NA single-objective light-sheet. DOI: [10.5281/zenodo.3244420](https://doi.org/10.5281/zenodo.3244420) (2019).

Appendices

A Detailed list of the main flex-SPIM parts

Table A1: List of main flex-SPIM components. Solid model and mechanical drawings for custom components are available upon request.

Subsystem/module	Component	Catalogue number	Vendor	Notes
	5×10 ft, anti-vibration optical table	INTEGRITY 4 VCS 510-8	Newport	
CW Laser bank	OBIS 445 nm LX	1185051	Coherent	Power: 75 mW
	OBIS 488 nm LX	1220123	Coherent	Power: 150 mW
	OBIS 561 nm LS	1280720	Coherent	Power: 150 mW
	OBIS 647 nm LX	1196627	Coherent	Power: 120 mW
	$f = 20$ mm, 12.5 mm diameter lens	47-661	Edmund Optics	Beam expansion
Continued on next page				

Table A1 – continued from previous page

Subsystem/module	Component	Catalogue number	Vendor	Notes
	$f = 8 \text{ mm}, 12.24 \text{ mm diameter lens}$	C240TME-A	Thorlabs	
	25 mm diameter broadband mirror	87-371	Edmund Optics	Beam combining
	Di02-R561 dichroic beam splitter	Di02-R561-25x36	Semrock	Beam combining
	LM01-503-25 LaserMUX dichroic beam splitter	LM01-503-25	Semrock	Beam combining

Continued on next page

Table A1 – continued from previous page

Subsystem/module	Component	Catalogue number	Vendor	Notes
	LM01-466-25 LaserMUX dichroic beam-splitter 1 inch diameter broadband dielectric mirrors 30 mm cage cube-mounted variable beam-splitter 0.5 inch diameter mounted achromatic half-wave plate	LM01-466-25 BB1-E02 VA5-PBS251 AHWP05M-600	Semrock Thorlabs Thorlabs Thorlabs	Beam combining Broadband (400-750 nm) dielectric beam steering mirror Visible (420-680 nm) polarization optics Visible (400-800 nm) polarization optics

Continued on next page

Table A1 – continued from previous page

Subsystem/module	Component	Catalogue number	Vendor	Notes
	AOTF	AOTFnC- 400.650-TN	AA Quanta Tech, Optoelec- tronic	Tellurium dioxide crys- tal. Number of channels: 8. Wavelength range: 400-650 nm. Transmis- sion: > 90%. Aperture: 3 mm ² . Spectral reso- lution: 1-4 nm. Tuning time: < 4 μs
Driver for AOTF RF cable SMA connectors				
MPDS8C-D66- 22-74.158				
AA Quanta Tech				
Number of channels: 8. Communication: USB, RS232, RC03. Extinc- tion ratio: 120 dB.				
AA Quanta Tech				
Continued on next page				

Table A1 – continued from previous page

Subsystem/module	Component	Catalogue number	Vendor	Notes
	STAB, cable, SMC connectors	CBL- SCF200SCF- RG316	AA Quanta Tech	
NIR femtosecond-pulsed laser	Insight DS+	90044047	Spectra Physics	Tuning range: 680-1300 nm. Fixed output: 1040 nm. Repetition rate: 80 \pm 0.5 MHz. Built-in dispersion compensation used to minimize pulse width at the sample
30 mm cage cube-mounted variable beam-splitter				
VA5-PBS252				
Thorlabs				
NIR (690-1000 nm) polarization optics				
Continued on next page				

Table A1 – continued from previous page

Subsystem/module	Component	Catalogue number	Vendor	Notes
	1 inch diameter broadband dielectric mirrors	BB1-E03	Thorlabs	Broadband (750-1100 nm) dielectric beam steering mirror
	E-O Modulator	350-80-02 KD*P	Conoptics	
	2.7mm Aperture Galilean beam expander	BE02-05-B	Thorlabs	2×-5× optical beam expander
	800 nm long-pass filter, 1 inch diameter	FEL0800	Thorlabs	
Illumination-scanning optics	24 inch × 36 inch optical breadboard	B2436F	Thorlabs	
Continued on next page				

Table A1 – continued from previous page

Subsystem/module	Component	Catalogue number	Vendor	Notes
	66 mm construction rail	XT66-500	Thorlabs	Periscope
	1 inch kinematic mirror mount	KM100	Thorlabs	
	45° elliptical mirror mount	H45E1	Thorlabs	
	VIS elliptical mirror	BVE1-E02	Thorlabs	
	NIR elliptical mirror	BVE1-E03	Thorlabs	
	1 inch pedestal post, 1inch long	RS1P8E	Thorlabs	
Continued on next page				

Table A1 – continued from previous page

Subsystem/module	Component	Catalogue number	Vendor	Notes
	clamping platform for 66 mm rail 0.5 inch diameter silver mirror 0.5 inch diameter mounted achromatic half-wave plate 30 mm cage cube-mounted variable beam-splitter	XT66C4 PF05-03-P01 AHWP05M-600 VA5-PBS252	Thorlabs Thorlabs Thorlabs Thorlabs	Beam steering mirror Visible (400-800 nm) polarization optic NIR (690-1000 nm) polarization optics

Continued on next page

Table A1 – continued from previous page

Subsystem/module	Component	Catalogue number	Vendor	Notes
	2D scanning galvo mirror positioning system Mounting adapter for 2D galvo system $f = 150$ mm, 50 mm diameter lens $f = 200$ mm, 50 mm diameter lens	GVSM002 GCM102 VIS-NIR 49-391- INK VIS-NIR 49-392- INK	Thorlabs Thorlabs Edmund Optics Edmund Optics	Scan lens (achromatic doublet) Tube lens
Continued on next page				

Table A1 – continued from previous page

Subsystem/module	Component	Catalogue number	Vendor	Notes
	5×, 0.10 NA, 23 mm WD objective lens	LMPLN5XIR LWD M PLAN	Olympus	Excitation objective lens
Detection	20×, 1.0 NA, 2 mm WD objective lens	XLUMPLFLN-W	Olympus	Detection objective lens
	Filter wheel	Lambda 10-B	Sutter Instrument	Twin 1: 32 mm diameter. Twin 2: 25 mm diameter
	Filter wheel controller	Lambda 10-3	Sutter Instrument	
	609/54 nm BrightLine single-band bandpass	FF01-609/54-32	Semrock	Emission filter set for Twin 1
Continued on next page				

Table A1 – continued from previous page

Subsystem/module	Component	Catalogue number	Vendor	Notes
	680/42 nm BrightLine single-band bandpass filter	FF01-680/42-32	Semrock	
Continued on next page				

Table A1 – continued from previous page

Subsystem/module	Component	Catalogue number	Vendor	Notes
	609/54 nm BrightLine single-band bandpass filter	FF01-609/54- 25-STR	Semrock	Emission filter set for Twin 2
	680/42 nm BrightLine single-band bandpass filter	FF01-680/42- 25-STR	Semrock	
	525/45 nm single-band bandpass filter	FF01-525/45- 25-STR	Semrock	
	472/30 nm BrightLine single-band bandpass filter	FF02-472/30- 25-STR	Semrock	
Continued on next page				

Table A1 – continued from previous page

Subsystem/module	Component	Catalogue number	Vendor	Notes
	$f = 100$ mm, 50 mm diameter lens $f = 400$ mm, 75 mm diameter lens ORCA-Flash4.0 V3 Digital CMOS camera	VIS-NIR 49-284- INK VIS-NIR 88-598- INK C13440-20CU	Edmund Optics Edmund Optics Hamamatsu	Tube lens (for 11× magnification) Tube lens (for 44× magnification) Twin 1. Number of pixels: 2048 × 2048. Pixel size: $6.5 \mu\text{m}^2$. Full resolution frame rate: 100 frames/s (Camera link); 40 frames/s (USB). Quantum efficiency: 82% peak
Continued on next page				

Table A1 – continued from previous page

Subsystem/module	Component	Catalogue number	Vendor	Notes
	ORCA-Flash4.0 V2 Digital CMOS camera	C11440-22CU	Hamamatsu	Twin 2. Similar specifications to camera on Twin 1.
Sample mounting	Sample chamber	Custom	Protolabs	Material: Delrin 150 black acetal homopolymer
	Clamping rings	Custom	Protolabs	Material: Delrin 150 black acetal homopolymer; used to clamp glass windows to sample chamber
	Heat exchanger	Custom	Protolabs	Material: Aluminum 6061-T651 or Cooper
	Caddy	Custom	Protolabs	Material: WaterShed XC 11122
Continued on next page				

Table A1 – continued from previous page

Subsystem/module	Component	Catalogue number	Vendor	Notes
	Dive bar	Custom	Protolabs	Material: Stainless steel 316/316L
	Dive bar to go-niometer mount	Custom	Protolabs	Material: Stainless Steel 316/316L
	Dual-axis go-niometer	GN2/M	Thorlabs	
	Metric baseplate	UBP2/M	Thorlabs	
	Breadboard	MB1012	Thorlabs	For sample stack-up
	High-purity silicone Rubber .010" thick	87315K62	McMaster-Carr	Material: 55A Durometer; gasket used to clamp tightly seal glass windows to sample chamber
Continued on next page				

Table A1 – continued from previous page

Subsystem/module	Component	Catalogue number	Vendor	Notes
	High-purity silicone Rubber .020" thick 40mm glass cov- erslips 31mm glass cov- erslips	87315K63 10200-060 NC1491415	McMaster-Carr VWR Fisher Scientific	Used as bottom window for sample chamber Used as side windows for sample chamber
Motion control	nPFocus1000 piezo stage Controller LC.400 LS-50 linear stage; 16 TPI (z-stage)	3715250 200761 LS-50-AMERL	nPoint nPoint Applied Scien- tific Instrumen- tation	1000 μm travel 1 Axis LS-50 3D stage stack-up
Continued on next page				

Table A1 – continued from previous page

Subsystem/module	Component	Catalogue number	Vendor	Notes
	<p>Linear encoder option for z-drive (to attaining resolutions down to 50 nm)</p> <p>LS-50 linear stage; 4 TPI (x- and y-stages)</p> <p>Mount/bracket for linear stages</p> <p>Plate for attaching linear stage to breadboard</p>	<p>LE-Z</p> <p>LS-50-BMERL</p> <p>LS-5013</p> <p>LS-5012</p>	<p>Applied Scientific Instrumentation</p> <p>Applied Scientific Instrumentation</p> <p>Applied Scientific Instrumentation</p> <p>Applied Scientific Instrumentation</p>	

Table A1 – continued from previous page

Subsystem/module	Component	Catalogue number	Vendor	Notes
	Tiger controller, with xyz cards and joysticks	TG16_BASIC	Applied Scientific Instrumentation	
Instrument control	Supermicro motherboard with Intel C612 AHCI SATA controller NI PXIe-1073 Integrated MXIe, 5 peripheral slots, PCIe-8361, 3 m cable	X10DRH-CT 781161-01	CDW-G National Instruments	See (1) below for specifications
Continued on next page				

Table A1 – continued from previous page

Subsystem/module	Component	Catalogue number	Vendor	Notes
	Power cord, AC, U.S., 120 VAC, 2.3 m NI PXIe-6363, X Series DAQ (32 AI, 48 DIO, 4 AO) CB-68LPR I/O connector block SHC68-68-EPM shielded cable, 68-D-type to 68 VHDCI offset, 2 m	763000-01 781056-01 777145-02 192061-02	National Instruments National Instruments National Instruments National Instruments	
Continued on next page				

Table A1 – continued from previous page

Subsystem/module	Component	Catalogue number	Vendor	Notes
	Mainframe with RS-232 computer interface	SIM900	Stanford Research	
	Scaling amplifier	SIM983	Stanford Research	
	PicoScope 2000 Series oscilloscope	2207B		
	Pico Technologies BNC breakout box	2 channel; 70MHz PR35B32CMB	L-com	
Auxiliary	Monochrome CMOS camera	DCC3240M	Thorlabs	Behavior camera
Continued on next page				

Table A1 – continued from previous page

Subsystem/module	Component	Catalogue number	Vendor	Notes
	USB 3.0 I/O Cable 35-50 mm fixed focal length camera lens T-Cube LED Driver with Trigger Mode 780 nm, 200 mW mounted LED, 800 mA 1 inch diameter longpass filter	CAB-DCU-T3 MVL50M23 LEDD1B M780L3 FEL0750	Thorlabs Thorlabs Thorlabs Thorlabs Thorlabs	Cable for triggering Far-red LED Cut-on wavelength: 750 nm

(1) Windows 7 Professional w/SP1 64-Bit

- 1× SMC SuperChassis CSE-836BE1C-R1K03B
- 2× Intel Xeon E5-2650 V4 CPUs, 2.2GHz, 12-Core, 30M Cache, 105W
- 4× 32GB DDR4 2400MHz ECC Registered DIMMs (128GB Installed)
- 2× 10GbE NIC Ports - Intel X540 dual-port LAN, RJ45 (onboard)
- 1× Integrated IPMI 2.0 with dedicated LAN
- 1× MSI 2GB GDDR5 64-Bit GPU/Video card, N730K-2GD5LP/OC
- 8× Empty 3.5” Drive Bays with trays
- 1× H/W RAID Controller, LSI 3108, 2GB DDR3 Cache (S3108L-H8IR-16DD onboard)
Supported RAID Levels 0, 1, 5, 6, 10, 50, 60
- 2× 1000W Redundant Hot-Swap Power
- 1× Hot-Swap 512GB SATA 6Gb/s OS SSD drive, 2.5”, Samsung 850 Pro
- 8× Hot-Swap 4TB SATA 6Gb/s data drives, 7200 RPM, Seagate ST4000NM0035
- 1× DVDRW Slim Black SATA Samsung, SN-208FB/BEBE LG - #GTC0N

B List of the key SVIM parts

Table A2: Part numbers and descriptions of key components of SVIM setup.

Item	Acronym (Fig. 4.17)	Detailed descriptions	Part number	Manufacturer/Vendor
Laser system, visible 1-photon excitation	1P lasers	SOLE-6 Light Engine (lines used: 488, 561 nm)	SOLE-6 Light Engine	Omicron
Laser, near- infrared 2- photon excita- tion	2P laser	Chameleon Ultra 2	Chameleon Ultra 2	Coherent
Silver mirrors	MR		PF10-03-P01	Thorlabs
Polarizing beamsplitter	BS	Broadband, 620-1000 nm	PBS102	Thorlabs
Cylindrical lens	CL-1	$f = -75$ mm	LK1432RM-A	Thorlabs
Cylindrical lens	CL-2	$f = 150$ mm	LJ1629RM-A	Thorlabs
Cylindrical lens	CL-3	$f = 100$ mm	LF1567RM-A	Thorlabs
Continued on next page				

Table A2 – continued from previous page

Item	Acronym (Fig. 4.17)	Detailed descriptions	Part number	Manufacturer/Vendor
Galvos system, 2-dimensional	GV	6-mm aperture, silver mirrors	H8363	Cambridge Tech.
Scan lens	SL	$f = 110$ mm	LSM05-BB	Thorlabs
Tube lens, illu- mination	TL-I	$f = 200$ mm	AC508-200-B	Thorlabs
Illumination ob- jective, 10 \times	IO	NA = 0.3, $f = 20$ mm, water immer., WD = 3 mm	CFI Plan Fluor 10X W	Nikon
Sample chamber	SC	Machined from custom- design; black delrin	N/A	Proto Labs
Detection objec- tive 16 \times	DO	NA = 0.8, $f = 12.5$ mm, water immer., WD = 3 mm	CFI75 LWD 16X W	Nikon

Continued on next page

Table A2 – continued from previous page

Item	Acronym (Fig. 4.17)	Detailed descriptions	Part number	Manufacturer/Vendor
Detection objective 20×	DO	NA = 0.5, $f = 9$ mm, water immer., WD = 3.5 mm	UMPLFLN 20XW	Olympus
Filter, detection (green fluorescence)	FT	Pass band = 525/50 nm; 25-mm diameter	FF03-525/50- 25	Semrock
Filter, detection (red fluorescence)	FT	Pass band = 593/46 nm; 25-mm diameter	FF01-593/46- 25	Semrock
Tube lens, detection (used with 16× DO)	TL-D	$f = 400$ mm	AC508-400-A	Thorlabs
Tube lens, detection (used with 20× DO)	TL-D	$f = 180$ mm	AC508-180-A	Thorlabs
Continued on next page				

Table A2 – continued from previous page

Item	Acronym (Fig. 4.17)	Detailed descriptions	Part number	Manufacturer/Vendor
Micro-lens array	LA	Pitch = 150 μm , $f = 3.0$ mm, area = 16 \times 16 mm ²	APO-Q-P150-F3.0(633)	Flexible Optical B.V.
Relay lens	RL-1, RL-2	$f = 50$ mm; f/1.4	NIKKOR	Nikon
Detection camera	DC	Scientific CMOS, pixel size = 6.5 μm , 2560 \times 2160 pixels	Zyla 5.5	Andor

f : focal length

NA: numerical aperture

WD: working distance

C SVIM imaging and reconstruction parameters

Table A3: SVIM imaging and reconstruction parameters for vasculature results.

	Figures and Movies	Primary detection objective	Actual Magnification	Mode (excitation wavelength)	Laser power @ sample (mW)	Illumination z-extent (μm)	z -spacing (μm)	xy -pixel, acquired (μm)	xy -pixel, reconstructed (μm)	2D image z-slice rate (Hz)	3D captured volume rate (Hz)
		(a)			(b)	(c)	(d)	(e)	(f)	(g)	
Vasculature	Fig. 4.1c (SPIM)	16 \times , NA = 0.8	32 \times	SPIM (488 nm)	0.15	3.5	1	0.203	0.203	6 [#]	0.07*
	Fig. 4.1c (SVIM)	16 \times , NA = 0.8	32 \times	SVIM (488 nm)	1	100	2	0.203	0.311	10	10
	Figs. 4.3-4.6 (SPIM)	20 \times , NA = 0.5	20 \times	SPIM (488 nm)	0.15	3.5	1	0.325	0.325	6 [#]	0.023*
	Figs. 4.3-4.6 (100- μm SVIM)	20 \times , NA = 0.5	20 \times	SVIM (488 nm)	1	100	2	0.325	0.498	10	10
	Figs. 4.3-4.6 (200 μm SVIM)	20 \times , NA = 0.5	20 \times	SVIM (488 nm)	1.5	200	2	0.325	0.498	10	10
Continued on next page											

Table A3 – continued from previous page

	Figures and Movies	Primary detection objective	Actual Magnification	Mode (excitation wavelength)	Laser power @ sample (mW)	Illumination <i>z</i> -extent (μm)	<i>z</i> -spacing (μm)	<i>xy</i> -pixel, acquired (μm)	<i>xy</i> -pixel, reconstructed (μm)	2D image <i>z</i> -slice rate (Hz)	3D captured volume rate (Hz)
		(a)			(b)	(c)	(d)	(e)	(f)	(g)	
Bacteria-squid	Figs. 4.3-4.6 (300 μm SVIM)	20 \times , NA = 0.5	20 \times	SVIM (488 nm)	2	300	2	0.325	0.498	10	10
	Figs. 4.3-4.6 (550 μm SVIM)	20 \times , NA = 0.5	20 \times	SVIM (488 nm)	3	550	2	0.325	0.498	10	10
	Figs. 4.3-4.6 (Wide-field)	20 \times , NA = 0.5	20 \times	WF- LFM (488 nm)	4	Entire sam- ple	2	0.325	0.498	10	10
Bacteria-squid	Fig. 4.7a	20 \times , NA = 0.5	20 \times	WF- LFM (488 nm)	15	Entire sam- ple	2	0.325	0.498	20	20
	Figs. 4.7c and Fig. 4.18c-d	20 \times , NA = 0.5	20 \times	SVIM (488 nm)	15	100	2	0.325	0.498	20	20

Continued on next page

Table A3 – continued from previous page

		Figures and Movies		Primary detection objective	Actual Magnification	Mode (excitation wavelength)	Laser power @ sample (mW)	Illumination <i>z</i> -extent (μm)	<i>z</i> -spacing (μm)	<i>xy</i> -pixel, acquired (μm)	<i>xy</i> -pixel, reconstructed (μm)	2D image <i>z</i> -slice rate (Hz)	3D captured volume rate (Hz)
				(a)			(b)	(c)	(d)	(e)	(f)	(g)	
		Fig. 4.18b	20 \times , NA = 0.5	20 \times	SPIM (488 nm)	1	3.5	1	0.325	0.325	6#	0.035*	
		Movies 4.8- 4.10		Rendered from the same data as presented in Fig. 4.7a-c									
Heart-blood	Fig. 4.7d-g (Endo- cardium)	16 \times , NA = 0.8	32 \times	SVIM (488 nm)	10	150	2	0.203	0.311	90	90		
	Fig. 4.7d-g (Blood)	16 \times , NA = 0.8	32 \times	SVIM (561 nm)	15	150	2	0.203	0.311	90	90		
	Fig. 4.13a-b (Endo- cardium)	20 \times , NA = 0.5	20 \times	SVIM (488 nm)	10	150	2	0.325	0.498	90	90		
	Fig. 4.13d-e (Blood)	20 \times , NA = 0.5	20 \times	SVIM (561 nm)	15	150	2	0.325	0.498	90	90		
Continued on next page													

Continued on next page

Table A3 – continued from previous page

		Figures and Movies		Primary detection objective	Actual Magnification	Mode (excitation wavelength)	Laser power @ sample (mW)	Illumination <i>z</i> -extent (μm)	<i>z</i> -spacing (μm)	<i>xy</i> -pixel, acquired (μm)	<i>xy</i> -pixel, reconstructed (μm)	2D image <i>z</i> -slice rate (Hz)	3D captured volume rate (Hz)
				(a)			(b)	(c)	(d)	(e)	(f)	(g)	
		Movies 4.11, 4.12 Rendered from the same data as presented in Fig. 4.7d-g											
Brain	Fig. 4.14 (Wide-field)	20 \times , NA = 0.5	20 \times	WF-LFM (488 nm)	0.5	Entire sample	2	0.325	0.498	1	1		
	Fig. 4.14 (1P-SVIM)	20 \times , NA = 0.5	20 \times	1P-SVIM (488 nm)	0.4	100	2	0.325	0.498	1	1		
	Fig. 4.14 (2P-SVIM)	20 \times , NA = 0.5	20 \times	2P-SVIM (488 nm)	100	100	2	0.325	0.498	1	1		
	Figs. 4.15- 4.16	Identical parameters to Fig. 4.14h-j, for the respective imaging modalities											
Continued on next page													

Table A3 – continued from previous page

	Figures and Movies	Primary detection objective	Actual Magnification	Mode (excitation wavelength)	Laser power @ sample (mW)	Illumination <i>z</i>-extent (μm)	<i>z</i>-spacing (μm)	<i>xy</i>-pixel, acquired (μm)	<i>xy</i>-pixel, reconstructed (μm)	2D image <i>z</i>-slice rate (Hz)	3D captured volume rate (Hz)
		(<i>a</i>)			(<i>b</i>)	(<i>c</i>)	(<i>d</i>)	(<i>e</i>)	(<i>f</i>)	(<i>g</i>)	
	Fig. 4.2 (Beads)	16 \times , NA = 0.8	32 \times	SVIM (488 nm)	0.1	100	2	0.203	0.311	2	2

(*a*) Actual magnification was determined by the ratio of the focal length of the primary detection objective over the focal length of the tube lens used.

(*b*) Illumination *z*-extent in SPIM mode was determined by the nominal thickness of the light sheet at the center of the field of view. For SVIM modes, the illumination *z*-extent was controlled by setting the scanning amplitude of the illumination galvo (see Methods Section 4.4.1).

(*c*) Spacing in *z*-direction for SPIM was determined by the *z*-step size of the acquired *z*-stack. Spacing in SVIM was computationally set at the onset of the light-field reconstruction.

(*d*) Pixel size, acquired, was determined by the physical size of the camera pixel (6.5 μm) divided by the actual magnification used during imaging.

(*e*) Pixel size, reconstructed, for the SVIM/LFM cases, was computationally set at the onset of the light-field reconstruction. For SPIM, the same acquired pixel size was used.

(*f*) The 2D imaging *z*-slice rate was achieved by “back-to-back” exposures, incorporating

both the exposure time and camera readout time (approximately 10 ms for full camera frame). For the SPIM cases (#), the 2D imaging rate stated here also included the additional overhead time that was required to move the z -stage from one position to the next, which typically was the rate limiting factor. For our setup, this overhead time was about 125 ms, and when combined with the 10-ms camera readout time, set a hard limit of approximately 7.4 Hz for the z -slice rate.

(g) The 3D captured volume rate for the SPIM cases (*) were for z -stacks of depth = 100, 300, and 200 μm , for Figs. 4.1c, 4.3a, and 4.18, respectively. For the SVIM/LFM cases, upon 3D reconstruction of the raw 2D data, the 2D imaging rate simply became the captured volume rate. Note that the volume rates listed here have not been normalized by the number of diffraction-limited voxels contained in each volume - this issue is addressed in Supplementary Note 4.5.2 and Supplementary Table 4.1.